



NATIONAL CENTRE FOR NUCLEAR RESEARCH

DOCTORAL THESIS

**The gluon contribution to the Sivers
effect measurement at the COMPASS
experiment**

Author:

Adam SZABELSKI

Supervisor:

dr hab. Krzysztof KUREK, prof. NCBJ

Supporting supervisor:

dr Marcin STOLARSKI, LIP Lisbon

*Submitted in partial fulfillment
of the requirements for the degree of
Doctor of Philosophy*

October 24, 2016

To my parents,
the greatest pair of physicists I know

Abstract

The objective of this thesis is the measurement of the Sivers effect for gluons. The Sivers effect describes the correlation between the spin of the nucleon and the orbital motion of partons. It can be measured via Semi-Inclusive Deep Inelastic scattering of lepton on a transversely polarised proton and deuteron targets by determining the azimuthal asymmetry related to the modulation in the Sivers angle ϕ_{Siv} . In the thesis a method of obtaining the Sivers asymmetry for gluons is presented. It is based on the model of three single-photon-exchange processes: photon-gluon fusion (PGF), QCD Compton (QCDC) and leading process (LP). A method of simultaneous extraction of the Sivers asymmetries of the three processes with the use of Monte Carlo (MC) and neural networks (NN) approach is presented. The method has been applied to COMPASS data taken with 160GeV/c muon beam scattered off transversely polarised deuteron and transversely polarised proton target. For each target a data sample of events containing at least two hadrons with large transverse momentum has been selected. Finally the results for gluon Sivers asymmetry were obtained to be: $A_g^d = -0.14 \pm 0.15(stat.) \pm 0.06(syst.)$ at $\langle x_g \rangle = 0.13$ and $A_g^p = -0.26 \pm 0.09(stat.) \pm 0.08(syst.)$ at $\langle x_g \rangle = 0.15$.

Pomiar wkładu gluonów do efektu Siversa w eksperymentcie COMPASS.

Celem niniejszej dysertacji doktorskiej jest pomiar efektu Siversa dla gluonów. Efekt Siversa opisuje korelację między spinem nukleonu a ruchem orbitalnym partonów w tym nuklonie. Może być on zmierzony w procesie semi-inkluzywnego głęboko-nieelastycznego rozpraszania (ang. SIDIS) leptonów na poprzecznie spolaryzowanej tarczy protonowej lub deuteronowej poprzez wyznaczenie asymetrii azymutalnej powiązanej z modulacją w kącie Siversa ϕ_{Siv} . W niniejszej pracy zaprezentowana jest metoda wyznaczania tej asymetrii dla gluonów. Opiera się ona na modelu zakładającym trzy procesy kontrybuujące do rozpraszania lepton-nukleon: fuzja fotonowo-gluonowa (ang. PGF), chromodynamiczne rozpraszanie comptonowskie (ang. QCDC) oraz proces wiodący (ang. LP). Przedstawiona jest metoda jednoczesnego wyznaczania asymetrii Siversa wszystkich trzech procesów oparta jest na symulacjach Monte Carlo (MC) i wykorzystaniu sieci neuronowych (ang. NN). Metoda została użyta do analizy danych eksperymentu COMPASS zebranych z wiązką mionową o energii 160 GeV/c rozpraszanej na poprzecznie spolaryzowanych tarczach: deuteronowej i protonowej. Dla obu próbek danych dokonano selekcji par hadronów o dużym pędzie poprzecznym. Uzyskana asymetria Siversa dla gluonów wynosi: $A_g^d = -0.14 \pm 0.15(stat.) \pm 0.06(syst.)$ przy $\langle x_g \rangle = 0.13$ and $A_g^p = -0.26 \pm 0.09(stat.) \pm 0.08(syst.)$ przy $\langle x_g \rangle = 0.15$.

Contents

Abstract	iii
Streszczenie	iv
1 Introduction	1
2 Theoretical Framework	5
2.1 Deep Inelastic Scattering	5
2.1.1 Kinematic variables	5
2.1.2 DIS inclusive cross-section	7
2.1.3 The measurement of g_1 and g_2 . Cross-section asymmetries.	9
2.2 Parton model	12
2.2.1 Naive parton model	12
2.2.2 QCD improved parton model	13
2.3 Semi-Inclusive Deep inelastic scattering (SIDIS)	14
2.3.1 Transversity	14
2.3.2 Transverse Momentum Dependent structure functions (TMDs).	16
2.3.3 The Sivers effect and the orbital motion of gluons.	19
3 Nucleon spin decomposition in measurements	21
3.1 $\Delta\Sigma$ - the fraction of nucleon spin carried by quark spins	21
3.2 ΔG - the gluon spin contribution to the nucleon spin	26
3.2.1 Open Charm production	27
3.2.2 $\Delta g/g$ from high transverse momentum hadron pairs	27
3.2.3 $\Delta g/g$ from COMPASS for $Q^2 < 1$	30

3.2.4	$\Delta g/g$ from inclusive single hadrons and high- p_T hadron pairs from HERMES data	31
3.2.5	$\Delta g/g$ from single all- p_T hadrons for $Q^2 > 1 \text{ GeV}^2$	32
3.2.6	ΔG global fit with data from pp collisions	33
3.3	Quark and gluon orbital angular momentum	35
3.3.1	Sivers asymmetry measurements	35
3.3.2	General Parton Distributions	36
3.3.3	Calculations on QCD Lattice	37
3.4	Measurements giving access to Gluon Sivers Function	39
3.5	Future measurements of gluon Sivers effect	41
4	The COMPASS experiment at CERN	43
4.1	Introduction	43
4.2	The beamline	44
4.3	The polarised target	45
4.4	The COMPASS spectrometer	48
4.4.1	The Beam Telescope	48
4.4.2	Very small area trackers	49
4.4.3	Small Area Trackers	49
4.4.4	Large Area Trackers	49
4.4.5	Calorimeters	49
4.4.6	Muon Filters	50
4.4.7	Ring Imaging CHerenkov (RICH) detector.	50
4.5	Trigger System	50
4.6	DAQ - the data acquisition system	52
4.7	Data analysis	53
5	Statistical concepts for extracting signal and background asymmetry at COMPASS	55
5.1	Number of measured events and the asymmetry	55
5.2	Inputs to the raw asymmetry	57

5.2.1	Dilution factor	57
5.2.2	Beam and target polarisation	58
5.3	Asymmetry extraction with the optimisation of statistical errors	58
5.3.1	A very simple example	59
5.3.2	An example with unknown acceptance	60
5.3.3	Extracting signal and background asymmetry	62
6	Methods of extracting gluon asymmetries in the COMPASS experiment	65
6.1	Open Charm production	65
6.2	High- p_T hadron pair production	71
6.3	All- p_T method of $\Delta g/g$ extraction	75
7	Monte Carlo simulation and Neural Network training	81
7.1	LEPTO generator	81
7.1.1	Generation procedure	81
7.2	Cross-section parameterisations	82
7.3	First order QCD processes	83
7.4	Hadronisation	83
7.5	Parton shower	84
7.6	Simulation of experimental conditions	85
7.7	Comparison between data and Monte Carlo simulations	86
7.8	Neural Networks	87
7.9	Parameterisation	90
7.10	Validation of the neural network training	92
7.11	The gluon momentum fraction x_G and the quark momentum fraction in QCD Compton process x_C	93
8	The gluon contribution to the Sivers effect at the COMPASS experiment	97

8.1	Data selection	97
8.1.1	Discussion of the main cuts	97
8.1.2	Selection of the two data samples for the deuteron and proton targets	100
8.2	Two-hadron SIDIS cross-section	103
8.3	The weighted method for gluon Sivers asymmetry extraction	105
8.3.1	Analysis method test on a Monte Carlo sample	108
8.4	Results	108
8.4.1	Deuteron target	108
8.4.2	Proton target	109
8.4.3	Interpretation of statistical errors	110
8.5	Results with the Unbinned Maximum Likelihood method	111
8.6	COMPASS 2007 data set from transversely polarised protons	111
8.7	The gluon Sivers asymmetry measurement via J/Ψ production at COMPASS	113
8.7.1	Event selection	113
8.7.2	J/Ψ candidate selection	114
8.7.3	The Sivers asymmetry evaluation	116
8.7.4	Background subtraction	116
8.8	Conclusions	118
9	Systematic studies	119
9.1	Systematic error due to MC	119
9.2	False asymmetries	120
9.3	Influence of the generated false asymmetry on the final result	122
9.4	Cut on charges of the two leading hadrons	122
9.5	Radiative corrections systematics	122
9.6	Q^2 cut	124
9.7	Two x_{Bj} bins	125
9.8	Sivers + 7 other asymmetries	127

9.9	Single fit vs two fits in two ϕ_{Sivers} bins	128
9.10	Target polarisation and dilution factor: δP_T and δf	129
9.11	Systematic summary	129
10	Conclusions	131
A	Two-hadron SIDIS cross-section	133
B	Approximation of asymmetries by linear dependence on x	137
C	COMPASS spectrometer alignment	141
C.1	Alignment parameters	141
C.2	The principle of alignment	143
C.3	The alignment procedure	144
C.4	Exemplary plots	145
C.5	Quality criteria	147
	Abbreviations	149
	Bibliography	151
	Acknowledgements	158

List of Figures

2.1	Deep Inelastic Scattering (DIS)	5
2.2	angle definition in laboratory frame	6
2.3	Leptonic and hadronic part of the DIS process	8
2.4	F_2 structure function measurement results	10
2.5	xg_1 structure function measurement results	12
2.6	Feynman diagrams of the splitting functions	14
2.7	g_1 structure function measurement results	15
2.8	Semi-Inclusive Deep Inelastic Scattering (SIDIS)	16
2.9	Transverse Momentum Dependent structure functions (TMDs)	17
2.10	azimuthal angles	18
2.11	Chromodynamic lensing as a Sivvers mechanism.	19
3.1	Triangle diagram of axial anomaly	25
3.2	Parton distribution functions (PDFs)	26
3.3	Photon Gluon Fusion (PGF)	27
3.4	Feynman diagrams considered for $\gamma^* N$ scattering.	28
3.5	Process contribution to the high- p_T sample at low Q^2	31
3.6	Compilation of the $\Delta g/g$ measurements	33
3.7	Lowest order Feynman diagrams for p-p collisions	33
3.8	ΔG obtained from global fit to data	35
3.9	COMPASS results for the Sivvers asymmetries of identified hadrons. Proton. 36	
3.10	COMPASS results for the Sivvers asymmetries of identified hadrons. Deuteron. 37	
3.11	General Parton Distributions from Hard Exclusive Meson Production at COMPASS.	38
3.12	Illustration of the periodic lattice and its degrees of freedom.	38
3.13	The contributions of u and d quarks to the nucleon spin from QCD Lattice calculations.	39
3.14	A_N measurement at PHENIX with different choices for gluon Sivvers function 40	
3.15	The SSA A_N compared with PHENIX data as a function of p_T	41
4.1	The absolute value of the muon beam polarisation	45
4.2	COMPASS beamline scheme.	45

4.3	The dynamic nuclear polarisation for the proton-electron system.	46
4.4	The three-cell polarised COMPASS target	47
4.5	The top view of COMPASS 2004 muon setup.	48
4.6	The sketch of the most relevant elements for the trigger system.	51
4.7	Kinematic coverage by triggers	52
4.8	General architecture of the DAQ system.	53
6.1	Photon Gluon Fusion (PGF)	65
6.2	Invariant mass spectra for the $D_{k\pi}^0$ and $D_{k\pi}^*$ samples	67
6.3	Examples of NLO processes contributing to the muoproduction of $c\bar{c}$ pair	70
6.4	COMPASS Open Charm NLO result	70
6.5	All- p_T method. Binning in x	78
6.6	LO $\Delta g/g$ measurements	79
7.1	Illustration of the acceptance-rejection method.	82
7.2	Iterative string fragmentation into hadrons.	84
7.3	Selected Feynman diagrams of the PGF process with gluon emissions treated by Parton Shower mechanism.	85
7.4	Kinematic variable distributions in MC and Data high-pt samples nor- malised to the same number of events. Deuteron Data and MC2004. . . .	86
7.5	Kinematic variable distributions in MC and Data high-pt samples nor- malised to the same number of events. Proton Data and MC2010.	87
7.6	Multilayer perceptron (MLP) neural network.	88
7.7	Schematic representation of a neuron $E_i^{(k)}$	88
7.8	Neuron activation functions	89
7.9	Neural Network output for the proton 2010 data sample and the three given target values PGF - (0, 0), QCDC - (1, 0) and LP - (1/2, $\sqrt{3}/2$) . . .	91
7.10	Neural Network training validation - p_T^2 dependence. Deuteron target. . .	92
7.11	Neural Network training validation - p_T^2 dependence. Proton target. . . .	93
7.12	Neural Network training validation - process fraction dependence. Deuteron target.	94
7.13	Neural Network training validation - process fraction dependence. Proton target.	94
7.14	Validation of the NN training for x_C (left) and x_G (right). Deuteron target.	95
7.15	Validation of the NN training for x_C (left) and x_G (right). Proton target.	95
8.1	COMPASS and HERMESS results of single hadron Sivers asymmetry measurement with the proton target.	98
8.2	Monte Carlo studies of correlations between the gluon azimuthal angle ϕ_G and the hadronic azimuthal angle ϕ_h or ϕ_2h	99

8.3	Dependence on the process fraction on the Siverson angle	105
8.4	Validation of the analysis method. Exemplary plot. $A_{PGF}^{SIM} = -0.25$, $A_{QCDC}^{SIM} = 0.2$, $A_{LP}^{SIM} = 0.05$	108
8.5	Period-by-period results for Siverson asymmetry of three processes: PGF, QCDC, LP. Deuteron target.	109
8.6	Period-by-period results for Siverson asymmetry of three processes: PGF, QCDC, LP. Proton target 2010.	110
8.7	Weighted method vs maximum likelihood method. Deuteron.	112
8.8	Weighted method vs maximum likelihood method. Proton.	112
8.9	Period-by-period results for Siverson asymmetry of three processes: PGF, QCDC, LP. Proton target 2007.	113
8.10	Dimuon invariant mass in the two z -intervals for the J/Ψ signal selection	115
8.11	The final Siverson asymmetry for two methods of background treatment. . .	118
9.1	A_{PGF} for different MC simulations.	120
9.2	False asymmetries. Compatibility with zero. Deuteron.	121
9.3	False asymmetries. Compatibility with zero. Proton.	121
9.4	False asymmetries. Compatibility with between upstream and downstream part of the target.	123
9.5	False asymmetries. Compatibility with between upstream and downstream part of the target.	123
9.6	Final result dependence on false asymmetry. For one target configuration: $\omega' = \omega(1.0 + 0.01 \sin \phi)$. Top panel: deuteron target. Bottom panel: proton target.	124
9.7	The influence of the cut on the hadron charges $q_1 \cdot q_2 = -1$. Deuteron. . .	125
9.8	The influence of the cut on the hadron charges $q_1 \cdot q_2 = -1$. Proton. . .	125
9.9	The influence of including radiative corrections in the MC simulations on the final results	126
9.10	Comparison between the standard analysis and the analysis with the cut $Q^2 < 20(GeV/c)^2$ applied.	126
9.11	Result of applying two x_{Bj} bins. Deuteron.	127
9.12	Result of applying two x_{Bj} bins. Proton.	127
9.13	Proof of the orthogonality of Siverson and 7 other SIDIS modulations. Deuteron.	128
9.14	Proof of the orthogonality of Siverson and 7 other SIDIS modulations. Proton.	128
9.15	One fit in two $\phi_{Siverson}$ bins vs two fits in each bin.	129
C.1	Exemplary residual plots	146
C.2	Misalignment in z of the SI01 station	146

C.3	Corrected z of the SI01 station	147
-----	---	-----

List of Tables

8.1	Statistics after cuts for whole deuteron target data (three period pairs) . .	102
8.2	Statistics after cuts for whole 2010 year (12 periods)	103
8.3	Effect of cuts for the J/Ψ events selection	115
8.4	Summary of the results of the gluon Siverts asymmetry extraction from J/Ψ production	117
9.1	Systematics summary.	129
B.1	Values of weighted averages of $x \langle x \rangle_{\beta\omega}$ for the three processes for all periods and target configurations. Deuteron.	138
B.2	Values of weighted averages of $x \langle x \rangle_{\beta\omega}$ for the three processes for all periods and target configurations. Proton 2010.	139

Chapter 1

Introduction

The world that surrounds us is built of atoms. Atoms consist of nuclei and pointlike electrons. Nuclei are built of protons and neutrons. Neutrons and protons have spin¹ $1/2$. Spin is a quantised entity and is a consequence of space-time symmetry. Since 1960s and the SLAC experiment we know that neutron and proton are composite objects. Feynman's parton model [1] described the experimental cross-section of high-energy lepton nucleon scattering (SLAC deeply inelastic scattering experiment [2]). In this model partons had negligible mass with respect to the nucleon mass and the number of partons in the nucleon could be infinite. The so-called 'quark model' proposed by Gell-Mann [3] and Zweig [4] predicted that nucleons consist of 3 quarks (having spin $1/2$) carrying $1/3$ of the nucleon mass each and a fraction of electric charge.

The differences between the two models and the fact that neither partons nor quarks were observed outside the nucleon was understood after D. Gross, F. Wilczek [5] and D. Politzer [6] worked out a theoretical description of the quark interactions in 1973. They proposed gluons as carriers of the strong interaction between quarks. Six years later gluons were experimentally proven to exist ([7]).

Today we understand the nucleon structure as built of 3 valence quarks (of spin $1/2$ and fractional electric charge) which exchange gluons (of spin 1 and zero electric charge) which may fluctuate for a short time into a quark-antiquark pair, the so-called sea quarks.

The spin of nucleons is measured to be $1/2$ and it is a natural expectation that it should be explained by the spin and orbital angular momentum of quarks and gluons. In the QCD improved parton model the spin of the nucleon can be decomposed to the contribution of quark helicity - $\Delta\Sigma$, contribution of orbital angular momentum of

¹throughout this thesis $\hbar = c = 1$ is assumed

quarks - L_q , contribution of gluon helicity - ΔG and contribution of gluon orbital angular momentum - L_g :

$$\frac{1}{2} = \frac{1}{2}\Delta\Sigma + L_q + \Delta G + L_g.$$

In this decomposition light-cone gauge is assumed. Throughout this thesis it will always be the case and gluon orbital angular momentum (OAM) will be used interchangeably with gluon collective orbital motion. It should be noted, however, that gluon OAM is not a well defined, gauge-invariant observable in the light-cone gauge.

The value of $\Delta\Sigma$ has been measured first at the SLAC experiment [8] by scattering polarised electrons on polarised protons. In a kinematic range where valence quarks dominate a sizeable cross-section asymmetries were obtained which seem to follow the theoretical expectations for $\Delta\Sigma$ to be ~ 0.6 . But the EMC experiment [9, 10] in broader kinematic range has shown much smaller contribution of quark polarisation to the nucleon spin what began the “nucleon spin crisis” and is still an unsolved problem. The EMC result has been confirmed by SMC [11], SLAC [12, 13] and HERMES [14]. The latest result of $\Delta\Sigma$ measurement has been obtained by COMPASS [15]: $\Delta\Sigma \in [0.26; 0.36]$. The interval limits reflect mainly the large uncertainty in the determination of the gluon contribution.

The next candidate was the contribution of the spin of the gluons - $\Delta G = \int \Delta g dx$. Several attempts were made to extract directly the gluon polarisation $\Delta g/g$ from COMPASS data. The so-called Open Charm analysis, selecting mesons with heavy quarks which originate in the nucleon sea described in [16] and selection of light hadron pairs with large transverse momentum described in [16] and [17] was performed. Both methods suffer from large statistical error and they do not exclude neither zero value nor a significant signal for $\Delta g/g$. The most recent preliminary analysis of COMPASS data based on hadron production [18] gives a nonzero value: $\Delta g/g = 0.113 \pm 0.038 \pm 0.035$. All three methods use a neural network (NN) approach and will be presented in Chapter 6 in detail. Recent global QCD analysis including data from Relativistic Heavy Ion Collider (RHIC) [19] gives a result of ΔG different from zero but not sufficient to solve the nucleon spin puzzle. It should be noted that all available data concerning Δg were obtained for relatively large x . The region of small x will be covered by the planned Electron Ion Collider (EIC) [20].

In the parton model the cross-section of the lepton nucleon scattering is fully described by the unpolarised structure function F_1 . The spin dependent part of the cross-section (accessible in measurement with polarised beam and polarised target) is described by the function g_1 in case of polarisation longitudinal to the virtual photon. The density function F_1 (unpolarised case) and the helicity function g_1 are not sufficient to describe

the nucleon at leading order. Another function called transversity - h_1 describes the correlation of parton spin to the transversely (with respect to the intermediate photon) polarised nucleon [21]. As the nucleon is described as a relativistic object moving with the speed of light helicity and transversity are not the same because boost and rotation do not commute.

These three functions, F_1, g_1, h_1 do not depend on intrinsic transverse momentum of partons - k_T . Functions which vanish after integration over k_T were expected to be small until the measurement of proton-proton collisions [22] ($pp^\uparrow \rightarrow \pi X$) which revealed a significantly large asymmetry. There are 8 k_T -dependent distribution functions including the Sivers function [23], describing the correlation of transverse momentum of quarks with the spin of a transversely polarised nucleon and connected to the parton's orbital angular momentum. Measurement of the Sivers function for gluons is the topic of this thesis.

The thesis has the following structure. In Chapter 2 the theoretical basis of the nucleon spin structure is shortly described. Chapter 3 gives a brief summary of the measurements of the nucleon spin decomposition elements. The COMPASS experiment is presented in Chapter 4. Chapters 5 and 6 are meant to be an introduction to describe the analysis method used in the thesis. The former provides basic statistical concepts for extracting asymmetries from COMPASS data, the latter describes in more detail (with respect to Chapter 3) three COMPASS analyses in which these concepts were applied. The necessary tools, the Neural Networks and Monte Carlo simulations are presented in Chapter 7. The final analysis method of the measurement of the gluon contribution to the Sivers effect at COMPASS is given in Chapter 8 which is the main chapter of this thesis. It contains the discussion of the data sample selection, the analysis method, the results and the discussion of statistical errors. Finally, the systematic studies are given in Chapter 9. Chapters 8 and 9 are the author's contribution to the spin physics.

In Appendix A a description of the cross-section for Semi-Inclusive Deep Inelastic Scattering two-hadron production is given. Some technical details concerning assumptions on the average values of asymmetries extracted in the analysis are the subject of Appendix B and the procedure of the alignment of the spectrometer (one of the author's responsibilities in the collaboration) is described in Appendix C.

Chapter 2

Theoretical Framework

2.1 Deep Inelastic Scattering

2.1.1 Kinematic variables

Deep Inelastic Scattering (DIS) is a process of scattering a point-like lepton off a nucleon:

$$l + N \rightarrow l' + X, \quad (2.1)$$

where the nucleon N breaks into the hadronic final state X . In Figure 2.1 a schematic DIS event is presented. A lepton is scattered on a proton via single photon exchange. To

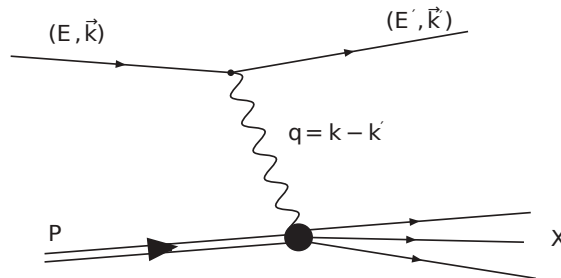


FIGURE 2.1: Deep Inelastic Scattering. Single photon exchange approximation. Figure from [17].

describe this DIS process cross-section for a given beam energy it is enough to use two independent Lorentz invariant variables: Q^2 - the virtuality of the intermediate photon and ν - the energy transferred to the nucleon defined in Equations (2.2) and (2.3):

$$Q^2 = -q^2 = (k - k')^2 \stackrel{lab}{=} 2(|\vec{k}||\vec{k}'| \cos \theta - EE' + m^2), \quad (2.2)$$

$$\nu = \frac{P \cdot q}{M} \stackrel{lab}{=} E - E', \quad (2.3)$$

where M is the nucleon mass and P is the initial nucleon momentum $P \stackrel{lab}{=} (M, \vec{0})$. The momenta of the incoming (k) and outgoing (k') lepton are defined as follows

$$k^\mu = (E, \vec{k}) \stackrel{lab}{=} (E, 0, 0, |\vec{k}|), \quad (2.4)$$

$$k'^\mu = (E', \vec{k}') \stackrel{lab}{=} (E', |\vec{k}'| \sin \theta \cos \phi, |\vec{k}'| \sin \theta \sin \phi, |\vec{k}'| \cos \theta). \quad (2.5)$$

The angles are defined in Figure 2.2. Instead of the two variables: Q^2 and ν one can

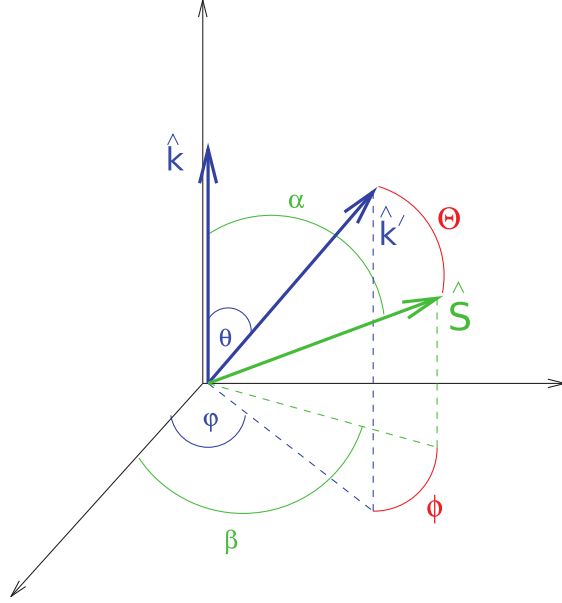


FIGURE 2.2: The definition of angles in the laboratory frame. Figure from [24].

use two other dimensionless variables:

$$x = \frac{Q^2}{2P \cdot q} = \frac{Q^2}{2M\nu}, \quad (2.6)$$

$$y = \frac{P \cdot q}{P \cdot k} \stackrel{lab}{=} \frac{\nu}{E}. \quad (2.7)$$

Here x is the Bjorken's scaling variable which has the meaning, in the infinite momentum frame, of nucleon momentum fraction carried by the struck parton and y is the fraction of lepton's energy transferred to the nucleon in the laboratory frame. Another quantity used to describe deep inelastic scattering is the invariant mass of the final hadronic state X ,

$$W^2 = (P + q)^2 = M^2 + \frac{Q^2}{x} - Q^2 = M^2 + 2M\nu - Q^2. \quad (2.8)$$

The inelastic kinematic region is defined by two conditions: $W^2 \gg M^2$ and $\nu \gg M$, while the Deep Inelastic Scattering region by the condition $Q^2 > 1\text{GeV}^2$.

2.1.2 DIS inclusive cross-section

The inclusive, meaning that the hadronic final state X is not measured, differential cross-section for lepton-nucleon scattering can be written in the form (as in [16])

$$\frac{d\sigma}{dE'd\Omega} = \left(\frac{E'}{M\nu}\right) \frac{d\sigma}{dx dy d\phi} = \left(\frac{Q^2 E'}{y M \nu}\right) \frac{d\sigma}{dx dQ^2 d\phi} = \frac{\alpha^2}{16\pi^2 Q^4} \frac{E'}{ME} L_{\mu\nu} W^{\mu\nu}, \quad (2.9)$$

where the scattered lepton energy is between E' and $E' + dE'$ and $\Omega(\theta, \phi)$ is the solid angle in which the scattered lepton was detected. $L_{\mu\nu}$ is the leptonic tensor and $W_{\mu\nu}$ is the hadronic tensor (for detailed derivation see [25, 26]). The leptonic tensor contains information about the emission of photon by lepton of mass m and spin s :

$$L^{\mu\nu}(k, s, k', s') = \bar{u}(k', s') \gamma^\mu u(k, s) \bar{u}(u, s) \gamma^\nu u(k', s'), \quad (2.10)$$

where u, \bar{u} denote the Dirac spinors and s, s' is the spin four-vector of incoming and scattered lepton. $L^{\mu\nu}$ can be decomposed into the symmetric and antisymmetric part both calculable in QED

$$L^{\mu\nu} = L_{(S)}^{\mu\nu} + iL_{(A)}^{\mu\nu}, \quad (2.11)$$

where

$$L_{(S)}^{\mu\nu} = 2k'^\mu k^\nu + 2k'^\nu k^\mu + 2(m^2 - k' \cdot k) g^{\mu\nu}, \quad (2.12a)$$

$$L_{(A)}^{\mu\nu} = 2m \epsilon^{\mu\nu\rho\sigma} q_\rho s_\sigma. \quad (2.12b)$$

Here $g^{\mu\nu}$ is the symmetric metric tensor and $\epsilon^{\mu\nu\rho\sigma}$ is the Levi-Civita antisymmetric tensor. s_σ - the lepton spin four-vector is present only in the antisymmetric part of $L^{\mu\nu}$. The hadronic tensor describes the internal structure of the nucleon. By definition

$$W_{\mu\nu} = \langle P, S | j_\mu j_\nu^\dagger | P, S \rangle, \quad (2.13)$$

where S is the spin four-vector of the nucleon with momentum P . Here $S \cdot P = 0$ and $S^2 = -1$. In the laboratory frame where the nucleon is at rest $S \stackrel{lab}{=} (0, \sin \alpha \cos \beta, \sin \alpha \sin \beta, \sin \alpha)$. Here α and β are defined by Figure 2.2. Also $W^{\mu\nu}$ can be decomposed into symmetric and antisymmetric part

$$W^{\mu\nu} = W_{(S)}^{\mu\nu} + iW_{(A)}^{\mu\nu}, \quad (2.14)$$

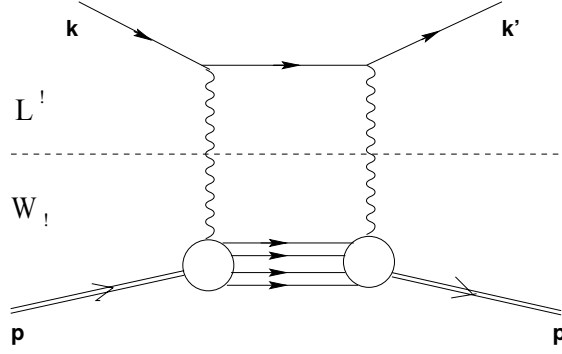


FIGURE 2.3: Separation of leptonic and hadronic part of the DIS process. Figure from [16].

In general $W^{\mu\nu}$ cannot be calculated directly as it depends on non-perturbative QCD. However, it can be parametrised by spin-averaged and spin-dependent structure functions in the following way

$$W_{(S)}^{\mu\nu} = 2F_1 \left(-g^{\mu\nu} + \frac{q^\mu q^\nu}{2} \right) + \frac{2F_2}{P \cdot q} \left(P^\mu - \frac{P \cdot q}{q^2} q^\mu \right) \left(P^\nu - \frac{P \cdot q}{q^2} q^\nu \right), \quad (2.15a)$$

$$W_{(A)}^{\mu\nu} = \frac{2Mg_1}{P \cdot q} \epsilon^{\mu\nu\rho\sigma} q_\rho S_\sigma + \frac{2Mg_2}{(P \cdot q)^2} \epsilon^{\mu\nu\rho\sigma} q_\rho ((P \cdot q)S_\sigma - (s \cdot q)P_\sigma). \quad (2.15b)$$

The structure functions of the nucleon, F_1, F_2, g_1, g_2 , are typically presented as functions of x and Q^2 and are measured in experiments. The first two describe the unpolarised structure of the nucleon while the latter pair contains information about the nucleon spin orientation. Equations (2.15a) and (2.15b) can be simplified by means of lepton current conservation ($q_\mu L^{\mu\nu} = 0$) which implies that terms containing q^μ vanish.

The differential cross-section described in equation 2.9 can now be split into the symmetric and antisymmetric part where only the latter depends on the spin of lepton and nucleon. Taking into account that the contraction of symmetric and antisymmetric tensors cancel one gets

$$\begin{aligned} \frac{d\sigma}{dx dQ^2 d\phi} &= \frac{\alpha^2 y^2}{16\pi^2 Q^6} \left\{ 2Q^2 \left(1 - \frac{2m^2}{Q^2} \right) F_1 + 4M \left(\frac{E'}{y} - \frac{Q^2}{4Ey} \right) F_2 \right. \\ &+ 4mM^2 Ey \left[\frac{(S \cdot q)(s \cdot q)}{(P \cdot q)(P \cdot q)} + 2x \frac{s \cdot S}{P \cdot q} \right] g_1 \\ &\left. + 4mMQ^2 \left[\frac{s \cdot S}{P \cdot q} - \frac{(s \cdot P)(S \cdot q)}{(P \cdot q)(P \cdot q)} \right] g_2 \right\} \end{aligned} \quad (2.16)$$

The symmetric and antisymmetric part of the differential cross-section can now be named as $\bar{\sigma}$ - the spin-averaged cross-section - and $\Delta\sigma$ - spin-dependent cross-section. The latter can be split into $\Delta\sigma^{\parallel}$ - the longitudinally polarised cross-section, and $\Delta\sigma^{\perp}$ - the transversely polarised cross-section:

$$\sigma = \bar{\sigma} - \frac{1}{2} h_l \Delta\sigma = \bar{\sigma} - \frac{1}{2} h_l (\cos \alpha \Delta\sigma_{\parallel} + \sin \alpha \cos \phi \Delta\sigma_{\perp}), \quad (2.17)$$

where $h_l = \pm 1$ is the lepton helicity, the angles are defined in Figure 2.2 and

$$\bar{\sigma} \equiv \frac{d^3 \bar{\sigma}}{dx dQ^2 d\phi} = \frac{\alpha^2 y}{4\pi Q^4} \left[\frac{y}{2} \left(1 - \frac{2m^2}{Q^2} \right) F_1 + \frac{1}{2xy} \left(1 - y - \frac{\gamma^2 y^2}{4} \right) F_2 \right], \quad (2.18a)$$

$$\Delta\sigma_{\parallel} \equiv \frac{d^3 \Delta\sigma_{\parallel}}{dx dQ^2 d\phi} = \frac{\alpha^2 y}{4\pi Q^4} \left[\left(2 - y - \frac{\gamma^2 y^2}{2} - \frac{2m^2 y^2}{Q^2} \right) g_1 + \gamma^2 y g_2 \right], \quad (2.18b)$$

$$\cos \phi \Delta\sigma_{\perp} \equiv \frac{d^3 \Delta\sigma_{\perp}}{dx dQ^2 d\phi} = \cos \phi \frac{\alpha^2 y}{4\pi Q^4} \gamma \sqrt{1 - y - \frac{\gamma^2 y^2}{4}} (y g_1 + 2g_2), \quad (2.18c)$$

with $\gamma = \frac{2Mx}{\sqrt{Q^2}} = \frac{2Mx}{Q} = \frac{Q}{Ey}$ which is small in COMPASS kinematics since the beam energy is high. The structure functions $F_1(x, Q^2)$ and $F_2(x, Q^2)$, which describe the unpolarised part of the cross-section $\bar{\sigma}$, have been measured experimentally in wide range of x and Q^2 both with proton and deuteron targets. The results of several experiments are presented in Figure 2.4. They show that in the Bjorken limit ($\nu Q^2 \rightarrow \infty$ and $x = \frac{Q^2}{2M\nu}$) and in the mid-values of x F_2 does not depend on Q^2 what is known as Bjorken scaling. Moreover the Callan-Gross relation [27] holds: $2xF_1(x) = F_2(x)$ what is consistent with the fact that quarks are particles of spin 1/2.

Structure functions g_1 and g_2 can be measured in experiments with polarised beam and polarised target. The cross-section $\Delta\sigma_{\parallel}$ and $\Delta\sigma_{\perp}$, defined by equations 2.18b and 2.18c, refer to a configuration where the nucleon spin is (anti)parallel or orthogonal to the lepton beam momentum direction. g_1 can be measured in the (anti)parallel configuration where g_2 is strongly suppressed by a factor γ^2 . Then this result can be used to disentangle g_2 from the orthogonal cross-section measurement (where the contributions of g_1 and g_2 are similar) using the previously measured g_1 .

The above formulas hold when a 1/2 spin target is taken into consideration. However, COMPASS has taken data (analysis of which will be also part of this thesis) with deuteron target of spin 1. In this case the cross-section formula becomes more complex and needs 8 structure functions. It can be shown, however, that the structure functions b_{1-4} (so-called quadrupole structure functions) are negligible [29, 30]. When quadrupole structure functions are neglected, asymmetry decompositions are the same for nucleon and deuteron target.

2.1.3 The measurement of g_1 and g_2 . Cross-section asymmetries.

As it has been written above a measurement of g_1 and g_2 requires polarised beam and polarised target. By changing the polarisation of the target (or the beam) one can measure parallel or antiparallel cross-sections. In the difference of the two the unpolarised part of the cross-section (i.e. F_1 and F_2) cancels out. For better treatment

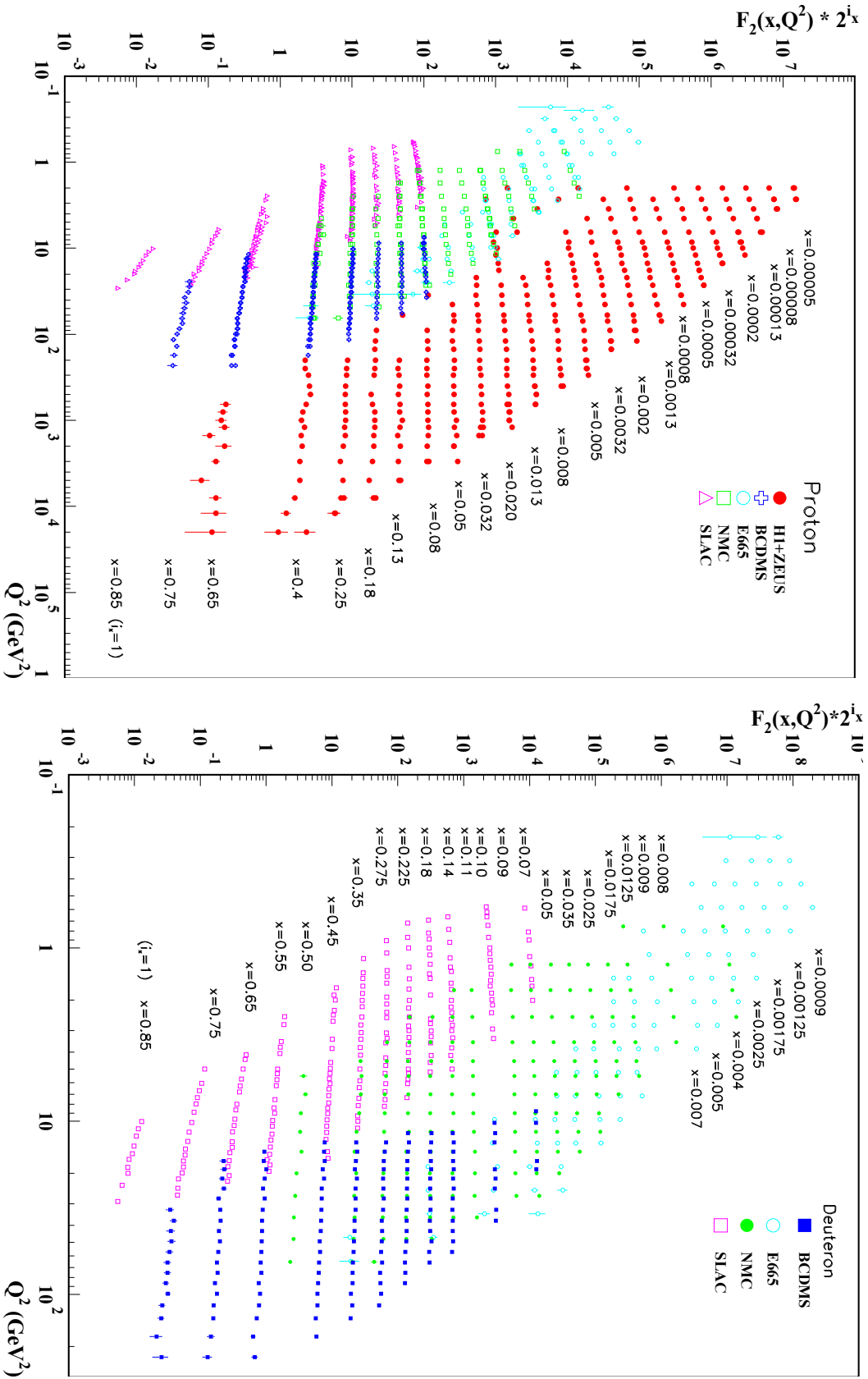


FIGURE 2.4: The proton (left) and deuteron (right) structure functions $F_2(x, Q^2)$ measured on a fixed target with electron beam (SLAC) and muon beam (BCDMS, E665, NMC) and e-p collider HERA scattering positrons on protons(ZEUS, H1). Figure from [28].

of systematic effects (mainly acceptance of the detector) asymmetries are measured. For the lepton-nucleon cross-section one can define longitudinal double spin asymmetry

$$A_{LL} = \frac{\sigma^{\leftarrow\leftarrow} - \sigma^{\rightarrow\rightarrow}}{\sigma^{\leftarrow\leftarrow} + \sigma^{\rightarrow\rightarrow}} \quad (2.19)$$

and transverse spin asymmetry

$$A_T = \frac{\sigma^{\rightarrow\downarrow} - \sigma^{\rightarrow\uparrow}}{\sigma^{\rightarrow\downarrow} + \sigma^{\rightarrow\uparrow}}, \quad (2.20)$$

where \rightarrow denotes the beam polarisation which does not change at COMPASS and depends on the beam kinematics while \Rightarrow represents the target polarisation. More interesting physics quantities are virtual photon-nucleon cross-section asymmetries:

$$A_1 = \frac{\sigma_{1/2}^T - \sigma_{3/2}^T}{\sigma_{1/2}^T + \sigma_{3/2}^T}, \quad A_2 = \frac{\sigma_{1/2}^{TL}}{\sigma_{1/2}^T + \sigma_{3/2}^T}. \quad (2.21)$$

Here the subscript of σ is the total angular momentum of the virtual photon-nucleon system and the superscript corresponds to the initial and final state of the virtual photon. Asymmetries A_1 and A_2 are related to the spin dependent structure functions in the following way

$$A_1 = \frac{g_1 - \gamma^2 g_2}{F_1}, \quad A_2 = \gamma \frac{g_1 + g_2}{F_1}. \quad (2.22)$$

The double spin asymmetries defined in Equations (2.19) and (2.20) which are measured in experiments can be expressed in terms of A_1 and A_2 :

$$A_{LL} = D(A_1 + \eta A_2) \quad A_T = d(A_2 - \xi A_1), \quad (2.23)$$

with kinematic factors:

$$D = \frac{y \left(1 + \gamma^2 \frac{y}{2}\right) (2 - y)}{y^2(1 + \gamma^2) + 2 \left(1 - y - \frac{\gamma^2 y^2}{4}\right) (1 + R)}, \quad (2.24)$$

$$\eta = \frac{\gamma \left(1 - y - \frac{\gamma^2 y^2}{4}\right)}{\left(1 + \gamma^2 \frac{y}{2}\right) \left(1 - \frac{y}{2}\right)}, \quad (2.25)$$

$$d = \frac{\sqrt{1 - y - \frac{\gamma^2 y^2}{4}}}{\left(1 + \gamma^2 \frac{y}{2}\right) \left(1 - \frac{y}{2}\right)} D, \quad (2.26)$$

$$\xi = \frac{\gamma \left(1 - \frac{y}{2}\right)}{1 + \gamma^2 \frac{y}{2}}. \quad (2.27)$$

The factor D , known as depolarisation factor of the virtual photon, can be understood as the fraction of the longitudinal beam polarisation transferred to the photon. It is equal to zero when $y = 0$ and is close to one when $y = 1$. Therefore experiments with high y are most sensitive to the spin dependent structure functions. The quantity R given by

$$R = \frac{\sigma^L}{\sigma^T} = \frac{F_2}{2xF_1}(1 + \gamma^2) - 1 \quad (2.28)$$

is the ratio of longitudinal and transverse photon-nucleon cross-section.

Taking into account the fact that g_2 is strongly suppressed by a factor γ^2 and that η is also small it can be easily shown that

$$g_1(x) \approx \frac{F_1(x)A_{LL}(x)}{(1 - \gamma^2)D(y)}. \quad (2.29)$$

Results of measurements of g_1 structure functions are presented in Figure 2.5.

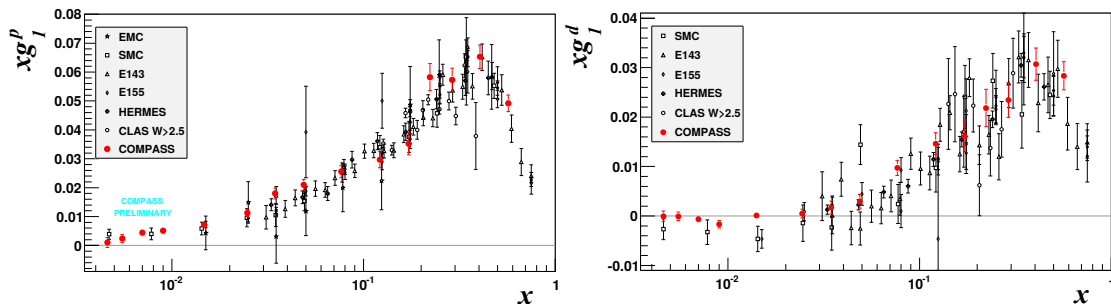


FIGURE 2.5: The spin dependent structure function $xg_1(x)$ of the proton (left) and the deuteron(right) measured in deep inelastic scattering of electrons/positrons (E143, E155, HERMES, CLAS) and muons (EMC, SMC, COMPASS).

2.2 Parton model

2.2.1 Naive parton model

In the naive quark parton model (QPM) the nucleon is described as a composition of point-like particles which have spin 1/2 and carry fractional charge. These particles are naturally identified as quarks. The nucleon is described in infinite momentum frame where the nucleon momentum along the z axis is infinite. Masses and transverse momenta of quarks are negligible. The Bjorken x variable can be then interpreted as nucleon momentum fraction carried by the parton. In DIS, where the parton interacts with the virtual photon, it is assumed that, within the time frame of this interaction, the partons do not interact with each other and therefore are considered as free objects. The hadronic part of the lepton-nucleon scattering cross-section can be then formulated

as an incoherent sum of virtual photon absorption by a quark. Under these conditions the hadronic tensor $W^{\mu\nu}$ can be calculated. The structure functions can be expressed in the following way:

$$F_1(x) = \frac{1}{2} \sum_q e_q^2 [q^+(x) + q^-(x)] \equiv \frac{1}{2} \sum_q e_q^2 q(x), \quad (2.30)$$

$$F_2(x) = 2xF_1(x), \quad (2.31)$$

$$g_1(x) = \frac{1}{2} \sum_q e_q^2 [q^+(x) - q^-(x)] \equiv \frac{1}{2} \sum_q e_q^2 \Delta q(x), \quad (2.32)$$

$$g_2(x) = 0. \quad (2.33)$$

Here the superscript + denotes a quark with spin parallel to the nucleon spin and – a quark with spin antiparallel to the spin of the nucleon. The summation is over quark flavours and e_q stands for the charge of the given quark flavour. Equation (2.32) is once again the Callan-Gross relation [27].

Combining these expressions with 2.28 one gets $R \simeq 0$ what can be interpreted as the fact that in this naive model quarks cannot absorb longitudinally polarised virtual photons. In this model structure functions are expressed in terms of parton distribution functions (PDF) which do not depend on Q^2 . This is known as Bjorken scaling [31] and is true for region $x \sim 0.1$.

2.2.2 QCD improved parton model

The QCD improved parton model takes into account the interactions between quarks inside the nucleon. Then the decomposition of g_1 becomes Q^2 dependent:

$$\begin{aligned} g_1(x, Q^2) &= \frac{1}{2} \sum_q e_q^2 \int \frac{dy}{y} [\Delta q(y, Q^2) + \Delta \bar{q}(y, Q^2)] C_q(x/y, \alpha_s(Q^2)) \\ &+ \frac{\langle e_q^2 \rangle}{2} n_f \int \frac{dy}{y} \Delta G(y, Q^2) C_G(x/y, \alpha_s(Q^2)) \\ &= \frac{1}{2} \sum_q e_q^2 C_q(\alpha_s(Q^2)) \otimes [\Delta q(Q^2) + \Delta \bar{q}(Q^2)] \\ &+ \frac{\langle e_q^2 \rangle}{2} n_f C_G(\alpha_s(Q^2)) \otimes \Delta G(Q^2), \end{aligned} \quad (2.34)$$

where \otimes denotes the convolution integral and $\alpha_s(Q^2)$ is the QCD strong coupling constant. The coefficient functions C_i are calculable in a QCD perturbation series in α_s , and it has been done up to next-to-leading order [32, 33, 34]. Quarks interact by exchange of gluons which may for a moment produce a quark-antiquark pair. These are

so-called 'sea quarks', and antiquarks from the sea give contribution to the g_1 decomposition (denoted as $\Delta\bar{q} \equiv \bar{q}^+ - \bar{q}^-$ in the above equation). The QCD evolution (violation of the Bjorken scaling) is described by the Dokshitzer-Gribov-Lipatov-Altarelli-Parisi (DGLAP) [35, 36, 37] equations:

$$\begin{aligned} Q^2 \frac{d}{dQ^2} \begin{pmatrix} \Delta q \\ \Delta g \end{pmatrix} &= \frac{\alpha_s(Q^2)}{2\pi} \int_x^1 \frac{dy}{y} \begin{pmatrix} \Delta P_{qq} & \Delta P_{qG} \\ \sum_q \Delta P_{Gq} & \Delta P_{GG} \end{pmatrix} (x/y, \alpha_s(Q^2)) \begin{pmatrix} \Delta q \\ \Delta g \end{pmatrix} (y, Q^2) \\ &= \frac{\alpha_s(Q^2)}{2\pi} \begin{pmatrix} \Delta P_{qq} & \Delta P_{qG} \\ \sum_q \Delta P_{Gq} & \Delta P_{GG} \end{pmatrix} (\alpha_s(Q^2)) \otimes \begin{pmatrix} \Delta q \\ \Delta g \end{pmatrix} (Q^2). \end{aligned} \quad (2.35)$$

The splitting functions P_{ij} where indices i and j run over quarks, antiquarks and gluons have a probabilistic interpretation. $P_{ij}(x/y, \alpha_s(Q^2))$ is the probability that the parton i carries the x/y fraction of parent parton j of momentum $y > x$. The splitting functions can be calculated for certain processes (presented in Figure 2.6) using Feynman rules.

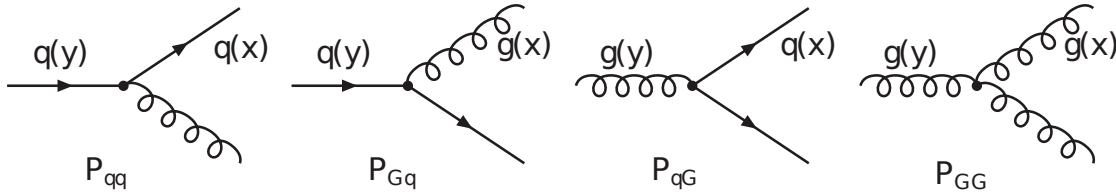


FIGURE 2.6: Feynman diagrams for the four splitting functions. The splitting function P_{ij} gives the probability that a parton i with momentum fraction x originates from parton j .

The scale breaking is presented in Figure 2.7 where several measurements of $g_1(x, Q^2)$ are shown.

2.3 Semi-Inclusive Deep inelastic scattering (SIDIS)

2.3.1 Transversity

Transversity h_1 describes a correlation between the parton and nucleon polarisation when the nucleon is polarised transversely to the direction of the virtual photon. The functions F_1, g_1, h_1 are the result of integration of Transverse Momentum Dependent structure functions (TMDs) over k_T (the intrinsic parton transverse momentum) and they are the only structure functions which do not vanish under such an integration. The information about k_T and hence about Transverse Momentum Dependent structure functions (TMDs) can be accessed by measuring azimuthal asymmetries of distributions of hadrons produced in the scattering process.

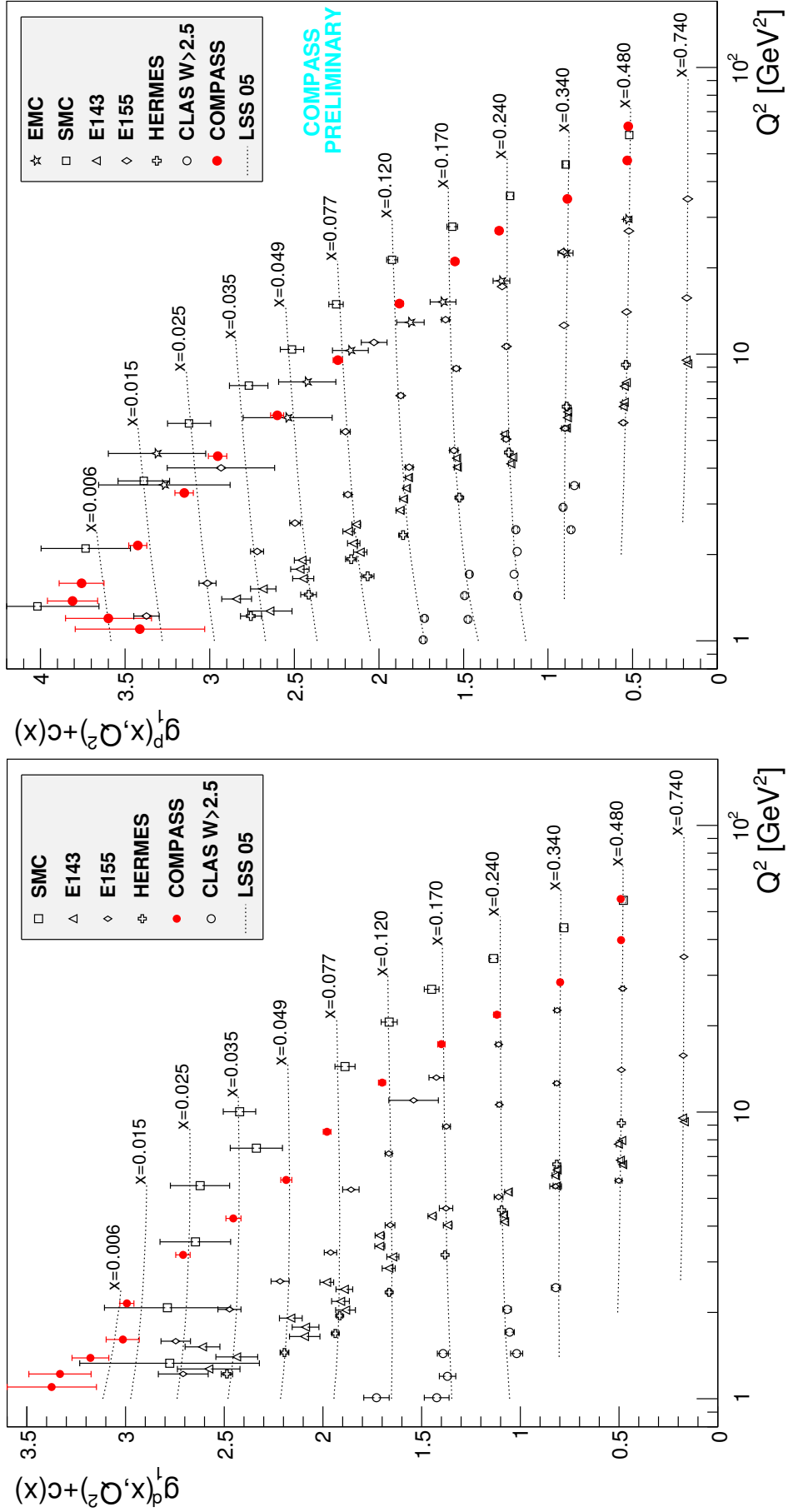


FIGURE 2.7: The proton (left) and deuteron (right) spin dependent structure functions $g_1(x, Q^2)$ measured on a fixed target with electron/positron beam (E143, E155, SLAC, HERMES) and muon beam (EMC, SMC, COMPASS). To align points to curves corresponding to fixed x LSS05 parametrisations [38] a constant $c(x) = 0.28(11.6 + i_x)$ is added to g_1 values and i_x is the number of x bin. Figure from [17].

2.3.2 Transverse Momentum Dependent structure functions (TMDs).

Beyond the collinear approximation and with a finite transverse momentum of the partons inside the nucleon, k_{\perp} , eight transverse momentum dependent PDFs are needed to fully describe the cross section at leading twist (Equation (2.39)). Apart from the scattered lepton the detection of hadrons produced in the process is necessary to be sensitive to the k_{\perp} distribution. To get access to TMDs one needs to study Semi-Inclusive Deep Inelastic Scattering (SIDIS) processes (see Figure 2.8):

$$l(\mathbf{k}) + N(\mathbf{P}) \rightarrow l(\mathbf{k}') + h(\mathbf{P}_h) + X. \quad (2.36)$$

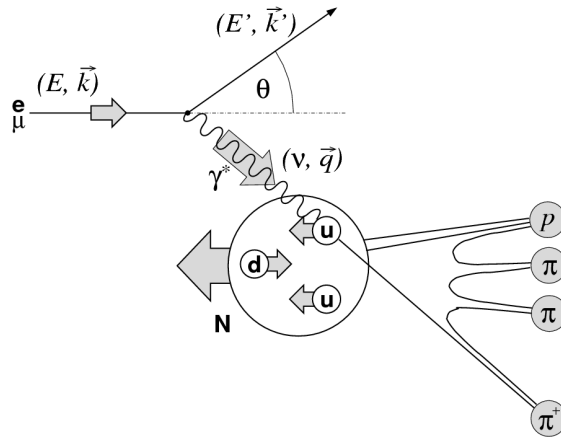


FIGURE 2.8: Semi-Inclusive Deep Inelastic scattering (SIDIS) of lepton on nucleon.

The intrinsic parton transverse momentum (with respect to the intermediate photon direction) - k_T - is small compared to the longitudinal component. However, if we take it into account we need 8 instead of 3 structure functions TMDs (see Figure 2.9). Among all TMDs in this thesis I will concentrate on Sivers structure function which describes the influence of the nucleon spin on the unpolarised parton distribution function and is directly related to parton's collective orbital motion. This relation is, however, model dependent.

The SIDIS cross-section is described in terms of two azimuthal angles presented in Figure 2.10: ϕ_S - the angle between the target spin and the lepton scattering plane and ϕ_h - the angle between the hadron momentum vector and the lepton scattering plane. They

		parton		
		U	L	T
nucleon	U	$F_1(x)$ 		
	L		helicity $g_1(x)$ 	
	T			transversity $h_1(x)$

(a)

		parton		
		U	L	T
nucleon	U	$f_1(x, k_T)$ 		Boer-Mulders $h_1^\perp(x, k_T)$
	L		helicity $g_1(x, k_T)$ 	worm gear L $h_{1L}^\perp(x, k_T)$
	T	Sivers $f_{1T}^\perp(x, k_T)$ 	worm gear T $g_{1T}^\perp(x, k_T)$ 	transversity $h_1(x, k_T)$ pretzelocity $h_{1T}^\perp(x, k_T)$

(b)

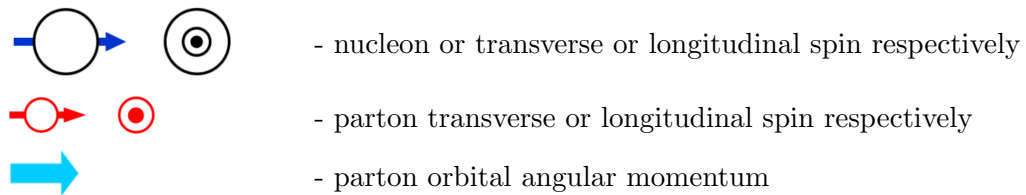


FIGURE 2.9: Structure functions. (a) integrated over intrinsic transverse momentum k_T , (b) Transverse Momentum Dependent structure functions (TMDs). The virtual photon direction points into the plane. The axes are labelled with U - unpolarised , L - longitudinally polarised, T - transversely polarised. Vertical axis corresponds to the nucleon polarisation and the horizontal axis to the parton polarisation.

can be expressed in the following way

$$\phi_S = \frac{(\mathbf{q} \times \mathbf{k}) \cdot \mathbf{S}}{|(\mathbf{q} \times \mathbf{k}) \cdot \mathbf{S}|} \arccos \left(\frac{(\mathbf{q} \times \mathbf{k}) \cdot (\mathbf{q} \times \mathbf{S})}{|\mathbf{q} \times \mathbf{k}| |\mathbf{q} \times \mathbf{S}|} \right), \quad (2.37)$$

$$\phi_h = \frac{(\mathbf{q} \times \mathbf{k}) \cdot \mathbf{P}_h}{|(\mathbf{q} \times \mathbf{k}) \cdot \mathbf{P}_h|} \arccos \left(\frac{(\mathbf{q} \times \mathbf{k}) \cdot (\mathbf{q} \times \mathbf{P}_h)}{|\mathbf{q} \times \mathbf{k}| |\mathbf{q} \times \mathbf{P}_h|} \right), \quad (2.38)$$

where \mathbf{S} is the target spin vector and \mathbf{P}_h is the hadron momentum vector. The cross-

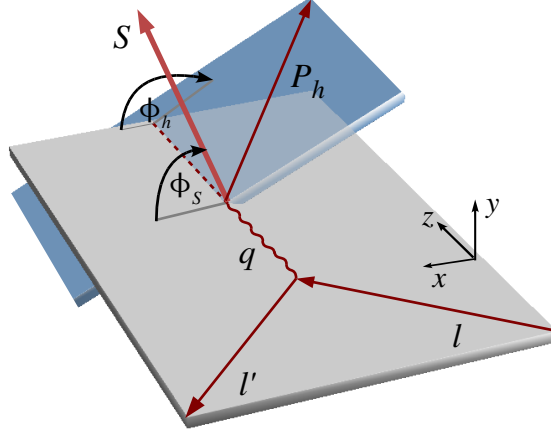


FIGURE 2.10: Definition of the azimuthal angles ϕ_h and ϕ_S , measured around the direction of the virtual photon - \mathbf{q} . Figure from [39]

section for SIDIS one hadron production reads ([40])

$$\begin{aligned} \frac{d\sigma}{dx dy d\psi dz d\phi_h dP_{h\perp}} = & \frac{\alpha^2}{xyQ^2} \frac{y^2}{2(1-\varepsilon)} \left(1 + \frac{\gamma^2}{2x} \right) \left\{ F_{UU,T} + \varepsilon F_{UU,L} + \sqrt{2\varepsilon(1+\varepsilon)} \cos \phi_h F_{UU}^{\cos \phi_h} \right. \\ & + \varepsilon \cos 2\phi_h F_{UU}^{\cos 2\phi_h} + \lambda_e \sqrt{2\varepsilon(1-\varepsilon)} \sin \phi_h F_{UU}^{\sin \phi_h} \\ & + S_{\parallel} \left[\sqrt{2\varepsilon(1+\varepsilon)} \sin \phi_h F_{UL}^{\sin \phi_h} + \varepsilon \sin (2\phi_h) F_{UL}^{\sin (2\phi_h)} \right] \\ & + S_{\parallel} \lambda_e \left[\sqrt{1-\varepsilon^2} F_{LL} + \sqrt{2\varepsilon(1-\varepsilon)} \cos \phi_h F_{LL}^{\cos \phi_h} \right] \\ & + |S_{\perp}| \left[\sin (\phi_h - \phi_S) \left(F_{UT,T}^{\sin (\phi_h - \phi_S)} + \varepsilon F_{UT,L}^{\sin (\phi_h - \phi_S)} \right) \right. \\ & + \varepsilon \sin (\phi_h + \phi_S) F_{UT}^{\sin (\phi_h + \phi_S)} + \varepsilon \sin (3\phi_h - \phi_S) F_{UT}^{\sin (3\phi_h - \phi_S)} \\ & + \left. \sqrt{2\varepsilon(1+\varepsilon)} \sin \phi_S F_{UT}^{\sin \phi_S} + \sqrt{2\varepsilon(1+\varepsilon)} \sin (2\phi_h - \phi_S) F_{UT}^{\sin (2\phi_h - \phi_S)} \right] \\ & + |S_{\perp}| \lambda_e \left[\sqrt{1-\varepsilon^2} \cos (\phi_h - \phi_S) F_{LT}^{\cos (\phi_h - \phi_S)} + \sqrt{2\varepsilon(1-\varepsilon)} \cos \phi_S F_{LT}^{\cos \phi_S} \right. \\ & + \left. \left. \sqrt{2\varepsilon(1-\varepsilon)} \cos (2\phi_h - \phi_S) F_{LT}^{\cos (2\phi_h - \phi_S)} \right] \right\}, \quad (2.39) \end{aligned}$$

where

$$\varepsilon = \frac{1 - y - \frac{1}{4}\gamma^2 y^2}{1 - y + \frac{1}{2}y^2 + \frac{1}{4}\gamma^2 y^2} \quad (2.40)$$

is the ratio of longitudinal and transverse photon flux. The eight transverse spin modulations from Equation (2.39) are independent from each other [40] and hence can be extracted from one data set simultaneously. In this thesis we will concentrate only on Sivers modulation ($\sin(\phi_h - \phi_S)$). The angle ψ is the azimuthal angle of l' around the lepton beam axis with respect to an arbitrary fixed direction, which in case of a transversely polarised target is chosen to be the direction of S .

2.3.3 The Sivers effect and the orbital motion of gluons.

Independently of the model there is a correlation between the Sivers effect and the orbital angular momentum (OAM). Currently, for quantification of this relation a model is needed. The most popular is the Burkardt model ([41, 42, 43]). This model bases on the relation of the Sivers function and the parton distribution in the transverse plane.

From the Gluon Sivers Function (GSF) it is possible, using the Burkardt model, to calculate the spatial gluon distribution in the transverse (with respect to the virtual photon) plane. The available measurements of the GSF are shortly presented in Section 3.4. The extraction of the Sivers effect for gluons from COMPASS SIDIS data is the main topic of this thesis.

There are two methods of describing the nucleon as a 3D object. One is x , the fraction of the nucleon momentum carried by the parton known as the Björken variable, vs k_\perp , with the use of TMDs. The other uses Fourier transform of General Parton Distributions (GPDs) [44] which gives a description in momentum fraction x and position in the transverse plane b_\perp (also referred to as the impact parameter). In the Burkardt model hadrons produced in a SIDIS event gain transverse momentum via Final State Interaction (FSI) with the strong field of the nucleon remnant (Fig. 2.11). This process is also known as QCD lensing. The asymmetric distribution of the parton in the transverse plane, $g_x(x, \vec{b}_\perp)$ produces an asymmetry in azimuthal angle and this is the Sivers asymmetry.

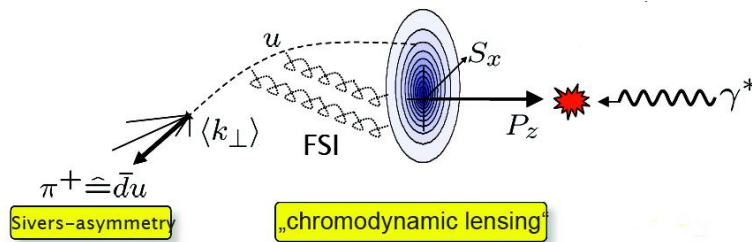


FIGURE 2.11: Chromodynamic lensing as a Sivers mechanism.

Asymmetric distribution of a parton and its OAM can be connected. A parton distribution in an unpolarised nucleon is described by a symmetric general parton distribution

(GPD), $g_{\hat{x}} = \mathcal{H}$. When the nucleon is polarised the distribution becomes asymmetric due to a nonzero spin-flip function \mathcal{E} what means a nonzero OAM of this parton:

$$g_{\hat{x}}(x, \vec{b}_{\perp}) = \mathcal{H}_g(x, \vec{b}_{\perp}) - \frac{1}{2M} \frac{\partial}{\partial b_y} \mathcal{E}_g(x, \vec{b}_{\perp}). \quad (2.41)$$

Chapter 3

Nucleon spin decomposition in measurements

Nucleon spin decomposition assuming light-cone gauge reads

$$\frac{1}{2} = \frac{1}{2}\Delta\Sigma + \Delta G + L_q + L_g, \quad (3.1)$$

where $\Delta\Sigma$ is the quark helicity contribution to the nucleon spin, ΔG is the gluon helicity contribution to the nucleon spin, L_q and L_g stand for orbital angular momentum (OAM) of quarks and gluons respectively.

In this chapter the measurements of $\Delta\Sigma$ and ΔG will be described. The results show that the parton spin contribution do not sum up to the nucleon spin. Up to now there are no direct measurements of parton OAM. However some manifestations of OAM existence may be studied. In this thesis the results of the measurement of the Sivers effect for gluons are described. These results may be an indication of the gluon OAM, L_g .

3.1 $\Delta\Sigma$ - the fraction of nucleon spin carried by quark spins

The first moment of $g_1(x, Q^2)$ contains information about the total quark helicity contribution to the nucleon spin. For the naive QPM

$$\Gamma_1 = \int_0^1 g_1(x) dx = \frac{1}{2} \sum_q e_q^2 \int_0^1 [\Delta q(x) + \Delta \bar{q}(x)] dx. \quad (3.2)$$

Writing $\Delta q \equiv \int_0^1 [\Delta q(x) + \Delta \bar{q}(x)] dx$ leads to expression for the first moment of $g_1(x)$ for proton:

$$\begin{aligned}\Gamma_1^p &= \frac{1}{2} \left(\frac{4}{9} \Delta u + \frac{1}{9} \Delta d + \frac{1}{9} \Delta s \right) \\ &= \frac{1}{12} (\Delta u - \Delta d) + \frac{1}{36} (\Delta u + \Delta d - 2\Delta s) + \frac{1}{9} (\Delta u + \Delta d + \Delta s).\end{aligned}\quad (3.3)$$

Doing the same for neutron reads

$$\Gamma_1^{p(n)} = \pm \frac{1}{12} a_3 + \frac{1}{36} a_8 + \frac{1}{9} a_0, \quad (3.4)$$

where

$$\begin{aligned}a_3 &= \Delta u - \Delta d, \\ a_8 &= \Delta u + \Delta d - 2\Delta s, \\ a_0 &= \Delta u + \Delta d + \Delta s.\end{aligned}\quad (3.5)$$

The terms a_i can be related to expectation values of the proton matrix elements of a $SU(3)$ flavour octet of quark axial-vector current [24]:

$$\langle P, S | J_{5\mu}^i | P, S \rangle = M a_i S_\mu, \quad i = 1, \dots, 8 \quad (3.6)$$

and

$$J_{5\mu}^i = \bar{\Psi} \gamma_5 \gamma_\mu \frac{\lambda_i}{2} \Psi. \quad (3.7)$$

Here λ_i are Gell-Mann matrices and Ψ is a column vector in flavour space:

$$\Psi = \begin{pmatrix} \Psi_u \\ \Psi_d \\ \Psi_s \end{pmatrix}. \quad (3.8)$$

The term a_0 is determined by the flavour singlet operator:

$$J_{5\mu}^0 = \bar{\Psi} \gamma_5 \gamma_\mu \Psi \quad (3.9)$$

and

$$\langle P, S | J_{5\mu}^0 | P, S \rangle = M a_0 S_\mu. \quad (3.10)$$

The quantities a_i ($i = 1, \dots, 8$) are independent of Q^2 because the octet currents are conserved however a_0 is a priori dependent on Q^2 as the singlet current is not conserved. This feature is known as axial anomaly [45, 46, 47, 48].

The axial charges - a_3 and a_8 - can be obtained in the measurements of β decay and spin 1/2 hyperon decays [24, 49, 28]:

$$a_3 = F + D \equiv \left| \frac{g_A}{g_V} \right| = 1.2694 \pm 0.0028, \quad (3.11)$$

$$a_8 = F - D = 0.585 \pm 0.025. \quad (3.12)$$

Here g_A/g_V is the ratio of axial-vector and vector coupling constant measured in neutron β decay. F and D are symmetric and antisymmetric couplings measured in hyperon decays. It should be noted here that the use of a_8 in DIS kinematics is debatable. In naive QPM the total contribution of quark helicities to the nucleon spin - $\Delta\Sigma = \Delta u + \Delta d + \Delta s = a_0$. By measuring Γ_1 , the first moment of g_1 , a_0 value can be obtained which in naive QPM is equal to $\Delta\Sigma$.

In QCD improved quark parton model the expression for $\Gamma_1^{p(n)}$ becomes more complicated:

$$\Gamma_1^{p(n)} = \frac{1}{12} \left[\left(\pm a_3 + \frac{1}{3} a_8 \right) E_{NS}(Q^2) + \frac{4}{3} a_0 E_S(Q^2) \right], \quad (3.13)$$

with

$$E_{NS}(Q^2) = 1 - \frac{\alpha_s}{\pi} - \left(\frac{3.58}{3.25} \right) \left(\frac{\alpha_s}{\pi} \right)^2 \dots, \quad (3.14)$$

$$E_S(Q^2) = 1 - \left(\frac{0.333}{0.040} \right) \frac{\alpha_s}{\pi} - \left(\frac{1.10}{-0.07} \right) \left(\frac{\alpha_s}{\pi} \right)^2 \dots \quad (3.15)$$

The values in brackets correspond to the number of flavours: the upper is for 3 flavours, the lower for 4 flavours. The result depends on the used renormalisation scheme. Here Modified Minimal Subtraction (\overline{MS}) renormalisation scheme is used [50]. The value of the difference between Γ_1^p and Γ_1^n leads to the Björken sum rule [51, 52]:

$$\Gamma_1^p - \Gamma_1^n = \frac{1}{6} \left| \frac{g_A}{g_V} \right| E_{NS}. \quad (3.16)$$

The agreement between DIS experiments measuring $\Gamma_1^{p(n)}$ and experiments measuring g_A/g_V in β decay is on the level of 5% [53].

The first result, obtained by the EMC collaboration [9, 10], of $\Delta\Sigma$ measurement: $\Delta\Sigma = 0.12 \pm 0.17$ began the so-called "spin crisis". The expectation of the naive QPM was that $\Delta\Sigma = 1$, taking into account relativistic effects $\Delta\Sigma \sim 0.6$, [54].

These results have shown the necessity of the use of the QCD improved quark parton model. Then g_1 does not only depend on Δq but also on ΔG . To present this relation it is convenient to rewrite the DGLAP Equations (2.35) in terms of flavour-singlet (S)

and flavour-nonsinglet (NS) polarised quark distributions:

$$Q^2 \frac{d}{dQ^2} \Delta q^{NS}(x, Q^2) = \frac{\alpha_s(Q^2)}{2\pi} \Delta P_{qq}^{NS}(\alpha_s(Q^2)) \otimes \Delta q^{NS}(Q^2), \quad (3.17)$$

$$Q^2 \frac{d}{dQ^2} \Delta q^S(x, Q^2) = \frac{\alpha_s(Q^2)}{2\pi} [\Delta P_{qq}^S(\alpha_s(Q^2)) \otimes \Delta q^S(Q^2) + 2n_f \Delta P_{qG}(\alpha_s(Q^2)) \otimes \Delta g(Q^2)], \quad (3.18)$$

$$Q^2 \frac{d}{dQ^2} \Delta g(x, Q^2) = \frac{\alpha_s(Q^2)}{2\pi} [\Delta P_{Gq}(\alpha_s(Q^2)) \otimes \Delta q^S(Q^2) + \Delta P_{qG}(\alpha_s(Q^2)) \otimes \Delta g(Q^2)], \quad (3.19)$$

where

$$\Delta q^S = \sum_q \Delta q(x, Q^2), \quad (3.20)$$

$$\Delta q^{NS} = \sum_q \left(\frac{e_q^2}{\langle e^2 \rangle} - 1 \right) \Delta q(x, Q^2), \quad (3.21)$$

with $\langle e^2 \rangle = \sum e_q n_f^{-1}$ and n_f is the number of flavours. The evolution of the flavour-nonsinglet quark distribution function does not depend on the gluon distribution function while the flavour singlet quark PDF evolution is sensitive to the evolution of gluon PDF.

The structure function g_1 given by equation 2.34 can now be rewritten in terms of the flavour-singlet and flavour-nonsinglet contributions:

$$\begin{aligned} g_1(x, Q^2) &= \frac{1}{2} \langle e^2 \rangle [\Delta C^{NS}(x, \alpha_s(Q^2)) \otimes \Delta q^{NS}(x, Q^2) + \Delta C^S(x, \alpha_s(Q^2)) \otimes \Delta q^S(x, Q^2)] \\ &+ 2n_f \Delta C^G(x, \alpha_s(Q^2)) \otimes \Delta g(x, Q^2). \end{aligned} \quad (3.22)$$

The splitting functions $\Delta C^{NS}, \Delta C^S, \Delta C^G$ are calculated up to next-to-leading order (NLO) in α_s [32, 33, 34]. As mentioned before the g_1 structure function is related not only to the quark parton distribution function (PDF) but also to gluon PDF. However in leading order (LO) $\Delta C^G = 0$ and g_1 does not depend on Δg . The dependence appears in NLO calculations. But in NLO the values of the splitting functions depend on the choice of factorisation and renormalisation scheme. In the \overline{MS} scheme $\Delta C^G = 0$ and Δg does not contribute directly to g_1 . On the other hand the Adler-Bardeen (AB) scheme gives $\Delta C^G \neq 0$ and g_1 as well as Γ_1 depends directly on Δg . $\Delta \Sigma$ can be written as the first moment of the flavour singlet quark distribution. Its values in the two aforementioned schemes are in the following relation

$$\Delta \Sigma_{\overline{MS}} = \Delta \Sigma_{AB} - n_f \frac{\alpha_s(Q^2)}{2\pi} \Delta G(Q^2), \quad (3.23)$$

where ΔG is the first moment of the gluons distribution

$$\Delta G(Q^2) = \int_0^1 \Delta g(x, Q^2) dx. \quad (3.24)$$

In the \overline{MS} scheme the quark distributions depend on the Q^2 evolution. In the AB scheme, on the other hand, quark distributions are evolution independent but $\Delta\Sigma$ is Q^2 dependent due to anomalous contribution of gluons represented by a triangle graph shown in Figure 3.1. This fact leads to a suggestion that in the AB scheme the measured small a_0 value might be explained by the anomalous gluon contribution [46, 47, 48].

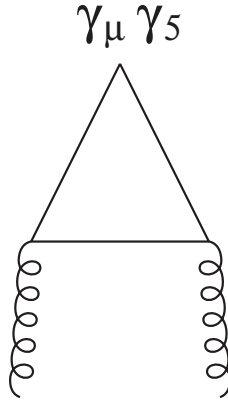


FIGURE 3.1: Triangle diagram giving rise to the axial anomaly. The gluons couple via the triangle to the axial current and thus contribute to the corresponding proton matrix element.

In perturbative QCD (pQCD) by means of the DGLAP Equations (2.35) it is possible to calculate $g_1(x, Q^2)$ at any Q^2 if one knows x-dependence of g_1 at given referential Q_0^2 . These calculations depend on Δq and ΔG . By measuring x-dependence of g_1 at several Q^2 values one can try to fit the DGLAP evolution (with parameters Δq and ΔG) to the experimental points. Also Semi-Inclusive DIS data are taken into account in these fits. The results of spin-independent and spin-dependent fits of pQCD are presented in Figure 3.2.

The pQCD analysis for all available g_1 measurements has been performed by the COMPASS collaboration. Two equivalent solutions were found: one with positive and one with negative ΔG . The final result for $\Delta\Sigma$ is

$$\Delta\Sigma \in [0.26; 0.36]. \quad (3.25)$$

To decrease the errors it is needed to perform measurements of $g_1(x, Q^2)$ in wider kinematic range. This will be possible in the planned Electron-Ion Collider experiment [20].

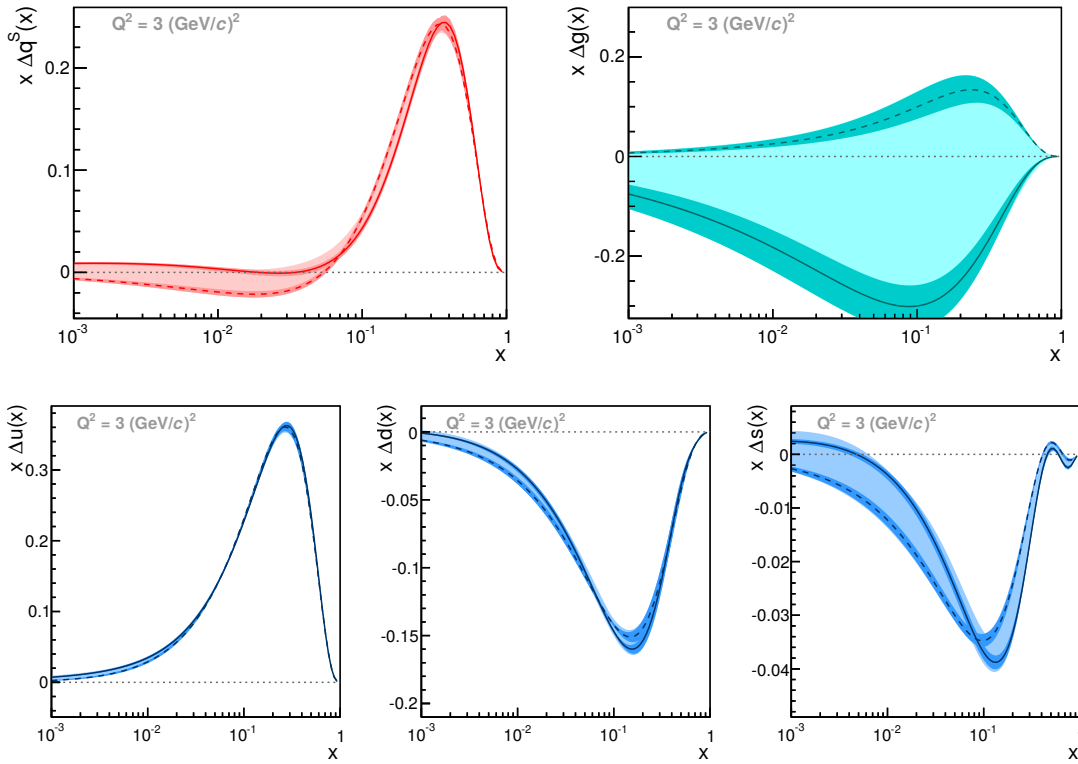


FIGURE 3.2: COMPASS results of the QCD fits to g_1 world data at $Q^2 = 3\text{GeV}^2$. The fit is performed for several sets of functional shapes. Top: singlet $x\Delta q^S(x)$ and gluon distribution $x\Delta g(x)$. Bottom: distributions of $x[\Delta q(x) + \Delta \bar{q}(x)]$ for different flavours (u, d and s). Continuous lines correspond to the fit with $\gamma_S = 0$, long dashed lines to the one with $\gamma_S \neq 0$. The dark bands represent the statistical uncertainties, only. The light bands, which overlay the dark ones, represent the systematic uncertainties.

3.2 ΔG - the gluon spin contribution to the nucleon spin

The observable ΔG is well defined and can be measured in experiments. The best way to evaluate it is to measure gluon helicity function Δg as a function of the gluon momentum fraction x_g and calculate its first moment

$$\Delta G = \int \Delta g(x_g) dx_g. \quad (3.26)$$

What can be measured directly and will be shortly presented in this Section, is the average gluon polarisation $\langle \Delta g/g \rangle$. It has been measured in a model-dependent way with the use of photon-gluon Fusion (PGF) process (Figure 6.1) by SMC [55], Hermes [56, 57] and COMPASS [58, 59, 18]. All these measurements cover relatively large x_g region. Small x_g region will be covered by the EIC experiment [20].

Constraints on gluon polarisation $\Delta g/g$ have been also obtained by PHENIX [60] and STAR [61] where the production of π^0 or high transverse momentum jets have been analysed.

3.2.1 Open Charm production

The production of hadrons containing charm quarks is a signature of the Photon Gluon Fusion process (see Figure 6.1). In the PGF process the interacting quark and gluon

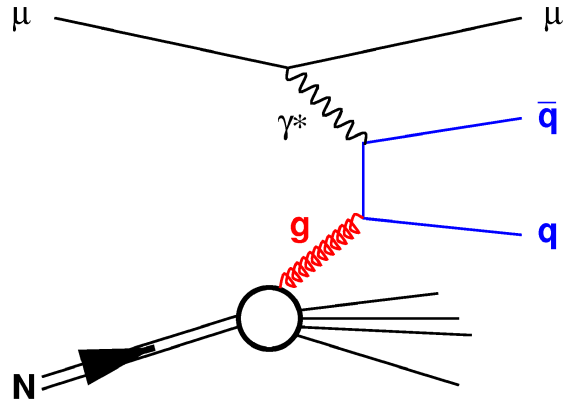


FIGURE 3.3: Photon Gluon Fusion (PGF)

produce a quark-antiquark pair. This hard process is the main source of heavy c quarks ($m_c = 1.5$ GeV) as the production via fragmentation of light quarks are strongly suppressed. Interaction of virtual photon with intrinsic charm quark, on the other hand, may be significant for large x_{Bj} which in the case of D_0 production is rather small.

In this method asymmetries of several decay channels of the D meson have been obtained with the use of weighted background subtraction. The analysis involved QCD calculations of the analysing power a_{LL} which relates the partonic asymmetry with the asymmetry on the measurable parton level. The calculation of a_{LL} has been done at leading order (LO) but may also involve next-to-leading order (NLO) corrections. Therefore two official COMPASS results are presented here:

$$\left\langle \frac{\Delta g}{g} \right\rangle^{LO} = -0.06 \pm 0.21(\text{stat.}) \pm 0.08(\text{syst.}) \quad (3.27)$$

$$\left\langle \frac{\Delta g}{g} \right\rangle^{NLO} = -0.13 \pm 0.15(\text{stat.}) \pm 0.15(\text{syst.}). \quad (3.28)$$

The Open Charm analysis will be discussed in more detail in Section 6.1 as background subtraction method is similar to the one used in the main analysis of this thesis.

3.2.2 $\Delta g/g$ from high transverse momentum hadron pairs

The lowest order perturbative QCD (LO pQCD) process of interaction of a virtual photon with a gluon is the PGF process. In the scattering of lepton on a nucleon $\gamma^* N \rightarrow hhX$ two other processes (mostly on light quarks u, d, s) are involved: leading process - photon absorption by quark and QCD Compton process - photon absorption by

quark with gluon emission in the final state. The processes are presented in Figure 3.4. The approximation of the lepton-nucleon scattering by these three processes is applied

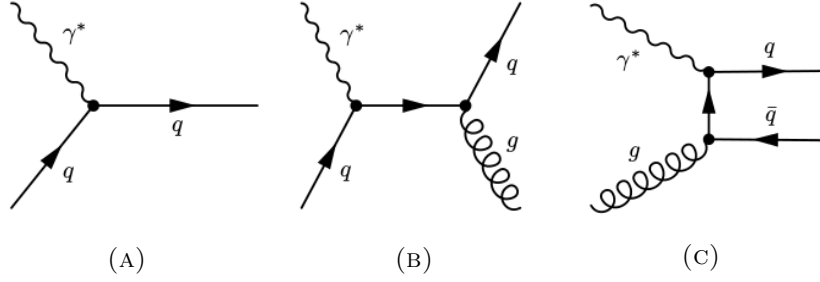


FIGURE 3.4: Feynman diagrams considered for γ^*N scattering: A) Leading order process (LP), B) gluon radiation (QCD Compton scattering), C) photon-gluon fusion (PGF).

in MC simulators: PYTHIA [62] which covers the region of $Q^2 < 1$ and LEPTO [63] which covers the region $Q^2 > 1$.

In the total two-hadron sample the leading process is dominating. The observed two hadrons from a LP event obtain transverse (w.r.t. the virtual photon) momentum only through fragmentation whereas in the other two processes transverse momentum is also gained in the two-body final state system. The cut on p_T of the hadrons suppresses the leading process. However, the final sample is still a mixture of the three processes and to extract $\Delta g/g$ MC simulations to obtain the fractions of the three processes are needed.

Three experimental results will be shortly described here: SMC for $Q^2 > 1$, COMPASS for $Q^2 < 1$ and for $Q^2 > 1$.

1. SMC at CERN ($Q^2 > 1$).

The SMC experiment was the COMPASS predecessor. It was placed in the same experimental hall and worked on the same 190 GeV polarised muon beam (however the intensity was five times smaller than in COMPASS times). It studied scattering polarised muons off polarised proton and deuteron targets. A deuterated butanol target was used for the latter. The detailed description of the SMC experimental setup is given in [64].

The gluon polarisation has been obtained from the equation

$$A^{lN \rightarrow l'hhX} = \frac{\Delta q}{q} (\langle a_{LL} \rangle^{LP} R^{LP} + \langle a_{LL} \rangle^{QCDC} R^{QCDC}) + \frac{\Delta g}{g} \langle a_{LL} \rangle^{PGF} R^{PGF}. \quad (3.29)$$

The quark asymmetry $\Delta q/q$ has been approximated by the value of A_1 obtained in inclusive measurement. The processes fractions were obtained with the use of the LEPTO generator [63].

For the gluon polarisation extraction a sample of high- p_T hadron pairs ($p_{T1}, p_{T2} > 0.7$ GeV, $\sum p_T^2 > 2.5$ GeV²) with $Q^2 > 1$ GeV² has been used. For both hadrons the cut on $x_F > 0.1$ and $z > 0.1$ has been applied to select current fragmentation region.

To obtain better signal purity a neural network was used to optimise the selection. As an input several inclusive (Q^2, x, y , the multiplicity of the tracks) and hadronic ($p_{T1}, p_{L1}, p_{T2}, p_{L2}, z_1, z_2$, charges of the two leading hadrons, and their azimuthal angle ϕ) variables were chosen. The NN has been trained on a MC sample where the target value was one for PGF and zero otherwise. The trained NN was applied to the real events and a threshold was set to select a sample with the optimised statistics and purity. The final result of this analysis [55] is:

$$\frac{\Delta g}{g} = -0.20 \pm 0.28(\text{stat.}) \pm 0.10(\text{syst.}) \quad (3.30)$$

at $x_g = 0.07$ and scale $\mu^2 = 3$ GeV².

2. COMPASS at CERN ($Q^2 > 1$).

The COMPASS experimental setup will be described in detail in Chapter 4. The high- p_T hadron pair for $Q^2 > 1$ GeV is the main subject of the PhD thesis [17]. It will be described in more detail in Section 6.2 as some of its basic statistical features, like event-by-event weighting with the use of NN, were used in this thesis. The main idea is to analyse two samples: inclusive and high- p_T . The inclusive sample is defined by the cuts in inclusive kinematic variables: Q^2, y, W . For the high- p_T sample it is additionally required for the event to contain at least two hadrons with $p_{T1} > 0.7$ GeV and $p_{T2} > 0.4$ GeV, $x_{F1,2} > 0$. Two equations are written for asymmetries measured in the two samples:

$$A_{LL}^{2h}(x_{Bj}) = R^{PGF} a_{LL}^{PGF} \frac{\Delta g}{g}(x_g) + R^{LP} DA_1^{LO}(x_{Bj}) + R^{QCDC} a_{LL}^{QCDC} A_1^{LO}(x_C), \quad (3.31)$$

$$A_{LL}^{incl}(x_{Bj}) = R_{incl}^{PGF} a_{LL}^{incl,PGF} \frac{\Delta g}{g}(x_g) + R_{incl}^{LP} DA_1^{LO}(x_{Bj}) + R_{incl}^{QCDC} a_{LL}^{incl,QCDC} A_1^{LO}(x_C). \quad (3.32)$$

The fractions in both samples differ $R_{incl}^i \neq R^i$ and from the set of two different equations for two unknowns $\frac{\Delta g}{g}$ and A_1^{LO} can be expressed in terms of A_{LL}^{incl} which has been taken from global fits. The details are presented in Section 6.2 The final value of this analysis is

$$\frac{\Delta g}{g} = 0.125 \pm 0.060(\text{stat.}) \pm 0.063(\text{syst.}) \quad (3.33)$$

at $x_g = 0.09$ and a scale of $\mu^2 = 3 \text{ GeV}^2$.

3.2.3 $\Delta g/g$ from COMPASS for $Q^2 < 1$

In this analysis the following criteria have been used: the p_T of the two fastest hadrons had to be $> 0.7 \text{ GeV}$ and their $\sum p_T^2 > 2.5 \text{ GeV}^2$ to suppress the contribution of the LP and to ensure factorisation; $0.35 < y < 0.9$ to remove regions not sensitive to Δg and regions with large radiative corrections; $x_F > 0$ to select the current fragmentation region and $M_{inv} > 1.5 \text{ GeV}$ to cut away the resonance production.

At low Q^2 not only the three hard subprocesses contribute to the cross-section but there is also considerable input from resolved photon processes. The contributions are presented in Figure 3.5. Three of them are treated as signal: PGF, $qg \rightarrow qq$, $gg \rightarrow gg$. "Low- p_T " labels non perturbative processes. This contribution and the contribution of the LP are neglected. The full expression for the measured double spin asymmetry is given by:

$$\begin{aligned}
A_{||}/D &= R^{PGF} \left\langle \frac{a_{LL}^{PGF}}{D} \right\rangle \frac{\Delta g}{g} + R^{QCDC} \left\langle \frac{a_{LL}^{QCDC}}{D} \right\rangle A_1 \\
&+ R^{qq \rightarrow qq} \left\langle \frac{a_{LL}^{qq \rightarrow qq}}{D} \right\rangle \frac{\Delta q}{q} \frac{\Delta q^\gamma}{q^\gamma} + R^{gq \rightarrow gq} \left\langle \frac{a_{LL}^{gq \rightarrow gq}}{D} \right\rangle \frac{\Delta q}{q} \frac{\Delta g^\gamma}{g^\gamma} \\
&+ R^{qg \rightarrow qg} \left\langle \frac{a_{LL}^{qg \rightarrow qg}}{D} \right\rangle \frac{\Delta g}{g} \frac{\Delta q^\gamma}{q^\gamma} + R^{gg \rightarrow gg} \left\langle \frac{a_{LL}^{gg \rightarrow gg}}{D} \right\rangle \frac{\Delta g}{g} \frac{\Delta g^\gamma}{g^\gamma}.
\end{aligned} \tag{3.34}$$

The fractions R^i are obtained from the PYTHIA generator [62]. The analysing power (partonic cross-section) a_{LL}^i is calculated at LO approximation using kinematics from the MC sample [65]. The polarised and unpolarised parton distributions in the nucleon, Δq and q , are taken from fits to global data [11, 12, 66, 67]. Also the unpolarised PDFs in the photon, q^γ, g^γ were taken from global data [68]. There are no data available for the polarised PDFs in the photon, $\Delta q^\gamma, \Delta g^\gamma$. They can be treated as a sum of calculable pQCD (point-like) term and non-perturbative (VMD) term. For the latter minimal and maximal scenarios [69] are considered. The official COMPASS results of this analysis taking into account data collected in 2002-2003 on deuteron target [70] reads

$$\frac{\Delta g}{g} = 0.024 \pm 0.089(\text{stat.}) \pm 0.057(\text{syst.}) \tag{3.35}$$

at $x_g \approx 0.095_{-0.04}^{+0.08}$ and scale $\mu^2 = 3 \text{ GeV}^2$. A more precise preliminary result of combined 2002-2004 data [71] gives

$$\frac{\Delta g}{g} = 0.016 \pm 0.058(\text{stat.}) \pm 0.055(\text{syst.}) \tag{3.36}$$

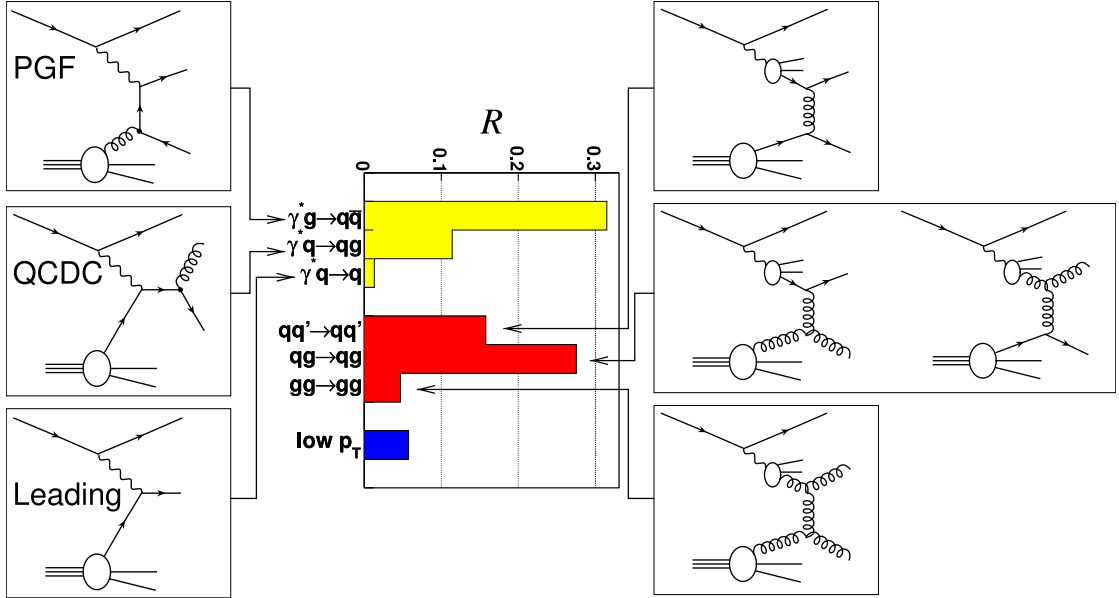


FIGURE 3.5: Relative contributions R of the dominant PYTHIA processes to the MC sample of high- p_T events at $Q^2 < 1 \text{ GeV}^2$. Left: point-like photon processes, right: resolved photon processes. Longitudinal photons, as well as minor resolved photon contributions, are not shown. Figure from [17].

3.2.4 $\Delta g/g$ from inclusive single hadrons and high- p_T hadron pairs from HERMES data

The HERMES experiment at the DESY laboratory used the HERA accelerator which has been shut down in 2007. However, the data analysis in the HERMES collaboration is still ongoing. The experimental setup is described in [72].

This analysis is described in the HERMES collaboration publication [57].

The method is based on PYTHIA [62]. Apart from the three aforementioned hard subprocesses which are LO pQCD also non-perturbative processes are taken into account. The analysis is based on the data taken with both hydrogen and deuterium targets. There were three main categories of events:

- "anti-tagged" single hadrons" - single hadrons with no scattered $e^{+'}$ detected. Contains mostly events with low Q^2 ($e^{+'}$ in the beam pipe). With the criterion - $p_{T(\text{beam})} > 1.0 \text{ GeV}$ the deuteron (proton) data sample in this category contains 1272k (419k) hadrons.
- "tagged" single inclusive hadrons" - the scattered positron has been detected with $Q^2 > 0.1 \text{ GeV}^2$, $W^2 > 4 \text{ GeV}^2$, and $y < 0.95$. For $p_{T(\gamma^*)} > 1 \text{ GeV}$ this deuteron (proton) data sample contains 53k (19k) hadrons.
- "inclusive pairs of hadrons" - The hadron pair sample consists of all pairs of charged hadrons with $p_{T(\text{beam})} > 0.5 \text{ GeV}$. Only in 10% of events a positron was detected.

With the additional requirement $\sum p_{T(\text{beam})}^2 > 2.0 \text{ GeV}^2$ the deuteron (proton) data sample contains 60k (20k) hadron pairs. With this requirement applied 6% of the ’’anti-tagged’ inclusive hadrons’’ are contained in this sample.

The asymmetry of the signal is given by

$$A^{SIG} \left\langle \frac{\Delta g}{g} \hat{a}(\hat{s}, \hat{t}, \mu^2, Q^2) \frac{\Delta f_a^{\gamma^*}(x_a, \mu^2)}{f_a^{\gamma^*}(x_a, \mu^2)} \right\rangle, \quad (3.37)$$

where \hat{a} is the analysing power calculable in pQCD. In order to calculate $\Delta f^\gamma/f^\gamma$, the photon polarisation, the averages of the maximal and minimal scenarios of the GRS [69, 73] helicity-dependent PDFs are used in conjunction with the GRS [68] helicity-averaged PDF. The background processes asymmetries are taken into account by

$$\left\langle \frac{\Delta g}{g} \right\rangle(p_T) = \frac{A^{meas}(p_T) - R^{BG} A_{MC}^{BG}(p_T)}{R^{SIG}(p_T) \left\langle \hat{a}(\hat{s}, \hat{t}, \mu^2, Q^2) \frac{\Delta f_a^{\gamma^*}}{f_a^{\gamma^*}} \right\rangle^{SIG}(p_T)}. \quad (3.38)$$

Here A_{MC}^{BG} is the average asymmetry of all background processes which are either negligible or taken from the world data as it is in case of the A_1 - the inclusive DIS photon-nucleon asymmetry. The fractions of each process R^i are taken from MC simulations.

The final result is

$$\frac{\Delta g}{g}(\langle x \rangle, \langle \mu^2 \rangle) = 0.049 \pm 0.034(\text{stat.}) \pm 0.010(\text{syst.-exp.})_{-0.099}^{+0.126}(\text{syst.-models}) \quad (3.39)$$

at scale $\langle \mu^2 \rangle = 1.35 \text{ GeV}^2$ and $\langle x \rangle = 0.22$.

The summary of the direct $\Delta g/g$ measurements is given in Figure 3.6.

3.2.5 $\Delta g/g$ from single all- p_T hadrons for $Q^2 > 1 \text{ GeV}^2$

This analysis [18] combines the approaches of the high- p_T analysis and the background subtraction of the Open Charm method. It will be described in more detail in Section 6.3. It is a method of solving a set of equations obtained not for different data samples like in the COMPASS high- p_T analysis but by weighting the equation for the number of events. It will be shown in Section 5.3 that this method is similar to the Unbinned Maximum Likelihood (UML) method. In this way an optimisation of statistical error is obtained. The result reads

$$\frac{\Delta g}{g} = 0.113 \pm 0.038(\text{stat.}) \pm 0.036(\text{syst.}) \quad (3.40)$$

at scale $\langle \mu^2 \rangle = 3 \text{ GeV}^2$ and $\langle x_g \rangle = 0.10$.

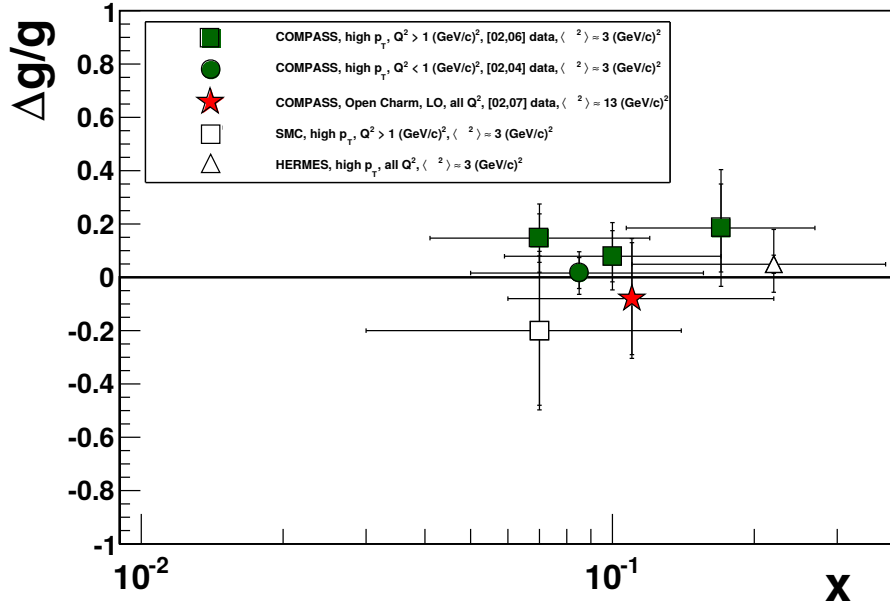


FIGURE 3.6: Compilation of the $\Delta g/g$ measurements from open charm and high- p_T hadron pair production by COMPASS [70, 59], SMC [55], HERMES [57] and Open Charm by COMPASS [58] as a function of x_g . The horizontal bars mark the range in x_g for each measurement, the vertical ones give the statistical precision and the total errors (if available). Figure from [16].

3.2.6 ΔG global fit with data from pp collisions

The measurements of polarised proton-proton collisions are performed at Brookhaven laboratory in USA at the Relativistic Heavy Ion Collider (RHIC). There are two experiments dedicated to the proton spin structure: STAR and PHENIX. The data collected in the years 2002-2006 and 2009 were taken with the centre-of-mass energy $\sqrt{s} = 200$ GeV.

The processes involving gluons are prompt photon production, quark-gluon and gluon-gluon fusion with jet production (see Figure 3.7). Both, prompt photon and jet produc-

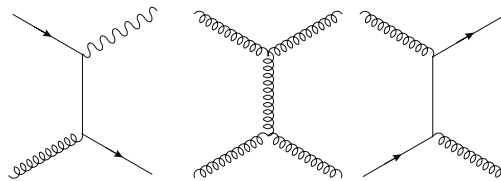


FIGURE 3.7: Selected lowest-order Feynman diagrams for elementary processes with gluons in the initial state in p-p collisions: quark-gluon Compton process with prompt photon production (left), gluon-gluon (centre) and gluon-quark (right) scattering for jet production.

tion suffer from large background. For the former it is the $\pi^0 \rightarrow \gamma\gamma$ decay, for the latter

the jet channels of quark-quark interactions. The big advantage of the RHIC collider is high data statistics.

The polarised protons are obtained from the polarised proton source and after three steps of acceleration they are injected into the two RHIC rings. Vertical polarisation of the protons during acceleration is maintained by the use of a magnetic field shape called "Siberian Snakes" which flips the spins of protons compensating the depolarisation effects. The maximum polarisation has been measured to be 30% in 2003, 65% in 2006. The average polarisation in 2009 reached 56%. The polarisation is rotated to the longitudinal direction directly before the collision.

The STAR detector [74] is designed to track and identify charged particles and is very well suited for jet reconstruction. The main advantage of the PHENIX detector [75] is a very precise calorimeter enabling π^0 identification especially in the mid-rapidity region. It has also good performance in lepton registration.

Both experiments measure the asymmetry between parallel (++) and anti-parallel (+-) polarised proton-proton collisions:

$$A_{LL}^{exp} = \frac{1}{P_1 P_2} \frac{\sigma^{++} - \sigma^{+-}}{\sigma^{++} + \sigma^{+-}}, \quad (3.41)$$

where P_1 and P_2 are the polarisations of the colliding beams. The measured asymmetry is the sum of asymmetries of different partonic reactions i :

$$A_{LL}^i = \frac{\Delta f_1^i}{f_1^i} \frac{\Delta f_2^i}{f_2^i} a_{LL}^i. \quad (3.42)$$

The $\Delta f^i/f^i$ are the ration of spin-dependent and spin averaged parton density functions. The partonic cross-section asymmetries a_{LL}^i are calculable in perturbative QCD.

The asymmetry of the signal $\Delta g/g$ is impossible to be separated or to be obtained from experimental asymmetry by background asymmetry subtraction. Therefore different scenarios of $\Delta g(x)$ distribution are assumed and corresponding double spin asymmetries of a given final state are evaluated. These scenarios are then compared to the data.

The method of global fit to both SIDIS and RHIC data has been developed by D. de Florian, R. Sassot, M. Stratmann, W. Vogelsang [76] (known as DSSV). The result obtained without 2009 RHIC data show very small contribution of ΔG . The analysis has been repeated by the same authors with the 2009 RHIC data [19]. This result is significantly different from zero and is presented in Figure 3.8. The newest result has been published by the STAR collaboration [61] where the authors use the NNPDF collaboration fit to the early data [77] and modify it by reweighting with the 2006 and

2009 STAR inclusive jet A_{LL} results. The obtained value of ΔG is 0.21 ± 0.10 . The latest global fits are presented in Figure 3.8.

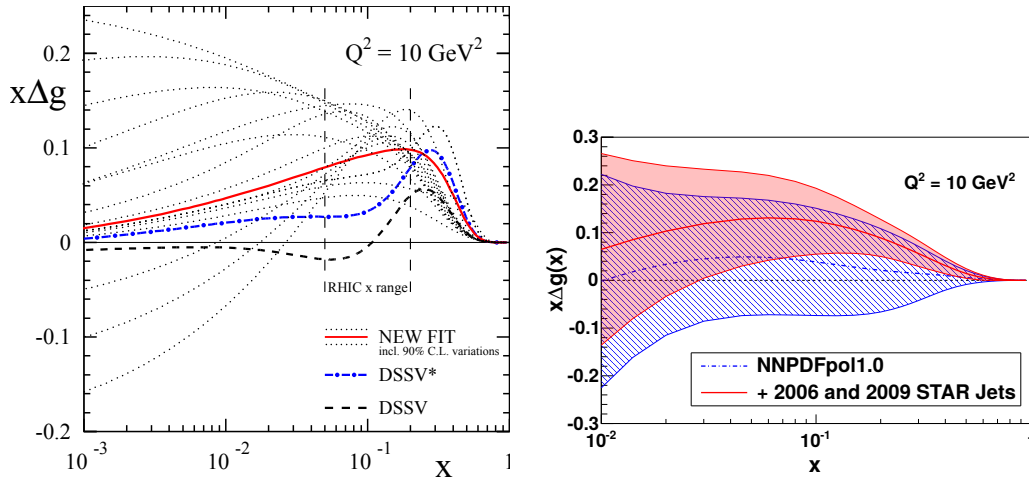


FIGURE 3.8: Left panel: gluon helicity distribution at $Q^2 = 10 \text{ GeV}^2$. The dotted lines present the gluon densities for alternative fits that are within the 90% C.L. The x -range primarily probed by the RHIC data is indicated by the two vertical dashed lines. Right panel:(Colour online.) Gluon polarisations from NNPDF(blue dot-dashed curve, hatched uncertainty band) [77], and from a modified version of NNPDF that obtained when including the 2006 and 2009 STAR inclusive jet A_{LL} results through reweighting (red solid curve and uncertainty band).

3.3 Quark and gluon orbital angular momentum

The orbital angular momentum (OAM) of partons cannot be directly accessed via measurement. One of the signatures of the parton orbital motion is the Sivers effect [23]. The transition from the Sivers effect to the OAM is, however, model dependent. The other possibility to access quark and gluon OAM is via the generalised parton distribution (GPD) function $E^{q,g}$ and the Ji's sum rule [78]. OAM of quarks and gluons have been also calculated on the Lattice QCD.

3.3.1 Sivers asymmetry measurements

Measurements of the Sivers asymmetries for charged pions and charged and neutral kaons produced in semi-inclusive deep-inelastic scattering of high energy leptons off transversely polarised protons were obtained both by COMPASS [79] and HERMES [80] experiments. The Sivers asymmetries are found to be positive for positive pions and kaons and compatible with zero otherwise. The results are presented in Figure 3.9. COMPASS has also published results of the Sivers asymmetry for identified hadrons with the deuteron target. As presented in Figure 3.10 the results are compatible with

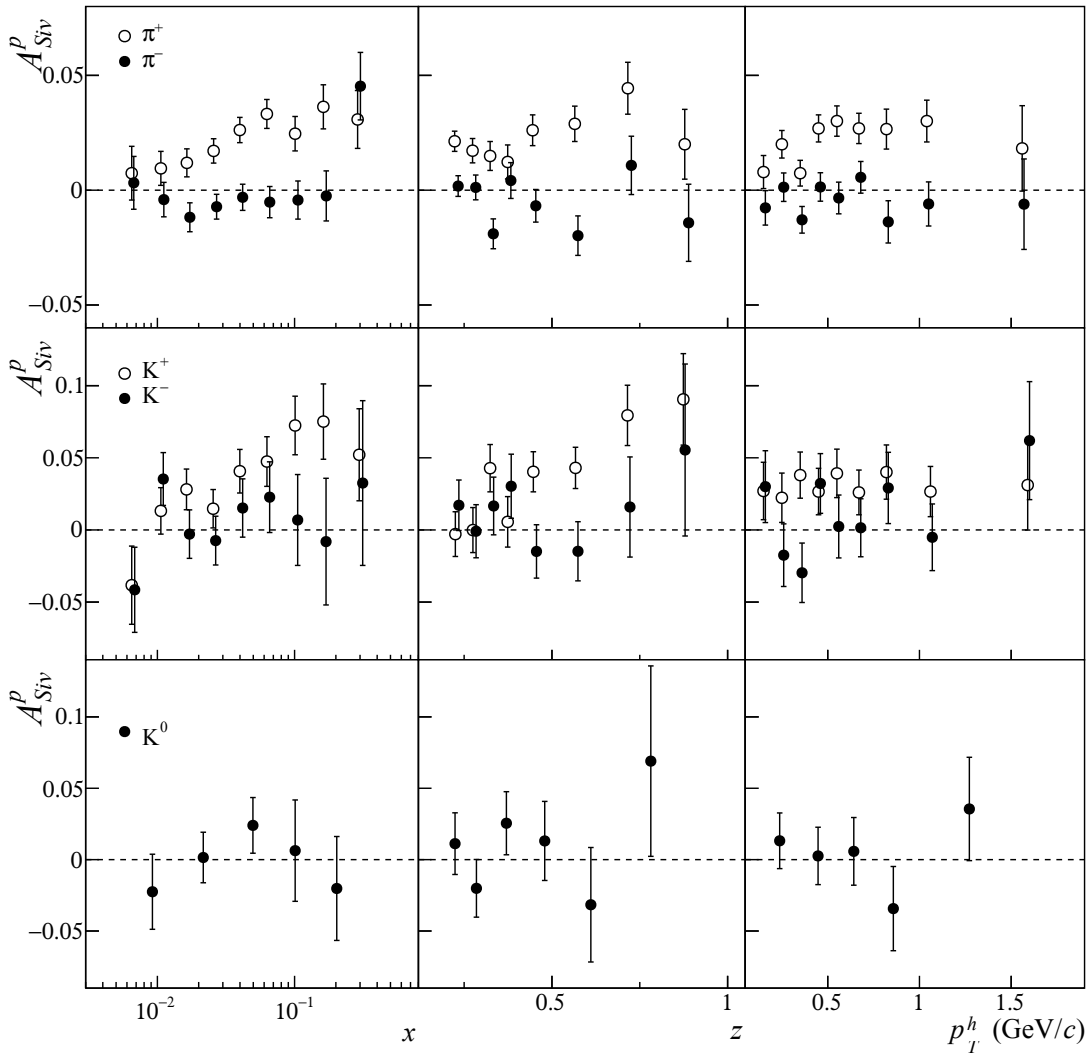


FIGURE 3.9: COMPASS results of the Sivers asymmetries for charged pions (top), charged kaons (middle) and neutral kaons (bottom) as a function of x, z and p_T^h . COMPASS data taken with the proton target.

zero. The nonzero result for positive hadrons on proton target and zero on deuteron (isoscalar) target suggests that the Sivers effects from u and d quark are different from zero but of opposite sign.

3.3.2 General Parton Distributions

Polarised GPDs contain information about parton's orbital angular momentum. In particular OAM can be obtained from GPD E via the Ji's sum rule [78]. COMPASS has obtained results from ρ^0 meson production with transversely polarised proton and deuteron targets [81] based on Hard Exclusive Meson Production process (see Figure 3.11). The

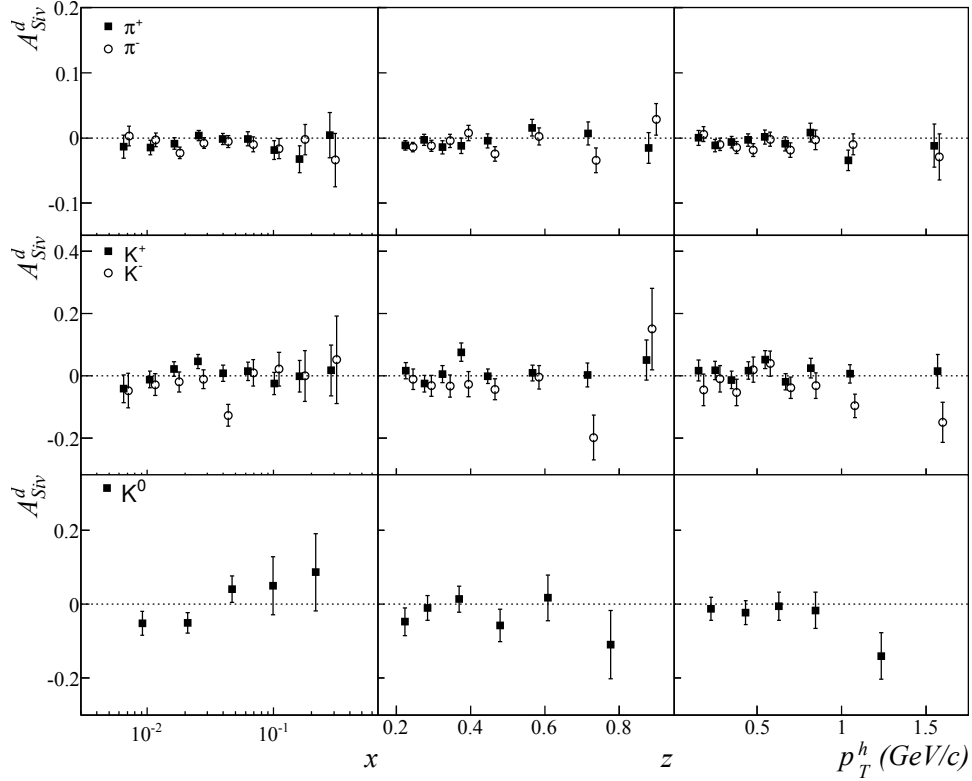


FIGURE 3.10: Siivers asymmetry measured by COMPASS against x , z and p_T^h for pions and kaons. COMPASS data taken with the deuteron target.

cross-section of this process contain azimuthal angle modulations similar to the modulations in the SIDIS single hadron cross-section 2.39. The asymmetry $A_{UT}^{\sin(\phi-\phi_S)}$ is sensitive to GPD E . The results, both for proton and deuteron targets, are compatible with zero (see Figure 3.11) which indicates that GPD E for u and d quarks is of the same value but opposite sign ($E^u \approx -E^d$). This fact is consistent with the hypothesis that OAM of u and d quarks cancel in the nucleon.

3.3.3 Calculations on QCD Lattice

QCD lattice calculation is a very effective and fast developing tool of theoretical calculation based on QCD first principles. The calculations are evaluated numerically on a quantised phase space called lattice (see Figure 3.12) with the use of the QCD Lagrangian. The renormalisation requires setting certain renormalisation constants (see [83] for details). The results of the total $J^{u,d}$ and separated spin $S^{u,d}$ and OAM $L^{u,d}$ u and d quark contribution to the spin of the nucleon is presented in Figure 3.13. The fine lattice spacing used in the calculations is $a = 0.084$ fm and the number of flavours $N_f = 2 + 1$. For renormalisation several values of pion mass down to 300 MeV have been applied. Results of two methods of obtaining the quark masses: domain wall fermions (DWF) [84] and hybrid (Hy) action - DWF for valence quarks and improved Asqtad

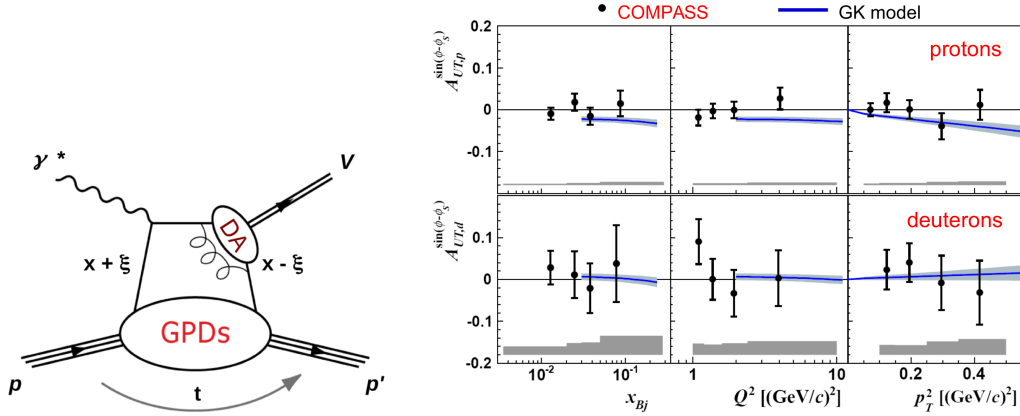


FIGURE 3.11: Left: Hard Exclusive Meson Production (HEMP) "handbag" diagram. Right: COMPASS results of the $A_{UT}^{\sin(\phi-\phi_S)}$ asymmetry on deuteron and proton targets as a function of x_{Bj} , Q^2 and p_T^2 . Error bars show statistical uncertainties, while the systematic ones are represented by grey bands at the bottom. The curves show the prediction of the GPD model by Goloskokov and Kroll [82] using the set of parameters called 'variant 1'. They are calculated at $W = 8.1$ GeV and $p_T^2 = 0.2$ GeV^2 for the left and middle panels, and at $W = 8.1$ GeV and $Q^2 = 2.2$ GeV^2 for the right panels. The theoretical error bands reflect uncertainties of GPD parametrisations. Blue line is the Goloskokov-Kroll model expectation.

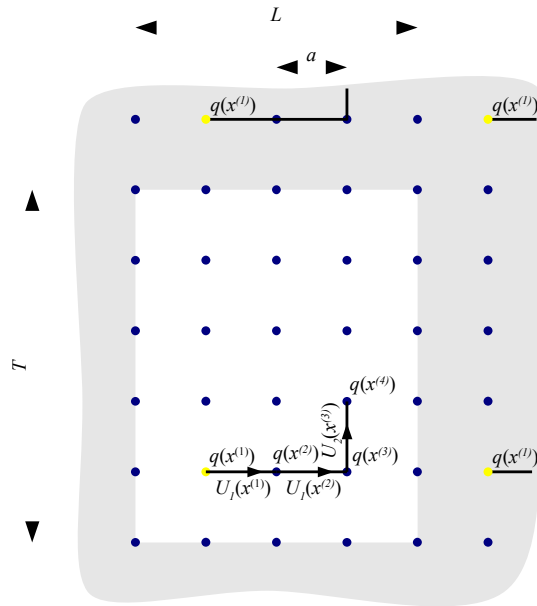


FIGURE 3.12: Illustration of the periodic lattice and its degrees of freedom.

action [85]. These calculations confirm that the contribution of OAM of u and d quarks to the nucleon spin can be opposite and cancel one another. There seems to be room for significant contribution of gluon OAM.

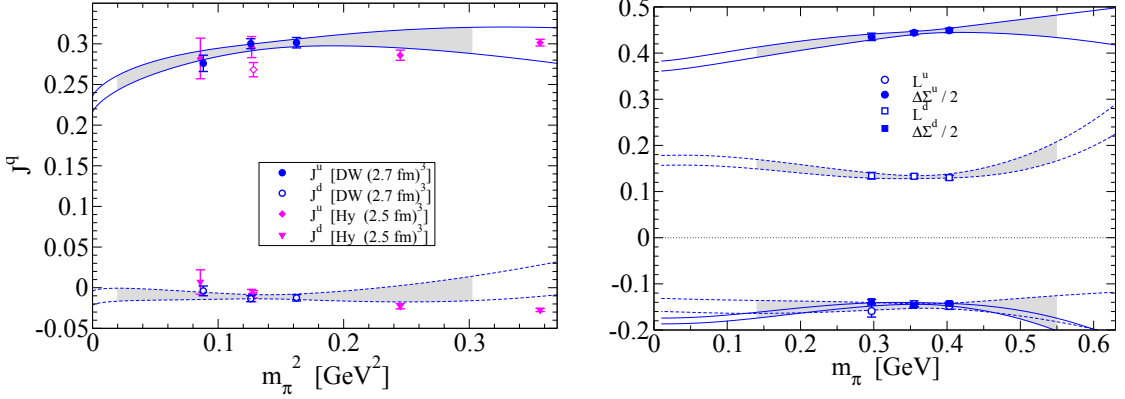


FIGURE 3.13: Left: u and d quark contributions to the nucleon spin from the domain wall and hybrid action calculations. Right: u and d quark spin and orbital momentum from the domain wall calculations.

3.4 Measurements giving access to Gluon Sivers Function

The Sivers effect for gluons can be evaluated from both proton-proton collisions and semi-inclusive DIS experiments. The results of the left-right asymmetry A_N (Equation (3.43)) obtained by the PHENIX collaboration for the $pp^\uparrow \rightarrow \pi^0 X$ lead to model dependent constraints on the Gluon Sivers Function (GSF) published in [86].

$$A_N = \frac{\sigma_L - \sigma_R}{\sigma_L + \sigma_R} \quad (3.43)$$

The results, presented in Figure 3.14, obtained in the mid-rapidity and negative x_F region where gluon contribution should be dominant, show that the GSF is small or even zero. In order to evaluate theoretically A_N the assumption of a generalised QCD factorisation scheme which involves unintegrated TMD parton distribution and fragmentation function $\hat{D}_{\pi/c}(z, k_{\perp\pi})$ are made. In the given kinematic region A_N is largely dominated by the Sivers effect and then the following equation holds [86]

$$\begin{aligned} \frac{E_\pi d\sigma^\uparrow}{d^3\mathbf{p}_\pi} - \frac{E_\pi d\sigma^\downarrow}{d^3\mathbf{p}_\pi} \simeq \sum_{a,b,c,d} \int \frac{dx_a dx_b dz}{\pi x_a x_b z^2 s} d^2\mathbf{k}_{\perp a} d^2\mathbf{k}_{\perp b} d^3\mathbf{k}_{\perp\pi} \delta(\mathbf{k}_{\perp\pi} \cdot \hat{\mathbf{p}}_c) \mathbf{J}(k_{\perp\pi}) \\ \times \Delta \hat{f}_{a/p^\uparrow}(x_a, \mathbf{k}_{\perp a}) \hat{f}_{b/p}(x_b, \mathbf{k}_{\perp b}) \hat{s}^2 \frac{d\hat{\sigma}^{ab \rightarrow cd}}{d\hat{t}}(x_a, x_b, \hat{s}, \hat{t}, \hat{u}) \delta(\hat{s} + \hat{t} + \hat{u}) \hat{D}_{\pi/c}(z, k_{\perp\pi}), \end{aligned} \quad (3.44)$$

where

$$\Delta \hat{f}_{a/p^\uparrow}(x_a, \mathbf{k}_{\perp a}) \equiv \hat{f}_{a/p^\uparrow}(x_a, \mathbf{k}_{\perp a}) - \hat{f}_{a/p^\downarrow}(x_a, \mathbf{k}_{\perp a}) = \Delta^N \hat{f}_{a/p^\uparrow}(x_a, k_{\perp a}) \cos \phi_a \quad (3.45)$$

is referred to as the Sivers distribution function of parton a inside a transversely polarised (along the Y -axis) proton (moving along the Z-axis) and ϕ_a is the azimuthal angle of the intrinsic transverse momentum $\mathbf{k}_{\perp a}$ of parton a . The extra phase-space factor $\mathbf{J}(k_{\perp \pi})$ is the proper invariant Jacobian factor for the transformation from the parton momentum \mathbf{p}_c to the hadron momentum \mathbf{p}_π . In the model the TMDs and the fragmentation function are assumed to be Gaussian-like.

The curves in Figure 3.14 represent different scenarios for the gluon and sea-quark Sivers function:

- dot-dashed line - no sea quark contribution, GSF chosen to saturate the natural positivity bound:

$$\Delta^N \hat{f}_{g/p^\uparrow}(x, k_T) = -2\hat{f}_{g/p^\uparrow}(x, k_T), \quad (3.46)$$

- solid line - all valence and sea-quarks contribution included and a non-vanishing positive Sivers function for sea-quarks which saturates the positivity bound $\Delta^N \hat{f}_{q_s/p^\uparrow}(x) \equiv \hat{f}_{q_s/p}(x)$ together with the largest negative GSF. Dashed line represents the contribution of the GSF. Dotted line shows the quark contribution.

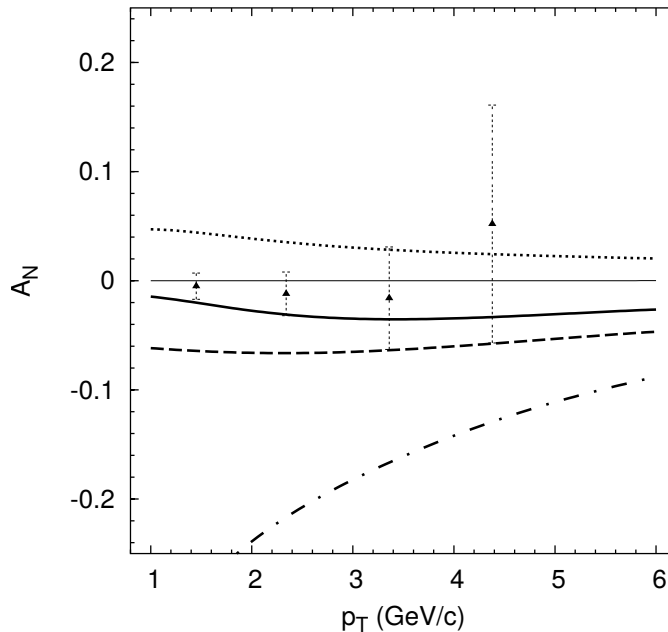


FIGURE 3.14: A_N measurement at PHENIX two scenarios: positive GSF and no sea-quark contribution (dot-dashed line), negative GSF and positive sea-quark contribution (solid line) divided into gluon (dashed line) and quark contribution (dotted line).

Recently a new analysis of all PHENIX data has been published [87]. The authors use two parametrisations of quark Sivers function obtained from SIDIS measurements KRE-SIDIS1 [88] and DSS-SIDIS2 [89]. Again Gaussian-like function are chosen to represent the GSF and the fragmentation functions. A fit to the PHENIX A_N measurement is performed with

$$\chi^2 = \sum \frac{(A_N^{gluon} + A_N^{quark} - A_N^{exp})^2}{\sigma_{exp}^2 + \sigma_{quark}^2}, \quad (3.47)$$

where σ_{exp} is the error of the experimental point and σ_{quark} is the uncertainty of the theoretical prediction of the quark contribution. The results are shown in Figure 3.15. These results show very small, almost negligible Gluon Sivers Function. It should be noted, however, that the results depend strongly on the applied models. The uncertainties of the theoretical predictions are proportional to the obtained value and hence very small under the assumptions made.

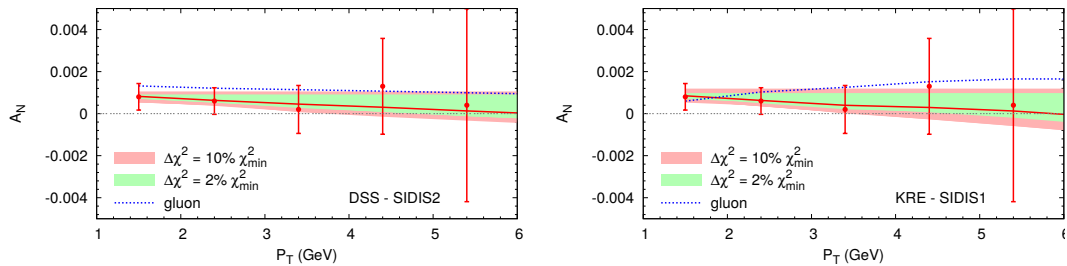


FIGURE 3.15: The SSA A_N , red solid line, compared with PHENIX data [90] at $\sqrt{s} = 200$ GeV and at mid-rapidity, as a function of P_T (in the lower P_T range), obtained adopting the SIDIS2 set [89] (left panel) and the SIDIS1 set [88] (right panel) for the quark Sivers functions. The red (green) band represents a tolerance of 10% (2%) in χ^2 . The gluon contribution to A_N , blue dotted line, is also shown.

3.5 Future measurements of gluon Sivers effect

Measurements of single spin asymmetries (SSA) similar to the aforementioned PHENIX experiment could be done at AFTER@LHC where the beam of protons or lead ions of the LHC would be scattered on a fixed transversely polarised target [91]. Such collisions would have a centre-of-mass energy of 115 GeV for proton beam and 72 GeV for lead beam. LHC provides high luminosity what enables study of the rare processes like J/Ψ production to measure gluon Sivers effect directly. Also Sivers effect for quarks and gluons could be measured with larger precision via polarised Drell-Yann and prompt photon production, and the gluon contribution can be estimated more precisely. In addition, the comparison of $Pbp^\uparrow \rightarrow \gamma jet X$ and $pp^\uparrow \rightarrow \gamma jet X$ could be useful in determining the relative sizes of quark and gluon Sivers functions.

The golden channel for studying the gluon Sivers effect should be open charm production

at the Electron-Ion Collider (EIC) [20], $ep^\uparrow \rightarrow e'c\bar{c}X$. This reaction gives direct access to gluons. EIC kinematics should enable measurements at small x .

Chapter 4

The COMPASS experiment at CERN

4.1 Introduction

COMPASS (COmmon Muon Proton Apparatus for Structure and Spectroscopy) is a fixed target experiment at CERN. It uses the beam from the Super Proton Synchrotron (SPS). In the years 2002-2012 COMPASS has taken data for two main programs, nucleon structure and hadron spectroscopy. Since 2012 COMPASS entered phase II (described in the COMPASS II proposal, [92]) and in 2015 has been taking data for the Drell-Yan reaction. The measurement of the Deeply Virtual Compton Scattering (DVCS) reaction giving access to GPDs is planned for 2016 and 2017.

The hadron structure program consists of both longitudinal and transverse spin structure of the nucleon. In both cases polarised muon beam and polarised targets have been used. COMPASS has obtained a precise result for the contribution of the quark spin to the spin of the nucleon $\Delta\Sigma$, [93]. In the same publication the collaboration estimated the gluon spin contribution ΔG from the QCD evolution. It should be noted, however, that the precision of this measurement is based on the assumption of the applied evolution model. Results of different approaches to the direct measurement of gluon polarisations from SIDIS data have been published in [58] - Open Charm, [59] - high- p_T hadron pairs and [18] - all- p_T hadrons. COMPASS has been also taking data with transversely polarised targets obtaining results of the Collins and Sivers asymmetry measurements for identified hadrons, [94, 79]. The paper on other asymmetries, giving access to different Transverse Momentum Dependent structure functions (TMDs), from the cross-section given in Equation (2.39) is in preparation. The SIDIS data are also used to obtain hadron multiplicities needed for calculation of fragmentation functions.

The General Parton Distributions (GPDs) has been studied with the use of data taken with transversely polarised target via the Hard Exclusive Meson Production (HEMP). Results of this analysis have been published in [81, 95]. In 2012 a test run of the DVCS measurement has been performed with an unpolarised liquid hydrogen target and a recoil proton detector surrounding the target area. The actual measurement is planned for the years 2016 and 2017.

The hadron spectroscopy program has been using the hadron (a mixture of pions, kaons and protons) beam scattered off unpolarised liquid hydrogen and nuclear targets. The cross-sections of these processes enable to collect high statistics in relatively short time. The analysis method is called the Partial Wave Analysis (PWA) method and the most important results are the radiative width for the $a_2(1320)$ and $\pi_2(1670)$ resonances [96] and the discovery of the $a_1(1420)$ resonance [97]. In addition a very important results have been obtained in a pion polarisability measurement via the Primakoff reaction [98].

In the year 2015 COMPASS has been taking data with pion beam and transversely polarised target to measure the asymmetries of the Drell-Yan reaction. It is an alternative way to access TMDs and a test of our understanding of QCD.

Here the setup for the muon beam and transversely polarised target will be described as data collected in this configuration have been used to extract the Sivers asymmetry for gluons.

4.2 The beamline

The COMPASS experiment is situated on the CERN M2 beamline coming from SPS. The SPS synchrotron produces 400 GeV protons which hit a 500 mm beryllium target (called T6) producing hadrons (mostly pions). The intensity of the proton beam is of the order of 10^{13} protons per spill. Magnets situated behind the T6 target enable momentum and charge selection of the hadron beam (172 GeV for the nominal 160 GeV muon beam). Then in the 600 m long decay channel approximately 10% of pions decay into muons. As this is a parity violating reaction muons are naturally 100% polarised in the rest frame. In the laboratory frame the polarisation is $\sim 80\%$ [64]. The sign of the polarisation depends on the muon charge. For the 160 GeV μ^+ beam the polarisation is about -80% (see Figure 4.1). The 1.1 m beryllium absorber stops the remaining hadrons. This absorber is followed by another set of dipole and quadrupole magnets which shape and clean the muon beam. Muons are delivered to the experimental hall through a 250 m long channel. The momentum spread of the final beam is typically 5% with respect to the nominal momentum. The beamline scheme is presented in Figure 4.2.

The Beam Momentum Stations (BMS) built of scintillating fiber detectors enable beam momentum reconstruction and set the time reference. Details of the beam reconstruction algorithm and procedure can be found in [99].

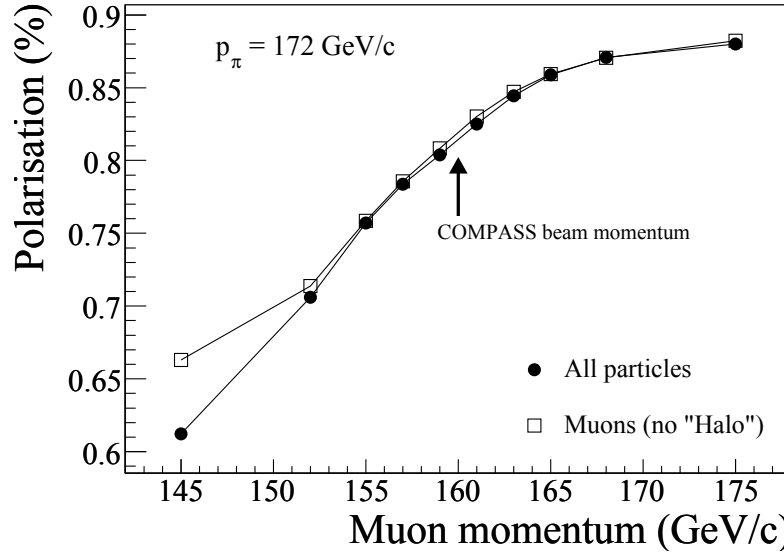


FIGURE 4.1: The absolute value of the muon beam polarisation as a function of the muon momentum. The dependence is shown for the initial 172 GeV pion beam.

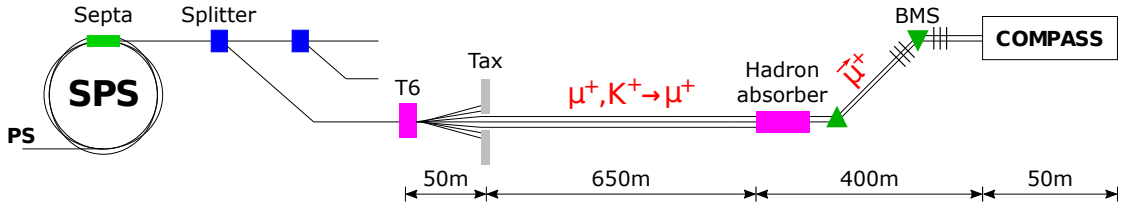


FIGURE 4.2: COMPASS beamline scheme.

4.3 The polarised target

The objective of building and maintaining a polarisation of a deuteron or proton target is very difficult to achieve and it has been a big success of the COMPASS target group to cope with this task. Especially that the length of the target has to be large enough to obtain reasonable rates with small DIS cross-section. In order to build and maintain the polarisation the target material has been cooled to about 50 mK in the frozen spin mode and put in a homogeneous 2.5 T magnetic field. For the cooling an efficient $^3\text{He}/^4\text{He}$ dilution refrigerator has been used and to produce the magnetic field a superconducting solenoid magnet has been utilised. This magnet enables polarisation of the target in the longitudinal direction. An additional dipole magnet of 0.5 T allowed rotation of longitudinal polarisation and obtaining transverse polarisation of the target. In case of the transversely polarised target in order to change the direction of polarisation it has to be destroyed and rebuilt in the opposite direction.

The procedure of building of the polarisation is called Dynamic Nuclear Polarisation (DNP) [100]. Due to the nucleon magnetic moment of nucleons it is very hard to polarise them directly. The electrons in the atoms are easily polarisable and in the 2.5 T field and a temperature of a few degrees Kelvin a 99.8% polarisation of electrons is obtained. By means of microwave radiation this polarisation is transferred to the nucleons. Microwaves of characteristic energy needed for simultaneous spin flip of the proton and the electron are radiated on the target material. This energy depends, in the proton target case, on the total final spin of the electron-proton system (0 or 1) therefore the direction of the spin of the proton can be chosen by the proper choice of microwave frequency (illustrated in Figure 4.3). The high magnetic moment of electrons causes them to relax in milliseconds to the lower energy state. At the same time low magnetic moment of nucleons keeps them polarised as the spontaneous spin flip is of low probability. The relaxation time of the polarisation built in this way is approximately 1000 h. The average relaxation rate for the transverse mode is about 1% per day.

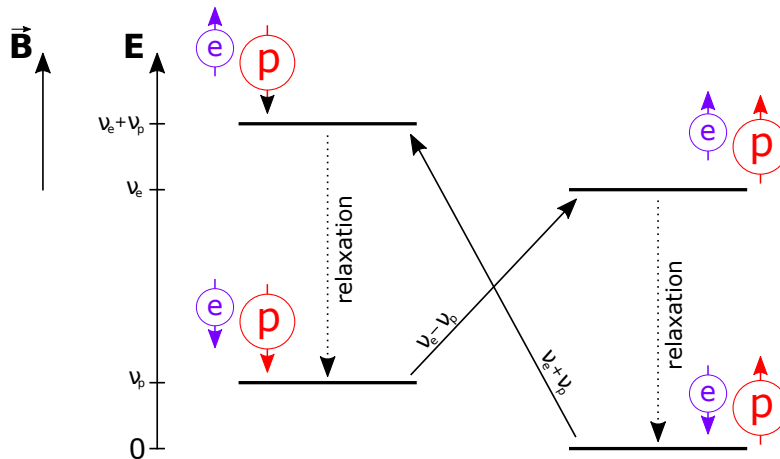


FIGURE 4.3: The dynamic nuclear polarisation for the proton-electron system.

The main difference between the setup with the deuteron and the proton targets was the number of target cells. In the former case there were two 60 cm cells (upstream and downstream) and in the latter three cells of the length of 30 cm, 60 cm and 30 cm (upstream, centre and downstream). The scheme of the three cell target area is presented in Figure 4.4. The cells can be polarised in the direction or opposite direction to the solenoid field by applying microwaves of certain frequencies. In this way at the same time both target polarisations are probed what enables control of the systematics. In case of the three-cell target the central cell is polarised oppositely to the outer cells. Polarisation in all cells is reversed every two or three days in case of the longitudinal polarisation and in case of the transverse polarisation on a weekly basis.

During the data taking important in the context of this thesis two target materials have been used: the deuterated lithium (${}^6\text{LiD}$) which will be referred as "deuteron target"

and ammonia (NH_3) referred as "proton target". The polarisation obtained for 6LiD is about 48% and for NH_3 is about 80%. The other important parameter of the target is the dilution factor (described in Section 5.2.1) which by definition is the ratio of the total cross-section of polarisable material in the target to the total cross-section of all target material. Taking into account the fact that the cooling substances (${}^4He/{}^3He$) are also present in the target area the values of the dilution factor are 38% for 6LiD and 15% for NH_3 .

The data taken with the deuteron target was taken before the upgrade of the spectrometer which took place in 2005. The main improvement was the radial acceptance due to the change of the solenoid magnet from ± 70 mrad to ± 180 mrad.

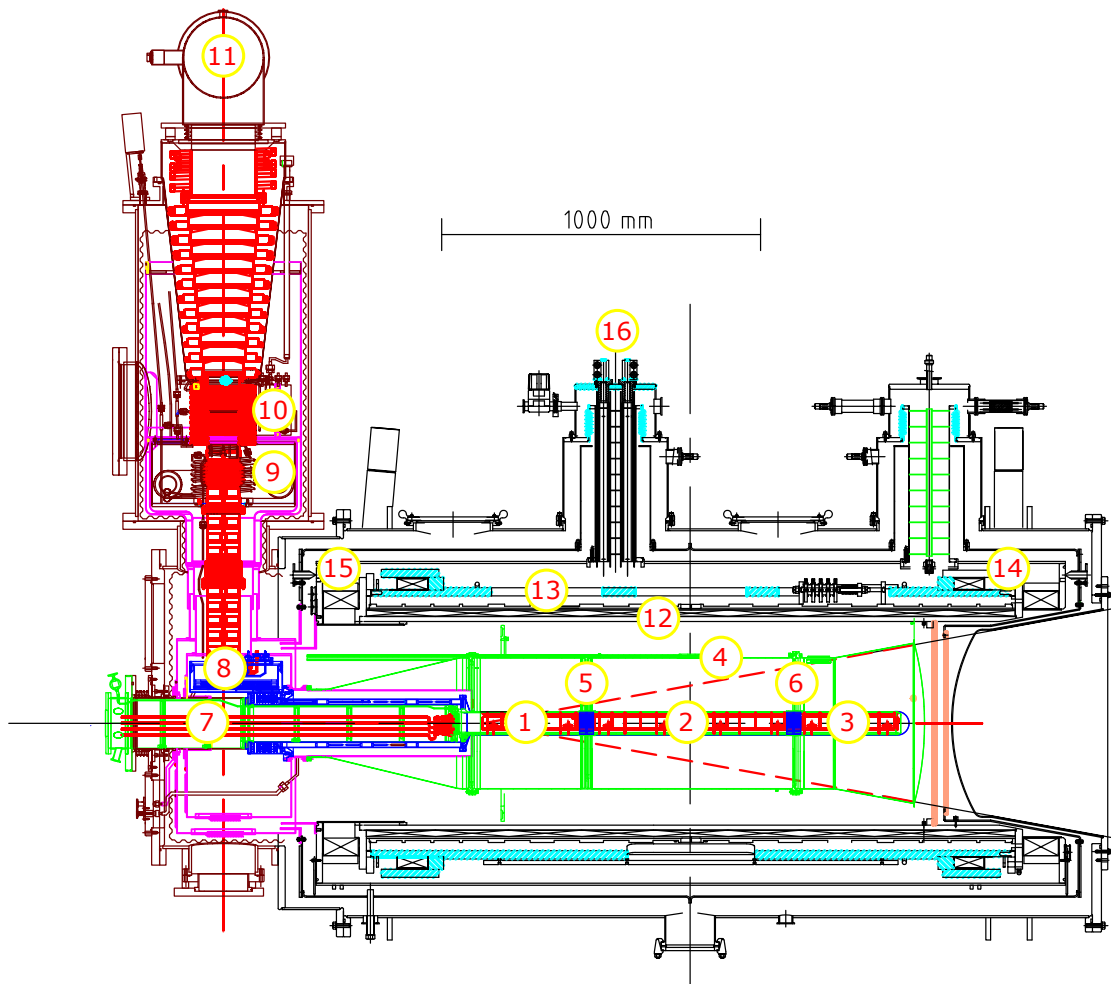


FIGURE 4.4: The sketch of the three-cell polarised COMPASS target according to [101]. The marked elements are: (1) upstream target cell, (2) middle target cell, (3) downstream target cell, (4) microwave cavity, (5) upstream microwave stopper, (6) downstream microwave stopper, (7) target holder, (8) still or 3He evaporator, (9) 4He evaporator, (10) 4He liquid/gas separator, (11) 3He pumping port, (12) solenoid magnet, (13) correction coils, (14) dipole coil, (15) solenoid end compensation coil and (16) magnet current leads. Figure from [99].

4.4 The COMPASS spectrometer

The COMPASS spectrometer can be divided into three main parts:

1. The Beam Telescope (BT) which measures the time, position and direction of the incoming beam.
2. The Large Angle Spectrometer (LAS) consisting of tracking detectors, calorimeters and muon filters surrounding the first magnet SM1.
3. The Small Angle Spectrometer (SAS) consisting of tracking detectors, calorimeters and muon filters surrounding the second magnet SM2.

For particle identification in the LAS area there is the Ring Imaging Cherenkov (RICH) detector. The LAS is set just behind the target area, its angular acceptance is ± 180 mrad (± 70 mrad before the upgrade in 2005). The dipole magnet SM1 has the bending power of 1 Tm. The bending power of the second magnet (in the SAS area) SM2 is 4.4 Tm. The schematic drawing of the COMPASS spectrometer is given in Figure 4.5.

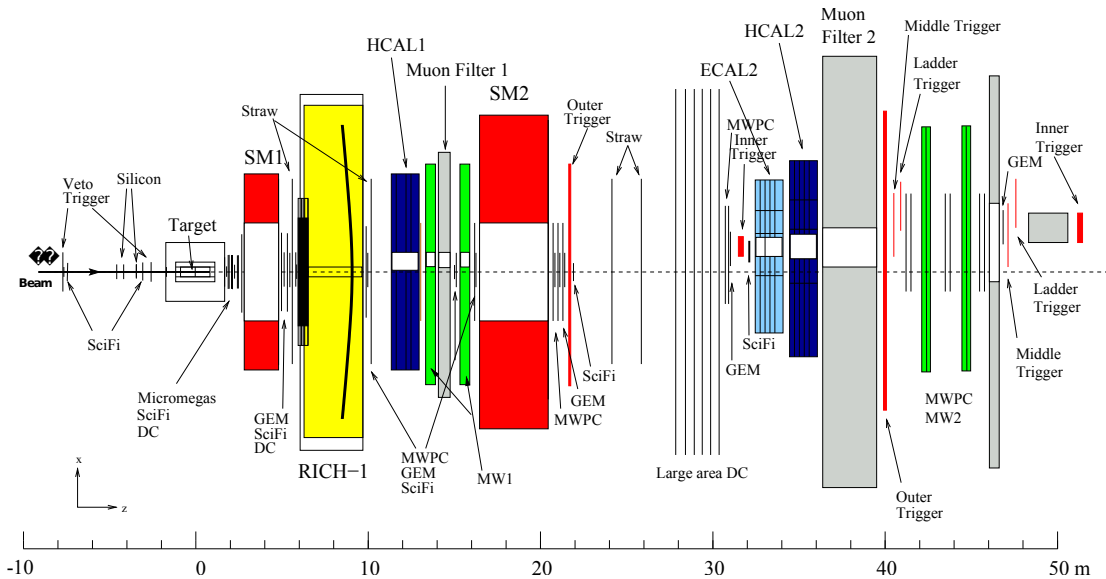


FIGURE 4.5: The top view of COMPASS 2004 muon setup.

4.4.1 The Beam Telescope

This part of the spectrometer consists of scintillating fiber detectors (FI) and silicon microstrip stations (SI). Scintillating fibers give precise time measurement of the incoming particles which is essential in the beam reconstruction. Both fiber stations and silicon detectors have good spatial resolution and they can handle high counting rates. This

features are needed for reconstruction of the interaction vertex and the scattering angle of the muon.

4.4.2 Very small area trackers

The structures of SAS and LAS are similar and consist of several types of detectors.

Very small area trackers are detectors operating close to the beam axis and therefore they need to be resistant to radiation damages, cope with high counting rates and have a good spacial resolution. Scintillating fibers (FI) are used for this purpose. Several FI station are placed both in LAS and SAS centred on the beam axis.

4.4.3 Small Area Trackers

These detectors cover the area up to 40 cm away from the beam axis. For this purpose gaseous type detectors which separate gas amplification area from the readout are used: GEM - Gas Electron Multiplier (GM) and MicroMeGas - Micromesh Gaseous Structure (MM). They introduce minimal amount of material into the beam and can operate in sufficiently high flux of incoming particles. GEM detectors cover also the beam axis area, however in normal data taking conditions their central parts are switched off in order to avoid damaging them. They are turned on during runs dedicated to alignment of the spectrometer when the beam intensity is low.

4.4.4 Large Area Trackers

In the outer parts of the spectrometer the particle flux is much less intensive. Therefore the granularity of the detectors can be lower. Good resolution is, however, still needed. Both of this features are satisfied by MultiWire Proportional Chambers (MWPC) and drift detectors. Straw Tubes (ST) and MWPCs are placed in both parts of the spectrometer. In the LAS Drift Chambers (DC) and in SAS large drift Chambers (W45) are used.

4.4.5 Calorimeters

Both LAS and SAS are equipped with electromagnetic and hadronic calorimeters. The Electromagnetic Calorimeters (ECAL1 and ECAL2) where in full operation since 2006. Earlier only part of ECAL2 was equipped with readout and ECAL1 was not installed. As these detectors are to measure electrons and photons and estimate their energies they

are essential in the DVCS and HEMP measurements which objective is to extract the GPDs. Hadronic Calorimeters (HCAL1 and HCAL2) provide discrimination between hadrons and muons. They are an important part of the trigger system.

4.4.6 Muon Filters

In order to identify muons muon wall detectors are placed in both LAS (MA) and SAS (MB). They are both composed of active part (proportional chambers in MA, drift chambers in MB) and an absorber (60cm of iron for MA and 2.4 m of concrete in case of MB). The Muon Filters have been used in COMPASS mainly to detect the scattered muon.

4.4.7 Ring Imaging CHerenkov (RICH) detector.

The RICH detector is placed in the LAS. Its role is to distinguish between different hadrons (pions, kaons and protons). It enables the measurement of particle velocity by the size of the ring of the Cherenkov light emitted in a C_4F_{10} pure gas. Velocity combined with the particle momentum obtained in magnetic spectrometers give particle identification. Pions, kaons and protons can be identified for momenta greater than 2.6, 9, 18 GeV respectively. The separation is possible for momenta up to 50 GeV.

4.5 Trigger System

The COMPASS Data Acquisition System (DAQ) can handle 25 kHz therefore a trigger system ([102]) has to be used to lower the signal rates entering the DAQ. The trigger system is designed to collect events with full range of the fractional energy of the virtual photon, $0 < y < 1$, and a large range of Q^2 , from a quasi-photoproduction at $Q^2 \approx 0$ to a maximum value allowed by the kinematics. It also provides time reference, taken from the BMS, for hit correlations and drift time calculations. The veto system, located upstream of the target, working with anti-coincidence with trigger logic protects from unnecessary triggering by the beam halo.

The COMPASS trigger system is based on hodoscope detectors but also uses calorimeter detectors. The schematic drawing of the most important elements of the trigger system is shown in Figure 4.6. Each part of the system is based on two hodoscope stations separated by an absorber, which suppresses the occupancy caused by hadrons and electrons. The hodoscopes trigger system consists of the following subsystems:

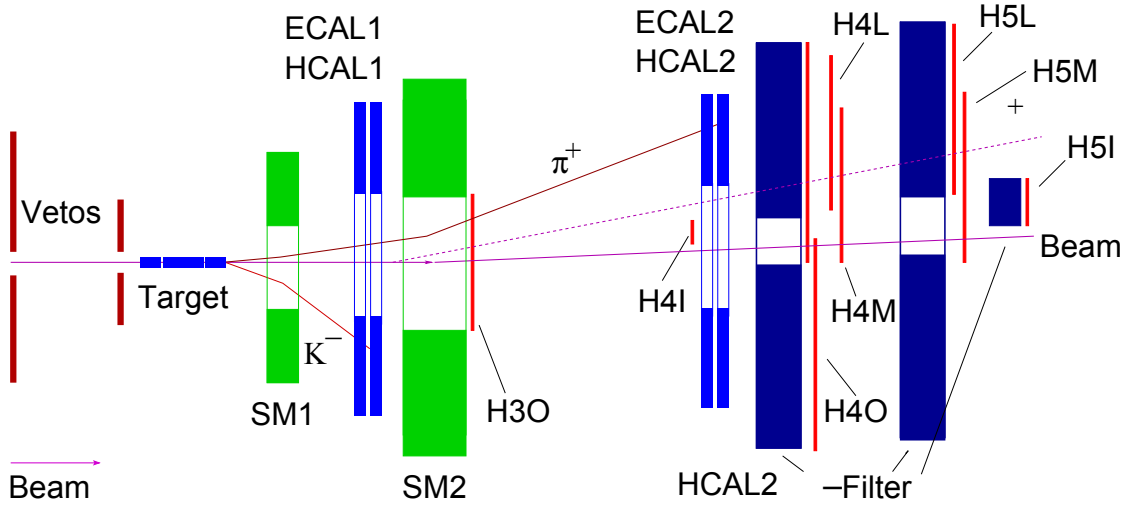


FIGURE 4.6: The sketch of the most relevant elements for the trigger system.

- Inner Trigger (IT) - composed of H4I and H5I hodoscope stations, covers the region of photoproduction (low Q^2) and very small energy loss of the scattered muon y ,
- Ladder Trigger (LT) - composed of H4L and H5L stations, covers small Q^2 large y region,
- Middle Trigger (MT) - composed of H4M and H5M stations, covers DIS region with small to moderate Q^2 ,
- Outer Trigger (OT) - composed of H3O and H4O stations, covers DIS region with moderate to large Q^2 .

The signal from each of the above-mentioned subsystems triggers the DAQ under two additional conditions: that there is no signal in the veto system and that, for certain triggers, the energy deposit in the hadronic calorimeters is above a 6 GeV threshold. In this way the contamination from radiative events, μe scattering and low energy halo tracks is reduced. In addition there is a pure Calorimetric Trigger (CT) which fires when an energy deposit exceeds 8 - 18 GeV. This trigger extends the Q^2 range to events where the scattered muon does not hit the hodoscope triggers.

All triggers of the system can be divided into three parts:

- Inclusive triggers (OT, inclMT)- the triggers that require only coincidence in the hodoscopes,
- Semi-inclusive triggers (IT, LT, MT) - the triggers that require certain energy deposit in the hadronic calorimeters in addition,
- Pure calorimetric trigger (CT) - the trigger which requires only certain energy deposit in the hadronic calorimeters.

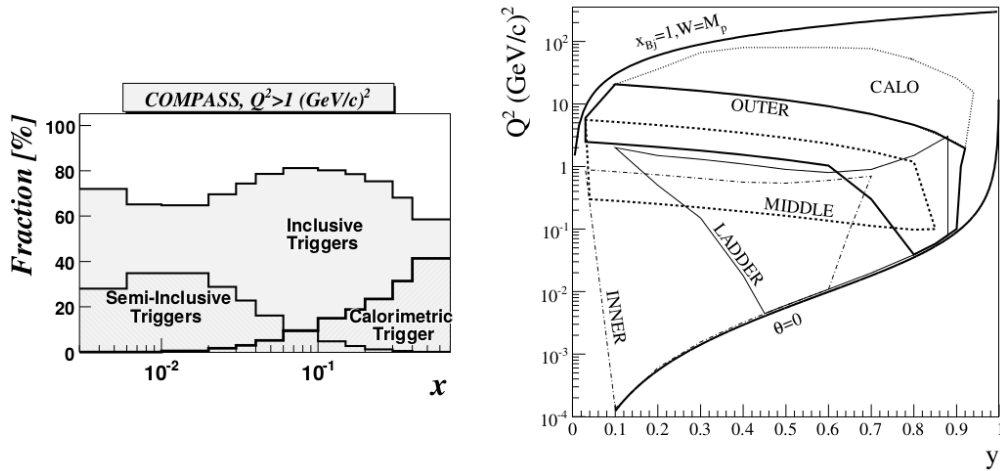


FIGURE 4.7: Left panel shows the fraction of inclusive, semi-inclusive, and calorimetric triggers as a function of x . Right panel presents the kinematical coverage in y and Q^2 for the COMPASS trigger subsystems. The two lines, $x_{Bj} = 1$; $W = M_p$ and $\theta = 0$ show the kinematic limits of elastic scattering and forward scattering, respectively.

Figure 4.7 shows the coverage of the kinematic regions by given triggers.

For calibrations, efficiency and alignment studies additional triggers exist:

- Beam Trigger (BT) - fires when a particle in the first FI station is detected,
- Veto Trigger (VT) - fires when a particle in the Veto detectors is detected,
- Random Trigger (RT) - the DAQ is started randomly.

Events recorded with these triggers usually contain small number of particles which makes the reconstruction and interpretation simpler.

4.6 DAQ - the data acquisition system

The data acquisition system (DAQ) described here has been used in the years in which the data analysed in this thesis has been collected. Recently the system has been changed by using (partially) different front-end electronics and programmable FPGA cards reducing the number of computers.

The role of the DAQ is to digitise the analog signals from the detectors, collect the incoming data when the trigger system fires, built events from the collected data and store them on disks. The digitisation takes place as close to the detectors as possible on the front-end boards. The readout drivers (CATCH and GeSiCa) concentrate the data into high bandwidth streams sent via optic links to the Readout Buffer computers (ROBs). Then the data is transferred using a gigabit Ethernet network to the Event

Builder computers. The Event Builders collect the information from all the detectors and combine it into events. The events are sent to Central Data Storage (CDR) at CERN and copied to long term storage tapes. The data acquisition (DAQ) software is based on DATE framework developed for the ALICE experiment at the LHC accelerator [103]. The scheme of the COMPASS DAQ system is shown in Figure 4.8.

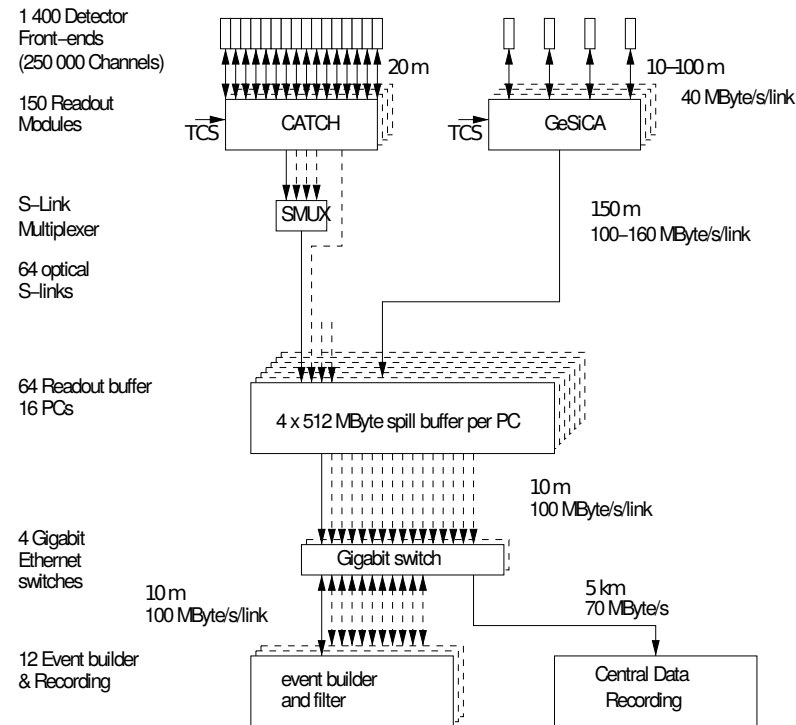


FIGURE 4.8: General architecture of the DAQ system. Digitised data from the detector front-ends are combined on the readout modules named CATCH and GeSiCA close to the detectors. The storage of the data during the spill and the event building is performed locally. The data are recorded at the CERN computer centre.

4.7 Data analysis

In order to ensure a correct performance of the DAQ and the detectors a constant monitoring during the data taking is required. For this purpose several tools are used:

- MurphyTV - allows for monitoring of readout errors that are returned by readout drivers,
- COOOL (Compass Object Oriented On Line) [82] - performs quick decoding of raw data and allows to create histograms of hit positions, time spectra etc.. This provides a monitoring of detector performance by comparison to reference histograms,

- DCS (Detector Control System) [83] - monitors all available parameters of various spectrometer elements e.g. temperatures, voltages, currents, NMR readings, gas flows. The implementation of safety “interlocks” in DCS prevents a detector damage due to abnormal operating conditions. Apart from monitoring it enables for interactive setting of detectors parameters.

The reconstruction - decoding the raw detector information into measured quantities (absolute hit positions, energy deposits in calorimeters, *etc.*), tracking of charged particles, vertexing (both interaction and decay vertices are positioned), calorimeter clustering - is performed by the CORAL package [104]. Finally also particle identification with the use of RICH information can be performed. The CORAL is used for data production where the raw data is reconstructed and stored in Data Summary Tapes (DST). It is also used for detector alignment (described in Appendix C) and calibration purposes. The author of this thesis was responsible for the alignment during the 2012 DVCS test run.

The DST data is used by PHAST program [105]. It provides a versatile tool for event filtration and analysis of events in terms of desired physics quantities. The second part of the off-line analysis focuses not on direct analysis of the recorded data but rather on the Monte Carlo (MC) simulations of the data using a selected physics model and a model of the spectrometer. The MC simulations performed in the scope of this thesis are presented in Chapter 7.

Chapter 5

Statistical concepts for extracting signal and background asymmetry at COMPASS

5.1 Number of measured events and the asymmetry

The double spin asymmetry is defined as

$$A_{LL} = \frac{\sigma^{\rightarrow\leftarrow} - \sigma^{\rightarrow\rightarrow}}{\sigma^{\rightarrow\leftarrow} + \sigma^{\rightarrow\rightarrow}}, \quad (5.1)$$

where \rightarrow denotes the beam polarisation which does not change at COMPASS and depends on the beam kinematics while \Rightarrow represents the target polarisation. The expected number of events in one cell polarised in a certain direction is given by the integral of the differential cross-section (including the unpolarised or anti-polarised nucleons in the target) $d^2\sigma$, the beam flux ϕ , the density of the scattering centres (nucleons) in the target n and the spectrometer acceptance a over all significant variables: x, Q^2 , time, etc., denoted by $\vec{\xi}$:

$$N = \int a\phi n \left(\frac{d^2\sigma}{dx dQ^2} \right) d\vec{\xi} \quad (5.2)$$

Here σ is a function of only x, Q^2 as for the inclusive measurement but the reasoning is similar in the semi-inclusive case. For example when at least two hadrons are detected together with the scattered muon the cross-section is a function of nine variables. For simplicity the differential cross-sections $\frac{d^2\sigma}{dx dQ^2}$ will be denoted by σ . Here the most general case of the deuteron target which has three possible spin projections $-1, 0, 1$ is presented. The beam flux will be denoted by $\phi^\uparrow, \phi^\downarrow$, where the arrows refer to the

parallel and anti-parallel polarisation and hence the beam polarisation $P_b = \frac{\phi^\uparrow - \phi^\downarrow}{\phi}$ with $\phi = \phi^\uparrow + \phi^\downarrow$. Similarly, the total number of deuterons can be expressed as $n_d = n^\uparrow + n^\downarrow + n^0$. Here the superscripts indicate the deuteron spin states and the target polarisation can be defined as $P_t = \frac{n^\uparrow - n^\downarrow}{n_d}$. Splitting the differential cross-section σ into all possible components:

$$\phi n \sigma = n_d \phi \sigma_d + \sum_A n_A \sigma_A = (\phi^\uparrow n^\uparrow + \phi^\downarrow n^\downarrow) \sigma^{\uparrow\uparrow} + \phi^\uparrow n^\downarrow + \phi^\downarrow n^\uparrow \sigma^{\uparrow\downarrow} + \phi n^0 \sigma^{\uparrow 0} + \phi \sum_A n_A \sigma_A, \quad (5.3)$$

where the arrows in $\sigma^{\uparrow\uparrow}$ denote the beam spin and the target spin respectively. As only relative spin orientation matters it holds $\sigma^{\uparrow\uparrow} = \sigma^{\downarrow\downarrow}, \sigma^{\uparrow\downarrow} = \sigma^{\downarrow\uparrow}, \sigma^{\uparrow 0} = \sigma^{0\uparrow}$. The term $\sum_A n_A \sigma_A$ corresponds to all nucleons in the target which are not polarisable. Using the definition of P_t and P_b and introducing the asymmetry $A = \frac{\sigma^{\uparrow\downarrow} - \sigma^{\uparrow\uparrow}}{\sigma^{\uparrow\downarrow} + \sigma^{\uparrow\uparrow}}$ and the averaged differential cross-section $\bar{\sigma} = \frac{\sigma^{\uparrow\downarrow} + \sigma^{\uparrow\uparrow}}{2}$ gives

$$\phi n \sigma = \phi n_d \bar{\sigma} - \phi n_d \bar{\sigma} P_b P_t A + \phi \sum_A n_A \sigma_A. \quad (5.4)$$

Here it was assumed that the asymmetry of the unpolarised deuteron cross-section $\sigma^{\uparrow 0}$ is equal to the spin averaged cross-section $\bar{\sigma}$. In the proton target case the situation is simpler as we have only two possible spin projections and $n^0 = 0$. Taking into account the depolarisation factor D which describes the polarisation transfer from the incoming muon to the virtual foton we can introduce the dilution factor (described in more detail in Section 5.2.1:

$$f = \frac{n_d \sigma_d}{n_d \sigma_d + \sum_A n_A \sigma_A} = \frac{n_d \bar{\sigma} (1 + D P_b P_t A)}{n \bar{\sigma} (1 + D P_b P_t A) + \sum_A n_A \sigma_A} = \frac{n_d \bar{\sigma}}{n_d \bar{\sigma} + \sum_A n_A \sigma_A}, \quad (5.5)$$

where the last equality assumes that that $D P_b P_t A$ is small. Hence the number of events is given by

$$N = \int d\vec{\xi} a \phi n \sigma_0 (1 - f D P_b P_t A). \quad (5.6)$$

Here $\sigma_0 = \frac{n_d \bar{\sigma} + \sum_A n_A \sigma_A}{n}$ is the total spin-averaged cross-section. The depolarisation factor D is a function of y and can be calculated event by event. It is worth mentioning here that the Sivers asymmetry does not depend on the beam polarisation and that the depolarisation factor is equal 1. The derivation of Equation (5.6) for the transversely polarised target is exactly the same as in the longitudinal case presented above. The number of events in a given angle ϕ is given by

$$N(\phi) = \int d\vec{\xi} a \phi n \sigma_0 (1 + f D P_t A(\phi)) \quad (5.7)$$

with

$$A(\phi) = \frac{\sigma^\uparrow - \sigma^\downarrow}{\sigma^\uparrow + \sigma^\downarrow}. \quad (5.8)$$

The sign of the Sivers asymmetry is positive for when it is positive for the upward polarisation of the COMPASS target cell.

5.2 Inputs to the raw asymmetry

The raw asymmetry is defined with the use of Equation (5.6):

$$A_{raw} = fDP_bP_tA \quad (5.9)$$

and is a quantity which is measured directly in experiments. In this section the inputs to the raw asymmetry are discussed.

5.2.1 Dilution factor

In principle the dilution factor f is a measure of the fraction of interaction in the polarisable material. In the calculation of the dilution factor not only pure target material (${}^6\text{LiD}$ or NH_3) has to be taken into account but also ${}^3\text{He}$ and ${}^4\text{He}$ used for the cooling and C, F, Ni and Cu from the NMR coils. Nucleons in different materials have different cross-sections and therefore f depends on the event kinematics. The definition of bare dilution factor is natural:

$$f(x, Q^2) = \frac{n_p \sigma_p(x, Q^2)}{n_p \sigma_p + \sum_A n_A \sigma_A(x, Q^2)}, \quad (5.10)$$

where the subscript p denotes the polarisable material and A stands for the non-polarisable materials. It is useful to rewrite the above equation in the following form

$$f = \frac{n_p}{n_p + \sum_A n_A \frac{\sigma_A}{\sigma_p}} \quad (5.11)$$

The ratio σ_A/σ_p is approximately proportional to the ratio of unpolarised structure function F_2^A/F_2^p . The dilution factor is computed using a parametrisation of the cross section ratios measured by NMC and EMC experiments and the composition of the material inside the COMPASS target [106]. The calculation of the dilution factor takes into account purity of the target material, nuclear effects and radiative correction obtained from the TERAD program [107].

5.2.2 Beam and target polarisation

The beam polarisation P_b is calculated for the measured beam momentum on the event-by-event basis using a parameterisation, as discussed in Section 4.2. In Figure 4.1 the dependence of the beam polarisation on its momentum is presented for year 2004. The relative uncertainty of the beam polarisation is 5% [108]. The target polarisation P_t is measured by the NMR coils (cf. Section 4.3) several times per run, which typically takes 30-60 minutes, and then averaged to obtain a single polarisation value for a given run. The relative precision of the target polarisation measurement is 5% [108]. Transverse polarisation is not measured directly. Longitudinal polarisation before rotation to the transverse position measured and after each data taking period the polarisation is rotated to the longitudinal direction and measured again. The Sivers effect measurement is affected by the target polarisation but not by the beam polarisation.

5.3 Asymmetry extraction with the optimisation of statistical errors

In this section two methods of asymmetry extraction will be discussed: the weighted method and the Unbinned Maximum Likelihood method. In this section $\alpha = an\phi\sigma_0$ will be the generalised acceptance and $\beta = fDP_bP_t$. The probability distribution $n(\xi)$ is introduced:

$$N = \int n(\xi)d(\xi). \quad (5.12)$$

For simplicity the probability distribution will be considered as a function of only one variable x and the generalisation is straightforward.

Three basic examples are going to be presented:

1. Very simple. A case with known acceptance with $n(x) = \alpha(x)(1 + \beta(x)A)$.
2. Single asymmetry, realistic case (unknown acceptance) - $n(x) = \alpha(x)(1 + \beta(x)A)$.
3. Realistic case with signal and background asymmetry -

$$n(x) = \alpha(x) \left(1 + \frac{s}{s+b}\beta(x)A_s + \frac{b}{s+b}\beta(x)A_b \right).$$

For each example it will be shown that the extracted asymmetry is the same and the estimated statistical errors are (almost) the same.

5.3.1 A very simple example

Here perfect acceptance is assumed and for simplicity it is put as 1. Let us assume that β is a function of x and A is a constant. Then the number of events distribution $n(x)$ is given by:

$$n(x) = \alpha(x)(1 + \beta(x)A). \quad (5.13)$$

Here $\int n(x)dx = N = N_0(1 + \langle\beta\rangle A)$ with $N_0 = \int \alpha(x)dx$. For a given variable η the following notation and approximations are used

$$\langle\eta\rangle = \frac{\int \alpha(x)\eta(x)dx}{\int \alpha(x)dx} \stackrel{\beta A \ll 1}{\approx} \frac{\int n(x)\eta(x)dx}{\int n(x)dx} \stackrel{N \rightarrow \infty}{\approx} \frac{1}{N} \sum_{i=1}^N \eta_i. \quad (5.14)$$

THE WEIGHTED METHOD

Let us integrate Equation (5.13) with a for the moment arbitrary weight $\omega(x)$:

$$p := \int n(x)\omega(x)dx = \int \alpha(x)\omega(x)dx + A \int \omega(x)\alpha(x)\beta(x)dx = N_0\langle\omega\rangle + AN_0\langle\omega\beta\rangle, \quad (5.15)$$

$$A = \frac{p - N_0\langle\omega\rangle}{N_0\langle\omega\beta\rangle} = \frac{(N - N_0)\langle\omega\rangle}{N_0\langle\omega\beta\rangle}. \quad (5.16)$$

Using $(\delta p)^2 = (\delta \sum_{i=1}^N \omega_i)^2 = \sum_{i=1}^N (\delta \omega_i)^2 = \sum_{i=1}^N \omega_i^2$ the statistical error of A reads

$$(\delta A)^2 = \left(\frac{\partial A}{\partial p} \delta p \right)^2 = \frac{\sum_{i=1}^N \omega_i^2}{(N_0\langle\omega\beta\rangle)^2} = \frac{N\langle\omega^2\rangle}{(N_0\langle\omega\beta\rangle)^2}. \quad (5.17)$$

Looking for the optimal choice of ω :

$$\frac{\partial(\delta A)}{\partial \omega_i} = \frac{\partial}{\partial \omega_i} \left(\frac{\sum_{j=1}^N \omega_j^2}{(\sum_{j=1}^N \omega_j \beta_j)^2} \frac{N}{N_0^2} \right) = 0. \quad (5.18)$$

Then for every index i it holds

$$2\omega_i(\sum \omega_j \beta_j)^2 - 2\beta_i \sum \omega_j \beta_j \sum \omega_j^2 = 0 \Rightarrow \omega_i = \beta_i. \quad (5.19)$$

Comparing the optimal error for $\omega_i = \beta_i$ and the one obtained without weighting $\omega = 1$ the statistical uncertainty decreases by a factor $\sqrt{\langle\beta\rangle^2/\langle\beta^2\rangle}$. The optimised value of asymmetry is

$$A = \frac{(N - N_0)\langle\beta\rangle}{N_0\langle\beta^2\rangle} \quad (5.20)$$

THE UNBINNED MAXIMUM LIKELIHOOD METHOD

The likelihood function \mathcal{L} in the extended unbinned maximum likelihood method is given

by [109]:

$$\mathcal{L} = e^{-\int n(x)dx} \prod_{i=1}^N n_i. \quad (5.21)$$

In our simple case $\int n(x)dx = N_0(1 + \langle\beta\rangle A)$ and $n_i = \alpha_i(1 + \beta_i A)$. Searching for the maximum of $\ln \mathcal{L}$ gives

$$\frac{\partial \ln \mathcal{L}}{\partial A} = -N_0 \langle\beta\rangle + \sum_{i=1}^N \frac{\beta_i}{1 + \beta_i A} \approx -N_0 \langle\beta\rangle + \sum_{i=1}^N \beta_i - A \sum_{i=1}^N \beta_i^2. \quad (5.22)$$

Hence

$$A = \frac{(N - N_0) \langle\beta\rangle}{N \langle\beta^2\rangle} \quad (5.23)$$

and

$$(\delta A)^2 = - \left(\frac{\partial^2 \ln \mathcal{L}}{(\partial A)^2} \right)^{-1} = \frac{1}{N \langle\beta^2\rangle}. \quad (5.24)$$

With the choice $\omega_i = \beta_i$ the two methods are equivalent under the condition that $N_0/N \approx 1$ which is true when $\langle\beta\rangle A \ll 1$. It is also easy to show that:

$$\chi^2 \equiv \frac{(p - N_0 \langle\omega\rangle - N_0 \langle\omega\beta\rangle A)^2}{(\delta p)^2} \quad (5.25)$$

gives $\chi^2/2 = -\ln \mathcal{L} + \text{const.}$ when $\omega_i = \beta_i$ and $N_0/N \approx 1$.

5.3.2 An example with unknown acceptance

Let us assume a more general case where we do not know $N_0 = \int \alpha(x)dx$. In the unbinned maximum likelihood method an assumption on the dependence of α on x has to be assumed. The simplest case is when α does not depend on x :

$$n_t(x) = \alpha_t(1 + \beta_t(x)A), \quad (5.26)$$

where $t = u, u', d, d'$ is the target configuration as in the COMPASS setup. To solve the problem without knowing α_t one further assumption has to be made:

$$\frac{\alpha_u \alpha_{d'}}{\alpha_{u'} \alpha_d} = 1, \quad (5.27)$$

what means that the ratio of acceptances in the upstream and downstream cell does not change with the polarisation reversal. In case of the weighted method the situation is a

little different. For any $\alpha(x)$ it holds

$$p_t := \sum_{i=1}^{N_t} \approx \int n_t(x) \omega_t(x) dx = \tilde{\alpha}_t (1 + \langle \beta_t \rangle_{\omega_t} A), \quad (5.28)$$

where $\tilde{\alpha}_t = \int \alpha_t(x) \omega_t(x) dx$ and $\langle \beta_t \rangle_{\omega_t} = \frac{\int \alpha_t(x) \omega_t(x) \beta_t(x) dx}{\int \alpha_t(x) \omega_t(x) dx} \stackrel{\beta_t A \ll 1}{\approx} \frac{\sum^{N_t} \omega_i \beta_i}{\sum^{N_t} \omega_i}$. The general formula for χ^2 reads

$$\chi^2 = (\vec{N}_{obs} - \vec{N}_{exp}) Cov^{-1} (\vec{N}_{obs} - \vec{N}_{exp})^T, \quad (5.29)$$

where $\vec{N}_{obs} = \{p_u, p_d, p_{u'}, p_{d'}\}$ and $\vec{N}_{exp} = \{\tilde{\alpha}_u (1 + \langle \beta_u \rangle_{\omega_u} A), \tilde{\alpha}_d (1 + \langle \beta_d \rangle_{\omega_d} A), \tilde{\alpha}_{u'} (1 + \langle \beta_{u'} \rangle_{\omega_{u'}} A), \tilde{\alpha}_{d'} (1 + \langle \beta_{d'} \rangle_{\omega_{d'}} A)\}$. The covariance matrix elements are given by $cov(p_x, p_y)$. In this example the covariance matrix is diagonal since the measurements in different cells don't interfere:

$$Cov = \begin{pmatrix} \sum_{i=1}^{N_u} \omega_i^2 & 0 & 0 & 0 \\ 0 & \sum_{i=1}^{N_d} \omega_i^2 & 0 & 0 \\ 0 & 0 & \sum_{i=1}^{N_{u'}} \omega_i^2 & 0 \\ 0 & 0 & 0 & \sum_{i=1}^{N_{d'}} \omega_i^2 \end{pmatrix} \quad (5.30)$$

The modified assumption on acceptances now reads:

$$\frac{\tilde{\alpha}_u \tilde{\alpha}_{d'}}{\tilde{\alpha}_{u'} \tilde{\alpha}_d} = 1. \quad (5.31)$$

Note, that it is reasonable to assume:

$$\frac{\alpha_u(x) \alpha_{d'}(x)}{\alpha_{u'}(x) \alpha_d(x)} = 1. \quad (5.32)$$

Then Equation (5.31) holds if $\frac{\omega_u(x) \omega_{d'}(x)}{\omega_{u'}(x) \omega_d(x)} = 1$. The smallest statistical error of solving the set of Equations (5.28) is $\omega = \beta$. If with this choice Assumption 5.31 would be satisfied then this method would be statistically optimal and valid for any kind of acceptance. Moreover it would be equivalent with the unbinned maximum likelihood method when the acceptance is a constant. Unfortunately in case of the COMPASS experiment it is, in general, not the case. Under real conditions the target polarisation P_t drops with time. Therefore to avoid a systematic error $\omega = \beta/P_t$ is chosen. Then

the weighted method is not statistically perfect (however close to optimal) but does not require any condition on the generalised acceptance. On the other hand the Unbinned Maximum Likelihood method is statistically optimal but some constraint on the generalised acceptance has to be made. Both methods have been applied to obtain the main results of this thesis and the difference is insignificant (Section 8.5).

5.3.3 Extracting signal and background asymmetry

Let us consider an example similar to the very simple case discussed in Section 5.3.1 but now

$$A = R^S A^S + R^B A^B, \quad (5.33)$$

where R_A and R_B are the fractions of signal and background respectively. On an event-by-event basis the fractions have the meaning of the probability that the event is a signal or a background. More generally R_A, R_B can be functions of x . For example R can be a function of invariant mass like in the Open Charm analysis described in Section 6.1. Probabilities can be also assigned by the NN trained on MC data with process identification. Like in the "very simple example" it is assumed that $N_0 = \int \alpha(x) dx$ is known.

WEIGHTED METHOD

The formula for the distribution of events $n(x) = \alpha(x)(1 + \beta^S(x)A_S + \beta^B(x)A_B)$ is weighted twice: with the weight of the signal $\omega^S(x)$ and the weight of the background $\omega^B(x)$:

$$\begin{aligned} p^S &:= \sum_{i=1}^N \omega_i^S &= N_0 \langle \omega^S \rangle + N_0 \langle \omega^S \beta^S \rangle A^S + N_0 \langle \omega^S \beta^B \rangle A^B \\ p^B &:= \sum_{i=1}^N \omega_i^B &= N_0 \langle \omega^B \rangle + N_0 \langle \omega^B \beta^S \rangle A^S + N_0 \langle \omega^B \beta^B \rangle A^B. \end{aligned} \quad (5.34)$$

Once again the set of equations may be solved by minimising $\chi^2 = (\vec{N}_{obs} - \vec{N}_{exp})^T Cov^{-1} (\vec{N}_{obs} - \vec{N}_{exp})$. In this case the covariance matrix can be approximated by $Cov_{S,B} \approx cov(p^S, p^B) = \sum \omega_S \omega_B$:

$$Cov = \begin{pmatrix} \sum_i (\omega_i^S)^2 & \sum_i \omega_i^S \omega_i^B \\ \sum_i \omega_i^S \omega_i^B & \sum_i (\omega_i^B)^2 \end{pmatrix}. \quad (5.35)$$

When $\omega_i^S = \beta_i^S$ and $\omega_i^B = \beta_i^B$ then the inverse of the error matrix reads

$$\frac{1}{2} \frac{\partial^2 \chi^2}{\partial A^m \partial A^n} = \begin{pmatrix} \frac{N_0^2}{N^2} \sum_i (\beta_i^S)^2 & \frac{N_0^2}{N^2} \sum_i \beta_i^S \beta_i^B \\ \frac{N_0^2}{N^2} \sum_i \omega_i^S \beta_i^B & \frac{N_0^2}{N^2} \sum_i (\beta_i^B)^2 \end{pmatrix}. \quad (5.36)$$

With $m, n = S, B$ and $(\langle \beta^S \rangle A^S + \langle \beta^B \rangle A^B) \ll 1 \Rightarrow N_0 \approx N$ the error matrix is equal to the inverse of the covariance matrix of the measurement given by Equation (5.35) what means the choice of weighting is optimal. The signal and background asymmetries are given by

$$A^S = \frac{(N - N_0)[\langle (\beta^B)^2 \rangle \langle \beta^S \rangle - \langle \beta^S \beta^B \rangle \langle \beta^B \rangle]}{N_0[\langle (\beta^S)^2 \rangle \langle (\beta^B)^2 \rangle - \langle \beta^S \beta^B \rangle^2]} \quad (5.37)$$

$$A^B = \frac{(N - N_0)[\langle (\beta^S)^2 \rangle \langle \beta^B \rangle - \langle \beta^S \beta^B \rangle \langle \beta^S \rangle]}{N_0[\langle (\beta^S)^2 \rangle \langle (\beta^B)^2 \rangle - \langle \beta^S \beta^B \rangle^2]}.$$

Note that the denominators are zero when $\beta_i^S = \beta_i^B$ because after weighting the two Equations (5.34) will be identical. The same happens when the weights do not change from event to event. This means it is better to choose a sample where the fractions R of the signal and of the background cover wide range of values. These features of the method motivate the sample selection given in Section 8.1. The extreme situation is when the sample can be divided into subsamples of signal and background then $\langle \beta^S \beta^B \rangle = 0$ and we obtain two equations similar to Equation (5.20).

UNBINNED MAXIMUM LIKELIHOOD

The probabilities for each event are given by $n_i = \alpha_i(1 + \beta_i^S A^S + \beta_i^B A^B)$. The likelihood function reads

$$\mathcal{L} = e^{-N_0(1 + \langle \beta^S \rangle A^S + \langle \beta^B \rangle A^B)} \prod_{i=1}^N n_i \quad (5.38)$$

The minimum necessary condition $\frac{\partial \ln \mathcal{L}}{\partial A^S} = \frac{\partial \ln \mathcal{L}}{\partial A^B}$ gives

$$A^S = \frac{(N - N_0)[\langle (\beta^B)^2 \rangle \langle \beta^S \rangle - \langle \beta^S \beta^B \rangle \langle \beta^B \rangle]}{N[\langle (\beta^S)^2 \rangle \langle (\beta^B)^2 \rangle - \langle \beta^S \beta^B \rangle^2]} \quad (5.39)$$

$$A^B = \frac{(N - N_0)[\langle (\beta^S)^2 \rangle \langle \beta^B \rangle - \langle \beta^S \beta^B \rangle \langle \beta^S \rangle]}{N[\langle (\beta^S)^2 \rangle \langle (\beta^B)^2 \rangle - \langle \beta^S \beta^B \rangle^2]}.$$

These values differ from the ones obtained with the weighted method (Equations (5.37)) by a factor N_0/N which as before can be approximated by 1 for small raw asymmetries. The covariance matrix obtained from the likelihood function $-\frac{\partial^2 \ln \mathcal{L}}{\partial A^m \partial A^n}$ is equal to the

covariance matrix of p^S, p^B from the weighted method. This shows that the weighting method and the unbinned likelihood method are identical for small asymmetries.

Chapter 6

Methods of extracting gluon asymmetries in the COMPASS experiment

6.1 Open Charm production

The production of hadrons containing c quarks is a signature of the Photon Gluon Fusion process (see Figure 6.1) In the PGF process the interacting quark and gluon

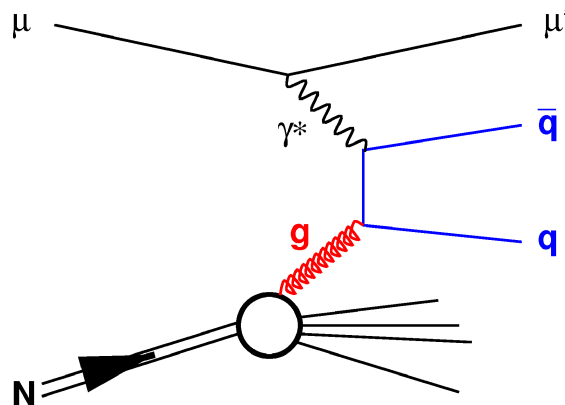


FIGURE 6.1: Photon Gluon Fusion (PGF)

produce a quark-antiquark pair. This hard process is the main source of heavy c quarks ($m_c = 1.5\text{GeV}$) as the production via fragmentation of light quarks or interaction of virtual photon with intrinsic charm quark is rare as is the appearance of charm quarks in the sea.

The longitudinal double spin cross-section asymmetry for $D^0(\bar{D}^0)$ meson production

events is defined as

$$A^{\mu N \rightarrow \mu' D^0 X} \equiv \frac{d\Delta\sigma}{2d\bar{\sigma}} = \frac{\sigma^{\leftarrow\leftarrow} - \sigma^{\rightarrow\rightarrow}}{\sigma^{\leftarrow\leftarrow} + \sigma^{\rightarrow\rightarrow}}, \quad (6.1)$$

where the arrows indicate relative beam (\rightarrow) and target (\Rightarrow) spin orientations. The decomposition of the differential cross-section for D^0 meson production, $d\sigma$ and $d\Delta\sigma$, show $\frac{\Delta g}{g}$ dependence:

$$d\sigma = g \otimes d\hat{\sigma} \otimes H, \quad (6.2)$$

$$d\Delta\sigma = \Delta g \otimes \Delta d\hat{\sigma} \otimes H. \quad (6.3)$$

Here \otimes denotes the convolution integrals as in Equation (2.34).

In LO $d\sigma$ and $d\Delta\sigma$ are spin averaged and spin dependent partonic cross-sections for $\mu g \rightarrow \mu' c\bar{c}$ reaction. g and Δg denote the spin averaged and spin dependent gluon PDFs respectively. The quark pair ($c\bar{c}$) fragments into charmed hadrons (mainly D mesons). H is the fragmentation function which is assumed to be spin-independent. The assumption of single-hadron independent fragmentation is not needed. The fragmentation described by H is a one charmed quark fragmentation into a D meson and any number of unobserved hadrons. In particular, H is described by the Lund string hadronisation model [110] used in many Monte-Carlo generators.

The spin-dependent cross-section, $d\Delta\sigma$ can be expressed in the following way

$$d\Delta\sigma = \frac{\Delta g}{g} g \otimes a_{LL} d\hat{\sigma} \otimes H \quad (6.4)$$

and a_{LL} is the analysing power which is defined as partonic level asymmetry of the polarisation dependent and polarisation averaged cross-sections:

$$a_{LL} = \frac{d\Delta\hat{\sigma}}{d\hat{\sigma}}. \quad (6.5)$$

Using Equation (6.2) and 6.4 the asymmetry given in Equation (6.1) can be rewritten in the following way

$$A^{\mu N \rightarrow \mu' D^0 X} = \left\langle \frac{\Delta g}{g} a_{LL} \right\rangle = \left\langle \frac{\Delta g}{g} \right\rangle_{a_{LL}} \langle a_{LL} \rangle, \quad (6.6)$$

where

$$\langle a_{LL} \rangle = \frac{a_{LL} g \otimes d\hat{\sigma} \otimes H}{g \otimes d\hat{\sigma} \otimes H}, \quad \left\langle \frac{\Delta g}{g} \right\rangle_{a_{LL}} = \frac{\frac{\Delta g}{g} a_{LL} g \otimes d\hat{\sigma} \otimes H}{a_{LL} g \otimes d\hat{\sigma} \otimes H}. \quad (6.7)$$

The analysing power a_{LL} depends on partonic kinematics and cannot be accessed experimentally event by event. It has been obtained with the use of MC generator and then assigned to each real event by a neural network (NN). The network is trained with the MC data using the measurable kinematic variables.

The asymmetry $A^{\mu N \rightarrow \mu' D^0 X}$ is obtained by subtracting a large combinatorial background. The method of the background subtraction are described in detail in Section 5.3. The number of events collected in a given target cell and time interval is given by [58]

$$\frac{dN}{dm dX} = a\phi n(s+b) \left[1 + P_t P_\mu f \left(\frac{s}{s+b} A^{\mu N \rightarrow \mu' D^0 X} + \frac{b}{s+b} A_B \right) \right], \quad (6.8)$$

where $m \equiv M_{K\pi}$ is the invariant mass of the reconstructed kaon-pion pair, X denotes the list of kinematic variables $\{Q^2, y, z, \dots\}$, a, ϕ, n are the spectrometer acceptance, the incident muon beam flux integrated over the time interval and the number of target nucleons respectively. Target polarisation P_t , muon beam polarisation P_μ and the dilution factor f are described in Section 5.1. The signal purity is given by the ratio $s/(s+b)$. The background asymmetry A_B is assumed to be independent of m .

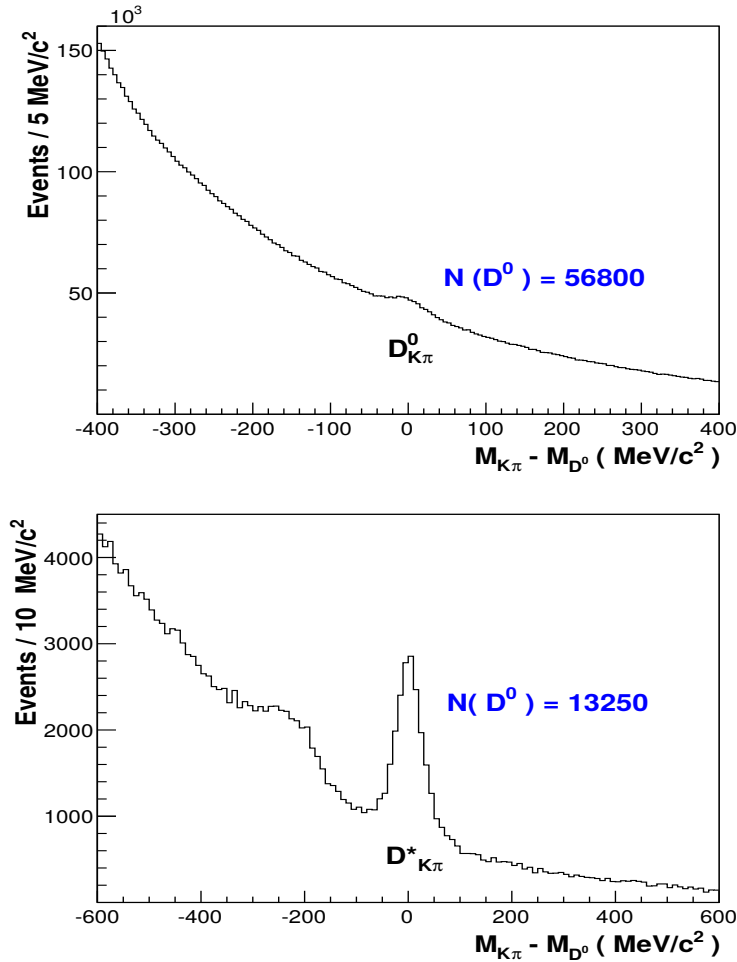


FIGURE 6.2: Invariant mass spectra for the $D^0_{K\pi}$ and $D^*_{K\pi}$ samples with approximate number of D^0 mesons above background. Figure from [58]

To extract $\Delta g/g$ from the background it is possible to integrate over X and obtain an m dependence of the number of events for different cell polarisations. Then the background asymmetry needs to be subtracted, and from Equation (6.8) with the use of Equation

(6.6) gluon polarisation can be obtained. The invariant mass spectrum of kaon-pion pairs is presented in Figure 6.2. In fact it is a weighted average gluon polarisation $\langle \Delta g/g \rangle_\beta$ where the proportionality coefficient $\beta = P_t P_\mu f a_{LL}$ is the weight. It can be proved, however (see Section 5.3.2, that, taking into account a systematic bias, it is preferable to weigh each event by β/P_t , [111]. In this way a reduction of statistical error by the value $\sqrt{\langle \beta^2 \rangle / \langle \beta \rangle^2}$ is obtained. Moreover it is better not to subtract the background but to use two weights, one for signal and one for background:

$$\omega_S = P_\mu f a_{LL} \frac{s}{s+b}, \quad (6.9a)$$

$$\omega_B = P_\mu f D \frac{b}{s+b}. \quad (6.9b)$$

Here D is the depolarisation factor accounting for the polarisation transfer from the lepton to the virtual photon and $A_B = D A_B^{\gamma^* N}$. (Note, that this definition of weights provides optimisation of the statistical and systematic error. The results published in [58] and presented in Section 3.2.1 has been obtained with different weight $\omega_S = P_\mu f D s / (s+b)$). Then Equation (6.8) can be rewritten in the form:

$$\frac{dN}{dm dX} = a \phi n(s+b) \left(1 + \beta_S \frac{\Delta g}{g} + \beta_B A_B^{\gamma^* N} \right). \quad (6.10)$$

Then this equation can be weighted with ω_S and ω_B what results in a set of equations:

$$\begin{aligned} \left\langle \sum_{i=1}^{N_t} \omega_{S,i} \right\rangle &= \int \omega_S(X, m) \frac{d^k N_t}{dm dX} dX dm \\ &= \tilde{\alpha}_{S,t} \left[1 + \langle \beta_S \rangle_{\omega_S} \left\langle \frac{\Delta g}{g} \right\rangle_{\beta_S \omega_S} + \langle \beta_B \rangle_{\omega_S} \left\langle A_B^{\gamma^* N} \right\rangle_{\beta_B \omega_S} \right], \end{aligned} \quad (6.11)$$

$$\begin{aligned} \left\langle \sum_{i=1}^{N_t} \omega_{B,i} \right\rangle &= \int \omega_B(X, m) \frac{d^k N_t}{dm dX} dX dm \\ &= \tilde{\alpha}_{B,t} \left[1 + \langle \beta_S \rangle_{\omega_B} \left\langle \frac{\Delta g}{g} \right\rangle_{\beta_S \omega_B} + \langle \beta_B \rangle_{\omega_B} \left\langle A_B^{\gamma^* N} \right\rangle_{\beta_B \omega_B} \right], \end{aligned} \quad (6.12)$$

where

$$\alpha_t = a_t \phi_t n_t (s+b) \quad (6.13)$$

$$\tilde{\alpha}_{S/B,t} = \int \omega_{S/B} \alpha_t dm dX \quad (6.14)$$

$$\langle \eta \rangle_{\omega_{S/B}} = \frac{\int \eta \omega_{S/B} \alpha_t dm dX}{\int \omega_{S/B} \alpha_t dm dX}. \quad (6.15)$$

Here t stands for the target cell before ($t = u, d$) and after ($t = u', d'$) the target polarisation rotation. The number of events observed for the given target configuration t is

denoted by N_t . Altogether there are eight equations for twelve unknowns, $\langle \Delta g/g \rangle_{\beta_S \omega_S}$, $\langle \Delta g/g \rangle_{\beta_S \omega_B}$, $\langle A_B^{\gamma^* N} \rangle_{\beta_B \omega_S}$, $\langle A_B^{\gamma^* N} \rangle_{\beta_B \omega_B}$ and eight acceptance factors $\alpha_{S/B,t}$. The factors $\langle \beta_{S/B} \rangle_{\omega_{S/B}}$ have been obtained from data using the approximate formula:

$$\langle \beta_{S/B} \rangle_{\omega_{S/B}} \approx \frac{\sum_{i=1}^{N_t} \beta_{S/B} \omega_{S/B}}{\sum_{i=1}^{N_t} \omega_{S/B}}. \quad (6.16)$$

The number of unknowns can be reduced. Firstly by assuming that

$$\left\langle \frac{\Delta g}{g} \right\rangle_{\beta_S \omega_S} = \left\langle \frac{\Delta g}{g} \right\rangle_{\beta_S \omega_B} \equiv \left\langle \frac{\Delta g}{g} \right\rangle, \quad (6.17)$$

$$\left\langle A_B^{\gamma^* N} \right\rangle_{\beta_S \omega_S} = \left\langle A_B^{\gamma^* N} \right\rangle_{\beta_S \omega_B} \equiv \left\langle A_B^{\gamma^* N} \right\rangle. \quad (6.18)$$

Secondly assuming that the acceptance ratio before and after field reversal is the same:

$$\frac{\tilde{\alpha}_{S/B}^u}{\tilde{\alpha}_{S/B}^d} = \frac{\tilde{\alpha}'_{S/B}}{\tilde{\alpha}''_{S/B}}. \quad (6.19)$$

This reduces the number of unknowns to eight. The number of seven unknowns is obtained by assuming that signal and background events are affected by the acceptance variations in the same way. The set of equations is now overdetermined and can be solved with the standard least square minimisation procedure as shown in Section 5.3. Using this method $\Delta g/g$ at LO accuracy is obtained.

This method optimises the statistical error and is (assuming $\beta A \ll 1$) equivalent to the maximum likelihood method [112].

To extract the $\Delta g/g$ value an evaluation of a_{LL} is needed. This can be done at LO:

$$A^{\mu N} = DA^{\gamma N} = a_{LL} \frac{\Delta g}{g}, \quad (6.20)$$

where a_{LL} is the analysing power (also called "partonic asymmetry") of the process $\mu g \rightarrow \mu' c \bar{c}$. The values of a_{LL} have been calculated for MC events and then have been assigned by a NN to every real event. The obtained LO result is

$$\left\langle \frac{\Delta g}{g} \right\rangle^{LO} = -0.08 \pm 0.21(stat.) \pm 0.09(syst.). \quad (6.21)$$

However a_{LL} can be calculated at NLO and this have been done. The examples of NLO diagrams for the muoproduction of $c \bar{c}$ are presented in Figure 6.3. The final result with the use of NLO calculation reads

$$\left\langle \frac{\Delta g}{g} \right\rangle^{NLO} = -0.20 \pm 0.21(stat.) \quad (6.22)$$

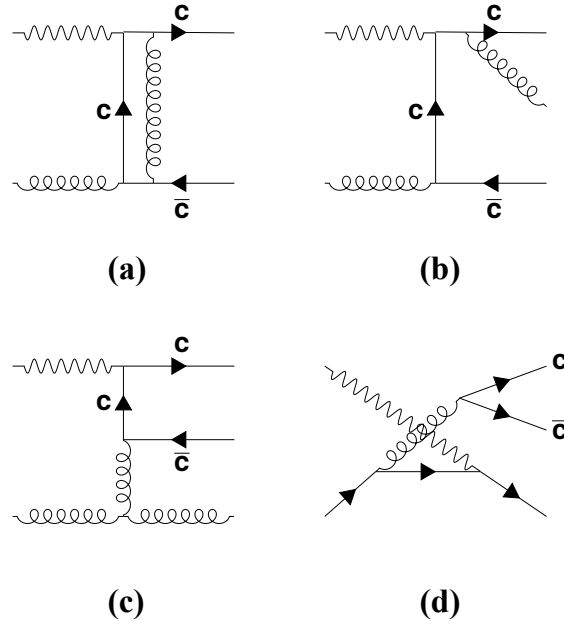


FIGURE 6.3: Examples of NLO processes contributing to the muoproduction of $c\bar{c}$ pair: a) virtual correction, b), c) gluon bremsstrahlung, d) light quark background. Figure from [58].

at $\langle x_g \rangle \approx 0.28$ and at scale $\mu^2 \approx 13 \text{ GeV}^2$. The result is plotted in Figure 6.4 together with the global fits, DSSV and LSS that include DIS and SIDIS asymmetries. The COMPASS NLO fits include the $\langle \Delta g/g \rangle^{NLO}$ result. The mean asymmetry as in Equation

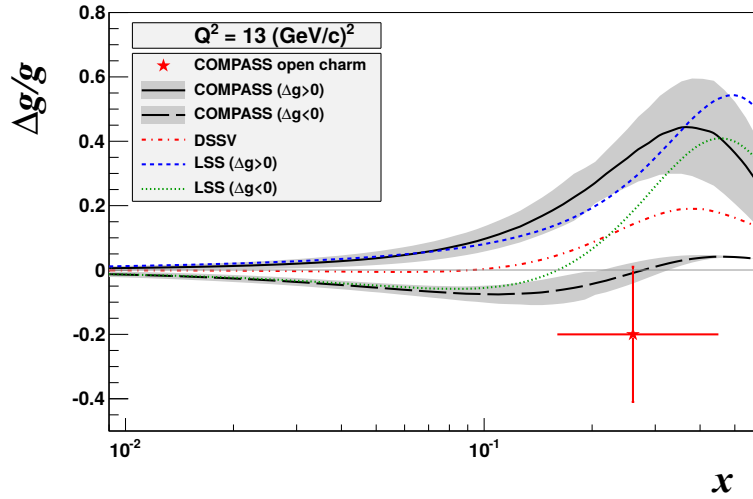


FIGURE 6.4: The present NLO measurement of the gluon polarisation $\Delta g/g$ at $\mu^2 = 13 \text{ GeV}^2$, compared to the NLO QCD fits of COMPASS with $\Delta g > 0$ (continuous line) and $\Delta g < 0$ (long-dashed), of LSS (dashed and dotted curves respectively) and of DSSV (dashed-dotted curve), all at the same value of $Q^2 = 13 \text{ GeV}^2$. The measurement error and the error bands are statistical, horizontal bar marks an interval of x_g in which $\Delta g/g$ is determined. Figure from [16].

(6.15) is given by

$$\left\langle \frac{\Delta g}{g}(X, m) \right\rangle_{\beta\omega} = \frac{\int dmdX \Delta g/g(X, m) \omega(X, m) \beta(X, m) \alpha(X, m)}{\int dmdX \omega(X, m) \beta(X, m) \alpha(X, m)}. \quad (6.23)$$

Once again $m \equiv M_{K\pi}$ and $X = x_g, Q^2, z_1, z_2$. Introducing $X' = Q^2, z_1, z_2$ and assuming linearity of $\Delta g/g$ in x_g what means $\Delta g/g(X, m) = a(x_g - \langle x_g \rangle) + \Delta g/g(\langle x_g \rangle, X', m)$, where a is a number, the above equation reads

$$\left\langle \frac{\Delta g}{g}(X, m) \right\rangle_{\beta\omega} = \left\langle \frac{\Delta g}{g}(\langle x_g \rangle, X', m) \right\rangle_{\beta\omega} \equiv \frac{\Delta g}{g}(\langle x_g \rangle) \quad (6.24)$$

when

$$\langle x_g \rangle_{\omega\beta} \equiv \frac{\int dmdX \alpha(X, m) x_{Bj} \omega(X, m) \beta(X, m)}{\int dmdX \alpha(X, m) \omega(X, m) \beta(X, m)} \approx \frac{\sum_i x_{Bj}^i \beta^i \omega_i}{\sum_i \beta_i \omega_i}. \quad (6.25)$$

The last approximation assumes that the raw asymmetries are small $\beta A_{Sivers} \ll 1$. Note that the definition of $\langle x_g \rangle_{\omega\beta}$ is such that β_i and ω_i carry information about the distribution of all kinematic variables X, m .

6.2 High- p_T hadron pair production

In the pQCD region defined by $Q^2 > 1 \text{ GeV}^2$ the spin-averaged and spin-dependent differential cross-sections contain three terms related to the three contributing processes (PGF, LP, QCDC):

$$d\sigma = g \otimes d\hat{\sigma}^{PGF} \otimes H + \left(\sum_q e_q^2 q \right) \otimes d\hat{\sigma}^{LP} \otimes H + \left(\sum_q e_q^2 q \right) \otimes d\hat{\sigma}^{QCDC} \otimes H, \quad (6.26)$$

$$d\Delta\sigma = \Delta g \otimes d\Delta\hat{\sigma}^{PGF} \otimes H + \left(\sum_q e_q^2 \Delta q \right) \otimes d\Delta\hat{\sigma}^{LP} \otimes H + \left(\sum_q e_q^2 \Delta q \right) \otimes d\Delta\hat{\sigma}^{QCDC} \otimes H. \quad (6.27)$$

Here \otimes denotes the convolution integrals as in Equation (2.34). In LO $d\sigma$ and $d\Delta\sigma$ are spin averaged and spin dependent partonic cross-sections. g and Δg denote the spin averaged and spin dependent gluon PDFs respectively. Similarly q and Δq stand for the quark PDFs.

Using the Equations (6.4), (6.5), (6.7) the measured asymmetry as a function of x_{Bj} (all other variables are integrated over the experimental kinematic domain) can be expressed

as follows

$$A_{LL}^{2h}(\langle x \rangle) = \left\langle \frac{\Delta g}{g}(x_g) \right\rangle_{a_{LL}^{PGF} R^{PGF}} \langle a_{LL}^{PGF} R^{PGF} \rangle + \langle A_1^{LO}(x_{Bj}) \rangle_{DR^{LP}} \langle DR^{LP} \rangle \\ + \langle A_1^{LO}(x_C) \rangle_{a_{LL}^{QCDC} R^{QCDC}} \langle a_{LL}^{QCDC} R^{QCDC} \rangle, \quad (6.28)$$

where

$$A_1^{LO} \equiv \frac{\sum_q e_q^2 \Delta q}{\sum_q e_q^2 q}. \quad (6.29)$$

The partonic cross-sections a_{LL}^{PGF} and a_{LL}^{QCDC} have been calculated in [113]. The fraction of the process i is defined as

$$R^i \equiv \frac{d\sigma^i}{d\sigma} = \frac{d\sigma^i}{\sum_i d\sigma^i} \quad (6.30)$$

The weighted averages $\langle \rangle$ read

$$\langle a_{LL}^{PGF} R^{PGF} \rangle \equiv \frac{a_{LL}^{PGF} g \otimes d\hat{\sigma}^{PGF} \otimes H}{d\sigma}, \quad \left\langle \frac{\Delta g}{g} \right\rangle_{a_{LL}^{PGF} R^{PGF}} \equiv \frac{\Delta g / g a_{LL}^{PGF} g \otimes d\hat{\sigma}^{PGF} \otimes H}{a_{LL}^{PGF} g \otimes d\hat{\sigma}^{PGF} \otimes H} \quad (6.31)$$

for PGF. Similar definitions hold for LP and QCDC. Assuming linearity on x of A_1 and $\frac{\Delta g}{g}$ Equation (6.24) holds and Equation (6.28) can be rewritten in the form

$$A_{LL}^{2h}(\langle x \rangle) = \frac{\Delta g}{g} (\langle x_g \rangle_{a_{LL}^{PGF} R^{PGF}}) \langle a_{LL}^{PGF} R^{PGF} \rangle + A_1^{LO}(\langle x \rangle) \langle DR^{LP} \rangle \\ + A_1^{LO}(\langle x_C \rangle_{a_{LL}^{QCDC} R^{QCDC}}) \langle a_{LL}^{QCDC} R^{QCDC} \rangle. \quad (6.32)$$

Similar formula is obtained for the asymmetry of the inclusive sample:

$$A_{LL}^{incl}(\langle x \rangle) = \frac{\Delta g}{g} (\langle x_g \rangle_{a_{LL}^{incl,PGF} R_{incl}^{PGF}}) \langle a_{LL}^{incl,PGF} R_{incl}^{PGF} \rangle + A_1^{LO}(\langle x \rangle) \langle DR_{incl}^{LP} \rangle \\ + A_1^{LO}(\langle x_C \rangle_{a_{LL}^{incl,QCDC} R_{incl}^{QCDC}}) \langle a_{LL}^{incl,QCDC} R_{incl}^{QCDC} \rangle. \quad (6.33)$$

The weighted averages of x_C and x_g were found to be similar in both samples. Hence, the following holds:

$$\langle x_g \rangle_{a_{LL}^{PGF} R^{PGF}} \approx \langle x_g \rangle_{a_{LL}^{incl,PGF} R_{incl}^{PGF}} \equiv \langle x_g \rangle \\ \langle x_C \rangle_{a_{LL}^{QCDC} R^{QCDC}} \approx \langle x_C \rangle_{a_{LL}^{incl,QCDC} R_{incl}^{QCDC}} \equiv \langle x_C \rangle \quad (6.34)$$

To combine Equations (6.32) and (6.33) it is necessary to find the expression for $A_{LL}^{incl}(\langle x_C \rangle)$:

$$A_{LL}^{incl}(\langle x_C \rangle) = \frac{\Delta g}{g} (\langle x'_g \rangle) \langle a_{LL}^{incl,PGF} R_{incl}^{PGF} \rangle + A_1^{LO}(\langle x_C \rangle) \langle DR_{incl}^{LP} \rangle \\ + A_1^{LO}(\langle x'_C \rangle) \langle a_{LL}^{incl,QCDC} R_{incl}^{QCDC} \rangle. \quad (6.35)$$

Here $\langle x'_g \rangle$ and $\langle x'_C \rangle$ are the average fractions of momentum of the nucleon carried by the struck parton at $\langle x \rangle = \langle x_C \rangle$. Neglecting terms proportional to $\frac{R_{incl}^{PGF} R_{incl}^{QCDC}}{(R_{incl}^{LP})^2}$ or $\frac{(R_{incl}^{QCDC})^2}{(R_{incl}^{LP})^2}$ one gets

$$A_1^{LO}(\langle x \rangle) = \frac{1}{\langle DR_{incl}^{LP} \rangle} \left(A_{LL}^{incl}(\langle x \rangle) - \frac{\Delta g}{g}(\langle x_g \rangle) \left\langle a_{LL}^{incl,PGF} R^{PGF} \right\rangle - A_{LL}^{incl}(\langle x_C \rangle) \frac{\left\langle a_{LL}^{incl,QCDC} R_{incl}^{QCDC} \right\rangle}{\langle DR_{incl}^{LP} \rangle} \right), \quad (6.36)$$

similarly

$$A_1^{LO}(\langle x_C \rangle) = \frac{1}{\langle DR_{incl}^{LP} \rangle} \left(A_{LL}^{incl}(\langle x_C \rangle) - \frac{\Delta g}{g}(\langle x'_g \rangle) \left\langle a_{LL}^{incl,PGF} R^{PGF} \right\rangle - A_{LL}^{incl}(\langle x'_C \rangle) \frac{\left\langle a_{LL}^{incl,QCDC} R_{incl}^{QCDC} \right\rangle}{\langle DR_{incl}^{LP} \rangle} \right). \quad (6.37)$$

Substituting Equations (6.36) and (6.37) into Equation 6.32:

$$\begin{aligned} A_{LL}^{2h}(\langle x \rangle) &= \frac{\Delta g}{g}(\langle x_g \rangle) \left\langle a_{LL}^{PGF} R^{PGF} \right\rangle \\ &- \frac{\langle DR_{incl}^{LP} \rangle}{\langle DR_{incl}^{LP} \rangle} \frac{\Delta g}{g}(\langle x_g \rangle) \left\langle a_{LL}^{incl,PGF} R_{incl}^{PGF} \right\rangle \\ &- \frac{\left\langle a_{LL}^{QCDC} R_{incl}^{QCDC} \right\rangle}{\langle DR_{incl}^{LP} \rangle} \frac{\Delta g}{g}(\langle x'_g \rangle) \left\langle a_{LL}^{incl,PGF} R_{incl}^{PGF} \right\rangle \\ &+ \frac{\langle DR_{incl}^{LP} \rangle}{\langle DR_{incl}^{LP} \rangle} \left[A_{LL}^{incl}(\langle x \rangle) - A_{LL}^{incl}(\langle x_C \rangle) \frac{\left\langle a_{LL}^{incl,QCDC} R_{incl}^{QCDC} \right\rangle}{\langle DR_{incl}^{LP} \rangle} \right] \\ &+ \frac{\left\langle a_{LL}^{QCDC} R_{incl}^{QCDC} \right\rangle}{\langle DR_{incl}^{LP} \rangle} \left[A_{LL}^{incl}(\langle x_C \rangle) - A_{LL}^{incl}(\langle x'_C \rangle) \frac{\left\langle a_{LL}^{incl,QCDC} R_{incl}^{QCDC} \right\rangle}{\langle DR_{incl}^{LP} \rangle} \right]. \end{aligned} \quad (6.38)$$

Instead of working with averages the terms standing next to the asymmetries $\Delta g/g$, A_{LL}^{incl} can be evaluated event-by-event with the use of a NN trained on several MC samples.

The formula for the function $A_{LL}^{2h}(x)$ reads [16]:

$$\begin{aligned}
A_{LL}^{2h}(x) &= \frac{\Delta g}{g}(x_g) \left[a_{LL}^{PGF} R^{PGF} - \frac{R^{LP}}{R_{incl}^{LP}} a_{LL}^{incl,PGF} R_{incl}^{PGF} \right] \\
&\quad - \frac{a_{LL}^{QCDC} R^{QCDC}}{DR_{incl}^{LP}} \frac{\Delta g}{g}(x'_g) a_{LL}^{incl,PGF} R_{incl}^{PGF} \\
&\quad + \frac{R^{LP}}{R_{incl}^{LP}} \left[A_1(x) - A_1(x_C) \frac{a_{LL}^{incl,QCDC} R_{incl}^{QCDC}}{DR_{incl}^{LP}} \right] \\
&\quad + \frac{a_{LL}^{QCDC} R^{QCDC}}{R_{incl}^{LP}} \left[A_1(x_C) - A_1(x'_C) \frac{a_{LL}^{incl,QCDC} R_{incl}^{QCDC}}{DR_{incl}^{LP}} \right],
\end{aligned} \tag{6.39}$$

with $A_1 = A_{LL}^{incl}/D$.

Then a new definition of average x_g is applied

$$x_g^{av} = \frac{\alpha_1 x_g - \alpha_2 x'_g}{\alpha_1 - \alpha_2}, \tag{6.40}$$

where

$$\alpha_1 = a_{LL}^{PGF} R^{PGF} - a_{LL}^{incl,PGF} R^{LP} \frac{R_{incl}^{PGF}}{R_{incl}^{LP}} \tag{6.41}$$

$$\alpha_2 = a_{LL}^{incl,PGF} R^{QCDC} \frac{R_{incl}^{PGF}}{R_{incl}^{LP}} \frac{a_{LL}^{QCDC}}{D}. \tag{6.42}$$

This definition relies on the assumption that $\frac{\Delta g}{g}$ is linear in x_g which can be assured by proper binning. The formula which relates the gluon polarisation to the measured A_{LL}^{2h} asymmetry is the following

$$\frac{\Delta g}{g}(x_g^{av}) = \frac{A_{LL}^{2h}(x) - A^{corr}}{\alpha_1 - \alpha_2}, \tag{6.43}$$

with

$$\begin{aligned}
A^{corr} &= A_1(x) \frac{R^{LP}}{R_{incl}^{LP}} + A_1(x_C) \frac{1}{R_{incl}^{LP}} \left(a_{LL}^{QCDC} R^{QCDC} - a_{LL}^{incl,QCDC} R_{incl}^{QCDC} \frac{R^{LP}}{R_{incl}^{LP}} \right) \\
&\quad - A(x'_C) a_{LL}^{incl,QCDC} \frac{R_{incl}^{QCDC}}{R_{incl}^{LP}} \frac{R^{QCDC}}{R_{incl}^{LP}} \frac{a_{LL}^{QCDC}}{D}.
\end{aligned} \tag{6.44}$$

Similarly to the Open Charm method described in the previous section the sum of weights for each target configuration $t(= u, d, u', d')$ is calculated: $p_t = \sum_{i=0}^{N_t} \omega_i$, where the weight $\omega = fP_b(\alpha_1 - \alpha_2)$ is used. Then the gluon polarisation is estimated from the

following equation

$$\frac{p_u p_{d'}}{p_{u'} p_d} = \frac{(1 + \langle C_u \rangle_\omega + \langle \beta_u \rangle_\omega \Delta g / g(x_g^{av})) (1 + \langle C_{d'} \rangle_\omega + \langle \beta_{d'} \rangle_\omega \Delta g / g(x_g^{av}))}{(1 + \langle C_{u'} \rangle_\omega + \langle \beta_{u'} \rangle_\omega \Delta g / g(x_g^{av})) (1 + \langle C_d \rangle_\omega + \langle \beta_d \rangle_\omega \Delta g / g(x_g^{av}))}. \quad (6.45)$$

Here $C_t = f P_b P_t A^{corr}$ and $\beta_t = f P_b P_t (\alpha_1 - \alpha_2)$. The use of double ratio method provides cancellation of the acceptances, unpolarised cross-sections and the beam flux. The final value obtained in this analysis is

$$\frac{\Delta g}{g} = 0.125 \pm 0.060(\text{stat.}) \pm 0.063(\text{syst.}) \quad (6.46)$$

at $x_g = 0.09$ and a scale of $\mu^2 = 3 \text{ GeV}^2$.

The method used for this analysis provides two new features. Both data samples contain signal and background asymmetry but the proportions of signal and background are different in the two samples. This means that the two Equations (6.32) and (6.33) differ and form a solvable set of equations. The second feature is the weighting of the samples on event-by-event basis for which the NN trained on MC data is used. Both these features have been applied in the analysis called "all- p_T " and in the analysis which is the subject of this thesis.

6.3 All- p_T method of $\Delta g/g$ extraction

This method is based on the same principle of background asymmetry subtraction as described in Section 5.3 and used in the Open Charm method (Section 6.1).

In this analysis only one hadron in the final state is demanded and there is no lower cut on p_T of this hadron. The kinematics of the hadron together with the inclusive variables is used by the NN to assign (event-by-event) three weighting factors R^i in the same way as in the high- p_T method (Section 6.2). The formula for a single event based on Equation (6.33) reads

$$A_{LL}^h(x) = \frac{\Delta g}{g} (x_g) a_{LL}^{PGF} R^{PGF} + A_1^{LO}(x) D R^{LP} + A_1^{LO}(x_C) a_{LL}^{QCDC} R^{QCDC}. \quad (6.47)$$

The number of events for a given target cell $t = (u, d, u', d')$ can be expressed as

$$N_t(x) = \alpha_t(x) \left(1 + f P_b P_t A_{LL}^h(x) \right). \quad (6.48)$$

What means

$$N_t(x) = \alpha_t(x) \left(1 + \beta_t^{PGF} \frac{\Delta g}{g} (x_g) + \beta_t^{QCDC} A_1^{LO}(x_C) + \beta_t^{LP} A_1^{LO}(x) \right), \quad (6.49)$$

where

$$\beta_t^{PGF} = f P_t P_b R^{PGF} a_{LL}^{PGF}, \quad (6.50)$$

$$\beta_t^{LP} = f P_t P_b R^{LP} D, \quad (6.51)$$

$$\beta_t^{QCDC} = f P_t P_b R^{QCDC} a_{LL}^{QCDC}. \quad (6.52)$$

Both sides of Equation (6.49) may now be integrated with three different weights $p_t = \int N_t(x)\omega(x)dx \approx \sum_{i=1}^{N_t} \omega_i$. For optimisation of the statistical and systematic errors the weights for different processes $j = PGF, QCDC, LP$ are chosen to be $\omega^j = \beta^j/P_t$. As a result a set of equations is obtained:

$$\begin{aligned} p_t^j = \sum_{i=1}^{N_t} \omega_i^j = \tilde{\alpha}_t^j \left(1 + \langle \beta_t^G \rangle_{\omega^j} \left\langle \frac{\Delta g}{g}(x_g) \right\rangle \right. \\ \left. + \left\langle \beta_t^{QCDC} \right\rangle_{\omega^j} \langle A_1^{LO}(x_C) \rangle + \left\langle \beta_t^{LP} \right\rangle_{\omega^j} \langle A_1^{LO}(x_{Bj}) \rangle \right). \end{aligned} \quad (6.53)$$

The integrated acceptances $\tilde{\alpha}_t^j = \int dx \omega(x) \alpha_t(x)$ are to fulfil

$$\frac{\tilde{\alpha}_u^j \tilde{\alpha}_{d'}^j}{\tilde{\alpha}_d^j \tilde{\alpha}_{u'}^j} = 1, \quad (6.54)$$

for $j = PGF, LP, QCDC$ what means setting three constraints on the set of Equations (6.53). The weighted average is defined in the same way as in Section 6.1,

$$\langle \beta \rangle_{\omega} = \frac{\int \beta(x) \omega(x) \alpha_t(x) dx}{\int \omega(x) \alpha_t(x) dx} \approx \frac{\sum_i \beta_i \omega_i}{\sum_i \omega_i}. \quad (6.55)$$

Also $\langle \beta A \rangle_{\omega^j} = \langle \beta \rangle_{\omega^j} \langle A \rangle_{\omega^j}$ and $\langle A \rangle_{\omega^{LP}} = \langle A \rangle_{\omega^{QCDC}} = \langle A \rangle_{\omega^{PGF}}$ for $A = A_1^{LO}, \Delta g/g$ is assumed. To fulfil this assumption a special kind of binning has been introduced. It will be discussed later in this section. The set has twelve Equations (6.53) and 15 unknowns (twelve integrated acceptances and 3 asymmetries). Using the three constraints given by Equation (6.54) reduces the number of unknowns to twelve and the set is solvable.

Like described in Section 5.3 we can now construct two vectors:

$$\vec{N}_{obs} = \left(\sum_{i=0}^{N_u} \omega_i^G, \dots, \sum_{i=0}^{N_{d'}} \omega_i^C \right) \quad (6.56)$$

$$\vec{N}_{exp} = (N_{exp,G}^u, \dots, N_{exp,C}^{d'}), \quad (6.57)$$

where the expected number of events is given by

$$N_{exp,j}^t = \tilde{\alpha}_t(1 + A^{PGF} \langle \beta^G \rangle_{\omega_j} + A^{LP} \langle \beta^L \rangle_{\omega_j} + A^{QCDC} \langle \beta^C \rangle_{\omega_j}). \quad (6.58)$$

where t denotes target cells: $c = u, u', d, d'$, and $j = G, L, C$ for PGF, LP and QCD subprocesses, respectively. In this analysis $A_{PGF} = \left\langle \frac{\Delta g}{g}(x_g) \right\rangle$, $A^{LP} = \langle A_1^{LO}(x_{Bj}) \rangle$, $A^{QCDC} = \langle A_1^{LO}(x_C) \rangle$. The parameters ($A^{PGF}, A^{LP}, A^{QCDC}$) can be obtained by minimising χ^2 defined as

$$\chi^2 = (N_{exp}^{\vec{}} - N_{obs}^{\vec{}})^T Cov^{-1} (N_{exp}^{\vec{}} - N_{obs}^{\vec{}}). \quad (6.59)$$

The covariance matrix is defined as $Cov(p_x, p_y) \approx \sum_{N_c} \omega_x \omega_y$:

$$\begin{pmatrix} \sigma_{p_G^u}^2 & \cdots & 0 & Cov(p_G^u, p_L^u) & \cdots & 0 & Cov(p_G^u, p_C^u) & \cdots & 0 \\ \vdots & \ddots & \vdots & \vdots & \ddots & \vdots & \vdots & \ddots & \vdots \\ 0 & \cdots & \sigma_{p_G^{d'}}^2 & 0 & \cdots & Cov(p_G^{d'}, p_L^{d'}) & 0 & \cdots & Cov(p_G^{d'}, p_C^{d'}) \\ Cov(p_G^u, p_L^u) & \cdots & 0 & \sigma_{p_L^u}^2 & \cdots & 0 & Cov(p_L^u, p_C^u) & \cdots & 0 \\ \vdots & \ddots & \vdots & \vdots & \ddots & \vdots & \vdots & \ddots & \vdots \\ 0 & \cdots & Cov(p_G^{d'}, p_L^{d'}) & 0 & \cdots & \sigma_{p_L^{d'}}^2 & 0 & \cdots & Cov(p_L^{d'}, p_C^{d'}) \\ Cov(p_G^u, p_C^u) & \cdots & 0 & Cov(p_L^u, p_C^u) & \cdots & 0 & \sigma_{p_C^u}^2 & \cdots & 0 \\ \vdots & \ddots & \vdots & \vdots & \ddots & \vdots & \vdots & \ddots & \vdots \\ 0 & \cdots & Cov(p_G^{d'}, p_C^{d'}) & 0 & \cdots & Cov(p_L^{d'}, p_C^{d'}) & 0 & \cdots & \sigma_{p_C^{d'}}^2 \end{pmatrix}. \quad (6.60)$$

One can eliminate the acceptances from the equations and at the same time decrease the number of equations by writing

$$\begin{aligned} r_G &:= \frac{p_G^u p_G^{d'}}{p_G^d p_G^{d'}} = \frac{\tilde{\alpha}_G^u \tilde{\alpha}_G^{d'} (1 + \langle \beta_G^u \rangle_{\omega_G} A_{PGF} + \langle \beta_L^u \rangle_{\omega_G} A_{LP} + \langle \beta_C^u \rangle_{\omega_G} A_{QCDC})}{\tilde{\alpha}_G^d \tilde{\alpha}_G^{d'} (1 + \langle \beta_G^d \rangle_{\omega_G} A_{PGF} + \langle \beta_L^d \rangle_{\omega_G} A_{LP} + \langle \beta_C^d \rangle_{\omega_G} A_{QCDC})} \\ &\quad \times \frac{(1 + \langle \beta_G^{d'} \rangle_{\omega_G} A_{PGF} + \langle \beta_L^{d'} \rangle_{\omega_G} A_{LP} + \langle \beta_C^{d'} \rangle_{\omega_G} A_{QCDC})}{(1 + \langle \beta_G^{u'} \rangle_{\omega_G} A_{PGF} + \langle \beta_L^{u'} \rangle_{\omega_G} A_{LP} + \langle \beta_C^{u'} \rangle_{\omega_G} A_{QCDC})}, \\ r_L &:= \frac{p_L^u p_L^{d'}}{p_L^d p_L^{d'}} = \frac{\tilde{\alpha}_L^u \tilde{\alpha}_L^{d'} (1 + \langle \beta_G^u \rangle_{\omega_L} A_{PGF} + \langle \beta_L^u \rangle_{\omega_L} A_{LP} + \langle \beta_C^u \rangle_{\omega_L} A_{QCDC})}{\tilde{\alpha}_L^d \tilde{\alpha}_L^{d'} (1 + \langle \beta_G^d \rangle_{\omega_L} A_{PGF} + \langle \beta_L^d \rangle_{\omega_L} A_{LP} + \langle \beta_C^d \rangle_{\omega_L} A_{QCDC})} \\ &\quad \times \frac{(1 + \langle \beta_G^{d'} \rangle_{\omega_L} A_{PGF} + \langle \beta_L^{d'} \rangle_{\omega_L} A_{LP} + \langle \beta_C^{d'} \rangle_{\omega_L} A_{QCDC})}{(1 + \langle \beta_G^{u'} \rangle_{\omega_L} A_{PGF} + \langle \beta_L^{u'} \rangle_{\omega_L} A_{LP} + \langle \beta_C^{u'} \rangle_{\omega_L} A_{QCDC})}, \\ r_C &:= \frac{p_C^u p_C^{d'}}{p_C^d p_C^{d'}} = \frac{\tilde{\alpha}_C^u \tilde{\alpha}_C^{d'} (1 + \langle \beta_G^u \rangle_{\omega_C} A_{PGF} + \langle \beta_L^u \rangle_{\omega_C} A_{LP} + \langle \beta_C^u \rangle_{\omega_C} A_{QCDC})}{\tilde{\alpha}_C^d \tilde{\alpha}_C^{d'} (1 + \langle \beta_G^d \rangle_{\omega_C} A_{PGF} + \langle \beta_L^d \rangle_{\omega_C} A_{LP} + \langle \beta_C^d \rangle_{\omega_C} A_{QCDC})} \\ &\quad \times \frac{(1 + \langle \beta_G^{d'} \rangle_{\omega_C} A_{PGF} + \langle \beta_L^{d'} \rangle_{\omega_C} A_{LP} + \langle \beta_C^{d'} \rangle_{\omega_C} A_{QCDC})}{(1 + \langle \beta_G^{u'} \rangle_{\omega_C} A_{PGF} + \langle \beta_L^{u'} \rangle_{\omega_C} A_{LP} + \langle \beta_C^{u'} \rangle_{\omega_C} A_{QCDC})}. \end{aligned} \quad (6.61)$$

In this way we get 3 equations for 3 unknowns what helps with the convergence of the fit. For the new set of equations we need to recalculate the covariance matrix:

$$Cov_{new}(3, 3) = prop(12, 3)^T Cov(12, 12) prop(12, 3), \quad (6.62)$$

where $prop(12, 3)$ contains all partial derivatives: $\frac{\partial r_i}{\partial p_i^j}$.

For example two bins I and II of x_{Bj} can be applied. Then $\beta_I^{LP} = \beta^{LP}$ when $x_{Bj} \in I$ and $\beta_I^{LP} = 0$ for $x_{Bj} \in II$. Hence

$$\beta^{LP} A_1^{LO}(x_{Bj}) = \beta_I^{LP} A_1^{LO}(x_{Bj}^I) + \beta_{II}^{LP} A_1^{LO}(x_{Bj}^{II}). \quad (6.63)$$

Putting the last Equation into Equation (6.49) gives an extra asymmetry but also an extra weight can be set. With this binning there are more parameters to fit but more equations at the same time. The ranges of x_{Bj} and x_C overlap for sufficiently high x_{Bj} and in the common region the same binning is applied. In the overlap region for the same bin j $\langle A_1^{LO}(x_{Bj}^j) \rangle = \langle A_1^{LO}(x_C^j) \rangle$. The binning, $12x_{Bj}$, $6x_C$ and $1 - 3x_g$ bins, is presented in Figure 6.5. In total there were 76-84 equations of the type of Equation (6.53). The results obtained in this method are presented in Figure 6.6 together with

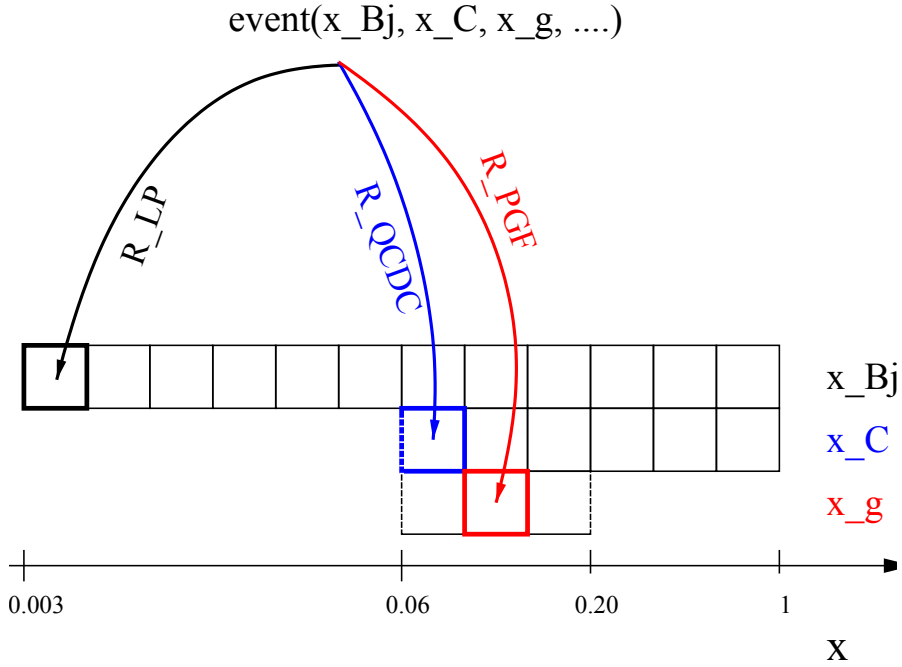


FIGURE 6.5: All- p_T method. Binning in x . The same event contributes several times in different x bins.

the results of COMPASS high- p_T hadron pair results and with the world $\Delta g/g$ LO measurements.

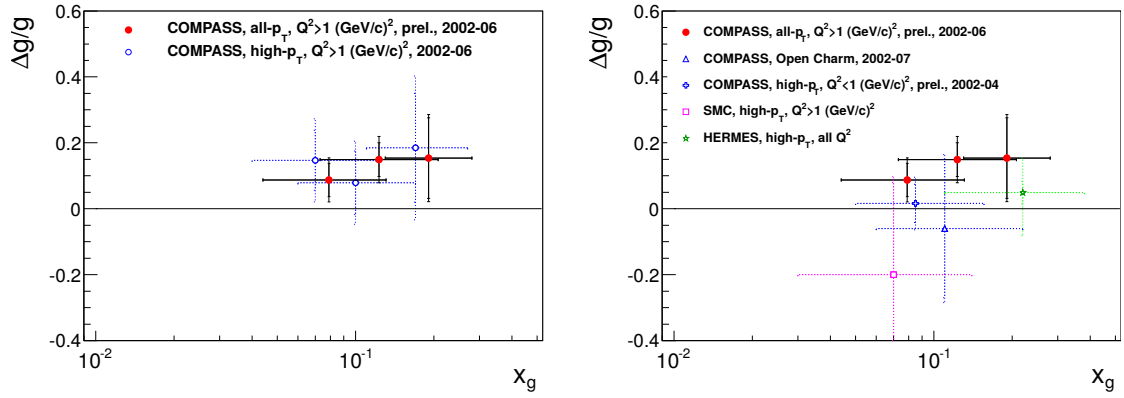


FIGURE 6.6: Left Panel: Comparison of the all- p_T analysis results with high- p_T hadron pair COMPASS analysis. The statistical errors of the all- p_T method are significantly smaller; Right Panel: Comparison of the all- p_T analysis results with world LO $\Delta g/g$ extractions.

The result in single x_g bin reads:

$$\frac{\Delta g}{g} = 0.113 \pm 0.038(\text{stat.}) \pm 0.036(\text{syst.}) \quad (6.64)$$

at scale $\langle \mu^2 \rangle = 3 \text{ GeV}^2$ and $\langle x_g \rangle = 0.10$.

Chapter 7

Monte Carlo simulation and Neural Network training

In this chapter the simulation chain is described in detail. First and main part of the simulation procedure is the LEPTO generator ([63]) which generates the physics process of muon-nucleon scattering and hadronisation. The latter has been tuned to the COMPASS data, by adjusting available LEPTO parameters, during previous analysis ([17]).

Second part of the MC chain is the description of the COMPASS spectrometer. For this purpose the collaboration developed a program called COMGEANT ([114]) based on GEANT3.

The last two parts are the same as for the experimental data analysis. Particle tracks, charges, energy are evaluated from signals collected from the detectors with the use of the CORAL software. Then PHAST software is applied for event-by-event analysis.

7.1 LEPTO generator

LEPTO generator uses leading order electroweak cross-sections and QCD correlations with the use of the first order matrix elements of PGF and QCDC processes. The fragmentation is implemented by application of the LUND model.

7.1.1 Generation procedure

The procedure applied to simulate the event kinematics for a chosen process is based on the experimentally measured cross-sections. For neutral current interactions a phase

space point, usually in the (x, Q^2) plane, has to be generated. The probability of this generation is proportional to the known cross-section.

The cross-section is parameterised separately for Q^2 and x . The simplified functional form f is the upper bound of the cross-section, $f(\chi) > d\sigma/d\chi$, $\chi = Q^2, x$ (Figure 7.1) and its cumulative distribution function (F) should be invertible. (This is done because the inverse cumulative distribution function is very difficult to evaluate directly from the cross-section.) Then an univocal value of χ can be obtained:

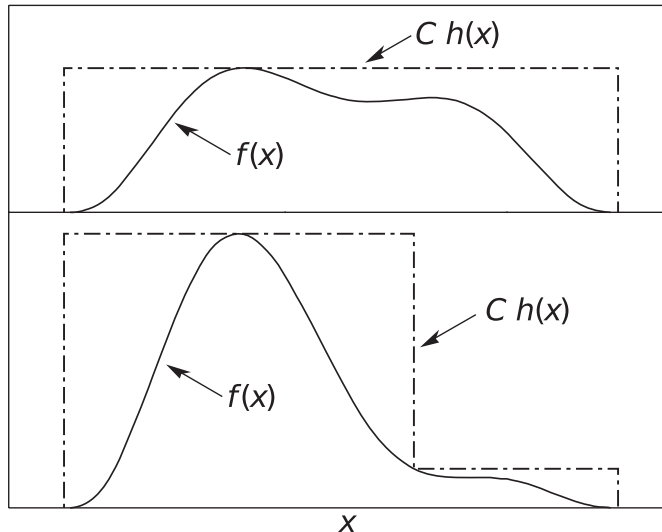


FIGURE 7.1: Illustration of the acceptance-rejection method. Random points are chosen inside the upper bounding figure ($Ch(x)$), and rejected if the ordinate exceeds $f(x)$. The lower figure illustrates a method to increase the efficiency by selecting an “envelope” that closer follows the variation of $f(x)$. The figure is from [28].

$$\chi = F^{-1}(u), \quad (7.1)$$

where u is generated from the uniform distribution and F^{-1} is an inverse of cumulative distribution of function f . As f is an envelope of the cross-section it may overestimate its value. Therefore another random number v is generated from uniform distribution and only when $vf(\chi) < d\sigma/d\chi$ the point is accepted.

7.2 Cross-section parameterisations

In the LO approximation the cross-section of the lepton-nucleon scattering can be written as

$$\frac{d^2\sigma}{dx dQ^2} = \frac{2\pi\alpha^2}{xQ^2} (1 + (1-y)^2) F_2(x, Q^2), \quad (7.2)$$

where the structure function F_2 can be parameterised in terms of $q(x, Q^2)$, $\bar{q}(x, Q^2)$ and $g(x, Q^2)$ parton density functions (PDFs). The parameterisation of the PDFs has been

chosen to be consistent with the NMC experiment [115] as it had a similar x, Q^2 coverage to COMPASS. The PDFs tables MSTW08LO have been used in further simulations.

7.3 First order QCD processes

The simulation model assumes only three processes contributing to the cross-section: leading process $\gamma q \rightarrow q$, QCD Compton scattering $\gamma q \rightarrow qg$ and Photon-Gluon Fusion (PGF) $\gamma g \rightarrow q\bar{q}$. Because all higher order processes are neglected the probabilities of the three processes - $P_{LP}, P_{QCDC}, P_{PGF}$ - sum up to one. The calculations of the first order matrix elements require assuming cut-offs to avoid singularities. (In full calculation soft and collinear divergences are cancelled by virtual corrections or absorbed by the PDFs). In the presented analysis the “ $z\hat{s}$ cut-off” scheme was used (it is the default option for LEPTO generator). It has two cut-off parameters: the fraction z_q of parton energy with respect to the virtual photon and the invariant mass of the partonic subsystem \hat{s} , to regulate separately the divergences with respect to the incoming parton direction and for the two produced partons, respectively. During the systematic studies two MC sample with parton shower off have been produced. In those cases the “ W^2 cut off” scheme was used.

The factorisation scale, appearing in parton densities and the renormalisation scale included in the expressions depending on the strong coupling constant α_s have been chosen to be equal Q^2 which is the default choice in LEPTO.

7.4 Hadronisation

The process of production of observable hadrons from the struck partons is based on the LUND model implemented in the JETSET package [62]. The model describes hadronisation by a colour triplet string which is stretched between the partons moving away from each other. When the string breaking is energetically favourable then quark-antiquark pairs appear. The process is iterative since the new pairs may have sufficient energy to stretch and break a new string. The string fragmentation mechanism is schematically presented in Figure 7.2. The transverse momentum is locally compensated between the quark antiquark pair. The k_T distribution is described in JETSET by two flavour independent Gaussian functions (one for the main distribution and the other one for the tails). The parameters of this distribution are adjustable in LEPTO and have been tuned to COMPASS data [17].

The other parameters which were tuned relate to the shape of the probability of the

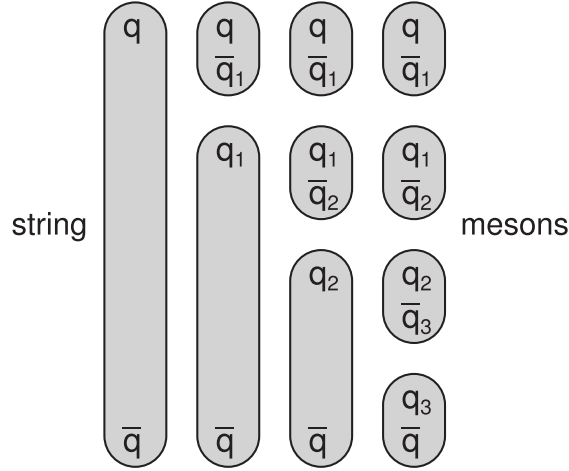


FIGURE 7.2: Iterative string fragmentation into hadrons. The string breaking continues as long as enough energy for the production of new $q\bar{q}$ pairs is available.

fraction z of the available energy taken by the newly created hadron:

$$f(z) = z^{-1}(1-z)^a e^{-bm_T^2/z}, \quad (7.3)$$

where $m_T^2 = m^2 + p_T^2$ and m is the mass of the hadron. Parameters a and b have been tuned to better describe the COMPASS data, [17].

Let us describe the hadronisation scenario for the leading process (LP). If the struck quark is a valence quark the string is stretched between the quark and the nucleon remnant (diquark in this case). Then the string is split according to the LUND fragmentation function f , given by Equation (7.3). When the struck quark (or antiquark) is a sea quark then the valence quarks separate into diquark and a single quark and two strings are formed: one between the struck quark and the diquark and the other between the sea antiquark and the single valence quark. The fraction of the nucleon longitudinal momentum assigned to the antiquark (the partner of the struck quark) is evaluated from the Altareli-Parisi splitting function $P(g \rightarrow q\bar{q})$ (*cf.* Section 2.2.2).

Similarly in the PGF process the remnant is splitted. Two strings are formed between the diquark and the produced quark and between the single valence quark and the antiquark from the pair.

For the QCDC process the string is stretched from the scattered quark via gluon to the target remnant.

7.5 Parton shower

Higher order QCD effects are taken into account in LEPTO by the parton shower (PS) approach. Extra gluons can be emitted before (initial state PS) or after (final state PS)

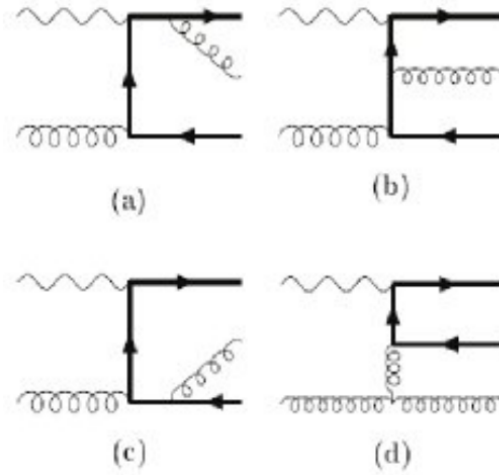


FIGURE 7.3: Selected Feynman diagrams of the PGF process with gluon emissions treated by Parton Shower mechanism. Figures (a-c) present final state showers while figure (d) shows a initial state one.

the boson vertex (Figure 7.3). With this method any higher order (in α_s) processes can be simulated but only in the leading $\log Q^2$ approximation. The Sudakov form factor governs the shower evolution. Inclusion of PS in the simulation strongly improves the data description. Therefore, for the final results the MC with PSON was used, while for systematic studies also simulations without PS have been tested.

7.6 Simulation of experimental conditions

The experimental setup of COMPASS and its response to the passage of particles produced in the considered reaction is simulated with the use of the COMGEANT package [114]. It is an implementation of the COMPASS spectrometer based on GEANT 3 [116] package which includes description of all materials in the experimental hall, magnetic fields, the passage of particles through them and the detectors response.

Signals from the detectors are then reconstructed with the same CORAL ([104]) package version as the one used for data reconstruction, so the tracking inefficiencies are taken into account in the simulation. The fully simulated and reconstructed events can then be analysed in the same way as data but more information (e.g. the process identification) is available in the MC events.

7.7 Comparison between data and Monte Carlo simulations

The tuning of the LEPTO fragmentation parameters is described in detail in [17]. For the systematic studies (Section 9.1) different MC settings and its influence on the final results have been studied. For all MC samples the agreement with corresponding data has been checked. In the plots presented here, the main MC sample (the MC sample which agrees best with the data) which is used to evaluate the final results is shown. There are two sets of plots: one for the simulations and data with the deuteron target (Figure 7.4) and the second with the proton target (Figure 7.5). Both sets contain distributions of six variables: x_{Bj} , Q^2 , y , p_{T1} , p_{T2} , p_{L1} , p_{L2} . These are used in the neural network (NN) training.

It should be noted that in case of the ammonia (NH^3) target in the generation of the interaction by LEPTO a pure proton target is simulated. The true proportion in the target material is 10 protons/ 7 neutrons. The latter is simulated in COMGEANT package for the material through which the products of interaction pass. The choice of a pure proton target in LEPTO is justified by the fact that from the MC simulations the processes fractions on protons are needed for the analysis. It may, however, have influence on the kinematic distribution comparison with data. In case of the deuteron (6LiD) target an equal number of protons and neutrons is simulated with the use of the LEPTO generator.

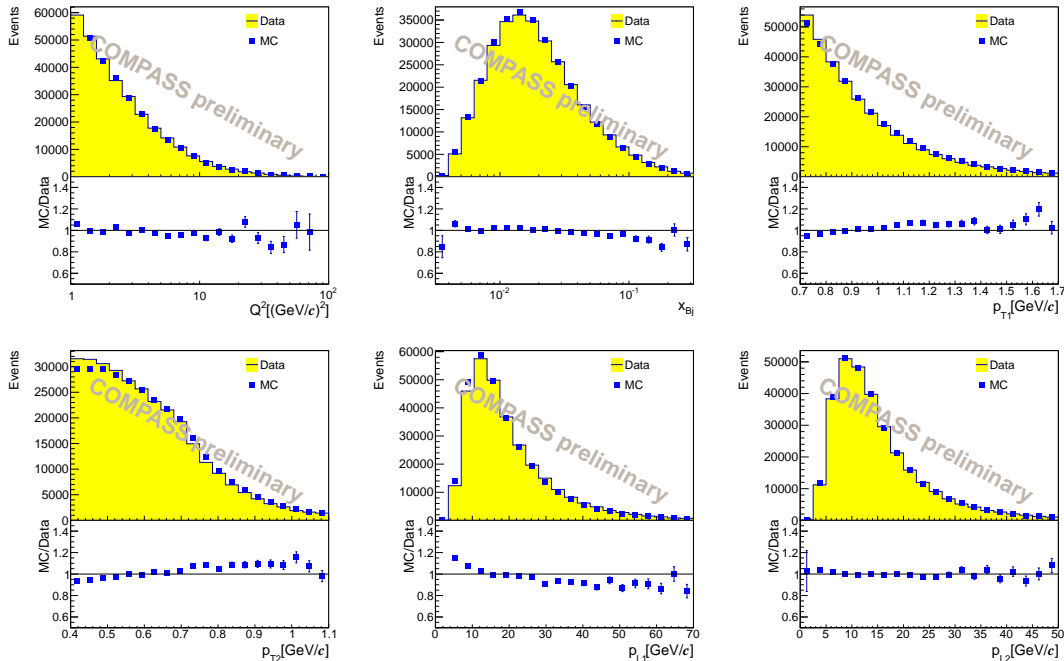


FIGURE 7.4: Kinematic variable distributions in MC and Data high-pt samples normalised to the same number of events. Deuteron Data and MC2004.

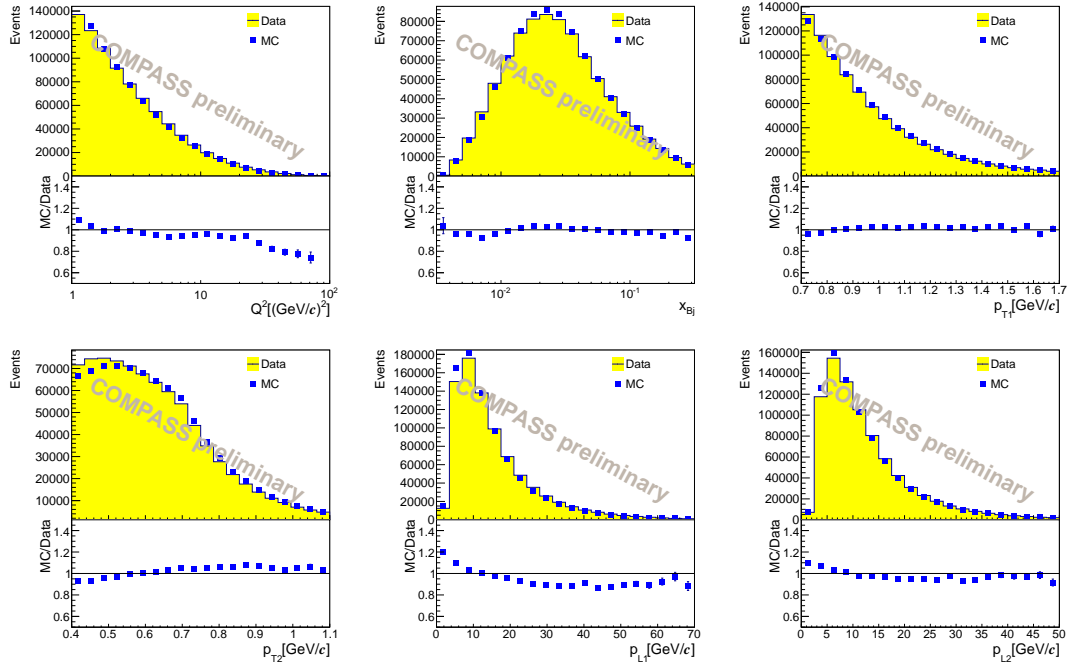


FIGURE 7.5: Kinematic variable distributions in MC and Data high-pt samples normalised to the same number of events. Proton Data and MC2010.

The agreement is satisfactory for both samples. The influence of the small discrepancy for large Q^2 for the proton data is studied in the systematics Section 9.6. The effect is very small as for large Q^2 the photon-gluon fusion process is rare.

7.8 Neural Networks

Artificial Neural Networks are a very powerful tool supporting data analysis. Typically they are applied to separate signal from noise. However, as it will be shown in the next Chapter, 8, it is sufficient and statistically more effective to assign weights on event-by-event basis. In this analysis a multilayer perceptron (MLP) neural network type has been used. In this type of network there is no feedback and the signal is propagated throughout the NN in one direction. In Figure 7.6 a schematic diagram of MLP is shown. The NN is composed of several layers of neurons. Neurons in each layer are connected only to neurons in the previous and next layer. The input signal is introduced through the input layer by setting states of its neuron and then is propagated through the hidden layers to the output layer via the connections between neurons. To parameterise the exclusive *OR* (*XOR*) logic function at least one hidden layer is needed. Already two hidden layers, however, are sufficient to cope with any parameterisation problem [117]. Each neuron has a number of inputs with assigned weights. Its state is a function of weighted input signals. Output signals are connected to the neurons in the next

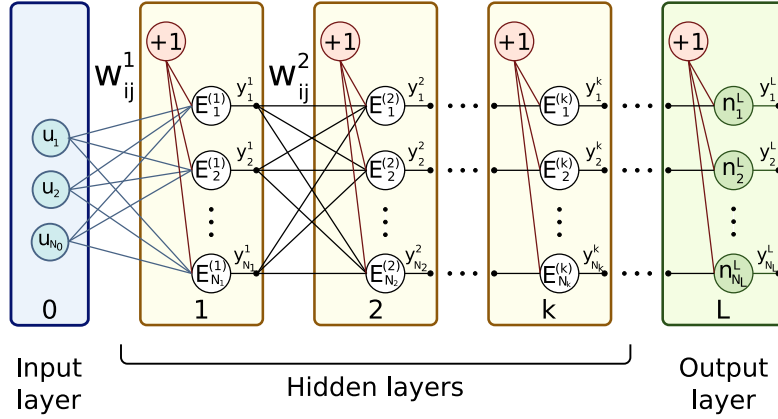


FIGURE 7.6: Multilayer perceptron (MLP) neural network. The “+1” inputs for each layers are the *bias terms* and allow for adjustment of the activation threshold.

layer. In most general MLP neural network with L layers each consisting of N_k neurons ($k = 1, 2, \dots, L$) the state of a neuron i from a layer k ($E_i^{(k)}$) is defined as

$$y_i^{(k)} = f \left(s_i^{(k)} \right), \quad (7.4)$$

where

$$s_i^{(k)} = \sum_{j=0}^{N_{k-1}} \omega_{ij}^{(k)} x_j^{(k)}, \quad f(x) = \begin{cases} 1 & \text{when } x \geq 0 \\ 0 & \text{when } x < 0 \end{cases}. \quad (7.5)$$

The input signals x_j of the neuron $E_j^{(k)}$ come from the neurons from the layer $k - 1$ and they are set differently for the input and other layers:

$$x_i^{(k)} = \begin{cases} u_i & \text{for } i > 0, k = 1 \\ y_i^{(k-1)} & \text{for } i > 0, k = 2, \dots, L \\ +1 & \text{for } i = 0, k = 1, \dots, L \end{cases}. \quad (7.6)$$

A simple scheme of a neuron with the input signals weighted by weights ω_{ij} is shown in Figure 7.7. The weights ω_{i0} are called bias terms which define the threshold value for

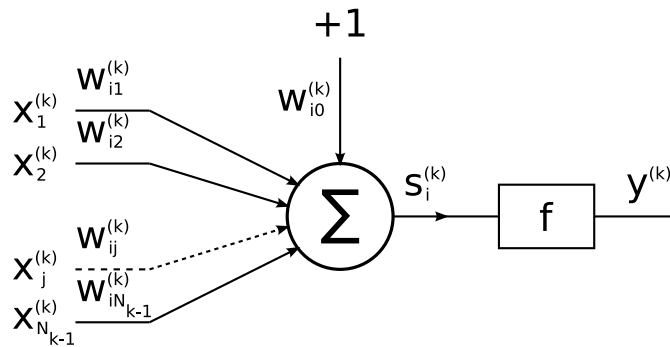


FIGURE 7.7: Schematic representation of a neuron $E_i^{(k)}$.

the neuron activation as combining the above Equations gives

$$y_i^{(k)} = \begin{cases} 1 & \text{when } \hat{s}_i^{(k)} + \omega_{i0}^{(k)} \geq 0 \\ 0 & \text{when } \hat{s}_i^{(k)} + \omega_{i0}^{(k)} < 0 \end{cases}, \quad \hat{s}_i^{(k)} = \sum_{j=1}^{N_{k-1}} \omega_{ij} x_j^{(k)}. \quad (7.7)$$

The activation function $f(x)$ is typically chosen a sigmoid function of the shape $f(x) = 1/(1 + \exp(-\beta x))$; $\beta > 0$ or a hyperbolic tangent $f(x) = \tanh(\alpha x/2)$; $\alpha > 0$. Different activation functions are presented in Figure 7.8. The choice of an activation function

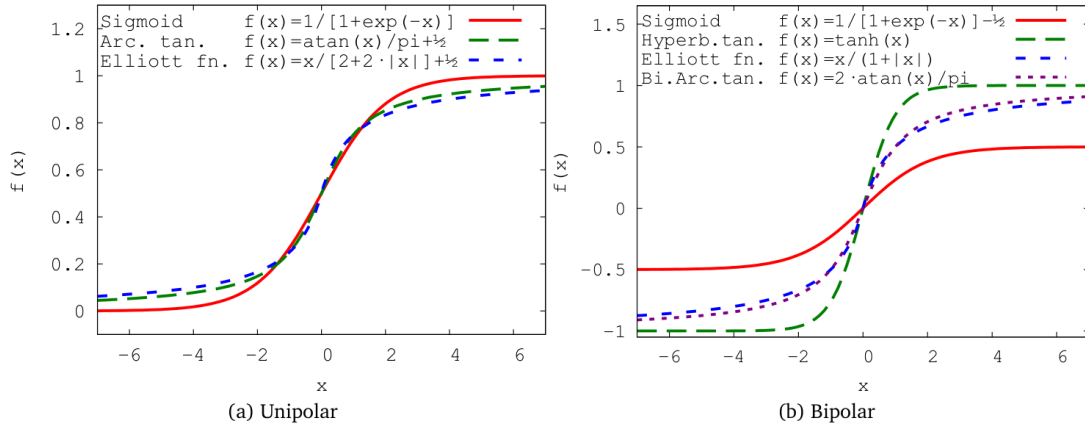


FIGURE 7.8: Neuron activation functions

sets the sensitivity of the network to the outliers. In this analysis a NN with unipolar sigmoid function has been used. The output layer neurons activation function is chosen as a simple linear function $f(x) = x$ what assures proportionality to the input signals. The learning procedure is performed by adjusting the weights corresponding to the connections between neurons. For purposes of this measurement a supervised training technique is used. For each input vector an expected output value $d_i(n)$ is known. On every iteration an error is calculated defined by the network response and the desired output. Here Mean Squares Error (MSE) is used

$$Q(n) = \sum_{i=1}^{N_L} \left(d_i(n) - y_i^{(L)}(n) \right)^2, \quad (7.8)$$

where L is the output layer. This choice ensures that the probabilistic interpretation of the NN results is justified.

An iterative procedure based on the steepest gradient algorithm is performed in order to minimise the error

$$\omega_{ij}^{(k)}(n+1) = \omega_{ij}^{(k)}(n) - \eta \frac{\partial Q(n)}{\partial \omega_{ij}^{(k)}(n)}, \quad (7.9)$$

where η is the step size. Let us consider

$$\frac{\partial Q(n)}{\partial \omega_{ij}^{(k)}(n)} = \frac{\partial Q(n)}{\partial s_i^{(k)}(n)} \frac{\partial s_i^{(k)}(n)}{\partial \omega_{ij}^{(k)}(n)} = \frac{\partial Q(n)}{\partial s_i^{(k)}(n)} x_j^{(k)}(n) = -2\delta_i^{(k)}(n)x_j^{(k)}(n); \quad (7.10)$$

$$\delta_i^{(k)}(n) = -\frac{1}{2} \frac{\partial Q(n)}{\partial s_i^{(k)}(n)}.$$

Thus, the weight after the n -th iteration is given by

$$\omega_{ij}^{(k)}(n+1) = \omega_{ij}^{(k)}(n) + 2\eta\delta_i^{(k)}(n)x_j^{(k)}(n). \quad (7.11)$$

For the MSE function the expression for $\delta_i^{(k)}(n)$ reads

$$\delta_i^{(k)} = \epsilon_i^{(k)}(n)f'(s_i^{(k)}(n)); \quad \epsilon_i^{(k)}(n) = \begin{cases} d_i(n) - y_i^{(L)}(n) & \text{for } k = L \\ \sum_{m=1}^{N_{k+1}} \delta_m^{(k+1)}(n)\omega_{mi}^{(k+1)} & \text{for } k = 1, \dots, L-1 \end{cases}. \quad (7.12)$$

Here f' is the derivative of f . In the considered case an "error back propagation" was used in which the error is first calculated for the output layer and then propagated towards the input layer. In the beginning of the training the step is fairly large and it is decreased when the error value is approaching minimum.

To avoid over-training (learning by heart) of the network the training set is randomly divided into two subsamples: the training set on which the network is trained and a testing set to monitor the training procedure. The error value from both sets is compared on every iteration and the training is stopped when the obtained values diverge.

A dynamic structure, where the network can add extra neurons or remove unused errors is applied. If the network modification leads to smaller error a new structure is set. Otherwise the previous state is restored. The modifications are made periodically and a new neuron appears in a random position. In this way the network can "jump out" from a local minimum to search for a global one.

In this analysis the NetMaker package [118] has been used. It was implemented for COMPASS and ICARUS neutrino experiment. The program is written in C# language and it has been optimised for working with large data sets. The trained neural network output is stored in a XML standard file. The author of this thesis has written a simple interface enabling evaluation of the trained NN output by ROOT and PHAST packages.

7.9 Parameterisation

The LEPTO model assumes three contributing processes: photon-gluon fusion (PGF), QCD Compton (QCDC) and leading process (LP). The expected neural network output

consists of three positive weights: R_{PGF} , R_{QCDC} , R_{LP} with:

$$R_{PGF} + R_{QCDC} + R_{LP} = 1. \quad (7.13)$$

Hence, there the output can be parameterised by two free and equivalent parameters o_1 and o_2 . The target values (t_1, t_2) assigned to MC events by process identification are the following: PGF - $(0, 0)$, QCDC - $(1, 0)$ and LP - $(1/2, \sqrt{3}/2)$, vertices of an equilateral triangle. The output of a trained network is presented in Figure 7.9.

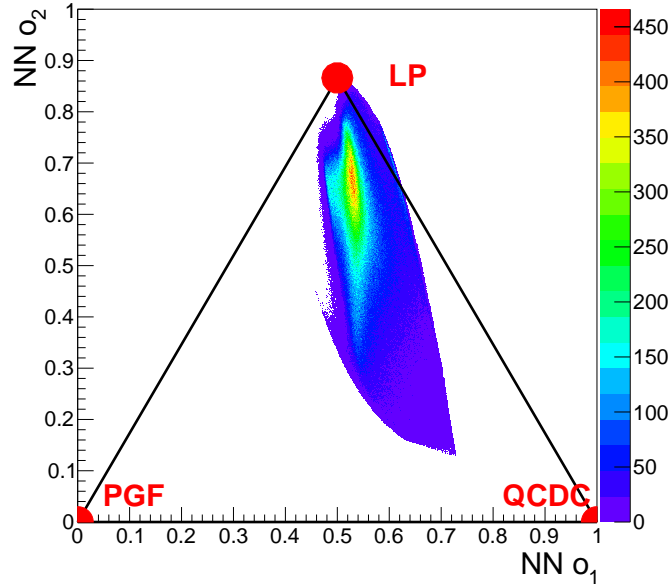


FIGURE 7.9: Neural Network output for the three given target values PGF - $(0, 0)$, QCDC - $(1, 0)$ and LP - $(1/2, \sqrt{3}/2)$. The separation of the sample is difficult and weighted method, which is statistically more optimal, is applied instead.

The probabilities R_{PGF} , R_{LP} , R_{QCDC} can be easily obtained from the NN output o_1 , o_2 :

$$R_{PGF} = 1 - o_1 - 1/\sqrt{3}o_2, \quad R_{QCDC} = o_1 - 1/\sqrt{3}o_2, \quad R_{LP} = 2/\sqrt{3}o_2. \quad (7.14)$$

The input vector is constructed of six kinematic variables: x_{Bj} , Q^2 , p_{T1} , p_{T2} , p_{L1} and p_{L2} . The transverse (p_T) and longitudinal (p_L) part of the leading and next-to-leading hadron momenta are obtained with respect to the virtual photon direction. The hadron with the largest transverse momentum is chosen as the leading hadron. The vector of the kinematic variables fully characterises the event kinematics and has been chosen to be the same as in the ΔG measurement described in [17] and shortly in Section 6.2. To assure equal sensitivity of the network to different input elements each input parameter distribution is normalised to have mean value zero and standard deviation one.

7.10 Validation of the neural network training

The neural network training is a complicated process and the minimisation of Mean Square Error can lead to a local minimum different from the global one despite the usage of the testing set. The method of NN training validation have been developed during the ΔG measurement from high- p_T hadron pairs ([17]). It is done with the use of different MC sample than the one used for the training. The sample is divided in two and both subsamples are binned with respect to a certain kinematic variable (e.g. $p_T^2 = p_{T1}^2 + p_{T2}^2$). For the first subsample particle identification from MC is used to obtain the fraction of one of the processes in each bin. As an example PGF probability for each bin i is obtained from

$$P_{MC}^i = N_{PGF}^i / N_{all}^i, \quad (7.15)$$

where N_{PGF}^i is the number of PGF events in bin i and N_{all}^i is the number of all events in this bin. For the second subsample in the same kinematic bins the average NN output for an MC event in each bin is evaluated, labelled as P_{NN} . The results of this exercise for p_T^2 obtained for the main MC settings are presented in Figures 7.10 (deuteron target) and 7.11 (proton target). The results show very good agreement between the NN output and the true MC process fraction. The p_T^2 dependence is important as the processes fractions

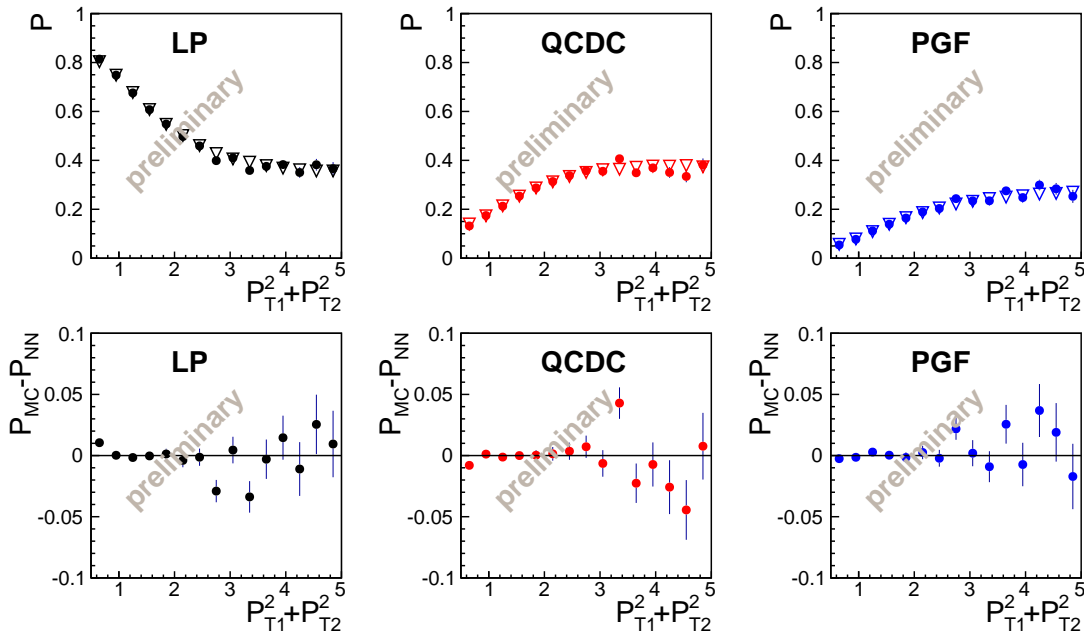


FIGURE 7.10: Neural Network training validation - p_T^2 dependence. Top panels: NN output P_{NN} - open triangles compared to MC process fraction P_{MC} - full circles in bins $p_T^2 = p_{T1}^2 + p_{T2}^2$. Bottom panels: difference $P_{MC} - P_{NN}$ in bins of p_T^2 . Monte Carlo simulations and Neural Network training prepared for measurements with deuteron target with the main MC settings.

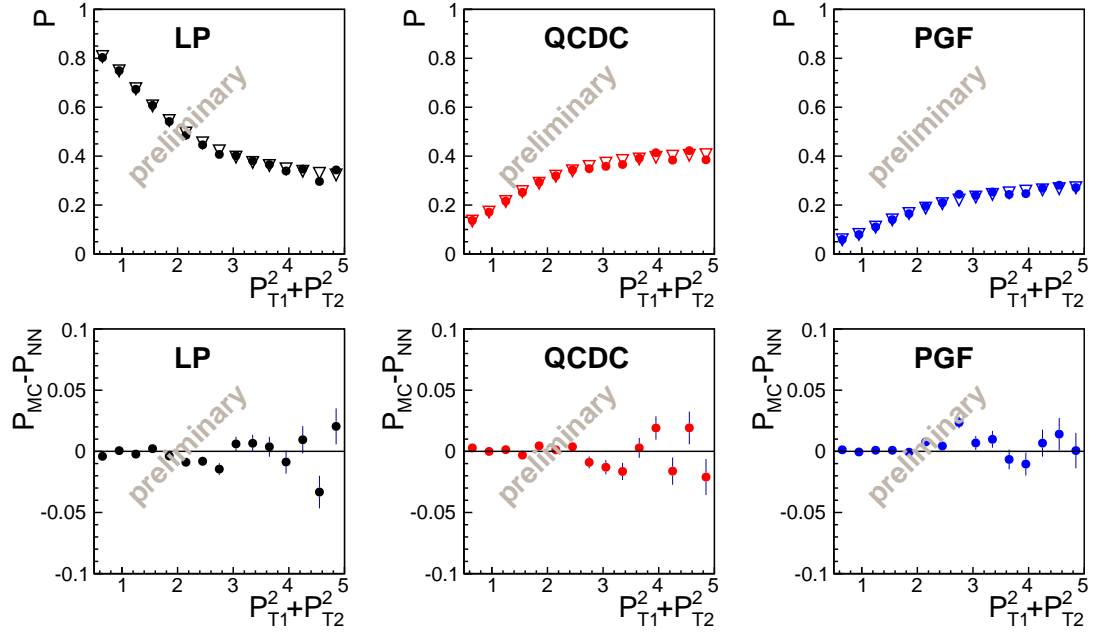


FIGURE 7.11: Neural Network training validation - p_T^2 dependence. Top panels: NN output P_{NN} - open triangles compared to MC process fraction P_{MC} - full circles in bins $p_T^2 = p_{T1}^2 + p_{T2}^2$. Bottom panels: difference $P_{MC} - P_{NN}$ in bins of p_T^2 . Monte Carlo simulations and Neural Network training prepared for measurements with proton target with the main MC settings for the 2010 data sample.

are sensitive to it. This is due to the fact that in the PGF and QCD Compton processes transverse momentum can be generated in the two-body final state system. Thus their fractions are enhanced with larger p_T^2 . During the analysis procedure similar plots have been produced for other kinematic variables (Q^2 , x_{bj} , y , p_{T1} , p_{T2} , p_{L1} , p_{L2}). This has been done for every NN training described in Section 9.1 prepared for the systematic studies. Apart from the kinematic dependence P_{MC} value in bins of P_{NN} have been evaluated (this time the MC sample is not divided). The expected dependence should be linear as it is shown in Figures 7.12 (deuteron target) and 7.13 (proton target). The agreement is satisfactory and thus a conclusion that the training is validated can be made. Again similar plots have been produced for NN trained with different MC settings which are not presented here for brevity.

7.11 The gluon momentum fraction x_G and the quark momentum fraction in QCD Compton process x_C

The fraction of the nucleon momentum carried by the struck parton is given by:

$$\xi = x_{Bj} \left(\frac{\hat{s}}{Q^2} + 1 \right), \quad (7.16)$$

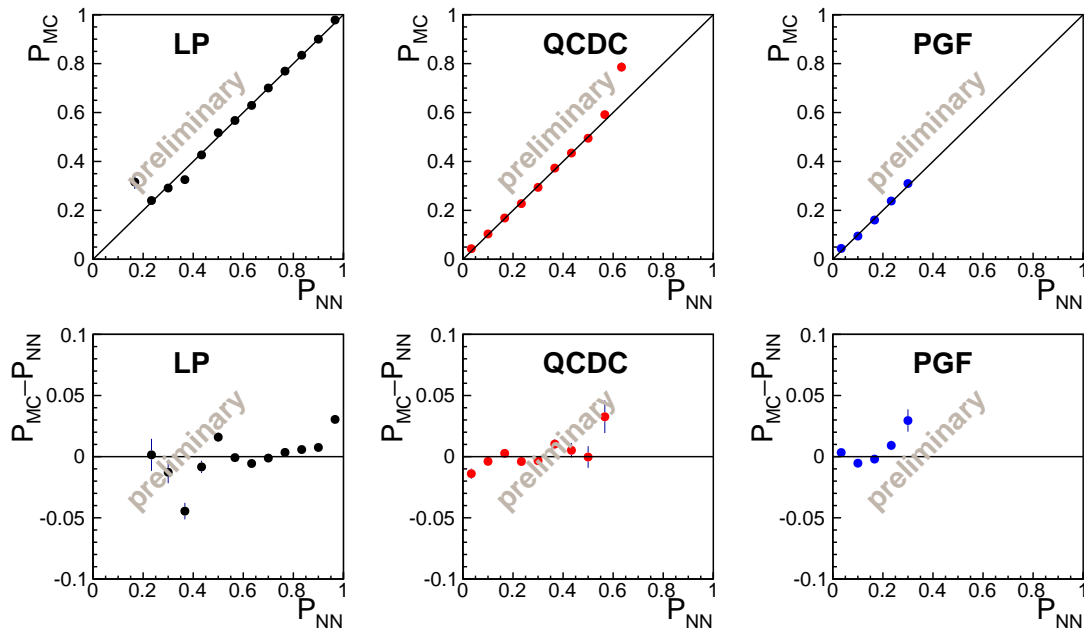


FIGURE 7.12: Neural Network training validation - process fraction dependence. Top panels: NN output P_{NN} - solid line compared to MC process fraction P_{MC} - full circles in bins P_{NN} . Bottom panels: difference $P_{MC} - P_{NN}$ in bins of P_{NN} . Monte Carlo simulations and Neural Network training prepared for measurements with deuteron target with the main MC settings.

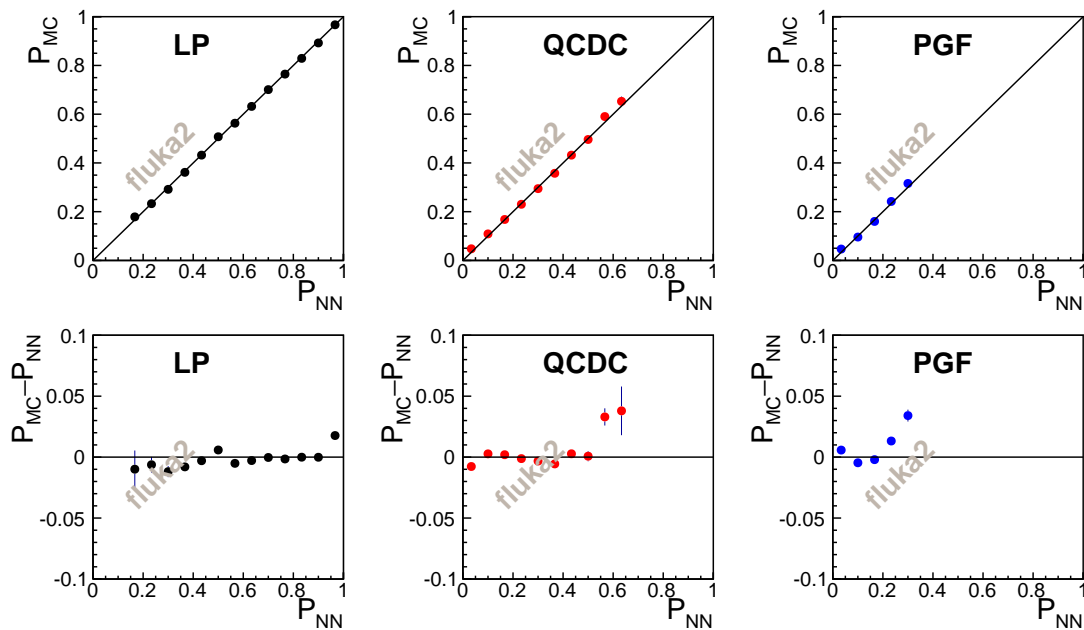


FIGURE 7.13: Neural Network training validation - process fraction dependence. Top panels: NN output P_{NN} - solid line compared to MC process fraction P_{MC} - full circles in bins P_{NN} . Bottom panels: difference $P_{MC} - P_{NN}$ in bins of P_{NN} . Monte Carlo simulations and Neural Network training prepared for measurements with proton target with the main MC settings for the 2010 data sample.

where \hat{s} is the Mandelstam variable for the hard process and is known for simulated PGF and QCDC events but cannot be directly determined from data. For LP $\xi = x_{Bj}$. A pure PGF (or QCDC) MC sample can be used to train a neural network to assign x_G (or x_C) to every event. The input is the same as in the processes fraction case ($Q^2, x_{Bj}, p_{T1}, p_{T2}, p_{L1}, p_{L2}$) and the output is just the value of x_G (x_C). The validation of this training is given in Figures 7.14 (deuteron) and 7.15 (proton).

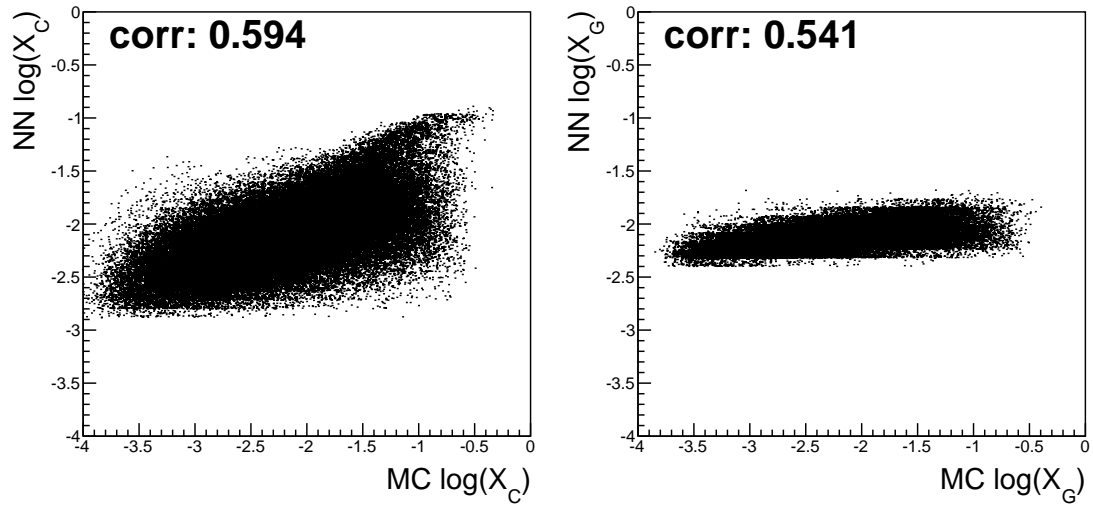


FIGURE 7.14: Validation of the NN training for x_C (left) and x_G (right). Deuteron target.

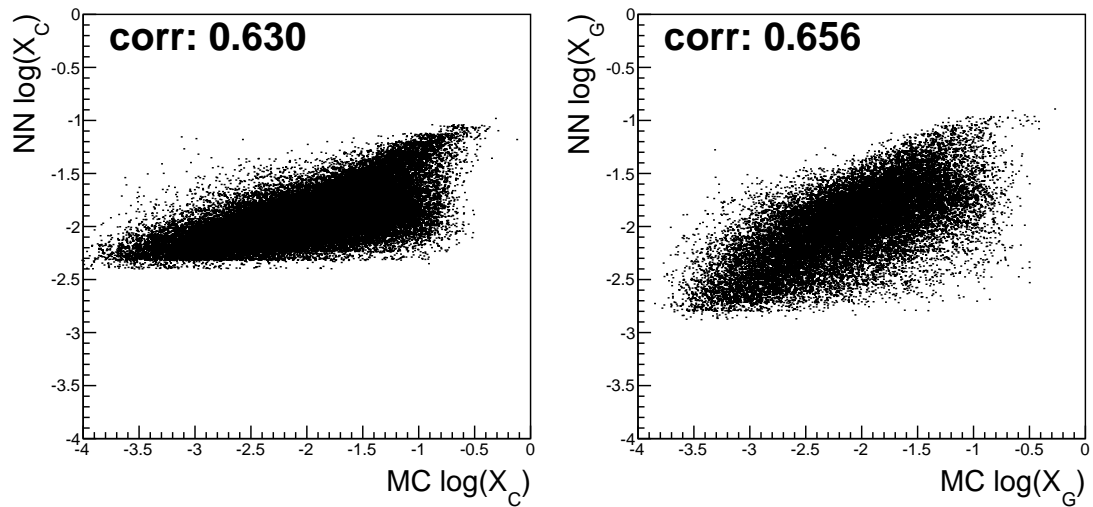


FIGURE 7.15: Validation of the NN training for x_C (left) and x_G (right). Proton target.

Chapter 8

The gluon contribution to the Sivers effect at the COMPASS experiment

8.1 Data selection

8.1.1 Discussion of the main cuts

The aim of the analysis presented here is to extract the gluon contribution to the Sivers effect. The method chosen for this purpose combines approaches presented in Chapter 6. The most similar approach has been applied in the all- p_T analysis described in Section 6.3. There are important differences, however. First of all in case of ΔG there exists a translation from the "intrinsic" asymmetry to the measured asymmetry called a_{LL} calculable in perturbative QCD. This is not the case for the Sivers effect. The nature of the "intrinsic" Sivers asymmetry, the translation from the Sivers function to the final state Sivers effect, is model dependent. Then, even the final state effect is strongly diluted by fragmentation as the azimuthal angle of the measured hadrons is affected by hadronisation process. As it will be shown later, for the measurement it is necessary to assume that the asymmetries of the processes involved are constant in all kinematic variables except x where linear dependence is assumed. The single hadron Sivers asymmetry (without process separation) has been shown before and is repeated here in Figure 8.1. The only strong dependence of the Sivers asymmetry is for the region of small p_T . This is why a cut for all considered hadrons $p_T > 0.4$ GeV has been chosen. On the other hand the region of p_T bin should be as wide as possible as the processes fractions for the sample vary with p_T . It has been shown in Section 5.3.3 that the variety

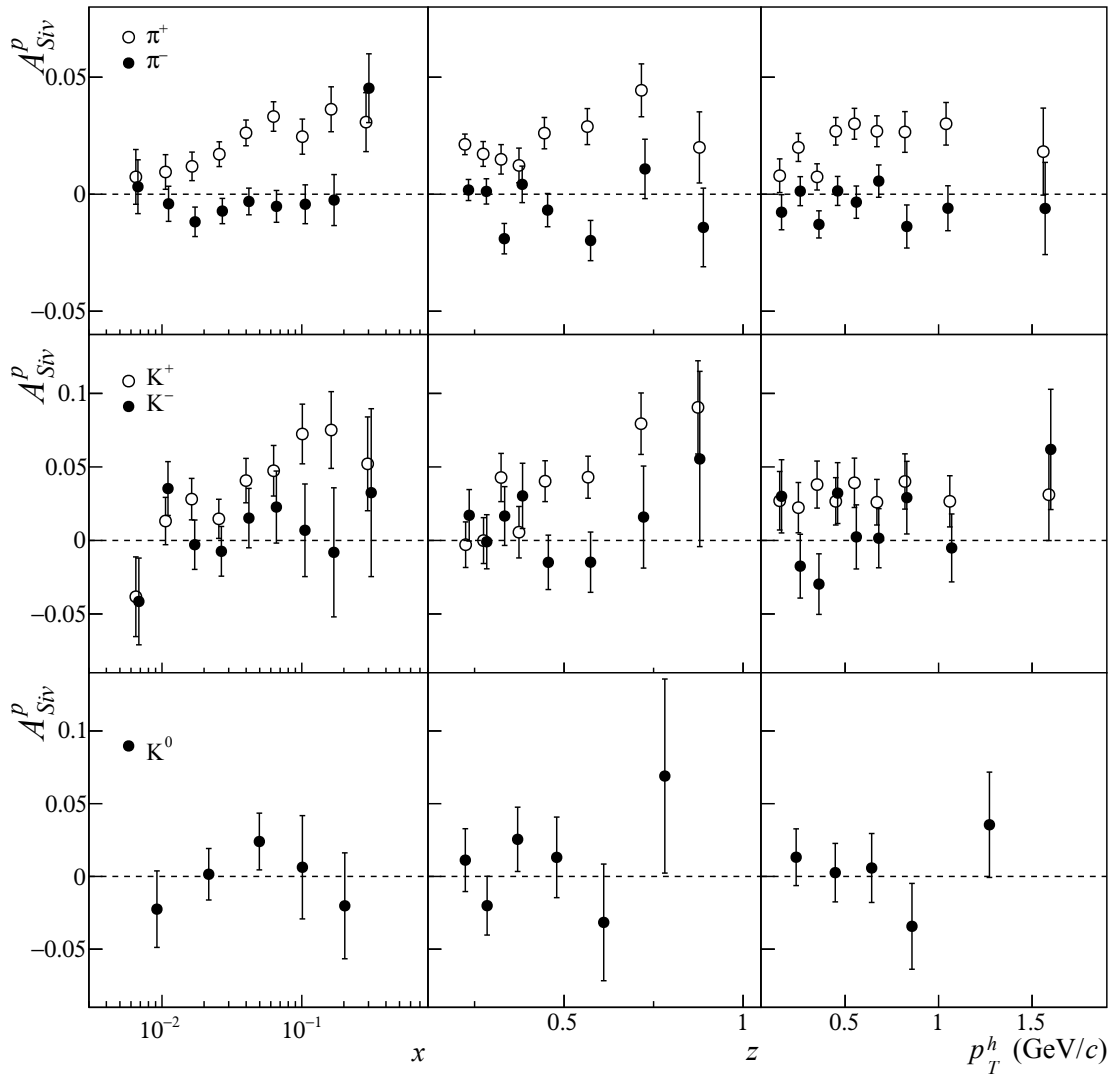


FIGURE 8.1: COMPASS and HERMES results of single hadron Sivers asymmetry measurement with the proton target. x, z and p_T dependence. Results show strong Sivers asymmetry dependence for small p_T .

of fractions values in the sample is crucial for the applied method. At the same time cutting on the hadrons transverse momenta reduces the statistics.

The important question was whether to choose single hadrons or hadron pairs. The latter choice seemed reasonable as the photon-gluon fusion produces a two-body final state. This has been decided by a Monte Carlo exercise. A sample of PGF events has been selected and the correlation between the gluon azimuthal angle and the azimuthal angle of the reconstructed hadrons has been studied. It should be noted here that only hadrons with $z > 0.1$ have been taken into consideration to select current fragmentation region. The results for single hadron transverse momentum and the sum of the two leading hadrons are shown in Figure 8.2. It has been decided to choose the sample with at least two hadrons and $p_{T1} > 0.7$ GeV and $p_{T2} > 0.4$ GeV. The sample with the

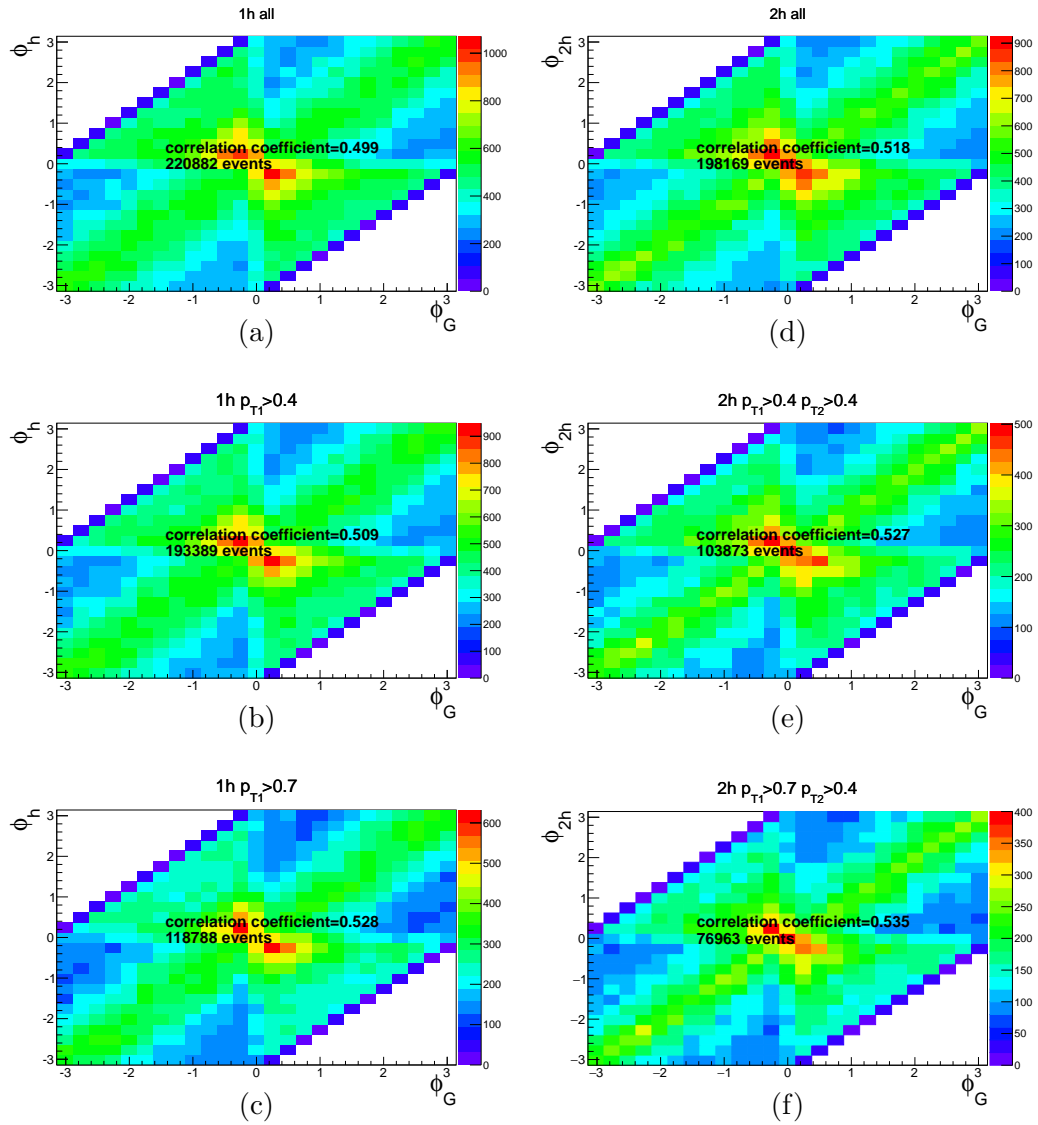


FIGURE 8.2: Monte Carlo studies of correlations between the gluon azimuthal angle ϕ_G and the hadronic azimuthal angle ϕ_h or ϕ_{2h} . The plots present correlations for different data selection. For the left column (abc) at least one hadron is demanded and: (a) no further cuts; (b) hadrons with $p_{T1} > 0.4$ GeV; (c) hadrons with $p_{T1} > 0.7$ GeV. For the write column (def) a sample with at least two hadrons is selected and: (f) no cut on p_{T1} and p_{T2} ; (e) $p_{T1} > 0.4$ GeV and $p_{T2} > 0.4$ GeV; (f) $p_{T1} > 0.4$ GeV and $p_{T2} > 0.4$ GeV.

demand of at least one hadron and stronger p_T cut has similar statistics and correlation factor but taking sum of momenta of the two leading hadrons is more intuitive in the view of two-body final state of the PGF process.

In the two hadron case a selection of opposite charge can also be done. This was not applied during the main selection but its influence has been studied in the systematic Section (9.4).

8.1.2 Selection of the two data samples for the deuteron and proton targets

TARGET POLARISATION.

In case of the deuteron target the target was divided in two cells ("up" and "down") polarised in opposite directions. In the proton case the target was constructed of three polarised cells ("up", "centre" and "down"). Central cell was polarised oppositely to the up and down cells. The polarisation in the cells were inverted every several days.

THE INTERACTION VERTEX.

The PHAST-defined "best primary vertex" (`e.iBestPrimaryVertex()`) is taken to select a interaction vertex. To ensure a position of the interaction vertex inside of the target material, the PHAST-defined function `PaAlgo::InTarget` is used. This routine rejects all the events where the projection of the incoming muon lies outside the most upstream ($z=-62.5$ cm) and the most downstream end ($z=+67.5$ cm) of the target. Interaction vertex events in between the target cells are also rejected. A further cut was applied to ensure identical beam intensity for the two (deuteron) or three (proton) target cells. The `PaAlgo::CrossCells` which assures that the beam trajectory passes through all target cells.

BEAM MUON.

The beam muon associated in the reconstructed data (miniDST) with the best interaction vertex is taken as the beam particle. A cut on a momentum of $140 \text{ GeV}/c < p_{beam} < 180 \text{ GeV}/c$. In addition (for the proton target sample) the associated track must have $\chi_{red}^2 = \chi_{tot}^2 / (N_{hits} - 5) < 4$.

PARTICLE IDENTIFICATION.

The identification of the scattered muon is slightly different for the deuteron and proton data samples. A combination of cuts with the use of PHAST functions `isMuPrimCoral()` and `CanBeMuon()` has been applied. In case of more than one μ in the event, the event is rejected too. If there exists another track satisfying the conditions for X/X_0 and χ^2 and has at least 6 hits in MA01 (muon wall) and at least 4 hits in MA02 (muon wall) the event is rejected. Moreover the μ track must not cross yoke of SM2.

In the proton case the scattered muon, μ' , is identified using the PHAST(version 7.136) (`[105]`) `isMuPrim(false, true, true, false)` which, in principle, should impose equivalent conditions as the ones given above. This difference arises from the principle of being consistent with other COMPASS analysis on transversely polarised deuteron and proton targets.

The scattered muon candidate, μ' , is required to be very penetrating and therefore a cut $X/X_0 > 30$ is used on the number of traversed radiation lengths. Here X is the measured length of the track of the particle, X_0 the average radiation length of the materials through which the particle passed. It is also required to pass through the active area of the trigger hodoscopes that have fired the trigger for the considered event. The event is also rejected when there is a high momentum particle passing through the absorber's hole. Additionally there is a requirement for the reduced χ^2 of the track fit ($\chi^2/ndf < 10$). The scattered muon track is required to have at least one hit in detectors upstream the SM1 magnet.

In case of more than one μ' candidate in the event, the event is rejected. Moreover the μ' track must not cross yoke of the second magnet SM2.

Two particles, coming from the interaction vertex, with the largest p_T with respect to the virtual photon four-momentum q are considered as hadron candidates. First of all, both of them should not be identified as muons. Therefore the number of radiation lengths corresponding to their tracks should be small ($X/X_0 < 10$). In order to avoid tracks reconstructed in the SM1 fringe field, we also require for a track of hadron candidate to have one hit before the SM1 magnet and one hit after SM1. Finally, there is a cut on the reduced χ^2 of the track fit ($\chi^2/ndf < 10$).

KINEMATIC CUTS.

There are two major reasons for choosing the high- p_T sample. First, with this choice the fraction of PGF in the sample is enhanced. Secondly it improves the correlation between the azimuthal angle of the gluon momentum and the azimuthal angle of the reconstructed sum of two leading hadron momenta.

The following cuts on inclusive kinematic variables were applied: $Q^2 > 1$ (GeV/c)² to select events in the perturbative region, $0.003 < x_{Bj} < 0.7$, $0.1 < y < 0.9$ and $W > 5$ GeV/c².

For further selection the high- p_T cut was used: $p_{T1} > 0.7$ GeV/c, $p_{T2} > 0.4$ GeV/c, which ensures that PGF fraction in the sample is enhanced and that the correlation between the azimuthal angle of the gluon and the azimuthal angle of the vector sum of two hadrons is stronger. The cuts $z_1 > 0.1$ and $z_2 > 0.1$ are used to select current fragmentation region and the cut $z_1 + z_2 < 0.9$ is applied to reject decay products of diffractively produced vector mesons. The list of cuts, statistics after each cut with its crosscheck are gathered in Tables 8.1 and 8.2.

deuteron		
cuts	# events after cut	percentage of total events
mini DST	1214158067	100%
≥ 4 particles in event	888719155	73.2%
BestPrimaryVertex()	797099263	65.65%
iMuPrimCoral()	496925126	40.93%
$\#mu' > 1$	493519435	40.65%
new mu' flag	493487059	40.64%
CanBeMuon()	491776987	40.5%
$\chi_{mu}^2/ndf < 10$	489700428	40.33%
CrossYoke()	489264574	40.3%
$\chi_{mu'}^2/ndf < 10$	485228133	39.96%
$X/X_0(mu') > 30$	423950392	34.92%
$Z_{First}(mu') < 350$	388352215	31.99%
$140 < P_{mu} < 180$	386928114	31.87%
CrossCells	275348777	22.68%
InTarget	232442156	19.14%
$W > 5$	224975534	18.53%
$Q^2 > 1$	20826864	1.72%
$0.003 < x_{Bj} < 0.7$	20668093	1.7%
$0.1 < y < 0.9$	20052924	1.65%
$\#hadrons \geq 2$	12520188	1.03%
$p_{T1} > 0.7$	2320824	0.19%
$z_1 \geq 0.1$	2172634	0.18%
$p_{T12} \geq 0.4$	1037793	0.09%
$z_2 \geq 0.1$	770990	0.06%
$z = z_1 + z_2 < 0.9$	747484	0.06%
final	747484	0.06%

TABLE 8.1: Statistics after cuts for whole deuteron target data (three period pairs)

2010 proton		
cuts	# events after cut	percentage of total events
mini DST	27889279577	100 %
≥ 4 particles in event	22560143966	80.89 %
BestPrimaryVertex()	21496813770	77.08 %
iMuPrim()	3628460819	13.01 %
CanBeMuon()	3628460244	13.01 %
$\chi_\mu^2/ndf < 10$	3628348463	13.01 %
$\chi_{\mu'}^2/ndf < 10$	3622460155	12.99 %
$X/X_0(\mu') > 30$	3538330516	12.69 %
$Z_{First}(\mu') < 350$	2866709555	10.28 %
$140 < P_\mu < 180$	2852443924	10.23 %
$\mu_{errbeam} \leq 4$	2620265555	9.4 %
CrossCells	2293426026	8.22 %
InTarget	1846646977	6.62 %
$W > 5$	1743173397	6.25 %
$Q^2 > 1$	143679400	0.52 %
$0.003 < x_{Bj} < 0.7$	140651648	0.5 %
$0.1 < y < 0.9$	130894917	0.47 %
$\#hadrons \geq 2$	95221468	0.34 %
$p_{T1} > 0.7$	22711725	0.08 %
$z_1 \geq 0.1$	18733398	0.07 %
$p_{T2} \geq 0.4$	10921467	0.04 %
$z_2 \geq 0.1$	6830653	0.02 %
$z = z_1 + z_2 < 0.9$	6619361	0.02 %
final	6619361	0.02 %

TABLE 8.2: Statistics after cuts for whole 2010 year (12 periods)

8.2 Two-hadron SIDIS cross-section

The full two-hadron cross-section given in Appendix A in terms of ϕ_h and $\phi_{R\perp}$, the azimuthal angles of $P_h = P_1 + P_2$ (sum of two leading hadron momenta) and $R = (P_1 - P_2)/2$ respectively. In the case of this analysis the angle $\phi_{R\perp}$ is not taken into consideration so the two-hadron cross-section is integrated over this angle. The number of partial waves is then reduced and l_{max} in Equations (A.2), (A.4), (A.3), (A.5), (A.6) and (A.7) is zero and hence $m = 0$. This leads to cross-section exactly the same as in the one hadron case (Equation (2.39)). Here the azimuthal angle of the sum of the two

hadrons momenta is denoted by ϕ_{2h} :

$$\begin{aligned}
\frac{d\sigma}{dx dy d\psi dz d\phi_h dP_{h\perp}} = & \\
& \frac{\alpha^2 y^2}{xyQ^2 2(1-\varepsilon)} \left(1 + \frac{\gamma^2}{2x}\right) \left\{ F_{UU,T} + \varepsilon F_{UU,L} + \sqrt{2\varepsilon(1+\varepsilon)} \cos \phi_{2h} F_{UU}^{\cos \phi_{2h}} \right. \\
& + \varepsilon \cos 2\phi_{2h} F_{UU}^{\cos 2\phi_h} + \lambda_e \sqrt{2\varepsilon(1-\varepsilon)} \sin \phi_{2h} F_{UU}^{\sin \phi_{2h}} \\
& + S_{\parallel} \left[\sqrt{2\varepsilon(1+\varepsilon)} \sin \phi_{2h} F_{UL}^{\sin \phi_h} + \varepsilon \sin(2\phi_{2h}) F_{UL}^{\sin(2\phi_{2h})} \right] \\
& + S_{\parallel} \lambda_e \left[\sqrt{1-\varepsilon^2} F_{LL} + \sqrt{2\varepsilon(1-\varepsilon)} \cos \phi_{2h} F_{LL}^{\cos \phi_{2h}} \right] \\
& + |\mathbf{S}_{\perp}| \left[\sin(\phi_{2h} - \phi_S) \left(F_{UT,T}^{\sin(\phi_{2h}-\phi_S)} + \varepsilon F_{UT,L}^{\sin(\phi_{2h}-\phi_S)} \right) \right. \\
& + \varepsilon \sin(\phi_{2h} + \phi_S) F_{UT}^{\sin(\phi_{2h}+\phi_S)} + \varepsilon \sin(3\phi_{2h} - \phi_S) F_{UT}^{\sin(3\phi_{2h}-\phi_S)} \\
& + \left. \sqrt{2\varepsilon(1+\varepsilon)} \sin \phi_S F_{UT}^{\sin \phi_S} + \sqrt{2\varepsilon(1+\varepsilon)} \sin(2\phi_h - \phi_S) F_{UT}^{\sin(2\phi_{2h}-\phi_S)} \right] \\
& + |\mathbf{S}_{\perp}| \lambda_e \left[\sqrt{1-\varepsilon^2} \cos(\phi_{2h} - \phi_S) F_{LT}^{\cos(\phi_{2h}-\phi_S)} + \sqrt{2\varepsilon(1-\varepsilon)} \cos \phi_S F_{LT}^{\cos \phi_S} \right. \\
& + \left. \left. \sqrt{2\varepsilon(1-\varepsilon)} \cos(2\phi_{2h} - \phi_S) F_{LT}^{\cos(2\phi_{2h}-\phi_S)} \right] \right\}, \tag{8.1}
\end{aligned}$$

where

$$\varepsilon = \frac{1 - y - \frac{1}{4}\gamma^2 y^2}{1 - y + \frac{1}{2}y^2 + \frac{1}{4}\gamma^2 y^2}. \tag{8.2}$$

As the target was transversely polarised and the beam was also polarised all eight terms with \mathbf{S}_{\perp} should be taken into consideration. It will be shown later (see Equation (8.10)) the expression for the number of events is integrated with a weight containing the Siverson modulation $\sin(\phi_{2h} - \phi_S)$. The other seven modulations are orthogonal and therefore can be neglected. The orthogonality has been tested during the systematic studies (see Section 9.8). The amplitudes in the Siverson modulation are given by [119]:

$$\begin{aligned}
F_{UT,T}^{\sin(\phi_{2h}-\phi_S)} &= \sum_q e_q^2 \int d^2\mathbf{k}_T d^2\mathbf{p}_T \delta^2\left(\mathbf{k}_T - \mathbf{p}_T - \frac{\mathbf{p}_{2h\perp}}{z}\right) \\
&\quad \times \frac{|\mathbf{k}_T|}{M} f_{1T}^{\perp}(x, \mathbf{k}_T) D_1(z, M_{2h}, |\mathbf{p}_T|) \cos(\phi_k - \phi_{2h}), \tag{8.3} \\
F_{UT,L}^{\sin(\phi_{2h}-\phi_S)} &= 0
\end{aligned}$$

where \mathbf{k} denotes the parton momentum in the distribution functions, \mathbf{p} the parton momentum occurring in the fragmentation functions, while \mathbf{p}_{2h} refers to the final hadron momentum. The Siverson function f_{1T}^{\perp} is convoluted with the unpolarised two-hadron fragmentation function D_1 .

8.3 The weighted method for gluon Sivers asymmetry extraction

Let us define the two hadron Sivers asymmetry by

$$A_T^{2h}(\phi_{Siv}) = \frac{d^8\sigma^\uparrow(\phi_{Siv}) - d^8\sigma^\downarrow(\phi_{Siv})}{d^8\sigma^\uparrow(\phi_{Siv}) + d^8\sigma^\downarrow(\phi_{Siv})}. \quad (8.4)$$

Here $\phi_{Siv} = \phi_{2h} - \phi_S$. Then the number of events in a ϕ_{Siv} bin is given by

$$N(\vec{x}, \phi_{Siv}) = \alpha(\vec{x}, \phi_{Siv}) \left(1 + f(\vec{x}) P_t A_T^{2h}(\vec{x}, \phi_{Siv}) \right), \quad (8.5)$$

where $\vec{x} = (x_{Bj}, Q^2, p_{T1}, p_{T2}, z_1, z_2)$. Throughout this Section only Sivers modulation will be taken into account:

$$N(\vec{x}, \phi_{Siv}) = \alpha(\vec{x}, \phi_{Siv}) (1 + f(\vec{x}) P_t A_{Siv}(\vec{x}) \sin \phi_{Siv}). \quad (8.6)$$

In the LO approximation it is possible to decompose the asymmetry defined in Equation (8.4):

$$\begin{aligned} A_T^{2h}(\phi_{Siv}) &= \frac{\Delta\sigma}{\bar{\sigma}}(\phi_{Siv}) \\ &= \frac{\bar{\sigma}_{PGF}}{\bar{\sigma}}(\phi_{Siv}) \frac{\Delta\sigma_{PGF}}{\bar{\sigma}_{PGF}}(\phi_{Siv}) + \frac{\bar{\sigma}_{QCDC}}{\bar{\sigma}}(\phi_{Siv}) \frac{\Delta\sigma_{QCDC}}{\bar{\sigma}_{QCDC}}(\phi_{Siv}) + \frac{\bar{\sigma}_{LP}}{\bar{\sigma}}(\phi_{Siv}) \frac{\Delta\sigma_{LP}}{\bar{\sigma}_{LP}}(\phi_{Siv}) \quad (8.7) \\ &= R_{PGF}(\phi_{Siv}) A_{PGF}^{2h}(\phi_{Siv}) + R_{QCDC}(\phi_{Siv}) A_{QCDC}^{2h}(\phi_{Siv}) + R_{LP}(\phi_{Siv}) A_{LP}^{2h}(\phi_{Siv}). \end{aligned}$$

Here $R_j = \bar{\sigma}_j/\bar{\sigma}$ is the fraction of each process j in a given data sample. It has been checked on Monte Carlo data produced with the LEPTO generator ([63]) that the fractions R_i do not depend on ϕ_{Siv} (Figure 8.3). Furthermore, it is assumed that the raw asymmetries are small. Hence, the Sivers asymmetry given in Equation (8.6) can be decomposed into asymmetries of the sub-processes:

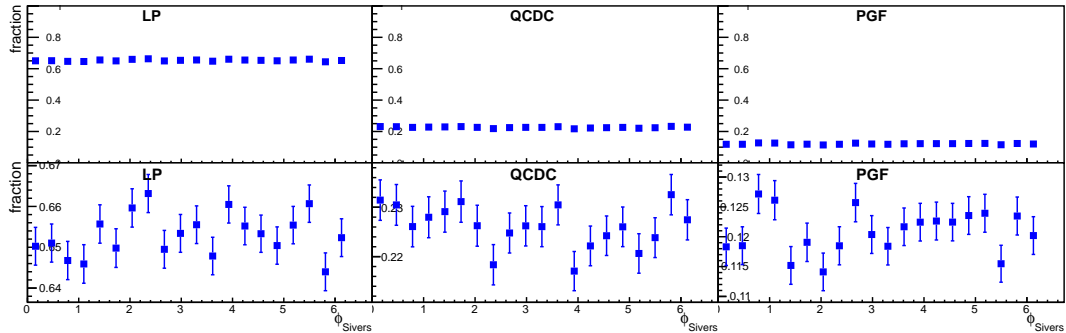


FIGURE 8.3: Monte Carlo simulation of the dependence of process fraction on the Sivers angle for the high- p_T hadron pair sample. The lower row is in larger scales.

$$A_{Siv} = R^{PGF} A_{Siv}^{PGF} + R^{QCDC} A_{Siv}^{QCDC} + R^{LP} A_{Siv}^{LP}. \quad (8.8)$$

Using Equation (8.8) and introducing $\beta_t^j(\phi_{Siv}) = R_j f P_T \sin \phi_{Siv}$ one can rewrite Equation (8.6):

$$N_t(\vec{x}, \phi_{Siv}) = \alpha_t(\vec{x}, \phi_{Siv}) \left(1 + \beta_t^{PGF}(\vec{x}, \phi_{Siv}) A_{Siv}^{PGF}(\vec{x}) + \beta_t^{QCDC}(\vec{x}, \phi_{Siv}) A_{Siv}^{QCDC}(\vec{x}) + \beta_t^{LP}(\vec{x}, \phi_{Siv}) A_{Siv}^{LP}(\vec{x}) \right), \quad (8.9)$$

which is similar to Equation (6.53). For each process weight is introduced chosen to be $\omega^j \equiv \beta^j / P_T$ which optimises the statistical and systematic error.

$$\begin{aligned} p_t^j &= \int d\vec{x} d\phi_{Siv} \omega^j(\vec{x}, \phi_{Siv}) N_t(\vec{x}, \phi_{Siv}) = \sum_{i=1}^{N_t} \omega_i^j \\ &= \tilde{\alpha}_t^j \left(1 + \langle \beta_t^{PGF} \rangle_{\omega^j} \langle A_{Siv}^{PGF}(\vec{x}) \rangle_{\beta_t^{PGF} \omega^j} + \langle \beta_t^{QCDC} \rangle_{\omega^j} \langle A_{Siv}^{QCDC}(\vec{x}) \rangle_{\beta_t^{QCDC} \omega^j} \right. \\ &\quad \left. + \langle \beta_t^{LP} \rangle_{\omega^j} \langle A_{Siv}^{LP}(\vec{x}) \rangle_{\beta_t^{LP} \omega^j} \right), \end{aligned} \quad (8.10)$$

where

$$\langle \beta \rangle = \frac{\int \beta \omega \alpha d\vec{x}}{\int \omega \alpha d\vec{x}} \approx \frac{\sum \beta \omega}{\sum \omega} \quad (8.11)$$

is the weighted mean and

$$\tilde{\alpha} = \int \alpha \omega d\vec{x} \quad (8.12)$$

is the integrated acceptance. Also linearity of A^j in x is assumed like in Section 6.1,

$$\langle A(\vec{x}) \rangle_{\beta \omega} = \langle A(\langle x \rangle, \vec{x}) \rangle_{\beta \omega} \equiv A(\langle x \rangle). \quad (8.13)$$

It can be also checked (see Appendix B) that

$$\begin{aligned} \langle x_g \rangle_{\omega^{PGF} \beta^{PGF}} &\approx \langle x_g \rangle_{\omega^{QCDC} \beta^{PGF}} \approx \langle x_g \rangle_{\omega^{LP} \beta^{PGF}} \equiv \langle x_g \rangle, \\ \langle x_C \rangle_{\omega^{PGF} \beta^{QCDC}} &\approx \langle x_C \rangle_{\omega^{QCDC} \beta^{QCDC}} \approx \langle x_C \rangle_{\omega^{LP} \beta^{QCDC}} \equiv \langle x_C \rangle, \\ \langle x_{Bj} \rangle_{\omega^{PGF} \beta^{LP}} &\approx \langle x_{Bj} \rangle_{\omega^{QCDC} \beta^{LP}} \approx \langle x_{Bj} \rangle_{\omega^{LP} \beta^{LP}} \equiv \langle x_{Bj} \rangle. \end{aligned} \quad (8.14)$$

Then Equation (8.10) with the use of Equations (8.13) and (8.14) can be rewritten in the form

$$\begin{aligned} p_t^j &= \sum_{i=1}^{N_t} \omega_i^j = \tilde{\alpha}_t^j \left(1 + \{ \beta_t^G \}_{\omega^j} A_{PGF}^{\phi_{Siv}}(\langle x_g \rangle) \right. \\ &\quad \left. + \{ \beta_t^{QCDC} \}_{\omega^j} A_{QCDC}^{\phi_{Siv}}(\langle x_C \rangle) + \{ \beta_t^{LP} \}_{\omega^j} A_{LP}^{\sin(\phi_{2h} - \phi_s)}(\langle x_{Bj} \rangle) \right). \end{aligned} \quad (8.15)$$

In order to avoid the integrated acceptance defined in Equation (8.12) and the denominator in Equation (8.11) from approaching zero binning in ϕ_{Siv} is introduced. Two bins $(\phi_{Siv}^I, \phi_{Siv}^{II}) = ([0, \pi], [\pi, 2\pi])$ have been applied assuming $A_I^j = A_{II}^j$. With the use of the constraint on integrated asymmetries in each bin

$$\frac{\tilde{\alpha}_u \tilde{\alpha}_{d'}}{\tilde{\alpha}_{u'} \tilde{\alpha}_d} = 1 \quad (8.16)$$

a set of 24 equations for 21 unknowns is obtained. It is much easier to make a fit with smaller number of parameters to use the double ratio method:

$$r^j := \frac{p_u^j p_{d'}^j}{p_{u'}^j p_d^j}. \quad (8.17)$$

In this way the integrated acceptances cancel out and a set of six equations for three unknowns is obtained. It can then be solved by fitting procedure of χ^2 minimisation,

$$\chi^2 = (\vec{R} - \vec{L})^T [prop(12, 3)^T Cov(12, 12) prop(12, 3)]^{-1} (\vec{R} - \vec{L}). \quad (8.18)$$

Vectors \vec{R} and \vec{L} are defined by right hand side and left hand side of Equations (8.17). The former contains the asymmetries - parameters of the fit, while the latter is given by the measured values of ω_i^j . The $Cov(12, 12)$ matrix elements refer to correlations between pairs of p_t^j defined in Equation (8.15) and can be approximated by $Cov(p_x, p_y) \approx \sum_{N_t} \omega_x \omega_y$ given by Equation (6.60). The propagation matrix $prop(12, 3)$ is given by $prop(m, n) = \partial r_n / \partial p_m$.

As discussed in Section 8.1 there is a p_T dependence of the measured Siverts asymmetries which seems to be connected to the fragmentation process. To calculate how strong this dilution is a fragmentation model has to be used. To keep the results independent of this model a high- p_T region has been selected where the asymmetries ($A_{PGF}, A_{QCDC}, A_{LP}$) seem to be constant. The asymmetries A^{LP} and A^{QCDC} should be equal on the "parton level" but not necessarily on the measured hadron level. Therefore the constraint used in the all- p_T $\Delta g/g$ between the asymmetries of the LP and QCDC process cannot be applied here. In the same time p_T range needs to be sufficiently large to have a wide range of the processes fractions in the bin. Taking all this into consideration it has been chosen to perform the analysis in a single p_T bin. Due to the small statistics also only a single x bin is applied.

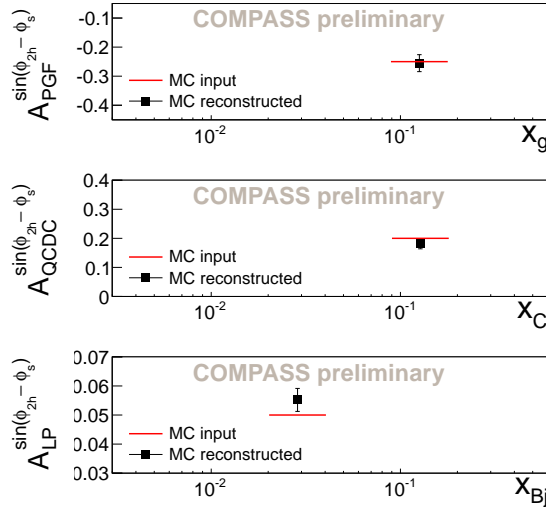


FIGURE 8.4: Validation of the analysis method. Exemplary plot. $A_{PGF}^{SIM} = -0.25$, $A_{QCDC}^{SIM} = 0.2$, $A_{LP}^{SIM} = 0.05$.

8.3.1 Analysis method test on a Monte Carlo sample

To validate the method we generate MC events. Each event is tagged with the label of the process (LP, QCDC, PGF) which was used to generate given event. Then every event is weighted by $1 + A_i^{SIM} \sin(\phi_{2h} - \phi_S)$, where i labels the process which is known in MC. We put the simulated asymmetries ($A_{PGF}^{SIM}, A_{QCDC}^{SIM}, A_{LP}^{SIM}$) to constant values. To such weighted MC sample we apply the described method of asymmetry extraction expecting to get $A_i^{extracted} \simeq A_i^{SIM}$. An exemplary result is shown in Fig. 8.4. The red lines indicate the simulated values and the points represent the extracted ones.

8.4 Results

8.4.1 Deuteron target

The data collected with the transversely polarised target are not large in statistics. It has been divided into three periods, namely "P1H-P1G", "W33-W34", "W36-W35". Each period contains four target configurations $t = u, d, u', d'$. The results are presented in Figure 8.5.

The final result is obtained by

$$A_{final} = \frac{\sum_{i=1}^3 \frac{A_i}{\sigma_i^2}}{\sum_{i=1}^3 \frac{1}{\sigma_i^2}}, \quad \sigma_{final}^2 = \frac{1}{\sum_{i=1}^3 \frac{1}{\sigma_i^2}} \quad (8.19)$$

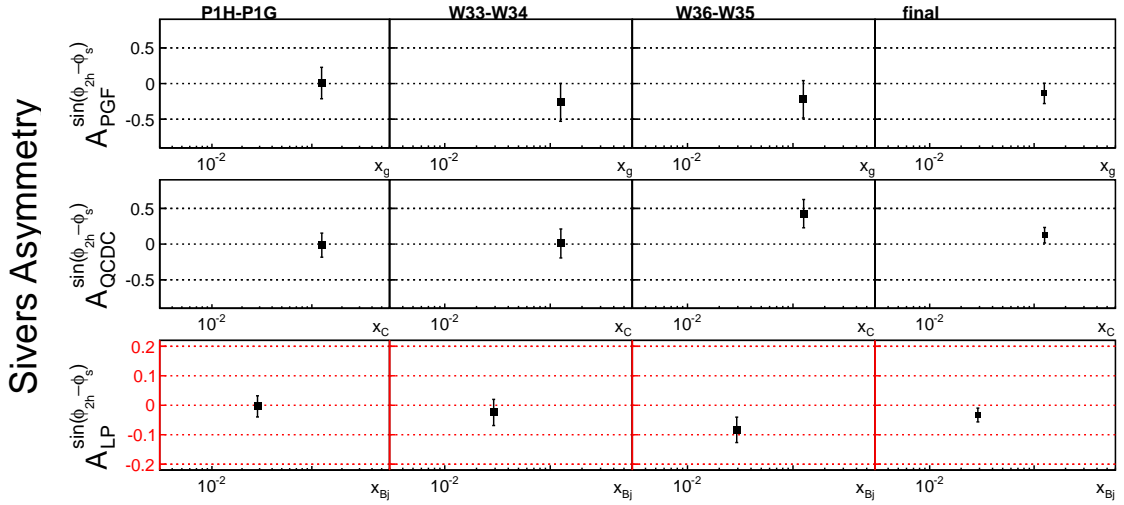


FIGURE 8.5: Period-by-period results for Siverts asymmetry of three processes: PGF, QCDC, LP. Deuteron target.

and it reads

$$\begin{aligned}
 \mathbf{A}_{\text{PGF},d}^{\text{Siv}} &= -0.14 \pm 0.15(\text{stat.}), \\
 A_{\text{QCDC},d}^{\text{Siv}} &= 0.12 \pm 0.11(\text{stat.}), \\
 A_{\text{LP},d}^{\text{Siv}} &= -0.033 \pm 0.024(\text{stat.}).
 \end{aligned}
 \tag{8.20}$$

$A_{\text{PGF},d}^{\text{Siv}}$ has been obtained at $\langle x_g \rangle = 0.13$ and at scale $\mu^2 = 3 \text{ GeV}^2$.

8.4.2 Proton target

Most of the COMPASS data with transversely polarised target has been collected in 2010 with the proton (NH_3) target. The data has been grouped into twelve periods each containing all target configuration. The three cell target is treated in the following way: the upstream and downstream cells are joined together and labelled by $u(u')$ as they have the same sign of polarisation. The central cell is labelled by $d(d')$. The positive polarisation (u, d) is chosen to point up. Results period-by-period together with the final results are shown in Figure 8.6.

$$\begin{aligned}
 \mathbf{A}_{\text{PGF},p}^{\text{Siv}} &= -0.26 \pm 0.09(\text{stat.}), \\
 A_{\text{QCDC},p}^{\text{Siv}} &= 0.13 \pm 0.05(\text{stat.}), \\
 A_{\text{LP},p}^{\text{Siv}} &= 0.34 \pm 0.012(\text{stat.}).
 \end{aligned}
 \tag{8.21}$$

$A_{\text{PGF},p}^{\text{Siv}}$ has been obtained at $\langle x_g \rangle = 0.15$ and at scale $\mu^2 = 3 \text{ GeV}^2$.

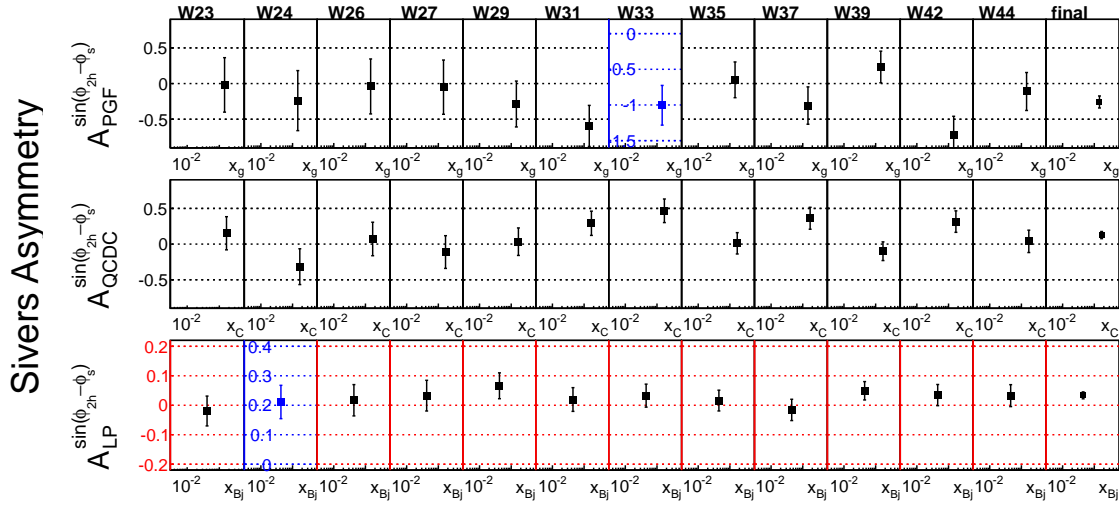


FIGURE 8.6: Period-by-period results for Sivers asymmetry of three processes: PGF, QCDC, LP. Proton target 2010.

The final results read:

8.4.3 Interpretation of statistical errors

The results given in the previous section are obtained with a three-parameter fit. The errors given above are the diagonal of the error matrix. The period-by-period distribution gives for deuteron:

$$\begin{aligned}
 \chi_{PGF}^2/ndf &= 0.76, & prob_{\chi^2} &= 0.86, \\
 \chi_{QCDC}^2/ndf &= 3.3, & prob_{\chi^2} &= 0.34, \\
 \chi_{LP}^2/ndf &= 2.1, & prob_{\chi^2} &= 0.56
 \end{aligned}
 \tag{8.22}$$

and for proton:

$$\begin{aligned}
 \chi_{PGF}^2/ndf &= 19.6, & prob_{\chi^2} &= 0.08, \\
 \chi_{QCDC}^2/ndf &= 17.5, & prob_{\chi^2} &= 0.13, \\
 \chi_{LP}^2/ndf &= 14.1, & prob_{\chi^2} &= 0.29.
 \end{aligned}
 \tag{8.23}$$

The results both for deuteron and for proton are compatible and thus can be merged in one data sample for each target. The results obtained with this method for deuteron are the following

$$\begin{aligned}
 A_{PGF,d}^{Siv} &= -0.13, \\
 A_{QCDC,d}^{Siv} &= 0.13, \\
 A_{LP,d}^{Siv} &= -0.035,
 \end{aligned}
 \tag{8.24}$$

with the error matrix

$$\left(\frac{1}{2} \frac{\partial^2 \chi^2}{\partial A^j \partial A^k} \right)^{-1} = \begin{pmatrix} 0.0198 & -0.0116 & -0.0006 \\ -0.0116 & 0.0115 & -0.0009 \\ -0.0006 & -0.0009 & 0.0005 \end{pmatrix}, \tag{8.25}$$

where $j, k = PGF, QCDC, LP$. Similar results for proton

$$\begin{aligned} A_{PGF,p}^{Siv} &= -0.26, \\ A_{QCDC,p}^{Siv} &= 0.12, \\ A_{LP,p}^{Siv} &= 0.035, \end{aligned} \tag{8.26}$$

with the error matrix

$$\left(\frac{1}{2} \frac{\partial^2 \chi^2}{\partial A^j \partial A^k} \right)^{-1} = \begin{pmatrix} 0.0070 & -0.0032 & -0.0006 \\ -0.0032 & 0.0025 & -0.0002 \\ -0.0001 & -0.0002 & 0.0001 \end{pmatrix}. \tag{8.27}$$

The naive expectation is that gluons are flavour-blind and the results obtained for deuteron and proton target could be combined. It should be taken into account that gluons originate from quarks of different flavours and this could influence the collective orbital motion of gluons differently for protons and neutrons. The two results are statistically compatible with each other but the uncertainties are rather large. The obtained precision does not authorise a conclusion that the Sivers effect for gluons is the same for deuteron and proton targets.

8.5 Results with the Unbinned Maximum Likelihood method

This analysis can be also performed with the use of the maximum likelihood method. Figures 8.7 and 8.8 show that there is practically no difference between the weighted method presented in this note and the maximum likelihood method. The difference in the final A_{PGF} is 0.008 that is 6% of σ_{stat} for deuteron and 0.004 that is 5% of σ_{stat} for proton. The difference is only due to use of different estimator so no systematic error due to the choice of statistical method is assigned.

8.6 COMPASS 2007 data set from transversely polarised protons

In 2007 COMPASS has dedicated part of the data taking run to measurements on transversely polarised proton target. The statistics of this data set is around 25% of the statistics collected during 2010 run. The problems with the agreement with the Monte Carlo simulation and collected data for the 2007 sample disables a proper systematic studies for different MC settings. Therefore only an estimation of the possible influence of this data sample has been made. The results, with the use of a MC simulation with

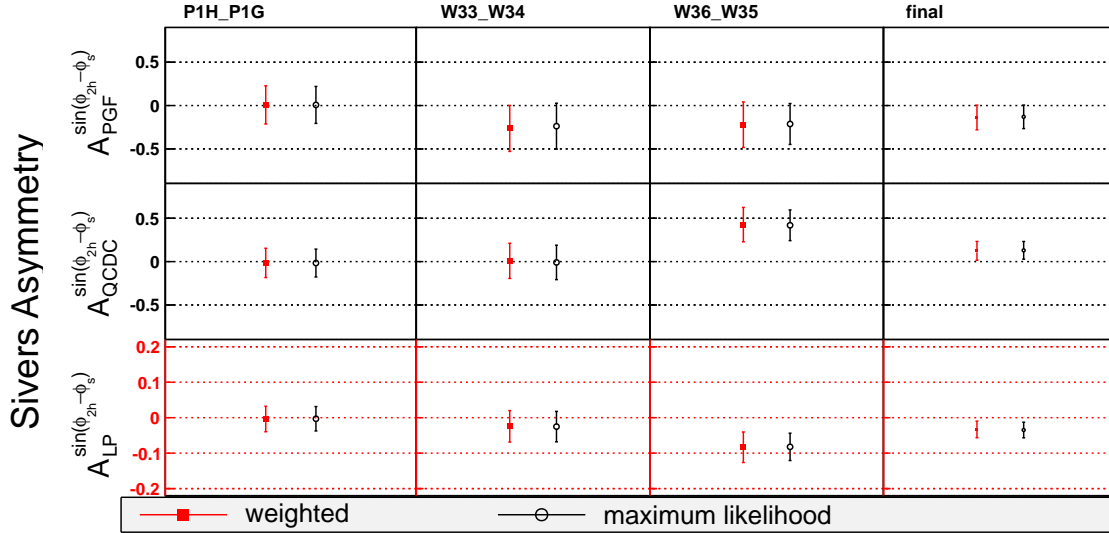


FIGURE 8.7: Weighted method vs maximum likelihood method. Deuteron.

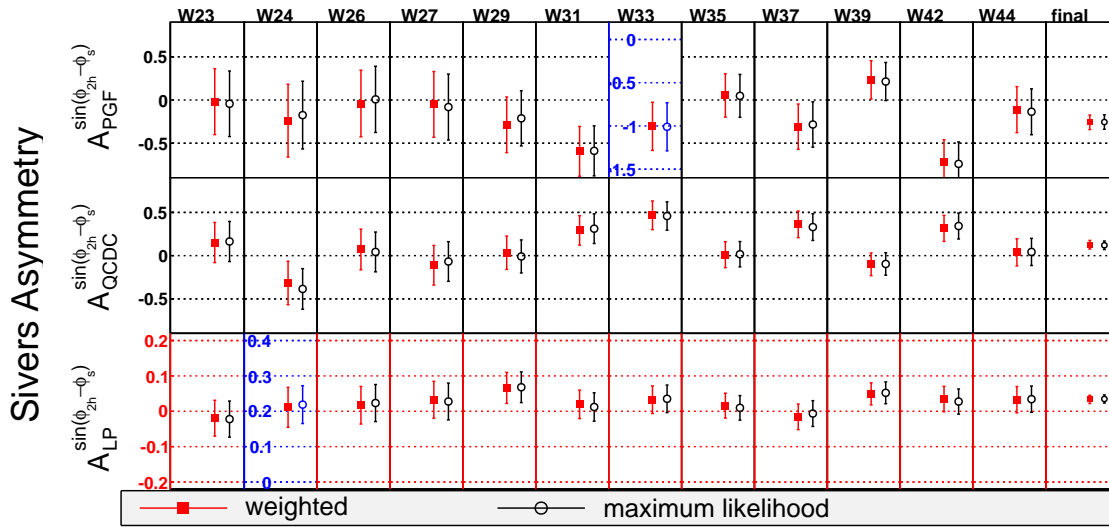


FIGURE 8.8: Weighted method vs maximum likelihood method. Proton.

satisfactory agreement with the data, are shown in Figure 8.9. The final results for the 2007 data sample are the following

$$\begin{aligned}
 A_{PGF,p} &= -0.13 \pm 0.13, \\
 A_{QCDC,p} &= 0.12 \pm 0.09, \\
 A_{LP,p} &= 0.001 \pm 0.018.
 \end{aligned}
 \tag{8.28}$$

The results are different but statistically compatible with the results obtained for the 2010 data sample (Equation (8.21)). Combining the two results for $A_{PGF,p}$ gives

$$A_{PGF,p} = -0.24 \pm 0.08,
 \tag{8.29}$$

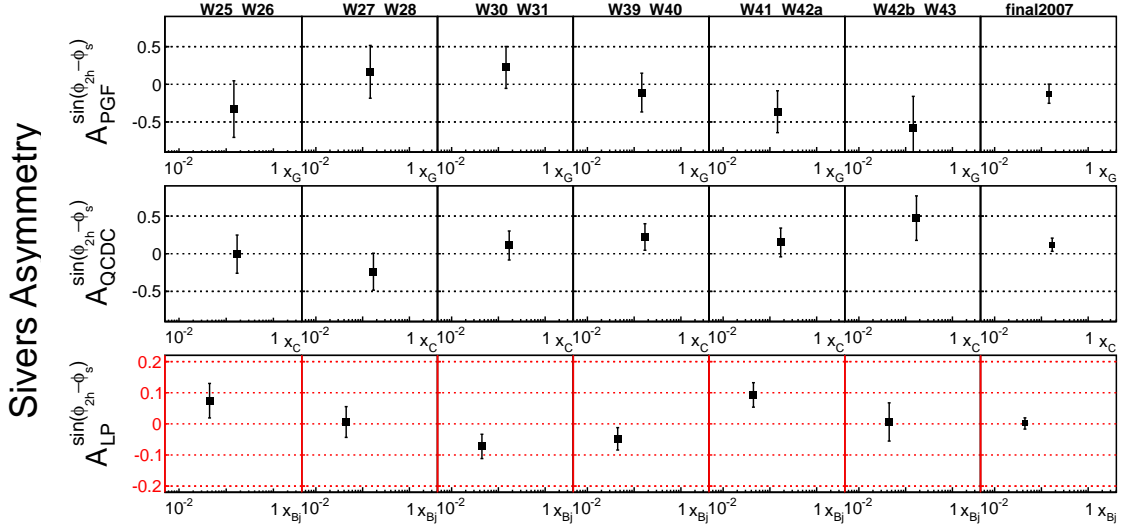


FIGURE 8.9: Period-by-period results for Sivers asymmetry of three processes: PGF, QCDC, LP. Proton target 2007.

what only slightly differs from the result for the 2010 data sample and hence 2007 data can be neglected in the further studies.

8.7 The gluon Sivers asymmetry measurement via J/Ψ production at COMPASS

The Sivers asymmetry in J/Ψ production in scattering of muons off transversely polarised protons $\mu^+ + p^\uparrow \rightarrow \mu' + J/\Psi + X$ is measured in two z -bins in the COMPASS 2010 data. 480 726 suitable events with outgoing $2\mu^+1\mu^-$ are selected, of which 8 026 $\mu^+\mu^-$ pairs with invariant mass compatible with $M_{J/\Psi}$ are made. The Sivers asymmetry is extracted using a simple double-ratio method and is found compatible with zero in the lower z bin and with a slight preference for negative value in the higher z bin.

8.7.1 Event selection

The 2010 data has been preselected with the following conditions:

- defined best interaction vertex,
- 3 outgoing particles identified as muons (plus any other outgoing particles not identified as muons)
- a scattered muon identified by the iMuPrim PHAST function ([105])

The further selection contain more detailed cuts:

- There is a beam particle in the vertex.
- There are at least 3 outgoing particles in the vertex.
- The beam track obeys $\chi^2/N_{df} < 10$.
- The beam muon momentum \vec{k} was measured and $k \in [140, 180]$ GeV.
- The beam track projection crosses both the most upstream and the most downstream end of the target cells.
- There are at least $2\mu^+$ and $1\mu^-$ among the outgoing particles. A muon identification is positive, if it
 - has crossed more than 30 radiation lengths,
 - last detection is behind Muon Wall 1 ($Z_{\text{last}} > 1495$ cm).

8.7.2 J/Ψ candidate selection

First few more conditions are checked:

- The event does not come from a bad spill (using a list produced for the SIDIS analysis, usually done already by Phast call).
- There are at least two μ^+ and one μ^- and not more 5 (but there can be any other particles).
- The outgoing muon tracks obey $\chi^2/N_{df} < 10$.

It is not possible to tell which one of the two μ^+ comes from the J/Ψ decay and which one is the scattered beam muon, so both possibilities are examined. For each combination the kinematic variables Q^2, x, z and $M_{\mu\mu}$ are calculated. Then:

- The variable z is checked to be in one of the two bins: $[0.3, 0.95]$, or $[0.95, 1.05]$.
- The invariant mass of the pair $M_{\mu\mu}$ is checked to be in $[2.999, 3.239]$ GeV (signal band, corresponds to $M_{J/\Psi} \pm 2\sigma$, where $M_{J/\Psi}$ and σ are parameters of the invariant mass fit) or in $[2.579, 2.939] \cup [3.299, 3.659]$ GeV (side-bands).

Cut	Events
Events after preselection	839 450
Beam track χ^2/N_{df}	827 424
$k \in [140, 180]$ GeV	770 421
One μ^- and two μ^+	483 940
Muon track $\chi^2/N_{df} < 10$	480 726
Both muon combinations	961 452
Vertex in cells	795 072
$z \in [0.3, 1.05]$	736 264
$M_{\mu\mu} \in [2.999, 3.239]$ GeV	8026
Or $M_{\mu\mu}$ in side-bands	4784

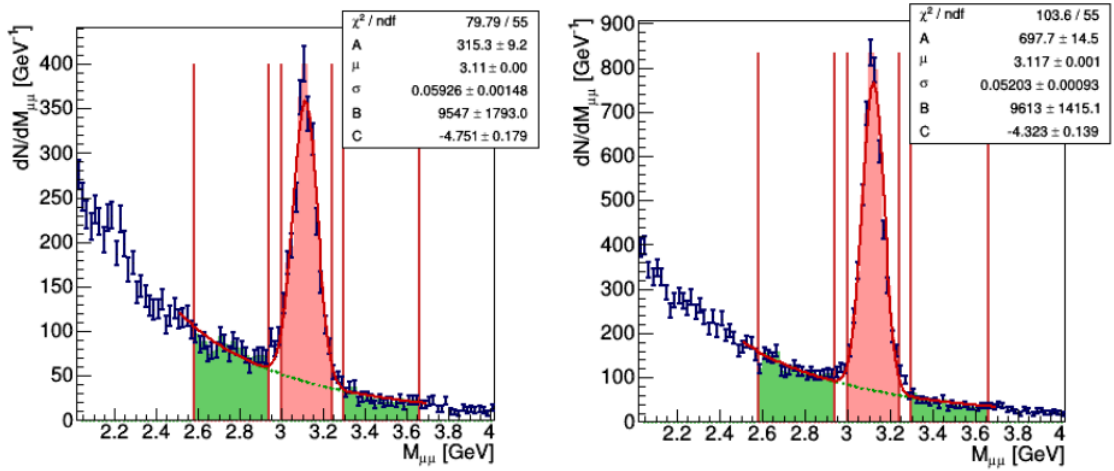
TABLE 8.3: Effect of cuts for the J/Ψ events selection

FIGURE 8.10: Dimuon invariant mass in the two z -intervals. The boundaries of the side-bands and the signal band are denoted by vertical red lines. The red fit to the data is the normal distribution plus background in the form $AN(M_{\mu\mu}, \mu, \sigma) + BM_{\mu\mu}^C$.

The dotted green line is the background estimation $BM_{\mu\mu}^C$.

The statistics after each cut is presented in Table 8.3.

The invariant mass distributions are shown in Figure 8.10 separately for the two z -bins together with the boundaries of the signal band and two side-bands, which are used to evaluate the asymmetry of the background. The good agreement of the centre and the width of the measured peak with the PDG reference ([28]) authorises the assumption that entries in the histograms that come from wrong choice of the scattered muon distribute in the same way as the physics background. Their can be treated as the physics background under a justified assumption that both physics and "wrong choice" background asymmetries are the same.

8.7.3 The Sivers asymmetry evaluation

The Sivers asymmetry is again the amplitude of the modulation $\sin(\phi_{p_T} - \phi_S)$, where p_T is the transverse (with respect to the virtual photon) momentum of the reconstructed J/Ψ . The asymmetry is evaluated by a simple method, where the histograms of counts in the cells are measured $N_t(\phi_i)$, ($t = ud, c, ud', c'$) with eight bins in the Sivers angle ϕ are combined to form a double-ratio:

$$A_{Siv}(\phi) = \frac{N_{ud}(\phi)N_{c'}(\phi)}{N_{ud'}(\phi)N_c(\phi)}. \quad (8.30)$$

The double ratio then should follow the formula

$$A_{Siv}(\phi) = C(1 + 4A_{Siv}^{raw} \sin \phi), \quad (8.31)$$

where A_{Siv}^{raw} is the raw Sivers asymmetry. A small correction due to the finite (but constant) bin width is applied, because the mean values of the expected distribution in the bins are different from the values at the bin centre. Therefore, instead of Equation (8.31), the bin contents follow a distribution of its mean values. For an i -th bin with width w and centre at ϕ_i it is

$$\langle A_{Siv(\phi)} \rangle_i = \frac{1}{w} \int_{\phi_i - w/2}^{\phi_i + w/2} A_{Siv}(\phi) d\phi = C \left(1 + \frac{8}{w} \sin(\omega/2) A_{Siv}^{raw} \sin \phi_i \right). \quad (8.32)$$

This function is fitted using a standard ROOT graph-fitting procedure. The asymmetry is calculated period-by-period and then an error-weighted mean is calculated:

$$A_{final} = \frac{\sum_{i=1}^{12} \frac{A_i}{\sigma_i^2}}{\sum_{i=1}^{12} \frac{1}{\sigma_i^2}}, \quad \sigma_{final}^2 = \frac{1}{\sum_{i=1}^{12} \frac{1}{\sigma_i^2}}. \quad (8.33)$$

8.7.4 Background subtraction

It is assumed that the asymmetry measured in the signal band A_{Siv}^{raw} gets contribution from the real asymmetry $A_{Siv}^{raw}|_{sig}$ and the asymmetry of the background $A_{Siv}^{raw}|_{bg}$ weighted by the numbers of signal and background events

$$A_{Siv}^{raw} = \frac{N_{sig}}{N_{tot}} A_{Siv}^{raw}|_{sig} + \frac{N_{bg}}{N_{tot}} A_{Siv}^{raw}|_{bg}. \quad (8.34)$$

If, in addition, one assumes the asymmetry of the background to be zero, the real asymmetry of the signal is

$$A_{Siv}^{raw}|_{sig} = \frac{N_{tot}}{N_{sig}} A_{Siv}^{raw}. \quad (8.35)$$

In this model, the background just dilutes the asymmetry of the signal. The asymmetry measured in the side-bands is indeed consistent with this assumption.

Another option is to assume that the background asymmetry is the same as the side-band asymmetry, then one can subtract it as

$$A_{Siv}^{raw}|_{sig} = \frac{N_{tot}}{N_{sig}} A_{Siv}^{raw} - \frac{N_{bg}}{N_{sig}} A_{Siv}^{raw}|_{side}. \quad (8.36)$$

In both cases one needs to know the number of signal and background events. The N_{tot} is obtained integrating the fit of the invariant mass peak

$$AN(M_{\mu\mu}, \mu, \sigma) + BM_{\mu\mu}^C \quad (8.37)$$

over the signal region ($N(x, \mu, \sigma)$ being the normal distribution). The N_{bg} is calculated integrating just the background term $B(M_{\mu\mu})^C$. This is done separately for the two z bins, since the signal-to-background ratios differ significantly (Figure 8.10). The signal to background and signal to total ratios were calculated to be $N_{sig}/N_{bg} = 4.31$, $N_{sig}/N_{tot} = 0.81$ for the first bin in z and $N_{sig}/N_{bg} = 5.25$, $N_{sig}/N_{tot} = 0.84$ for the second. The errors of the numbers of events are considered small with respect to the errors of the asymmetries and are not taken into account when propagating the errors through Equations (8.35) or (8.36). Both the dilution compensation and the background subtraction were applied on the weighted means, because the background is not expected to change over the year and the signal-to-background ratio can be measured more reliably using the bigger data sample.

The actual Sivers asymmetry A_{Siv} can be obtained from the raw asymmetry by division by the average target polarisation P_t and the dilution factor f

$$A_{Siv} = \frac{A_{Siv}^{raw}}{P_t f}. \quad (8.38)$$

A mean dilution factor, obtained by Phast function for every pair, is used. The value is $f = 0.15$. The average value of P_t is 0.80, The final Sivers asymmetry is in the Table 8.4 and Figure 8.11.

The results of this analysis show that the statistics of J/Ψ events in COMPASS is too

	$z \in [0.3, 0.95]$				$z \in [0.95, 1.05]$			
	A_{Siv}^{raw}	σ^{raw}	A_{Siv}	σ	A_{Siv}^{raw}	σ^{raw}	A_{Siv}	σ
Dilution compensated	-0.012	0.038	-0.11	0.32	-0.040	0.021	-0.33	0.18
Background subtracted	-0.006	0.039	-0.05	0.33	-0.034	0.021	-0.28	0.18

TABLE 8.4: Summary of the results of the gluon Sivers asymmetry extraction from J/Ψ production

small to draw any resolute conclusions. The errors in the two methods of the background treatment are similar due to the fact that the signal-to-noise ratio is large. This makes

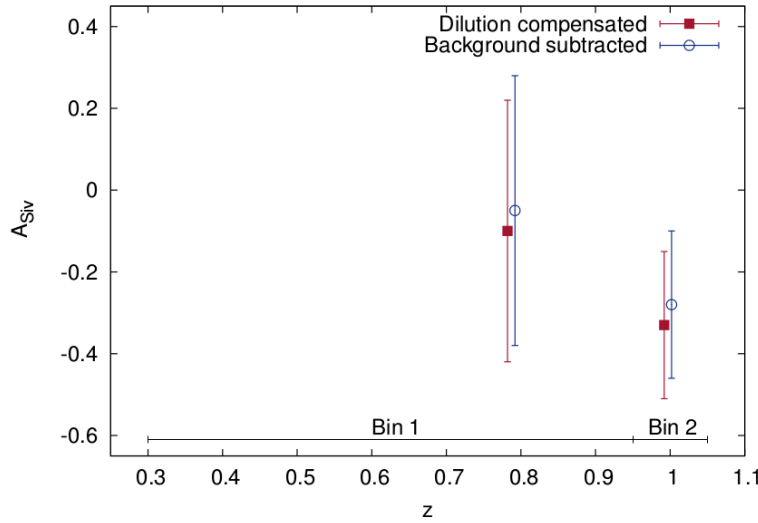


FIGURE 8.11: The final Sivers asymmetry for two methods of background treatment. The z coordinates of the points were shifted by ± 0.005 not to overlap.

it unnecessary to apply more advanced method of background subtraction presented in this thesis. The results, however, show the same tendency in the negative sign of the obtained Sivers asymmetry as in the case of semi-inclusive dihadron production.

8.8 Conclusions

The Sivers effect for gluons have been evaluated for the first time from the SIDIS data. The results were obtain from the COMPASS measurements on transversely polarised deuteron and proton targets. A novel weighted method of data analysis have been introduced and applied for the Sivers effect for gluons extraction. It has been tested with a simple Monte Carlo simulation and its final results perfectly agree with the more standard unbinned maximum likelihood method. The main results read

$$\begin{aligned} A_{\text{PGF,d}}^{\text{Siv}} &= -0.14 \pm 0.15(\text{stat.}) \pm 0.10(\text{syst.}), \\ A_{\text{PGF,p}}^{\text{Siv}} &= -0.26 \pm 0.09(\text{stat.}) \pm 0.06(\text{syst.}). \end{aligned} \quad (8.39)$$

The estimation of the systematic errors is given in the next Chapter. For both targets the results are negative. For the deuteron target the value is one σ below zero while for the proton target the value is over three σ below zero (0.257 ± 0.084). The last result seems particularly interesting and its theoretical interpretation can bring first information about the Gluon Sivers Function at the COMPASS scale.

Chapter 9

Systematic studies

9.1 Systematic error due to MC

Several different MC samples were produced for systematic studies, as in Ref. [17] differing by the choice of PDF model (CTEQ or MSTW), LEPTO tuning (default or tuned to COMPASS data), parton shower on or off, F_L from LEPTO or from the $R = \sigma_L/\sigma_T$. Namely:

1. LEPTO DEF. tuning, parton shower ON, PDF=CTEQ;
2. LEPTO DEF. tuning, parton shower OFF, PDF=MSTW;
3. LEPTO DEF. tuning, parton shower ON, PDF=MSTW;
4. LEPTO COMPASS tuning, parton shower ON, PDF=CTEQ;
5. LEPTO COMPASS tuning, parton shower OFF, PDF=MSTW;
6. LEPTO COMPASS tuning, parton shower ON, PDF=MSTW, NO FL;
7. LEPTO COMPASS tuning, parton shower ON, PDF=MSTW.

For each of them asymmetry A_{PGF} has been calculated in the same way as the final results and all of them were used in the systematics studies. The results are presented in Figure 9.1. Red colour indicates the MC used to obtain the final result. For both data sets MSTW08LO PDF table has been used. In the deuteron case CTEQ5L and in the proton case CTEQ10NLO tables have been applied.

The Monte Carlo versus data agreement is rather poor for the settings with parton shower off. This is why for the systematic error that is due to MC tuning the half of

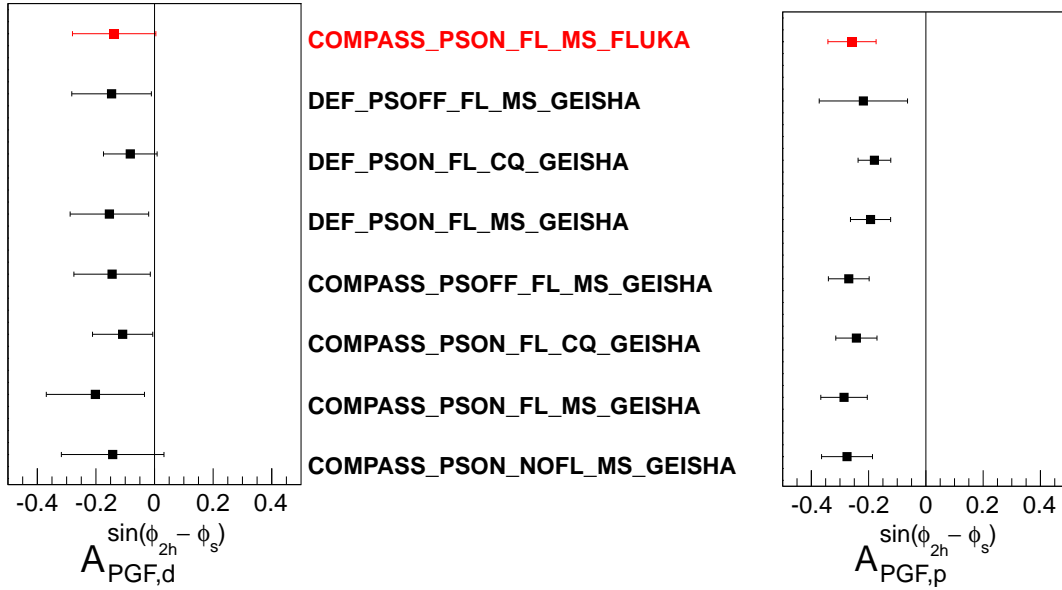


FIGURE 9.1: A_{PGF} for different MC simulations for deuteron (left) and proton (right) targets. Red colour indicates the settings used for the final results.

the maximum difference of obtained results has been chosen instead of the RMS of all results. The systematic error due to MC has been estimated to be 0.060 for deuteron and 0.054 for proton.

9.2 False asymmetries

The false asymmetries were calculated by extracting the asymmetries between the upstream and downstream cell and by dividing the central cell into 2 parts using the vertex Z coordinate. The central cell has been divided into $c_1 : Z < 2.5$ cm and $c_2 : Z > 2.5$ cm. Then A_{PGF} asymmetry was extracted between u and d and between c_1 and c_2 in the same way as it was done in the standard asymmetry extraction. In case of the two-cell target both cells were divided into two parts. The expected value is 0. The results are presented in Figures 9.2 and 9.3.

The overall final value and χ^2 for photon-gluon-fusion for deuteron is: $PGF : A_u = -0.60 \pm 0.25$, $\chi_u^2 = 6.4$, $A_d = -0.17 \pm 0.17$, $\chi_d^2 = 1.9$ and for proton $PGF : A_{ud} = -0.08 \pm 0.12$, $\chi^2(A_{ud} = 0) = 9.5$, $A_c = -0.09 \pm 0.12$, $\chi^2(A_c = 0) = 10.6$.

The second exercise is to calculate the asymmetry between upstream and downstream parts of the target cells. For the three-cell target the asymmetries between the upstream cell u and the upstream part of the central cell c_u and between the downstream part of the central cell c_d and the downstream cell d have been obtained. The results from the upstream and downstream part of the target should be compatible with each other.

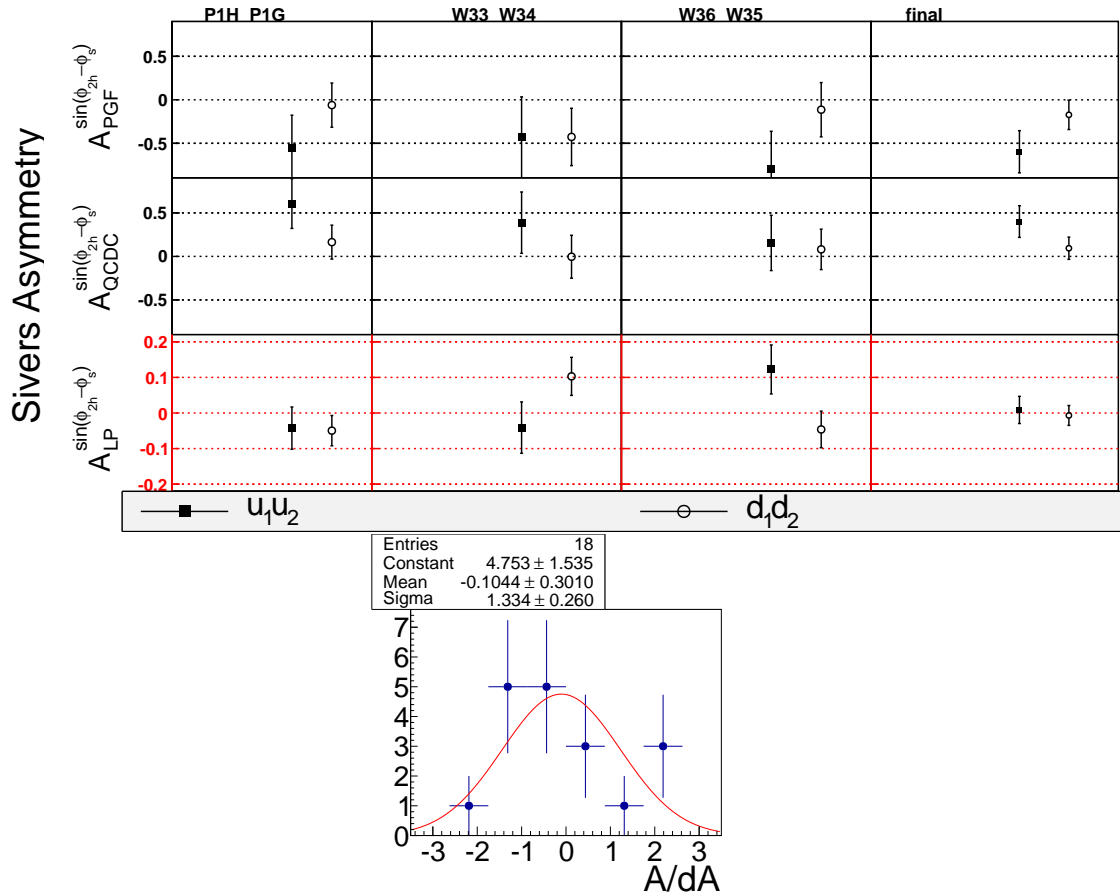


FIGURE 9.2: False asymmetries. Compatibility with zero. Deuteron.

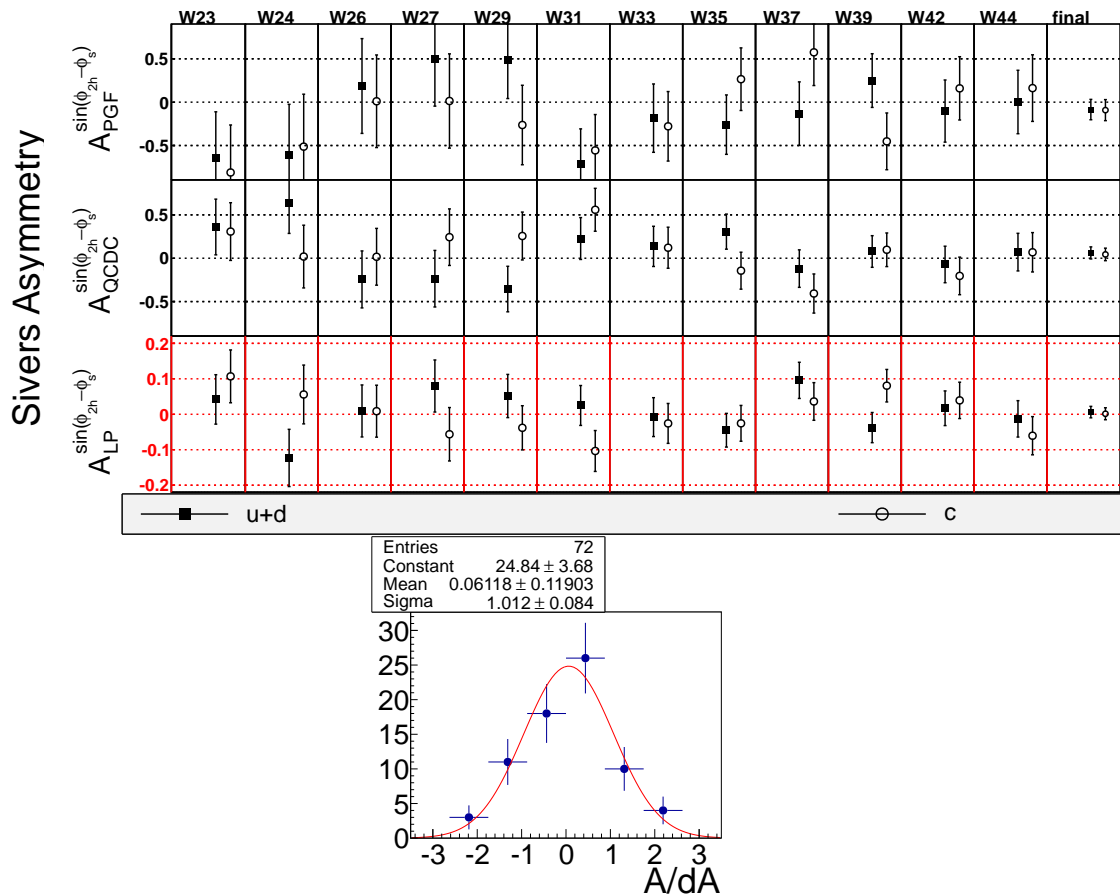


FIGURE 9.3: False asymmetries. Compatibility with zero. Proton.

They are presented in Figures 9.4 and 9.5 . In case of the deuteron the two samples differ. The obtained χ^2 between them is equal 7.0. The statistics is, however, too small to draw any conclusions. The χ^2 between the two values for PGF is 7.2 for 12 periods what means the two samples are compatible in terms of the extracted asymmetry.

9.3 Influence of the generated false asymmetry on the final result

To check the potential influence of the false asymmetry on the final result the artificial false asymmetry is generated by multiplying the weight of the one target configuration (in this case u) by a factor $1 + 0.01 \sin \phi_{Sivers}$. This factor is chosen arbitrarily but it is justified by a number of analyses carried out in COMPASS to estimate false asymmetries. The results are presented in Figure 9.6. The difference in the final A_{PGF} is for deuteron 0.016 that is 11% of σ_{stat} and for proton 0.032 that is 38% of σ_{stat} . However, due to the fact that the false asymmetries presented in Section 9.2 are compatible with zero no systematic error is assigned to this exercise as given in the summary in Table 9.1

9.4 Cut on charges of the two leading hadrons

An extra cut can be made on the leading and next-to-leading hadron charges, $q_1 \cdot q_2 = -1$ as the hadrons originate from the quark-antiquark pair. This cut reduces the statistics by 33% so it was decided not to apply it for the crosschecked result. Here a systematic error due to this cut is estimated. A new NN was trained by a MC containing the extra cut on the charges. The results are presented in Figures 9.7 and 9.8. The difference in the final A_{PGF} is 0.05 for deuteron that is 33% of σ_{stat} . For proton the estimated error is 0.038 that is 44% of σ_{stat} . The expected statistical fluctuation due to the sample reduction is on the level of 55% of σ_{stat} . No systematic error is assign to this exercise as given in Table 9.1.

9.5 Radiative corrections systematics

In this analysis a MC production for 2010 setting is used and it does not contain radiative corrections. RC can change the kinematics and therefore may have an influence on the fractions assigned by the NN. Using existing MC+RADGEN for 2006 settings a new NN has been trained. Then it was applied on the 2010 data. Results are shown in Figure 9.9. The difference in the final A_{PGF} is 0.018 that is 21% of σ_{stat} .

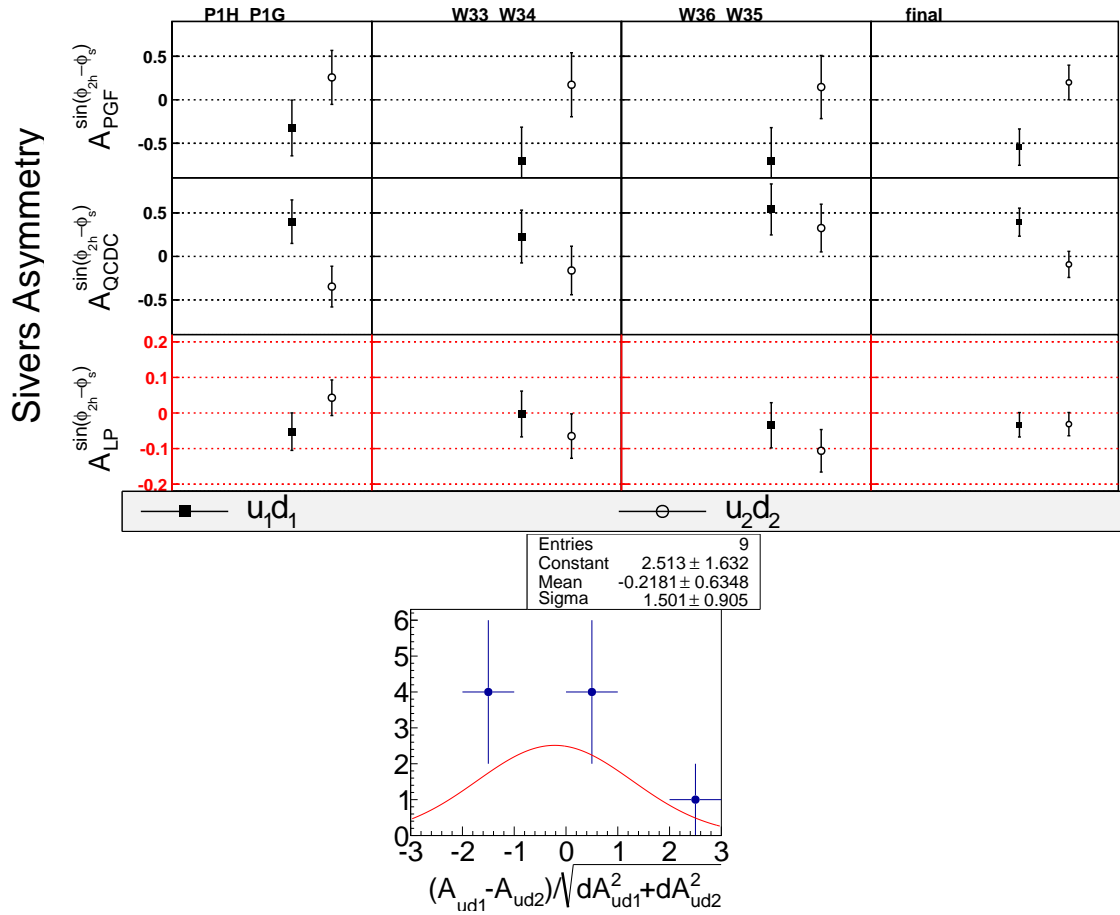


FIGURE 9.4: False asymmetries. Compatibility with between upstream and downstream part of the target.

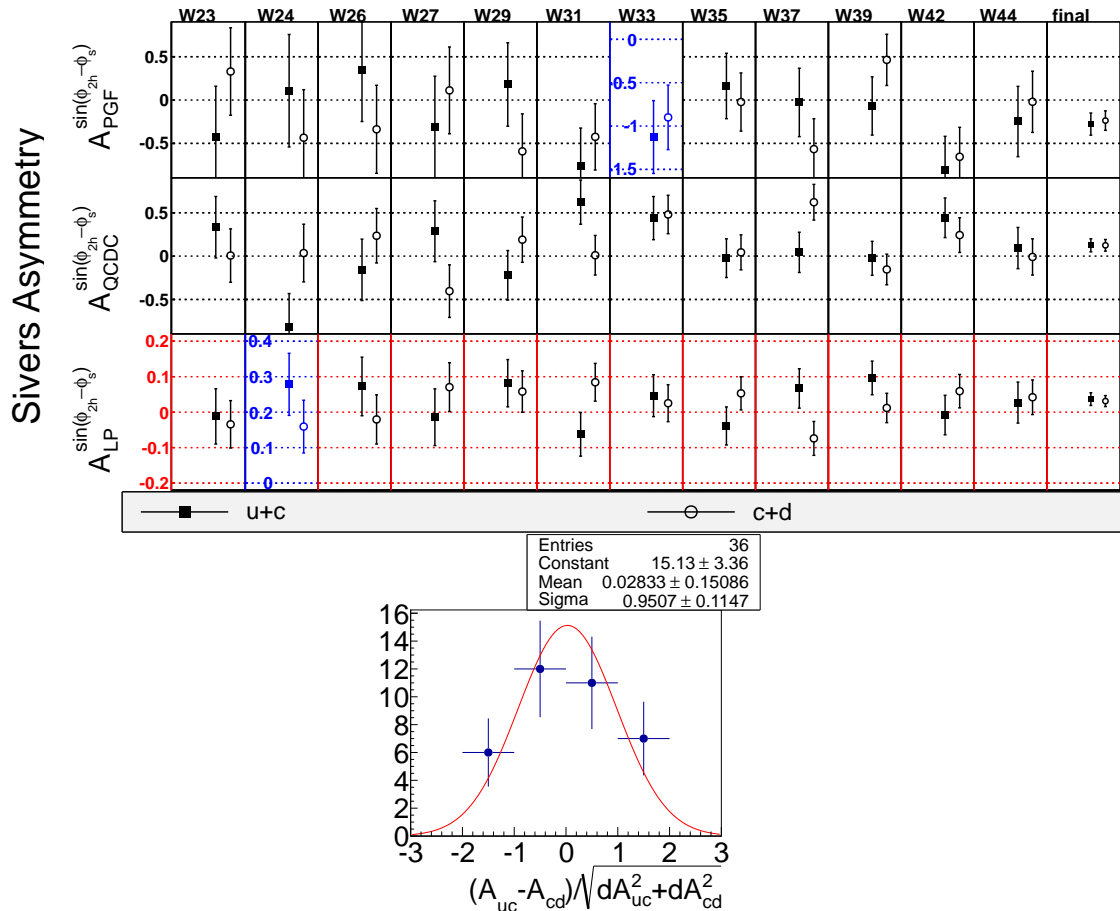


FIGURE 9.5: False asymmetries. Compatibility with between upstream and downstream part of the target.

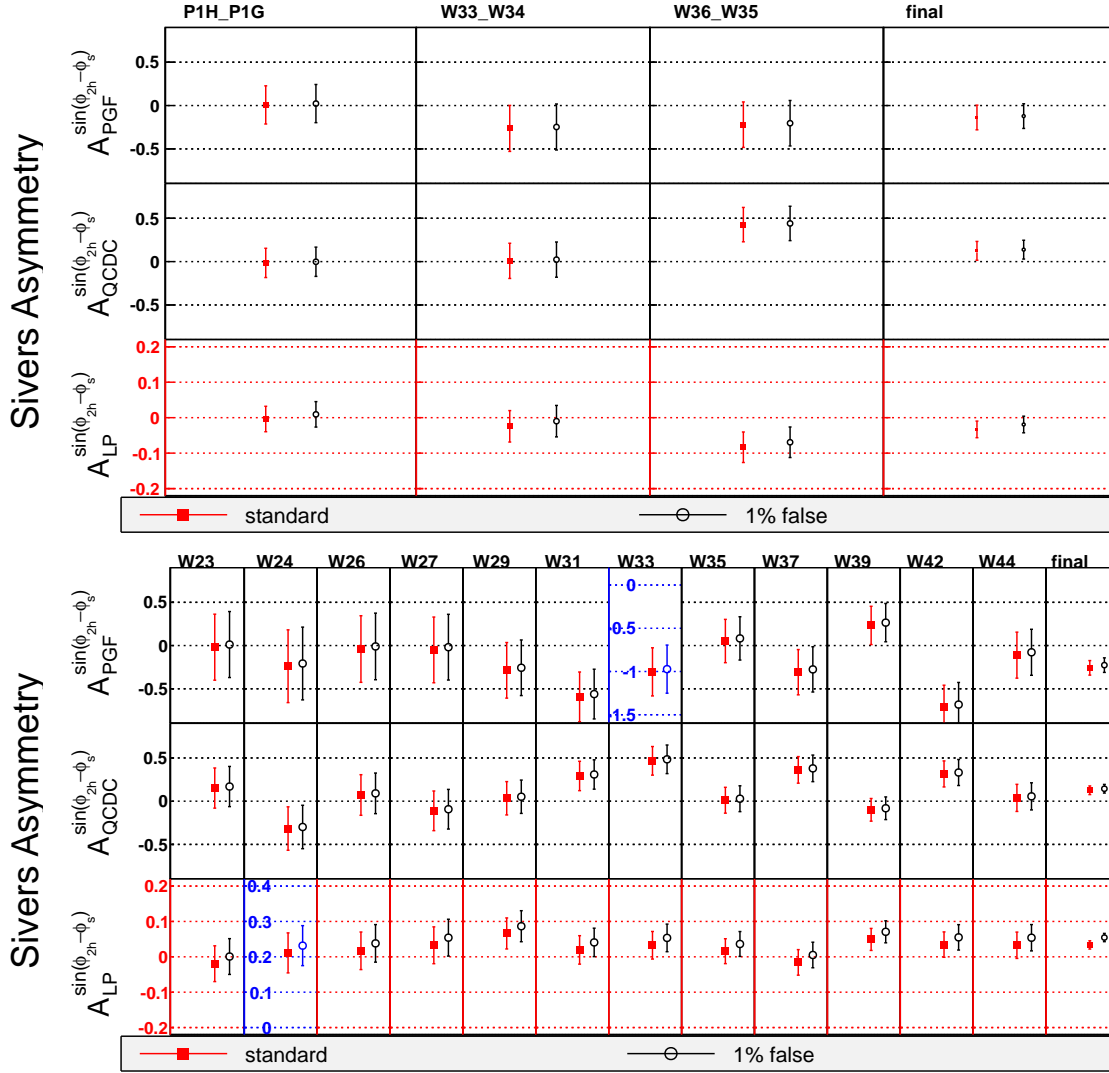
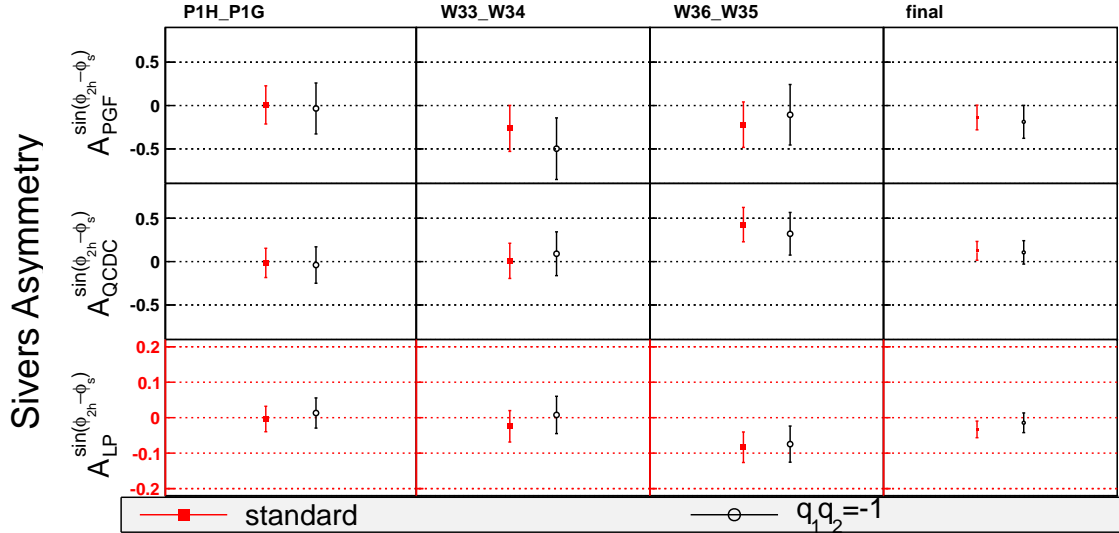
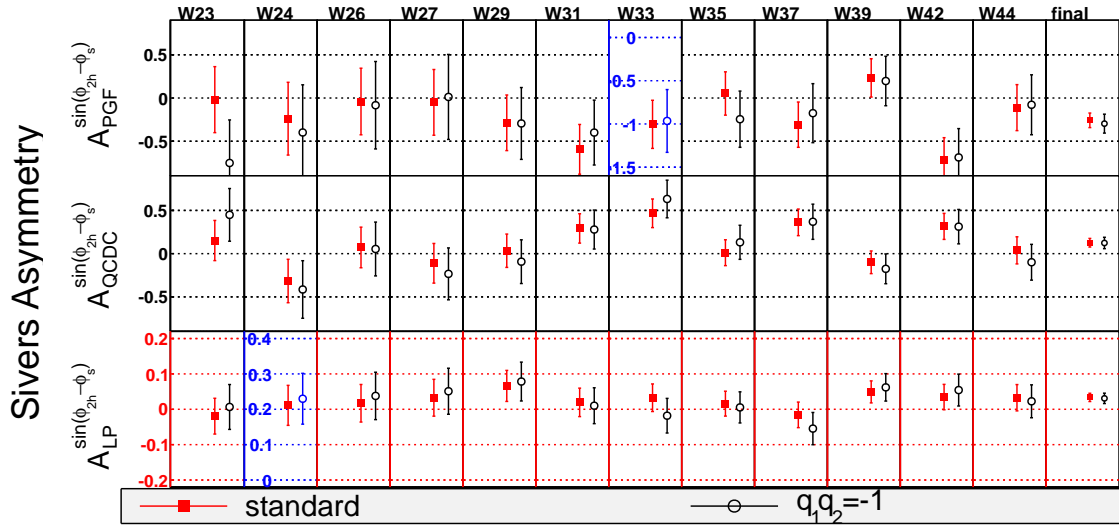


FIGURE 9.6: Final result dependence on false asymmetry. For one target configuration: $\omega' = \omega(1.0 + 0.01 \sin \phi)$. Top panel: deuteron target. Bottom panel: proton target.

9.6 Q^2 cut

In Figure 7.5 the comparison between MC and data for Q^2 is presented and it shows small discrepancy for large Q^2 . Here the influence of the cut $Q^2 < 20(\text{GeV}/c)^2$ on the final result is shown. This time the same NN was used to the data with and without the cut as Q^2 was used for the NN training and the network distinguishes between smaller and larger Q^2 domain. The results are shown in Figure 9.10. The difference in the final A_{PGF} is 0.014 that is 16.5% of σ_{stat} . The statistics reduction due to the cut is almost 10% which means a possible 32% σ_{stat} statistical fluctuation. Hence no systematic error is assigned as indicated in Table 9.1.

FIGURE 9.7: The influence of the cut on the hadron charges $q_1 \cdot q_2 = -1$. Deuteron.FIGURE 9.8: The influence of the cut on the hadron charges $q_1 \cdot q_2 = -1$. Proton.

9.7 Two x_{Bj} bins

The weighted method described in this text allows to apply binning for one process asymmetry leaving the asymmetry of the two remaining processes. In this section binning in x_{Bj} is applied (for the LP). In Figures 9.11 and 9.12 the result of such a binning is presented. The difference in the final A_{PGF} for deuteron is 0.07 that is 47% of σ_{stat} and for proton 0.011 that is 13% of σ_{stat} .

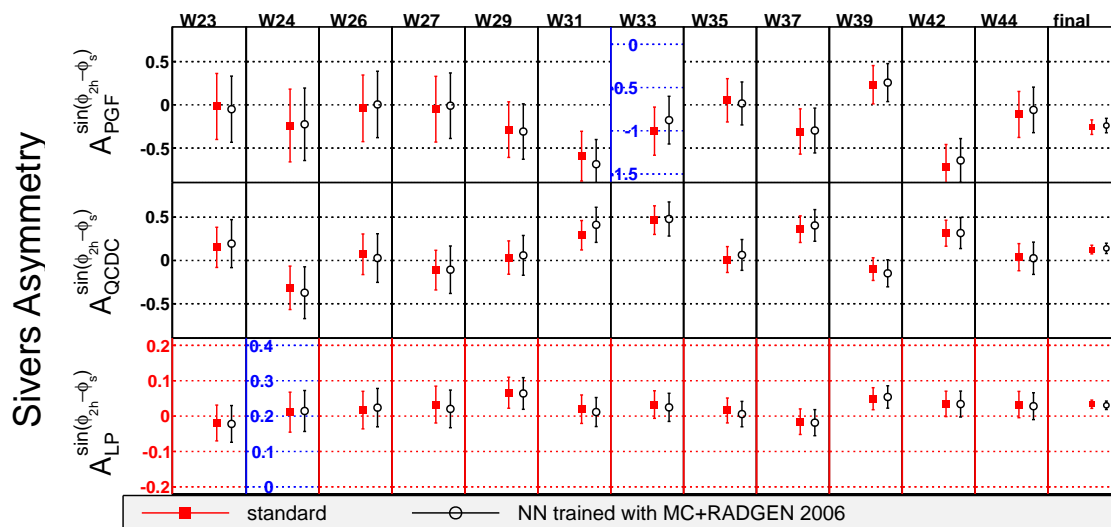


FIGURE 9.9: Standard value with the use of MC 2010 without radiative corrections compared to the results obtained with MC+RADGEN 2006 for 2010 data. The plotted histograms show negligible difference of the fractions of the three processes in the two MC samples

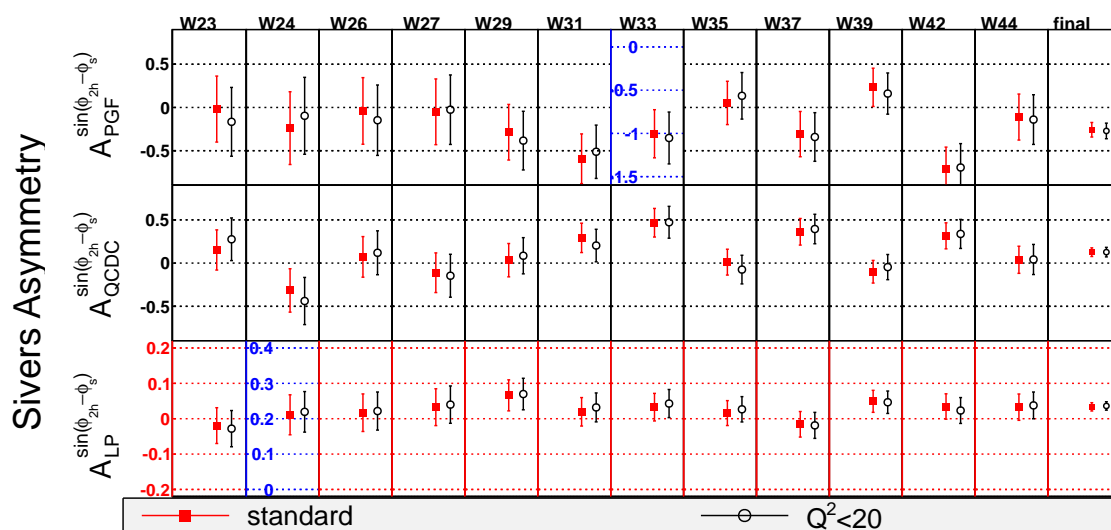
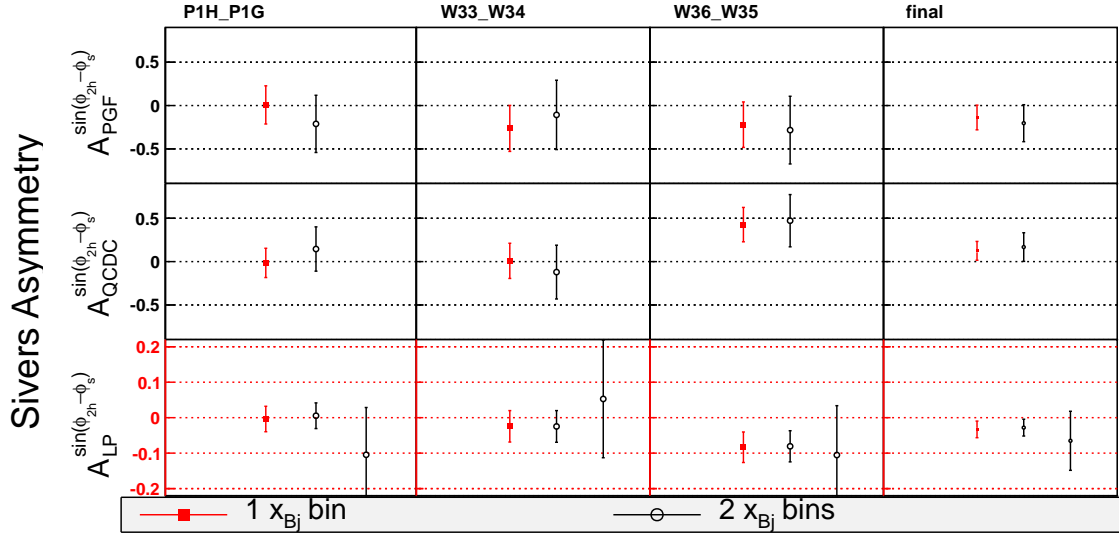
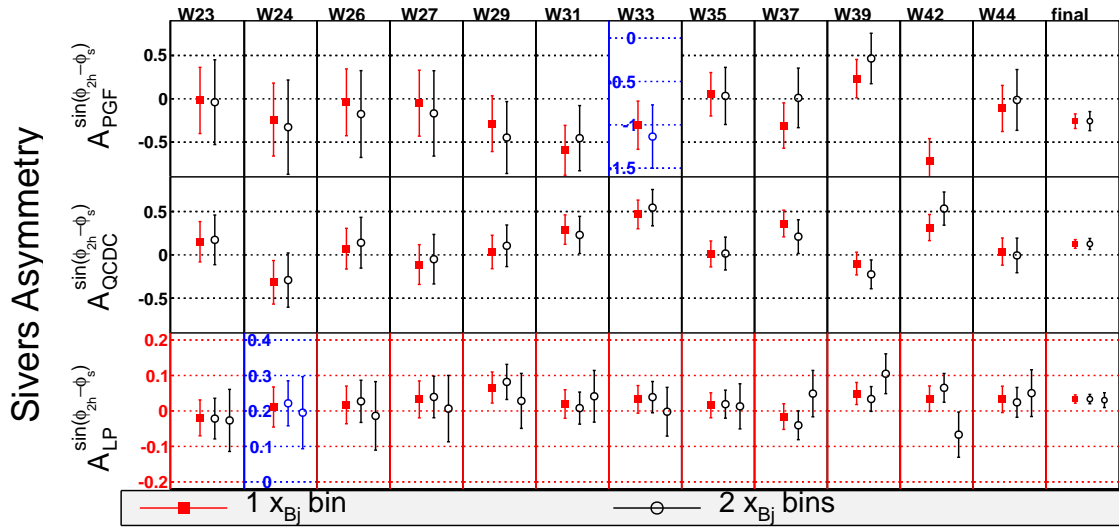


FIGURE 9.10: Comparison between the standard analysis and the analysis with the cut $Q^2 < 20(GeV/c)^2$ applied.

FIGURE 9.11: Result of applying two x_{Bj} bins. Deuteron.FIGURE 9.12: Result of applying two x_{Bj} bins. Proton.

9.8 Sivers + 7 other asymmetries

Until now it was assumed that different modulations in the two-hadron SIDIS cross-section defined by Equation (8.1) are orthogonal. Here this assumption is tested. The possible interplay between different modulation is due to the fact that the spectrometer acceptance is not flat. Sivers asymmetry separated in the three subprocesses was extracted together with seven other standard SIDIS asymmetries. Only the Sivers asymmetry is divided into the three subprocesses. Hence, the fit has ten parameters. Figures 9.13 and 9.14 show that the difference is negligible. The difference in the final A_{PGF} is 0.005 that is 6% of σ_{stat} .

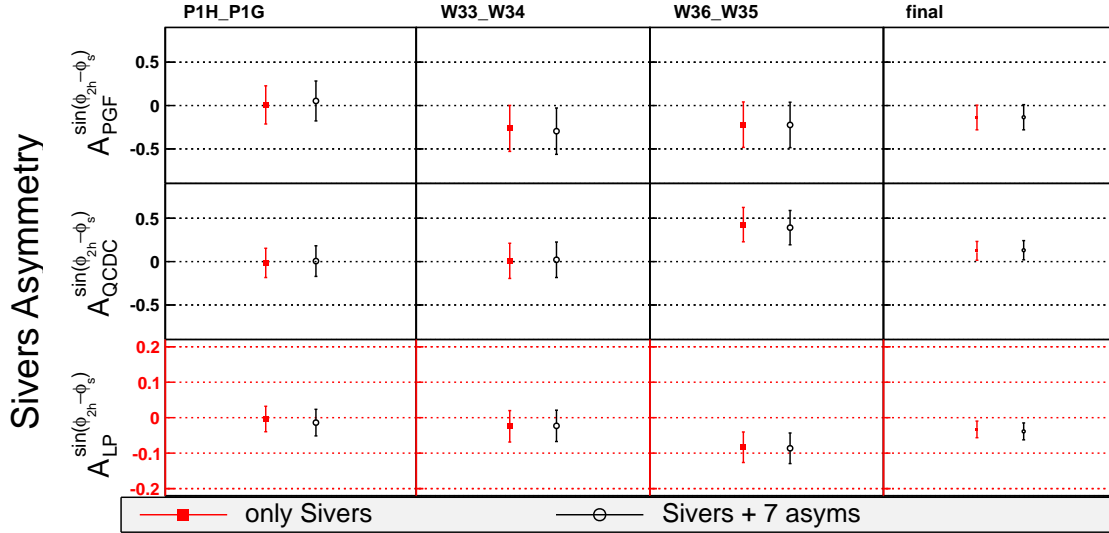


FIGURE 9.13: Proof of the orthogonality of Sivers and 7 other SIDIS modulations. Deuteron.

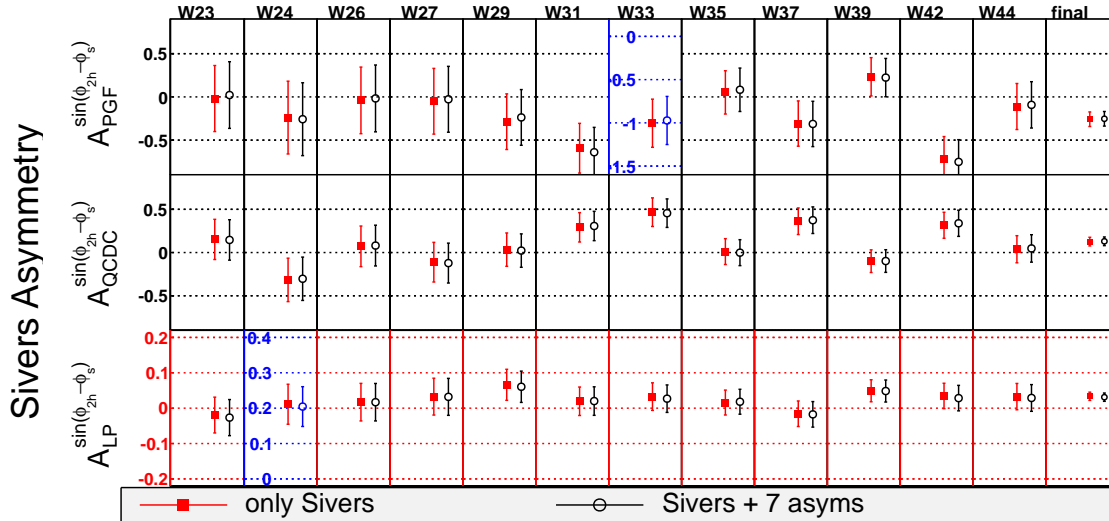
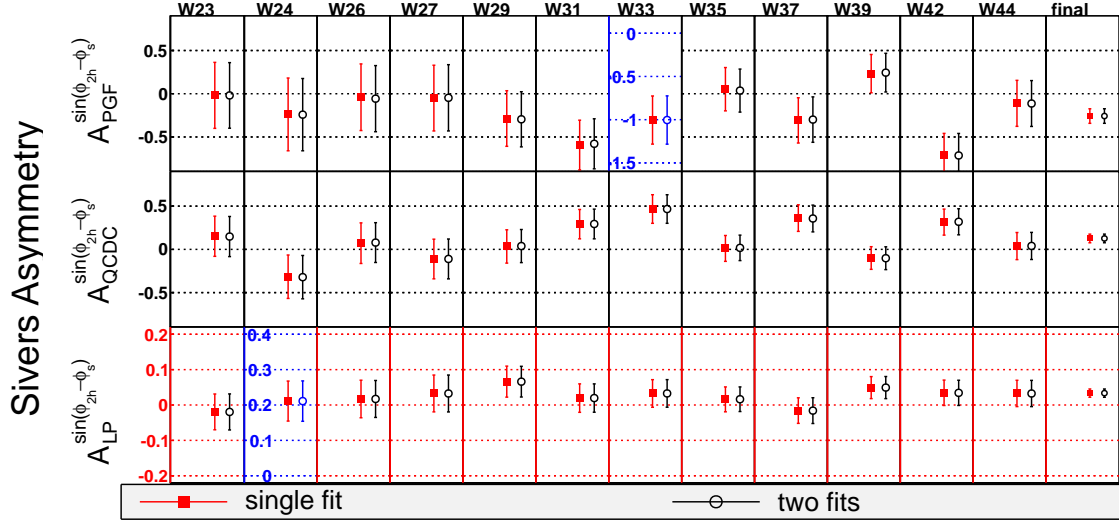


FIGURE 9.14: Proof of the orthogonality of Sivers and 7 other SIDIS modulations. Proton.

9.9 Single fit vs two fits in two ϕ_{Sivers} bins

As mentioned in Section 8.3 the data is separated into two ϕ_{Sivers} bins. There are two ways of extracting the asymmetry in the two bins. The first one is to perform single fit with the constraint $A(\text{1st bin})=A(\text{2nd bin})$, how main results of this theses were obtained. The second one is to make two fits separately and combine the results, how crosscheck was performed. The difference between the two methods is shown in Figure 9.15. The difference in the final A_{PGF} is 0.0002 that is $< 1\%$ of σ_{stat} .

FIGURE 9.15: One fit in two ϕ_{Sivers} bins vs two fits in each bin.

9.10 Target polarisation and dilution factor: δP_T and δf

Relative δP_T is taken as 5% and relative δf as 5%. It is assumed that the systematic error due to target polarisation and dilution factor is proportional to the given above and is negligible comparing to the systematic error of MC.

9.11 Systematics summary

source	deuteron			proton		
	value	assigned error	% $\sigma_{stat}(= 0.15)$	value	assigned error	% $\sigma_{stat}(= 0.085)$
Monte Carlo	0.060	0.060	40%	0.054	0.054	64%
False asymmetries	0.016	0	0%	0.032	0	0%
cut on hadron charges $q_1 \cdot q_2 = -1$	0.05	0	0%	0.038	0	0%
radiative corrections	0.018	0.018	12%	0.018	0.018	21%
large Q^2	-	-	-	0.014	0	0%
x_{Bj} binning	0.07	0.07	47%	0.011	0.011	13%
all asym vs only Sivers	0.003	0.003	2%	0.005	0.005	6%
ML vs Weighted	0.008	0	0%	0.004	0	0%
target polarisation	0.0075	0.0075	5%	0.0043	0.0043	5%
dilution factor	0.0075	0.0075	5%	0.0043	0.0043	5%
total $\sqrt{\sum \sigma_i^2}$	-	0.10	63%	-	0.06	69%

TABLE 9.1: Systematics summary.

Chapter 10

Conclusions

The aim of this thesis was the measurement of the Sivers effect for gluons in the COMPASS experiment. The main difficulty is the separation of the photon-gluon fusion events (scattering off gluons) from the statistically dominating events where the muon is scattered off a quark. The method presented in the thesis separates the asymmetries of scattering processes not the events themselves. It has been developed by the COMPASS collaboration for the $\Delta g/g$ measurements described in Chapter 6. Proper sample selection led to results which are much more precise than the method of selection of the clean J/Ψ channel (see Chapter 8).

The main results read

$$\begin{aligned} \mathbf{A}_{\text{PGF,d}}^{\text{Siv}} &= -\mathbf{0.14} \pm \mathbf{0.15}(\text{stat.}) \pm \mathbf{0.10}(\text{syst.}), \\ \mathbf{A}_{\text{PGF,p}}^{\text{Siv}} &= -\mathbf{0.26} \pm \mathbf{0.09}(\text{stat.}) \pm \mathbf{0.06}(\text{syst.}). \end{aligned} \tag{10.1}$$

The fact that the systematic errors are smaller than statistical ones suggests a need for more experimental data. It is interesting to compare the results on the deuteron and proton targets. They are statistically compatible with each other. This fact is satisfying from the point of view of the naive expectation that the gluons and their orbital motion in the nucleon should be flavour blind. The negative value for the proton target (three σ below zero) suggests a possibility that the orbital momentum of the gluons contributes to the nucleon spin. A theoretical interpretation of these results (possibly via the Burkardt model [41, 42, 43]) is needed.

The future of the experimental spin physics is the exploration of the low x region giving direct access to the quark-gluon sea. This is one of the objectives of the planned EIC experiment [20].

Appendix A

Two-hadron SIDIS cross-section

The two-hadron SIDIS cross-section has been derived in [119]. The total differential cross-section can be divided into parts of UU (unpolarised beam and unpolarised target), LU (longitudinally polarised beam and unpolarised target), UL (unpolarised beam and longitudinally polarised target), LL (longitudinally polarised beam and longitudinally polarised target), UT (unpolarised beam and transversely polarised target), LT (longitudinally polarised beam and transversely polarised target):

$$\frac{d\sigma}{dx_{Bj}dyd\psi dz_h d\phi_h dP_{h\perp}^2 d\phi_{R\perp} dM_h d\cos\theta} = d\sigma_{UU} + d\sigma_{LU} + d\sigma_{UL} + d\sigma_{LL} + d\sigma_{UT} + d\sigma_{LT}, \quad (\text{A.1})$$

where ψ is the azimuthal angle of the scattered muon, $P_h = P_1 + P_2$, $z_h = \frac{P \cdot P_h}{P \cdot q}$, ϕ_h and $\phi_{R\perp}$ are the azimuthal angles of P_h and $R = (P_1 - P_2)/2$ respectively, and $\cos\theta$ is the polar angle of the scattered muon. The parts of the two-hadron SIDIS cross-section can be written in the following form

$$\begin{aligned} d\sigma_{UU} = & \frac{\alpha^2}{2\pi xy Q^2} \left(1 + \frac{\gamma^2}{2x} \right) \\ & \times \sum_{l=0}^{l_{max}} \left\{ A(x, y) \sum_{m=0}^l \left[P_{l,m} \cos(m(\phi_h - \phi_{R\perp})) \left(F_{UU,T}^{P_{l,m} \cos(m(\phi_h - \phi_{R\perp}))} + \epsilon F_{UU,L}^{P_{l,m} \cos(m(\phi_h - \phi_{R\perp}))} \right) \right] \right. \\ & + B(x, y) \sum_{m=-l}^l P_{l,m} \cos((2-m)\phi_h + m\phi_{R\perp}) F_{UU}^{P_{l,m} \cos((2-m)\phi_h + m\phi_{R\perp})} \\ & \left. + V(x, y) \sum_{m=-l}^l P_{l,m} \cos((1-m)\phi_h + m\phi_{R\perp}) F_{UU}^{\cos((1-m)\phi_h + m\phi_{R\perp})} \right\} \end{aligned} \quad (\text{A.2})$$

$$\begin{aligned}
d\sigma_{LU} &= \frac{\alpha^2}{4\pi xy Q^2} \left(1 + \frac{\gamma^2}{2x}\right) \lambda_e \\
&\times \sum_{l=0}^{l_{max}} \left\{ C(x, y) \sum_{m=1}^l \left[P_{l,m} \sin(m(\phi_h - \phi_{R\perp})) 2 \left(F_{UU,T}^{P_{l,m} \cos(m(\phi_h - \phi_{R\perp}))} + \epsilon F_{UU,L}^{P_{l,m} \cos(m(\phi_h - \phi_{R\perp}))} \right) \right] \right. \\
&+ \left. W(x, y) \sum_{m=-l}^l P_{l,m} \sin((1-m)\phi_h + m\phi_{R\perp}) F_{LU}^{P_{l,m} \sin((1-m)\phi_h + m\phi_{R\perp})} \right\} \quad (A.3)
\end{aligned}$$

$$\begin{aligned}
d\sigma_{UL} &= \frac{\alpha^2}{4\pi xy Q^2} \left(1 + \frac{\gamma^2}{2x}\right) S_L \\
&\times \left\{ A(x, y) \sum_{l=1}^{l_{max}} \sum_{m=1}^l P_{l,m} \sin(-m\phi_h + m\phi_{R\perp}) F_{UL}^{P_{l,m} \sin(-m\phi_h + m\phi_{R\perp})} \right. \\
&+ B(x, y) \sum_{l=0}^{l_{max}} \sum_{m=1}^l P_{l,m} \sin((2-m)\phi_h + m\phi_{R\perp}) F_{UL}^{P_{l,m} \sin((2-m)\phi_h + m\phi_{R\perp})} \\
&+ \left. V(x, y) \sum_{m=-l}^l P_{l,m} \sin((1-m)\phi_h + m\phi_{R\perp}) F_{UL}^{P_{l,m} \sin((1-m)\phi_h + m\phi_{R\perp})} \right\} \quad (A.4)
\end{aligned}$$

$$\begin{aligned}
d\sigma_{LL} &= \frac{\alpha^2}{4\pi xy Q^2} \left(1 + \frac{\gamma^2}{2x}\right) \lambda_e S_L \\
&\times \sum_{l=0}^{l_{max}} \left\{ C(x, y) \sum_{m=0}^l 2^{2-\delta_{m0}} P_{l,m} \cos(m(\phi_h - \phi_{R\perp})) F_{LL}^{P_{l,m} \cos(m(\phi_h - \phi_{R\perp}))} \right. \\
&+ \left. W(x, y) \sum_{m=-l}^l P_{l,m} \cos((1-m)\phi_h + m\phi_{R\perp}) F_{LL}^{P_{l,m} \cos((1-m)\phi_h + m\phi_{R\perp})} \right\} \quad (A.5)
\end{aligned}$$

$$\begin{aligned}
d\sigma_{UT} &= \frac{\alpha^2}{4\pi xy Q^2} \left(1 + \frac{\gamma^2}{2x}\right) |\mathcal{S}_T| \\
&\times \sum_{l=0}^{l_{max}} \sum_{m=-l}^l \left\{ A(x, y) \left[P_{l,m} \sin((m+1)\phi_h - m\phi_{R\perp} - \phi_S) \right. \right. \\
&\times \left. \left. \left(F_{UT,T}^{P_{l,m} \sin((m+1)\phi_h - m\phi_{R\perp} - \phi_S)} + \epsilon F_{UT,L}^{P_{l,m} \sin((m+1)\phi_h - m\phi_{R\perp} - \phi_S)} \right) \right] \right. \\
&+ B(x, y) \left[P_{l,m} \sin((1-m)\phi_h + m\phi_{R\perp} + \phi_S) F_{UT}^{P_{l,m} \sin((1-m)\phi_h + m\phi_{R\perp} + \phi_S)} \right. \\
&+ P_{l,m} \sin((3-m)\phi_h + m\phi_{R\perp} - \phi_S) F_{UT}^{P_{l,m} \sin((3-m)\phi_h + m\phi_{R\perp} - \phi_S)} \\
&+ V(x, y) \left[P_{l,m} \sin(-m\phi_h + m\phi_{R\perp} + \phi_S) F_{UT}^{P_{l,m} \sin(-m\phi_h + m\phi_{R\perp} + \phi_S)} \right. \\
&+ \left. \left. P_{l,m} \sin((2-m)\phi_h + m\phi_{R\perp} - \phi_S) F_{UT}^{P_{l,m} \sin((2-m)\phi_h + m\phi_{R\perp} - \phi_S)} \right] \right\} \quad (A.6)
\end{aligned}$$

$$\begin{aligned}
d\sigma_{LT} &= \frac{\alpha^2}{4\pi xy Q^2} \left(1 + \frac{\gamma^2}{2x}\right) \lambda_e |\mathbf{S}_T| \\
&\times \sum_{l=0}^{l_{max}} \sum_{m=-l}^l \left\{ C(x, y) 2P_{l,m} \cos((1-m)\phi_h + m\phi_{R\perp} - \phi_S) F_{LT}^{P_{l,m} \cos((1-m)\phi_h + m\phi_{R\perp} - \phi_S)} \right. \\
&+ W(x, y) \left[P_{l,m} \cos(-m\phi_h + m\phi_{R\perp} + \phi_S) F_{LT}^{P_{l,m} \cos(-m\phi_h + m\phi_{R\perp} + \phi_S)} \right. \\
&\left. \left. + P_{l,m} \cos((2-m)\phi_h + m\phi_{R\perp} - \phi_S) F_{LT}^{P_{l,m} \cos((2-m)\phi_h + m\phi_{R\perp} - \phi_S)} \right] \right\}
\end{aligned} \tag{A.7}$$

The dependence of the cross section on the polar angle $\cos \theta$ and on the azimuthal angles $\phi_h, \phi_{R\perp}$, is transformed by expanding it on a basis of spherical harmonics. In particular, for the $\cos \theta$ dependence the basis of Legendre polynomials is adopted, the first few of which read

$$P_{0,0} = 1, \quad P_{1,0} = \cos \theta, \quad P_{1,1} = P_{1,-1} = \sin \theta \tag{A.8}$$

The following depolarisation factors have been used

$$A(x, y) = \frac{y^2}{2(1-\epsilon)} = \frac{1-y + \frac{1}{2}y^2 + \frac{1}{4}\gamma^2 y^2}{1+\gamma^2} \approx \left(1-y + \frac{1}{2}y^2\right), \tag{A.9}$$

$$B(x, y) = \frac{y^2}{2(1-\epsilon)} \epsilon = \frac{1-y - \frac{1}{4}\gamma^2 y^2}{1+\gamma^2} \approx (1-y), \tag{A.10}$$

$$C(x, y) = \frac{y^2}{2(1-\epsilon)} \sqrt{1-\epsilon^2} = \frac{y(1-\frac{1}{2}y)}{\sqrt{1+\gamma^2}} \approx y \left(1 - \frac{1}{2}y\right), \tag{A.11}$$

$$V(x, y) = \frac{y^2}{2(1-\epsilon)} \sqrt{2\epsilon(1+\epsilon)} = \frac{2-y}{1+\gamma^2} \sqrt{1-y - \frac{1}{4}\gamma^2 y^2} \approx (2-y) \sqrt{1-y}, \tag{A.12}$$

$$W(x, y) = \frac{y^2}{2(1-\epsilon)} \sqrt{2\epsilon(1-\epsilon)} = \frac{y}{\sqrt{1+\gamma^2}} \sqrt{1-y - \frac{1}{4}\gamma^2 y^2} \approx y \sqrt{1-y}. \tag{A.13}$$

In case of one hadron SIDIS, the hadronic tensor is built by using three four-vectors: q - virtual photon, P - nucleon momentum, P_h - hadron momentum and one pseudo four-vector, S - the spin of the nucleon. Since the target is a spin-1/2 particle, the hadronic tensor can be at most linear in S . By imposing the invariance under the usual transformations (parity, time-reversal, gauge), the hadronic tensor can be parametrised in terms of 18 structure function. In the two-particle-inclusive SIDIS, even in the simplest case when the target and the two final hadrons are unpolarised, the pseudo-vector S is replaced by R and the hadronic tensor does not necessarily need to be linear in R . Actually, the number of partial waves depending on $\phi_{R\perp}$ is in principle not limited, and so the number of structure functions is also not limited and l_{max} is infinite.

Appendix B

Approximation of asymmetries by linear dependence on \mathbf{x}

Repeating Equation (8.10)

$$\begin{aligned}
 p_t^j &= \sum_{i=1}^{N_t} \omega_i^j = \tilde{\alpha}_t^j (1 + \langle \beta_t^G \rangle_{\omega^j} \langle A_{PGF}^{\sin(\phi_{2h}-\phi_s)} \rangle_{\omega^j \beta_t^G}) \\
 &\quad + \langle \beta_t^L \rangle_{\omega^j} \langle A_{LP}^{\sin(\phi_{2h}-\phi_s)} \rangle_{\omega^j \beta_t^L} + \langle \beta_t^C \rangle_{\omega^j} \langle A_{QCDC}^{\sin(\phi_{2h}-\phi_s)} \rangle_{\omega^j \beta_t^C}.
 \end{aligned} \tag{B.1}$$

Here $j = G, L, C \equiv PGF, LP, QCDC$. Asymmetries $A_j^{\sin(\phi_{2h}-\phi_s)}(x_j)$ can be approximated with a linear function, as discussed in Section 6.1. To simplify the Equations (B.1) one needs to have $\langle x_j \rangle_{\omega^k \beta_t^j} \approx \langle x_j \rangle_{\omega^m \beta_b^j} \equiv \langle x_j \rangle$ $j, k, m = G, L, C$ and t, b run over ud, c, ud', c' 12 such values for each process can be approximated by $\langle x_j \rangle_{\omega^k \beta_t^j} \approx \left(\sum_i \omega_i^k \beta_i^j x_j^i \right) / \left(\sum_i \omega_i^k \beta_i^j \right)$. Here summation over i is performed for each target configuration t . The results for every period of 2010 are stored in the Tables B.1 and B.2. Taking the average value of $\langle x_{PGF} \rangle \equiv \langle x_G \rangle$, $\langle x_{LP} \rangle \equiv \langle x_{Bj} \rangle$ and $\langle x_{QCDC} \rangle \equiv \langle x_C \rangle$ one can rewrite equations (B.1) as follows:

$$\begin{aligned}
 p_t^j &= \sum_{i=1}^{N_t} \omega_i^j = \tilde{\alpha}_t^j (1 + \langle \beta_t^G \rangle_{\omega^j} A_{PGF}^{\sin(\phi_{2h}-\phi_s)}(\langle x_G \rangle)) \\
 &\quad + \langle \beta_t^L \rangle_{\omega^j} A_{LP}^{\sin(\phi_{2h}-\phi_s)}(\langle x_{Bj} \rangle) + \langle \beta_t^C \rangle_{\omega^j} A_{QCDC}^{\sin(\phi_{2h}-\phi_s)}(\langle x_C \rangle))
 \end{aligned} \tag{B.2}$$

P1G-P1H														
	ω_{LP}				ω_{QCDC}				ω_{PGF}				RMS	$\langle x \rangle$
	u	d	u'	d'	u	d	u'	d'	u	d	u'	d'		
$\langle x_{LP} \rangle$	0.0243	0.0322	0.0247	0.0321	0.0303	0.0376	0.0309	0.0375	0.0189	0.0218	0.019	0.022	0.0064	0.0276
$\langle x_{QCDC} \rangle$	0.1216	0.1406	0.1221	0.1404	0.1365	0.1563	0.1374	0.1562	0.123	0.1402	0.1235	0.1406	0.0116	0.1365
$\langle x_{PGF} \rangle$	0.1196	0.1244	0.1197	0.1245	0.1258	0.1314	0.1261	0.1316	0.1231	0.1286	0.1232	0.1288	0.0038	0.1256
W33-W34														
	ω_{LP}				ω_{QCDC}				ω_{PGF}				RMS	$\langle x \rangle$
	u	d	u'	d'	u	d	u'	d'	u	d	u'	d'		
$\langle x_{LP} \rangle$	0.025	0.0324	0.0245	0.0324	0.0315	0.0381	0.0309	0.0381	0.0192	0.0221	0.0192	0.0221	0.0065	0.028
$\langle x_{QCDC} \rangle$	0.1221	0.1406	0.1217	0.1407	0.1376	0.1569	0.1369	0.1569	0.1231	0.1409	0.1232	0.141	0.0119	0.1368
$\langle x_{PGF} \rangle$	0.1196	0.1245	0.1197	0.1246	0.1259	0.1317	0.126	0.1318	0.1229	0.1289	0.1232	0.1289	0.0039	0.1256
W36-W35														
	ω_{LP}				ω_{QCDC}				ω_{PGF}				RMS	$\langle x \rangle$
	u	d	u'	d'	u	d	u'	d'	u	d	u'	d'		
$\langle x_{LP} \rangle$	0.0251	0.0331	0.025	0.0327	0.0317	0.0391	0.0314	0.0384	0.0193	0.0222	0.0191	0.0221	0.0067	0.0283
$\langle x_{QCDC} \rangle$	0.1225	0.1413	0.1226	0.141	0.1374	0.1578	0.1376	0.1573	0.1232	0.141	0.1234	0.1406	0.0119	0.1371
$\langle x_{PGF} \rangle$	0.1198	0.1245	0.1198	0.1245	0.126	0.1317	0.126	0.1316	0.1231	0.1288	0.1232	0.1287	0.0038	0.1256

TABLE B.1: Values of weighted averages of $x \langle x \rangle_{\beta\omega}$ for the three processes for all periods and target configurations. Deuteron.

W23														
	ω_{LP}				ω_{QDC}				ω_{PGF}				RMS	$\langle x \rangle$
	u+d	c	u'+d'	c''	u+d	c	u'+d'	c'	u+d	c	u'+d'	c'		
$\langle x_{LP} \rangle$	0.0482	0.0486	0.049	0.0482	0.0487	0.0494	0.0496	0.0491	0.0269	0.0268	0.027	0.0269	0.0103	0.0415
$\langle x_{QDC} \rangle$	0.1664	0.1666	0.1669	0.1665	0.1758	0.1758	0.1761	0.1757	0.1598	0.1592	0.1596	0.1594	0.0067	0.1673
$\langle x_{PGF} \rangle$	0.1412	0.1406	0.1414	0.1411	0.1537	0.1528	0.1536	0.1534	0.1427	0.1415	0.1425	0.1423	0.0056	0.1456
W24														
	ω_{LP}				ω_{QDC}				ω_{PGF}				RMS	$\langle x \rangle$
	u+d	c	u'+d'	c''	u+d	c	u'+d'	c'	u+d	c	u'+d'	c'		
$\langle x_{LP} \rangle$	0.0498	0.0497	0.0502	0.0485	0.0516	0.0513	0.052	0.0506	0.0278	0.0275	0.028	0.0275	0.0108	0.0429
$\langle x_{QDC} \rangle$	0.1678	0.1677	0.1684	0.1675	0.1784	0.1785	0.1796	0.1783	0.1608	0.161	0.1617	0.1611	0.0072	0.1692
$\langle x_{PGF} \rangle$	0.1412	0.1409	0.1413	0.1409	0.1541	0.1542	0.1546	0.1544	0.1426	0.1426	0.143	0.143	0.0059	0.1461
W26														
	ω_{LP}				ω_{QDC}				ω_{PGF}				RMS	$\langle x \rangle$
	u+d	c	u'+d'	c''	u+d	c	u'+d'	c'	u+d	c	u'+d'	c'		
$\langle x_{LP} \rangle$	0.0501	0.0499	0.0506	0.0505	0.0517	0.0516	0.0521	0.0521	0.0277	0.0275	0.0274	0.0277	0.0111	0.0432
$\langle x_{QDC} \rangle$	0.168	0.1679	0.1679	0.1684	0.1782	0.1784	0.1779	0.1792	0.1606	0.1607	0.1601	0.1616	0.0073	0.1691
$\langle x_{PGF} \rangle$	0.1411	0.1407	0.1408	0.1413	0.1538	0.1539	0.1534	0.1548	0.1425	0.1423	0.1419	0.1432	0.0058	0.1458
W27														
	ω_{LP}				ω_{QDC}				ω_{PGF}				RMS	$\langle x \rangle$
	u+d	c	u'+d'	c''	u+d	c	u'+d'	c'	u+d	c	u'+d'	c'		
$\langle x_{LP} \rangle$	0.0499	0.0494	0.0498	0.0497	0.0513	0.051	0.0515	0.0514	0.0275	0.0274	0.0276	0.0273	0.0109	0.0428
$\langle x_{QDC} \rangle$	0.1678	0.1675	0.1676	0.1674	0.178	0.1783	0.178	0.1776	0.1607	0.1608	0.1605	0.1602	0.0072	0.1687
$\langle x_{PGF} \rangle$	0.1409	0.1409	0.1409	0.1404	0.1539	0.154	0.1537	0.1533	0.1427	0.1425	0.1424	0.142	0.0058	0.1456
W29														
	ω_{LP}				ω_{QDC}				ω_{PGF}				RMS	$\langle x \rangle$
	u+d	c	u'+d'	c''	u+d	c	u'+d'	c'	u+d	c	u'+d'	c'		
$\langle x_{LP} \rangle$	0.0494	0.0482	0.0499	0.0489	0.0513	0.0502	0.0515	0.0505	0.0275	0.0275	0.0277	0.0274	0.0106	0.0425
$\langle x_{QDC} \rangle$	0.1674	0.1668	0.1677	0.1671	0.1782	0.1777	0.1782	0.1778	0.1605	0.1604	0.1606	0.1606	0.0072	0.1686
$\langle x_{PGF} \rangle$	0.1404	0.1401	0.1407	0.1406	0.1535	0.1532	0.1537	0.1537	0.1419	0.1417	0.1421	0.1423	0.0058	0.1453
W31														
	ω_{LP}				ω_{QDC}				ω_{PGF}				RMS	$\langle x \rangle$
	u+d	c	u'+d'	c''	u+d	c	u'+d'	c'	u+d	c	u'+d'	c'		
$\langle x_{LP} \rangle$	0.0519	0.0509	0.0514	0.0512	0.0543	0.0538	0.0541	0.054	0.0279	0.028	0.0282	0.028	0.0117	0.0445
$\langle x_{QDC} \rangle$	0.1693	0.1689	0.1691	0.1689	0.1803	0.1802	0.1806	0.1801	0.1613	0.1612	0.1616	0.1611	0.0078	0.1702
$\langle x_{PGF} \rangle$	0.1407	0.1402	0.1407	0.1403	0.1541	0.1539	0.1543	0.1539	0.1422	0.1416	0.1422	0.1419	0.0061	0.1455
W33														
	ω_{LP}				ω_{QDC}				ω_{PGF}				RMS	$\langle x \rangle$
	u+d	c	u'+d'	c''	u+d	c	u'+d'	c'	u+d	c	u'+d'	c'		
$\langle x_{LP} \rangle$	0.0528	0.053	0.0527	0.0518	0.0557	0.056	0.0552	0.0545	0.0286	0.0282	0.0282	0.0282	0.0122	0.0454
$\langle x_{QDC} \rangle$	0.1703	0.1702	0.17	0.1696	0.1818	0.1816	0.1813	0.1811	0.1621	0.1618	0.1617	0.1617	0.0081	0.1711
$\langle x_{PGF} \rangle$	0.1412	0.1403	0.1406	0.1404	0.1548	0.1544	0.1543	0.1543	0.1425	0.142	0.1423	0.142	0.0062	0.1458
W35														
	ω_{LP}				ω_{QDC}				ω_{PGF}				RMS	$\langle x \rangle$
	u+d	c	u'+d'	c''	u+d	c	u'+d'	c'	u+d	c	u'+d'	c'		
$\langle x_{LP} \rangle$	0.0525	0.0516	0.0519	0.0519	0.0552	0.0546	0.0544	0.055	0.0282	0.0281	0.0281	0.0283	0.0119	0.045
$\langle x_{QDC} \rangle$	0.1701	0.1693	0.1695	0.1699	0.1811	0.1808	0.1806	0.1816	0.1615	0.1612	0.1615	0.162	0.008	0.1708
$\langle x_{PGF} \rangle$	0.1407	0.14	0.1407	0.1407	0.1543	0.1538	0.1542	0.1548	0.1422	0.1415	0.1422	0.1423	0.0062	0.1456
W37														
	ω_{LP}				ω_{QDC}				ω_{PGF}				RMS	$\langle x \rangle$
	u+d	c	u'+d'	c''	u+d	c	u'+d'	c'	u+d	c	u'+d'	c'		
$\langle x_{LP} \rangle$	0.0519	0.0513	0.0517	0.0515	0.0546	0.0542	0.0545	0.0545	0.0282	0.0283	0.0283	0.0281	0.0118	0.0448
$\langle x_{QDC} \rangle$	0.1698	0.1696	0.1697	0.1697	0.1813	0.1813	0.1812	0.1816	0.162	0.1619	0.1619	0.1621	0.008	0.171
$\langle x_{PGF} \rangle$	0.141	0.1408	0.1411	0.1406	0.1548	0.1546	0.1546	0.1549	0.1426	0.1422	0.1425	0.1424	0.0062	0.146
W39														
	ω_{LP}				ω_{QDC}				ω_{PGF}				RMS	$\langle x \rangle$
	u+d	c	u'+d'	c''	u+d	c	u'+d'	c'	u+d	c	u'+d'	c'		
$\langle x_{LP} \rangle$	0.0522	0.0511	0.052	0.0516	0.0552	0.0545	0.055	0.0547	0.0283	0.0282	0.0282	0.0281	0.0119	0.0449
$\langle x_{QDC} \rangle$	0.1696	0.1692	0.1695	0.1693	0.181	0.181	0.1807	0.1807	0.1614	0.1616	0.1613	0.1613	0.008	0.1705
$\langle x_{PGF} \rangle$	0.1403	0.14	0.1404	0.14	0.1541	0.1541	0.1539	0.1539	0.1417	0.1416	0.1418	0.1416	0.0062	0.1453
W42														
	ω_{LP}				ω_{QDC}				ω_{PGF}				RMS	$\langle x \rangle$
	u+d	c	u'+d'	c''	u+d	c	u'+d'	c'	u+d	c	u'+d'	c'		
$\langle x_{LP} \rangle$	0.053	0.0529	0.0527	0.0521	0.0557	0.056	0.0556	0.055	0.0282	0.0282	0.0283	0.0279	0.0123	0.0455
$\langle x_{QDC} \rangle$	0.1701	0.17	0.1699	0.1693	0.1812	0.1815	0.181	0.1805	0.1615	0.1616	0.1615	0.161	0.0081	0.1708
$\langle x_{PGF} \rangle$	0.1406	0.14	0.1405	0.1398	0.1542	0.1541	0.1543	0.1535	0.1421	0.1416	0.1422	0.1412	0.0062	0.1453
W44														
	ω_{LP}				ω_{QDC}				ω_{PGF}				RMS	$\langle x \rangle$
	u+d	c	u'+d'	c''	u+d	c	u'+d'	c'	u+d	c	u'+d'	c'		
$\langle x_{LP} \rangle$	0.0533	0.0527	0.0535	0.053	0.056	0.0556	0.0562	0.056	0.0282	0.0282	0.0282	0.0281	0.0125	0.0458
$\langle x_{QDC} \rangle$	0.1701	0.17	0.1703	0.1699	0.1812	0.1815	0.1812	0.1811	0.1614	0.162	0.1615	0.1612	0.0081	0.171
$\langle x_{PGF} \rangle$	0.1405	0.1405	0.1406	0.1398	0.1542	0.1546	0.1543	0.1537	0.1419	0.1423	0.1421	0.1413	0.0062	0.1455

TABLE B.2: Values of weighted averages of $x \langle x \rangle_{\beta\omega}$ for the three processes for all periods and target configurations. Proton 2010.

Appendix C

COMPASS spectrometer alignment

The objective of the alignment procedure is to determine the positions of the tracking detectors. The more accurate the the alignmnet is the more effective the tracking and vertex reconstruction is. A good alignment leads also to precise determination of the kinematic variables.

The alignment procedure is done in two stages. First is performed by surveyors, where the absolute (with respect to the experimental hall) positions of the detectors are measured directly with a $\sim 1\text{mm}$ precision. The second stage reconstructed particle tracks are used to evaluate the true detectors positions. The procedure described in details in [120] leads to an accuracy of a fraction of detector resolution in determination of its position.

The author was responsible for the alignment during 2012 DVCS (Deeply Virtual Compton Scattering) test run which last for almost two months.

C.1 Alignment parameters

The main COMPASS coordinate system is defined with respect to the experimental hall and consists of the following axes:

- Z axis - along the beam direction,
- Y axis - vertical, directed from bottom to top,
- X axis - defined in such a way that the system is right-handed.

For each detector a local coordinate system is defined:

- Z axis - the same as the main coordinate system,
- U axis - in the detector plane and perpendicular to the strips or wires (this is the coordinate measured by this detector plane),
- V axis - parallel to the strips or wires and defined in such a way that the system is right-handed (this coordinate is not measured by the given detector plane).

For alignment purposes the following set of parameters have been chosen to describe the position of the detector centre and its wires or strips:

- δu - the transverse detector offset perpendicular to the detector wires,
- δv - the transverse detector offset parallel to the detector wires,
- $\delta\theta$ - the rotational detector offset in a plane perpendicular to the beam axis,
- δz - the longitudinal detector offset along the beam axis,
- δp - the scaling factor of the nominal pitch (distance between the wires/strips)
 $p_{meas} = (1 + \delta p)p_{NOME}$.

To describe the rotational offsets out of the plane perpendicular to the beam axis two other parameters could be used $\delta\theta_u$ and $\delta\theta_v$. However the internal representation of detectors in COMPASS tracking software (CORAL) assumes that the detectors are perpendicular to the beam and the detector planes are manually align in such a way. This makes such parameters unusable in our case. Moreover if misalignments in θ_u and θ_v are small, their effect on the tracking would be of second order with respect to other parameters.

The δu value is obtained directly from the measurement. If a single plane is shifted in u then the obtained residual will not be centred at zero.

The transverse offset of a detector along the wires (δv) cannot be directly taken into account since the detector does not give any information about the position along this direction. However if a detector station consists of at least two planes with a non zero angle between the measured directions then the δv can be determined.

A misalignment in θ is visible on a δu vs v plot as the discrepancy between the hit and the reconstructed track should change with the position along the wire.

The δU vs V plot is sensitive to wrong pitch value or misalignment in z - position along the beam. Moreover, the pitch, p , and z misalignment can be easily seen on the δu vs θ . The difference between misalignment in z and in p is that the case of z the slope of

the δu vs θ should be larger in the outer parts of the detector plane than in the central parts while wrong pitch should affect the central and outer parts of the detector plane in the same way.

Examples of different kind of plots will be given in section C.4.

C.2 The principle of alignment

The alignment procedure is based on the difference between the measured hits and the corresponding positions of the reconstructed tracks. This difference, ΔS can be expressed as a function of three independent sets of parameters

$$\Delta S_j(u_j, \alpha^t, \alpha_j^a), \quad (\text{C.1})$$

where u_j is the hit position in the j -th detector, α^t are the track parameters (a curvature or a straight line) and α_j^a standing for the alignment parameters. Every track has a set of track parameters while the alignment parameters, α^a , are common to all tracks. The principle of the alignment procedure is to minimise the χ^2 defined as

$$\chi^2 = \sum_{i=1}^{N_{track}} \sum_{j=1}^{n_{det}} \frac{[\Delta S_{ij}(u_{ij}, \alpha_i^t, \alpha_j^a)]^2}{\sigma_j^2}. \quad (\text{C.2})$$

Here σ_j is the resolution of the j -th detector, n_{track} is the number of used tracks, n_{det} is the number of detectors contributing to track i and u_{ij} is the hit position corresponding to the track i measured by the j -th detector. Assuming linear dependence of ΔS on α^t and α^a it is true that

$$\Delta S_{ij} = \Delta S_{ij}^0 + \sum_k \frac{\partial \Delta S_{ij}}{\partial \alpha_k} \alpha_k, \quad (\text{C.3})$$

where $\Delta S_{ij}^0 \equiv \Delta S_{ij}(0, 0, 0)$ and k goes over all tracking and alignment parameters. Searching for the minimum requires all partial derivatives to be equal zero:

$$\frac{1}{2} \frac{\partial \chi^2}{\partial \alpha_m} = \sum_i \sum_j \frac{1}{\sigma_j^2} \frac{\partial \Delta S_{ij}}{\partial \alpha_m} \left(\Delta S_{ij}^0 + \sum_k \frac{\partial \Delta S_{ij}}{\partial \alpha_k} \alpha_k \right) = 0. \quad (\text{C.4})$$

Here m, k goes over all tracking and alignment parameters. This results in following matrix equation

$$\begin{pmatrix} \sum_i \sum_j \frac{1}{\sigma_j^2} \frac{\partial \Delta S_{ij}}{\partial \alpha_1} \frac{\partial \Delta S_{ij}}{\partial \alpha_1} & \cdots & \sum_i \sum_j \frac{1}{\sigma_j^2} \frac{\partial \Delta S_{ij}}{\partial \alpha_1} \frac{\partial \Delta S_{ij}}{\partial \alpha_m} & \cdots \\ \vdots & \ddots & \vdots & \vdots \\ \sum_i \sum_j \frac{1}{\sigma_j^2} \frac{\partial \Delta S_{ij}}{\partial \alpha_m} \frac{\partial \Delta S_{ij}}{\partial \alpha_1} & \cdots & \sum_i \sum_j \frac{1}{\sigma_j^2} \frac{\partial \Delta S_{ij}}{\partial \alpha_m} \frac{\partial \Delta S_{ij}}{\partial \alpha_m} & \cdots \\ \vdots & & \vdots & \ddots \end{pmatrix} \begin{pmatrix} \alpha_1 \\ \vdots \\ \alpha_m \\ \vdots \end{pmatrix} = - \begin{pmatrix} \sum_i \sum_j \frac{1}{\sigma_j^2} \frac{\partial \Delta S_{ij}}{\partial \alpha_1} \Delta S_{ij}^0 \\ \vdots \\ \sum_i \sum_j \frac{1}{\sigma_j^2} \frac{\partial \Delta S_{ij}}{\partial \alpha_m} \Delta S_{ij}^0 \\ \vdots \end{pmatrix}. \quad (\text{C.5})$$

Most of the terms are zero and hence the above equation can be rewritten in the following form

$$\left(\begin{array}{c|c|c|c} \sum_i C_i & \cdots & G_i & \cdots \\ \hline \vdots & \ddots & 0 & 0 \\ \hline G_i^T & 0 & \Gamma_i & 0 \\ \hline \vdots & 0 & 0 & \ddots \end{array} \right) \begin{pmatrix} \alpha_a \\ \vdots \\ \alpha_i^t \\ \vdots \end{pmatrix} = \begin{pmatrix} \sum_i b_i \\ \vdots \\ \beta_i \\ \vdots \end{pmatrix}. \quad (\text{C.6})$$

In this equation the matrices C_i, Γ_i, G_i and the vectors b_i and β_i contain contributions from the i -th track. The matrices C_i are symmetric matrices of dimension n_{det} while b_i is a vector of with size n_{det} and both contain partial derivatives of ΔS with respect to the alignment parameters α^a . The Γ_i are symmetric matrices of size v equal to the number of parameters per track (size of α_i^t vector). The β_i are vectors of size v . Both Γ_i and β_i include only derivatives of ΔS with respect to track parameters α_t . The G_i is a matrix with a row number of n_{det} and a column number of v and includes mixed terms of type $(\partial\Delta S_{ij}/\partial\alpha_j^a)(\partial\Delta S_{ij}/\partial\alpha_i^t)$.

Solving equation C.6 is very CPU time consuming. Fortunately the matrix in the given equation is sparse and has a special structure. It has been proven [121] that the alignment parameters can be extracted from much simpler equation

$$\alpha_a = (C')^{-1}b', \quad (\text{C.7})$$

where

$$C' = \sum_i C_i - \sum_i G_i \Gamma_i^{-1} G_i^T, \quad b' = \sum_i b_i - \sum_i G_i \Gamma_i^{-1} \beta_i. \quad (\text{C.8})$$

The C' matrix inversion which is the core of the alignment program is performed by a ‘‘Millepede’’ routine which was written by Volker Blobel, the co-author of Ref. [121].

C.3 The alignment procedure

The procedure of alignment consists of three main steps:

- low intensity alignment run with SM1 and SM2 switched off
- low intensity alignment run with nominal fields in SM1 and SM2
- nominal intensity physics data taking run

The low intensity of the alignment runs enables switching on GEM detector’s centres. The alignment without magnetic field simplifies the tracking as all tracks are assumed to be straight lines along the whole spectrometer. During the alignment runs special

trigger mix is used. The final alignment with physics data is usually splitted into two parts: alignment of the detectors downstream of the target and alignment of the Beam Telescope (BT) - detectors upstream of the target. In the former BT detectors are not use while in the latter positions of all other detectors are fixed.

The alignment procedure is relative. Two detectors has to be used as reference points. GEM detectors have been chosen as they are far enough from the magnets not to be affected by their fringe fields and they have good spacial resolution and suitable size. When the magnets are on (off) GM04 and GM10 (GM09) are used. Their positions are taken directly from the surveyor's measurements.

Every alignment step consists of several iterations (typically four or five) each consisting of three phases:

1. In the first one the data sample is reconstructed by the CORAL program using a description of the spectrometer stored in *detectors.dat* file. As an output, a ROOT [122] tree containing information about reconstructed tracks, hits and clusters is created.
2. In the second phase the information from the tree is used as an input for χ^2 minimisation performed by the Millepede. As a result a set of alignment parameters for each detector is obtained.
3. In the last phase the positions stored in *detectors.dat* file are updated using results from the second phase.

The parameters of different detectors can be fixed during different stages of the alignment procedure. The position along the beam z is usually fixed (obtained from the surveyor's measurements) during the whole procedure). Typically for the majority of the detectors the angle θ and the pitch p are fixed during the stage without magnetic field. The pitch is also typically fixed during the stage with magnetic field switched on while the angles are set free. In the final steps (with the use of physics data) all parameters are tuned at the same time apart from z .

C.4 Exemplary plots

In Figure C.1 exemplary residuals before and after the alignment procedure are presented.

The Figures bellow show two planes of silicon 01 detector (oriented at different angles). It can be seen, in Figure C.2 that the δU vs U plot is fine but there is a visible slope in

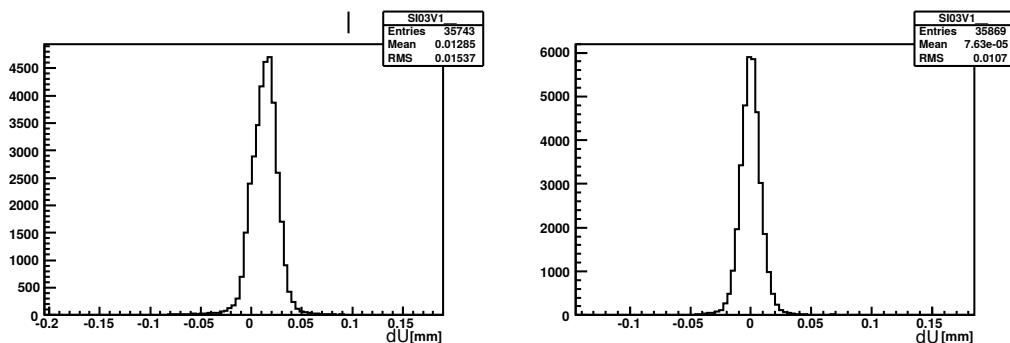


FIGURE C.1: Exemplary residual (δU histogram) plots for plane SI03 V1. Left panel: iteration nr 1 - before the alignment procedure. Right panel: after five iterations of the alignment algorithm.

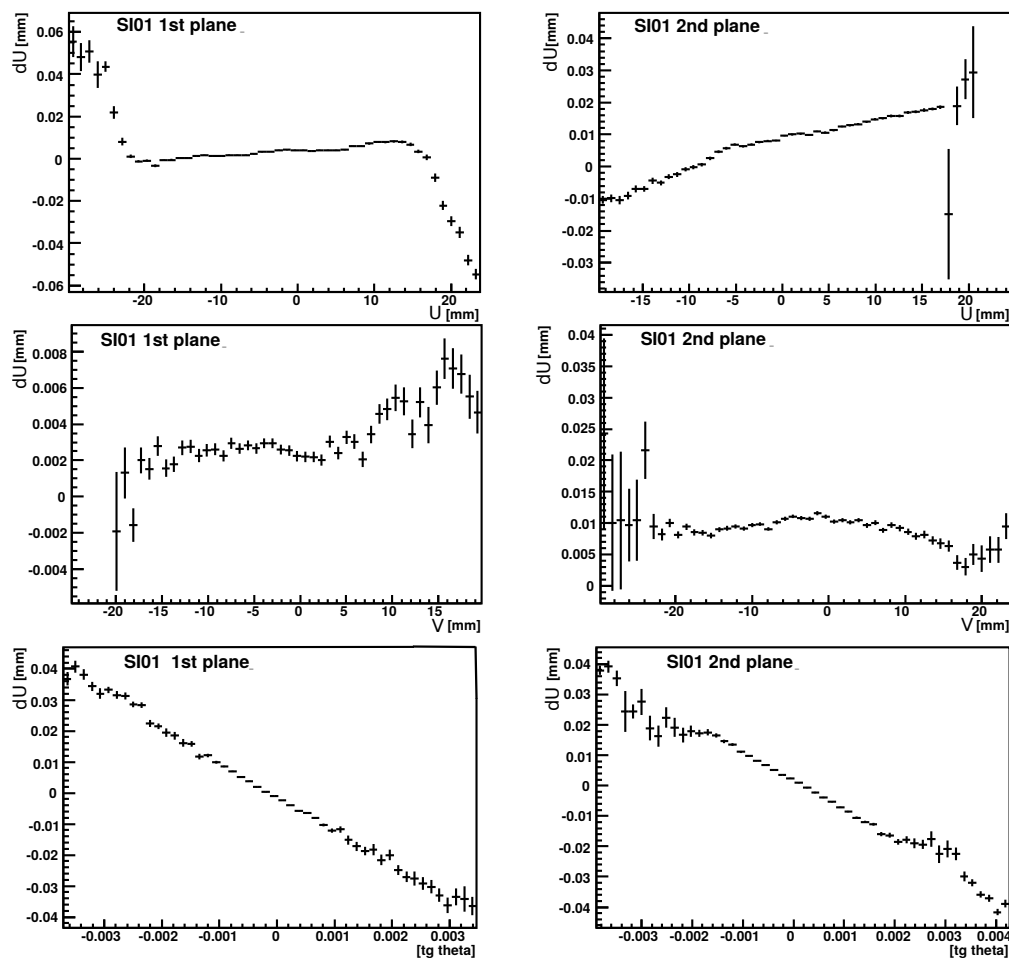


FIGURE C.2: Misalignment in z of the SI01 station. Top panel dU vs U - no slope - the angle θ is fine. Middle panel: dU vs V slope indicating the misalignment confirmed by the slope in the bottom panel: dU vs $\tan \theta$.

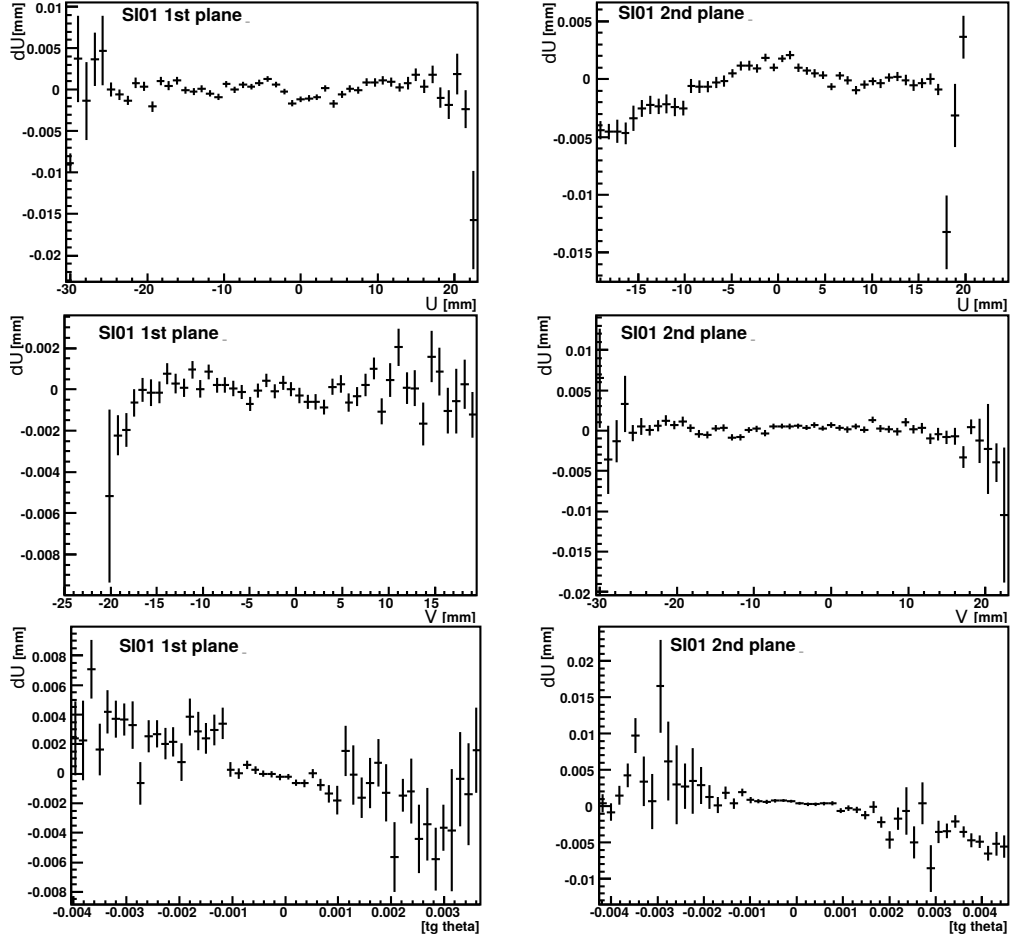


FIGURE C.3: Corrected z position of the SI01 station. Top panel dU vs U - no slope - the angle θ is fine. Middle panel: dU vs V slope indicating the misalignment confirmed by the slope in the bottom panel: dU vs $\tan \theta$.

the δU vs V plot and even more visible slope in the δU vs $\tan \theta$ plot. In Figure C.3 corrected z position of SI01 station is applied. The reason of a 5 cm discrepancy was the wrong recalculation of the detector position from the surveyor's measurements. The plots after the correction do not show any significant dependence.

C.5 Quality criteria

Apart from the local criteria, the plots composed of alignment parameters, described in Section C.1 there are also global criteria of the alignment:

- χ^2/ndf of all reconstructed tracks,
- agreement with particle data tables of reconstructed invariant masses of J/Ψ , K^0 , D^0 ,
- number of all reconstructed tracks per event,

- ratio of the numbers of tracks reconstructed in the LAS and the SAS,
- number of reconstructed vertices per event,
- number of tracks associated to vertex,
- fraction of events with reconstructed primary vertex.

During the DVCS 2012 test local criteria and the χ^2/ndf have been monitored for every iteration. The obtained mean value of the latter is 1.7. Pseudoefficiencies of all detector planes have been also monitored during the data taking. The data analysis carried out since the final alignment was ready did not show any evidence of misalignment from the global criteria given above.

Abbreviations

QCD	Q uantum C hromodynamics
DIS	D eep I nelastic S cattering
SIDIS	S emi- I nclusive D eep I nelastic S cattering
PDFs	P arton D istribution F unctions
TMDs	T ransverse M omentum D ependent D istribution F unctions
LP	L eading P rocess
QCDC	Q CD C ompton
PGF	P hoton- G luon F usion
LO	L eading O der
NLO	N ext-to- L eading O der
MC	M onte C arlo
NN	N eural N etwork
COMPASS	C OMmon M uon P roton A pparatus for S tructure and S pectroscopy

Bibliography

- [1] R. P. Feynman, “Very high-energy collisions of hadrons,” *Phys.Rev.Lett.* **23** (1969) 1415–1417.
- [2] M. Breidenbach, J. I. Friedman, H. W. Kendall, E. D. Bloom, D. Coward, *et al.*, “Observed Behavior of Highly Inelastic electron-Proton Scattering,” *Phys.Rev.Lett.* **23** (1969) 935–939.
- [3] M. Gell-Mann, “A Schematic Model of Baryons and Mesons,” *Phys.Lett.* **8** (1964) 214–215.
- [4] G. Zweig, “An SU(3) model for strong interaction symmetry and its breaking. Version 2,”.
- [5] D. J. Gross and F. Wilczek, “Ultraviolet Behavior of Nonabelian Gauge Theories,” *Phys.Rev.Lett.* **30** (1973) 1343–1346.
- [6] H. D. Politzer, “Reliable Perturbative Results for Strong Interactions?,” *Phys.Rev.Lett.* **30** (1973) 1346–1349.
- [7] **PLUTO** Collaboration, C. Berger *et al.*, “Evidence for Gluon Bremsstrahlung in $e^+ e^-$ Annihilations at High-Energies,” *Phys.Lett.* **B86** (1979) 418.
- [8] M. Alguard, W. Ash, G. Baum, J. Clendenin, P. Cooper, *et al.*, “Deep Inelastic Scattering of Polarized Electrons by Polarized Protons,” *Phys.Rev.Lett.* **37** (1976) 1261.
- [9] **European Muon** Collaboration, J. Ashman *et al.*, “A Measurement of the Spin Asymmetry and Determination of the Structure Function $g(1)$ in Deep Inelastic Muon-Proton Scattering,” *Phys.Lett.* **B206** (1988) 364.
- [10] **European Muon** Collaboration, J. Ashman *et al.*, “An Investigation of the Spin Structure of the Proton in Deep Inelastic Scattering of Polarized Muons on Polarized Protons,” *Nucl.Phys.* **B328** (1989) 1.
- [11] **Spin Muon** Collaboration, B. Adeva *et al.*, “A Next-to-leading order QCD analysis of the spin structure function $g(1)$,” *Phys.Rev.* **D58** (1998) 112002.
- [12] **E143** Collaboration, K. Abe *et al.*, “Measurements of the proton and deuteron spin structure functions $g(1)$ and $g(2)$,” *Phys.Rev.* **D58** (1998) 112003, [arXiv:hep-ph/9802357](#) [[hep-ph](#)].
- [13] **E155** Collaboration, P. Anthony *et al.*, “Measurements of the Q^{*2} dependence of the proton and neutron spin structure functions $g(1)^{*p}$ and $g(1)^{*n}$,” *Phys.Lett.* **B493** (2000) 19–28, [arXiv:hep-ph/0007248](#) [[hep-ph](#)].
- [14] **HERMES** Collaboration, A. Airapetian *et al.*, “Quark helicity distributions in the nucleon for up, down, and strange quarks from semi-inclusive deep-inelastic scattering,” *Phys.Rev.* **D71** (2005) 012003, [arXiv:hep-ex/0407032](#) [[hep-ex](#)].

- [15] **COMPASS** Collaboration, C. Adolph *et al.*, “The Spin Structure Function g_1^p of the Proton and a Test of the Bjorken Sum Rule,” [arXiv:1503.08935](#) [**hep-ex**].
- [16] K. Kurek, *Understanding the Nucleon’s Spin Structure. The Direct Gluon Polarisation Measurement at the COMPASS Experiment*. Habilitation thesis, National Centre for Nuclear Research, November, 2011. http://wwwcompass.cern.ch/compass/publications/theses/2011_hab_kurek.pdf.
- [17] K. Klimaszewski, *Determination of gluon polarisation in the nucleon from events with high- p_T hadron pairs in COMPASS experiment*. Phd thesis, Soltan Institute for Nuclear Studies, June, 2010. http://wwwcompass.cern.ch/compass/publications/theses/2010_phd_klimaszewski.pdf.
- [18] **COMPASS** Collaboration, M. Stolarski, “A new LO extraction of gluon polarisation from COMPASS DIS data,” *PoS DIS2014* (2014) 211.
- [19] D. de Florian, R. Sassot, M. Stratmann, and W. Vogelsang, “Evidence for polarization of gluons in the proton,” *Phys.Rev.Lett.* **113** no. 1, (2014) 012001, [arXiv:1404.4293](#) [**hep-ph**].
- [20] A. Accardi, J. Albacete, M. Anselmino, N. Armesto, E. Aschenauer, *et al.*, “Electron Ion Collider: The Next QCD Frontier - Understanding the glue that binds us all,” [arXiv:1212.1701](#) [**nucl-ex**].
- [21] J. P. Ralston and D. E. Soper, “Production of Dimuons from High-Energy Polarized Proton Proton Collisions,” *Nucl.Phys.* **B152** (1979) 109.
- [22] **FNAL-E704** Collaboration, D. Adams *et al.*, “Analyzing power in inclusive π^+ and π^- production at high $x(F)$ with a 200-GeV polarized proton beam,” *Phys.Lett.* **B264** (1991) 462–466.
- [23] D. W. Sivers, “Single Spin Production Asymmetries from the Hard Scattering of Point-Like Constituents,” *Phys.Rev.* **D41** (1990) 83.
- [24] M. Anselmino, A. Efremov, and E. Leader, “The Theory and phenomenology of polarized deep inelastic scattering,” *Phys.Rept.* **261** (1995) 1–124, [arXiv:hep-ph/9501369](#) [**hep-ph**].
- [25] F. Halzen and A. D. Martin, “QUARKS AND LEPTONS: AN INTRODUCTORY COURSE IN MODERN PARTICLE PHYSICS,”.
- [26] D. J. Griffiths, “INTRODUCTION TO ELEMENTARY PARTICLES,”.
- [27] J. Callan, Curtis G. and D. J. Gross, “High-energy electroproduction and the constitution of the electric current,” *Phys.Rev.Lett.* **22** (1969) 156–159.
- [28] **Particle Data Group** Collaboration, C. Amsler *et al.*, “Review of Particle Physics,” *Phys.Lett.* **B667** (2008) 1–1340.
- [29] P. Hoodbhoy, R. Jaffe, and A. Manohar, “Novel Effects in Deep Inelastic Scattering from Spin 1 Hadrons,” *Nucl.Phys.* **B312** (1989) 571.
- [30] H. Khan and P. Hoodbhoy, “Shadowing of deuteron spin structure functions,” *Phys.Lett.* **B298** (1993) 181–186.
- [31] J. Bjorken, “Asymptotic Sum Rules at Infinite Momentum,” *Phys.Rev.* **179** (1969) 1547–1553.
- [32] R. Mertig and W. van Neerven, “The Calculation of the two loop spin splitting functions $P^{(ij)}(1)(x)$,” *Z.Phys.* **C70** (1996) 637–654, [arXiv:hep-ph/9506451](#) [**hep-ph**].

- [33] W. Vogelsang, “A Rederivation of the spin dependent next-to-leading order splitting functions,” *Phys.Rev.* **D54** (1996) 2023–2029, [arXiv:hep-ph/9512218](#) [[hep-ph](#)].
- [34] W. Vogelsang, “The Spin dependent two loop splitting functions,” *Nucl.Phys.* **B475** (1996) 47–72, [arXiv:hep-ph/9603366](#) [[hep-ph](#)].
- [35] Y. L. Dokshitzer, “Calculation of the Structure Functions for Deep Inelastic Scattering and e^+e^- Annihilation by Perturbation Theory in Quantum Chromodynamics,” *Sov.Phys.JETP* **46** (1977) 641–653.
- [36] V. Gribov and L. Lipatov, “Deep inelastic $e p$ scattering in perturbation theory,” *Sov.J.Nucl.Phys.* **15** (1972) 438–450.
- [37] G. Altarelli and G. Parisi, “Asymptotic Freedom in Parton Language,” *Nucl.Phys.* **B126** (1977) 298.
- [38] E. Leader, A. V. Sidorov, and D. B. Stamenov, “Longitudinal polarized parton densities updated,” *Phys.Rev.* **D73** (2006) 034023, [arXiv:hep-ph/0512114](#) [[hep-ph](#)].
- [39] H. Wollny, *Measuring azimuthal asymmetries in semi-inclusive deep-inelastic scattering off transversely polarized protons*. Phd thesis, Fakultät für Mathematik und Physik Albert-Ludwigs-Universität Freiburg, April, 2010.
http://wwwcompass.cern.ch/compass/publications/theses/2010_phd_wollny.pdf.
- [40] A. Bacchetta, M. Diehl, K. Goeke, A. Metz, P. J. Mulders, *et al.*, “Semi-inclusive deep inelastic scattering at small transverse momentum,” *JHEP* **0702** (2007) 093, [arXiv:hep-ph/0611265](#) [[hep-ph](#)].
- [41] M. Burkardt, “Impact parameter space interpretation for generalized parton distributions,” *Int.J.Mod.Phys.* **A18** (2003) 173–208, [arXiv:hep-ph/0207047](#) [[hep-ph](#)].
- [42] M. Burkardt, “Chromodynamic lensing and transverse single spin asymmetries,” *Nucl.Phys.* **A735** (2004) 185–199, [arXiv:hep-ph/0302144](#) [[hep-ph](#)].
- [43] M. Burkardt and D. S. Hwang, “Sivers asymmetry and generalized parton distributions in impact parameter space,” *Phys.Rev.* **D69** (2004) 074032, [arXiv:hep-ph/0309072](#) [[hep-ph](#)].
- [44] D. Müller, D. Robaschik, B. Geyer, F. M. Dittes, and J. Hořejši, “Wave functions, evolution equations and evolution kernels from light ray operators of QCD,” *Fortsch. Phys.* **42** (1994) 101–141, [arXiv:hep-ph/9812448](#) [[hep-ph](#)].
- [45] S. L. Adler, “Axial vector vertex in spinor electrodynamics,” *Phys.Rev.* **177** (1969) 2426–2438.
- [46] R. Jaffe, “The Axial Anomaly and the Sum Rules for Spin Dependent Electroproduction,” *Phys.Lett.* **B193** (1987) 101.
- [47] G. Altarelli and G. G. Ross, “The Anomalous Gluon Contribution to Polarized Leptoproduction,” *Phys.Lett.* **B212** (1988) 391.
- [48] R. D. Carlitz, J. C. Collins, and A. H. Mueller, “The Role of the Axial Anomaly in Measuring Spin Dependent Parton Distributions,” *Phys.Lett.* **B214** (1988) 229.
- [49] E. Leader and D. B. Stamenov, “Can the polarization of the strange quarks in the proton be positive?,” *Phys.Rev.* **D67** (2003) 037503, [arXiv:hep-ph/0211083](#) [[hep-ph](#)].
- [50] W. A. Bardeen, A. Buras, D. Duke, and T. Muta, “Deep Inelastic Scattering Beyond the Leading Order in Asymptotically Free Gauge Theories,” *Phys.Rev.* **D18** (1978) 3998.

- [51] J. Bjorken, “Applications of the Chiral $U(6) \times (6)$ Algebra of Current Densities,” *Phys.Rev.* **148** (1966) 1467–1478.
- [52] J. Bjorken, “Inelastic Scattering of Polarized Leptons from Polarized Nucleons,” *Phys.Rev.* **D1** (1970) 1376–1379.
- [53] **COMPASS** Collaboration, M. Alekseev *et al.*, “The Spin-dependent Structure Function of the Proton g_1^p and a Test of the Bjorken Sum Rule,” *Phys.Lett.* **B690** (2010) 466–472, [arXiv:1001.4654 \[hep-ex\]](#).
- [54] S. D. Bass, “The Spin structure of the proton,”.
- [55] **Spin Muon (SMC)** Collaboration, B. Adeva *et al.*, “Spin asymmetries for events with high $p(T)$ hadrons in DIS and an evaluation of the gluon polarization,” *Phys.Rev.* **D70** (2004) 012002, [arXiv:hep-ex/0402010 \[hep-ex\]](#).
- [56] **HERMES** Collaboration, A. Airapetian *et al.*, “Measurement of the spin asymmetry in the photoproduction of pairs of high $p(T)$ hadrons at HERMES,” *Phys.Rev.Lett.* **84** (2000) 2584–2588, [arXiv:hep-ex/9907020 \[hep-ex\]](#).
- [57] **HERMES** Collaboration, A. Airapetian *et al.*, “Leading-Order Determination of the Gluon Polarization from high- $p(T)$ Hadron Electroproduction,” *JHEP* **1008** (2010) 130, [arXiv:1002.3921 \[hep-ex\]](#).
- [58] **COMPASS** Collaboration, C. Adolph *et al.*, “Leading and Next-to-Leading Order Gluon Polarization in the Nucleon and Longitudinal Double Spin Asymmetries from Open Charm Muoproduction,” *Phys.Rev.* **D87** no. 5, (2013) 052018, [arXiv:1211.6849 \[hep-ex\]](#).
- [59] **COMPASS Collaboration** Collaboration, C. Adolph *et al.*, “Leading order determination of the gluon polarisation from DIS events with high- p_T hadron pairs,” *Phys.Lett.* **B718** (2013) 922–930, [arXiv:1202.4064 \[hep-ex\]](#).
- [60] **PHENIX** Collaboration, A. Adare *et al.*, “Inclusive double-helicity asymmetries in neutral-pion and eta-meson production in $\bar{p} + \bar{p}$ collisions at $\sqrt{s} = 200$ GeV,” *Phys. Rev.* **D90** no. 1, (2014) 012007, [arXiv:1402.6296 \[hep-ex\]](#).
- [61] **STAR** Collaboration, L. Adamczyk *et al.*, “Observation of charge asymmetry dependence of pion elliptic flow and the possible chiral magnetic wave in heavy-ion collisions,” *Phys. Rev. Lett.* **114** no. 25, (2015) 252302, [arXiv:1504.02175 \[nucl-ex\]](#).
- [62] T. Sjostrand, “High-energy physics event generation with PYTHIA 5.7 and JETSET 7.4,” *Comput.Phys.Commun.* **82** (1994) 74–90.
- [63] G. Ingelman, A. Edin, and J. Rathsman, “LEPTO 6.5: A Monte Carlo generator for deep inelastic lepton - nucleon scattering,” *Comput.Phys.Commun.* **101** (1997) 108–134, [arXiv:hep-ph/9605286 \[hep-ph\]](#).
- [64] **Spin Muon (SMC)** Collaboration, D. Adams *et al.*, “Spin structure of the proton from polarized inclusive deep inelastic muon - proton scattering,” *Phys.Rev.* **D56** (1997) 5330–5358, [arXiv:hep-ex/9702005 \[hep-ex\]](#).
- [65] C. Bourrely, J. Soffer, F. Renard, and P. Taxil, “SPIN EFFECTS AT SUPERCOLLIDER ENERGIES,” *Phys.Rept.* **177** (1989) 319.
- [66] M. Gluck, E. Reya, M. Stratmann, and W. Vogelsang, “Models for the polarized parton distributions of the nucleon,” *Phys.Rev.* **D63** (2001) 094005, [arXiv:hep-ph/0011215 \[hep-ph\]](#).

- [67] M. Gluck, E. Reya, and A. Vogt, “Dynamical parton distributions revisited,” *Eur.Phys.J.* **C5** (1998) 461–470, [arXiv:hep-ph/9806404](#) [hep-ph].
- [68] M. Gluck, E. Reya, and I. Schienbein, “Radiatively generated parton distributions of real and virtual photons,” *Phys.Rev.* **D60** (1999) 054019, [arXiv:hep-ph/9903337](#) [hep-ph].
- [69] M. Gluck, E. Reya, and C. Sieg, “Spin dependent structure functions of real and virtual photons,” *Eur.Phys.J.* **C20** (2001) 271–281, [arXiv:hep-ph/0103137](#) [hep-ph].
- [70] COMPASS Collaboration, E. Ageev *et al.*, “Gluon polarization in the nucleon from quasi-real photoproduction of high-p(T) hadron pairs,” *Phys.Lett.* **B633** (2006) 25–32, [arXiv:hep-ex/0511028](#) [hep-ex].
- [71] C. Bernet *et al.*, “Measurement of $\Delta G/G$ in the production of high p T hadron pairs at low Q^2 (2004 data),” 2006. COMPASS note 2006-8.
- [72] HERMES Collaboration, K. Ackerstaff *et al.*, “The HERMES spectrometer,” *Nucl.Instrum.Meth.* **A417** (1998) 230–265, [arXiv:hep-ex/9806008](#) [hep-ex].
- [73] M. Gluck, E. Reya, and C. Sieg, “Spin dependent structure functions of the photon,” *Phys. Lett.* **B503** (2001) 285–291, [arXiv:hep-ph/0102014](#) [hep-ph].
- [74] STAR Collaboration, K. H. Ackermann *et al.*, “STAR detector overview,” *Nucl. Instrum. Meth.* **A499** (2003) 624–632.
- [75] PHENIX Collaboration, K. Adcox *et al.*, “PHENIX detector overview,” *Nucl. Instrum. Meth.* **A499** (2003) 469–479.
- [76] D. de Florian, R. Sassot, M. Stratmann, and W. Vogelsang, “Extraction of Spin-Dependent Parton Densities and Their Uncertainties,” *Phys.Rev.* **D80** (2009) 034030, [arXiv:0904.3821](#) [hep-ph].
- [77] NNPDF Collaboration, R. D. Ball, S. Forte, A. Guffanti, E. R. Nocera, G. Ridolfi, and J. Rojo, “Unbiased determination of polarized parton distributions and their uncertainties,” *Nucl. Phys.* **B874** (2013) 36–84, [arXiv:1303.7236](#) [hep-ph].
- [78] X.-D. Ji, “Gauge-Invariant Decomposition of Nucleon Spin,” *Phys. Rev. Lett.* **78** (1997) 610–613, [arXiv:hep-ph/9603249](#) [hep-ph].
- [79] C. Adolph, R. Akhunzyanov, M. Alexeev, G. Alexeev, A. Amoroso, *et al.*, “Collins and Sivers asymmetries in muonproduction of pions and kaons off transversely polarised proton,” [arXiv:1408.4405](#) [hep-ex].
- [80] HERMES Collaboration, A. Airapetian *et al.*, “Effects of transversity in deep-inelastic scattering by polarized protons,” *Phys. Lett.* **B693** (2010) 11–16, [arXiv:1006.4221](#) [hep-ex].
- [81] COMPASS Collaboration, C. Adolph *et al.*, “Exclusive ρ^0 muoproduction on transversely polarised protons and deuterons,” *Nucl. Phys.* **B865** (2012) 1–20, [arXiv:1207.4301](#) [hep-ex].
- [82] S. V. Goloskokov and P. Kroll, “The Target asymmetry in hard vector-meson electroproduction and parton angular momenta,” *Eur. Phys. J.* **C59** (2009) 809–819, [arXiv:0809.4126](#) [hep-ph].
- [83] S. N. Syritsyn, J. R. Green, J. W. Negele, A. V. Pochinsky, M. Engelhardt, P. Hagler, B. Musch, and W. Schroers, “Quark Contributions to Nucleon Momentum and Spin from Domain Wall fermion calculations,” *PoS LATTICE2011* (2011) 178, [arXiv:1111.0718](#) [hep-lat].

- [84] D. B. Kaplan, “A Method for simulating chiral fermions on the lattice,” *Phys. Lett.* **B288** (1992) 342–347, [arXiv:hep-lat/9206013](#) [[hep-lat](#)].
- [85] **MILC** Collaboration, K. Orginos, D. Toussaint, and R. L. Sugar, “Variants of fattening and flavor symmetry restoration,” *Phys. Rev.* **D60** (1999) 054503, [arXiv:hep-lat/9903032](#) [[hep-lat](#)].
- [86] M. Anselmino, U. D’Alesio, S. Melis, and F. Murgia, “Constraints on gluon Sivers distribution from RHIC results,” *AIP Conf.Proc.* **915** (2007) 567–570, [arXiv:hep-ph/0612209](#) [[hep-ph](#)].
- [87] U. D’Alesio, F. Murgia, and C. Pisano, “Towards a first estimate of the gluon Sivers function from A_N data in pp collisions at RHIC,” [arXiv:1506.03078](#) [[hep-ph](#)].
- [88] M. Anselmino, M. Boglione, U. D’Alesio, A. Kotzinian, F. Murgia, and A. Prokudin, “Extracting the Sivers function from polarized SIDIS data and making predictions,” *Phys. Rev.* **D72** (2005) 094007, [arXiv:hep-ph/0507181](#) [[hep-ph](#)]. [Erratum: *Phys. Rev.*D72,099903(2005)].
- [89] M. Anselmino, M. Boglione, U. D’Alesio, A. Kotzinian, S. Melis, F. Murgia, A. Prokudin, and C. Turk, “Sivers Effect for Pion and Kaon Production in Semi-Inclusive Deep Inelastic Scattering,” *Eur. Phys. J.* **A39** (2009) 89–100, [arXiv:0805.2677](#) [[hep-ph](#)].
- [90] **PHENIX** Collaboration, A. Adare *et al.*, “Measurement of transverse-single-spin asymmetries for midrapidity and forward-rapidity production of hadrons in polarized p+p collisions at $\sqrt{s}=200$ and 62.4 GeV,” *Phys. Rev.* **D90** no. 1, (2014) 012006, [arXiv:1312.1995](#) [[hep-ex](#)].
- [91] S. J. Brodsky, F. Fleuret, C. Hadjidakis, and J. P. Lansberg, “Physics Opportunities of a Fixed-Target Experiment using the LHC Beams,” *Phys. Rept.* **522** (2013) 239–255, [arXiv:1202.6585](#) [[hep-ph](#)].
- [92] **COMPASS** Collaboration, F. Gautheron *et al.*, “COMPASS-II Proposal,”.
- [93] **COMPASS** Collaboration, V. Y. Alexakhin *et al.*, “The Deuteron Spin-dependent Structure Function $g_1(d)$ and its First Moment,” *Phys.Lett.* **B647** (2007) 8–17, [arXiv:hep-ex/0609038](#) [[hep-ex](#)].
- [94] **COMPASS Collaboration** Collaboration, M. Alekseev *et al.*, “Collins and Sivers asymmetries for pions and kaons in muon-deuteron DIS,” *Phys.Lett.* **B673** (2009) 127–135, [arXiv:0802.2160](#) [[hep-ex](#)].
- [95] **COMPASS** Collaboration, C. Adolph *et al.*, “Transverse target spin asymmetries in exclusive ρ^0 muoproduction,” *Phys. Lett.* **B731** (2014) 19–26, [arXiv:1310.1454](#) [[hep-ex](#)].
- [96] **COMPASS** Collaboration, C. Adolph *et al.*, “Measurement of radiative widths of $a_2(1320)$ and $\pi_2(1670)$,” *Eur. Phys. J.* **A50** (2014) 79, [arXiv:1403.2644](#) [[hep-ex](#)].
- [97] **COMPASS** Collaboration, C. Adolph *et al.*, “Observation of a new narrow axial-vector meson $a_1(1420)$,” [arXiv:1501.05732](#) [[hep-ex](#)].
- [98] **COMPASS** Collaboration, C. Adolph *et al.*, “Measurement of the charged-pion polarizability,” *Phys. Rev. Lett.* **114** (2015) 062002, [arXiv:1405.6377](#) [[hep-ex](#)].
- [99] P. Sznajder, *Study of azimuthal asymmetries in exclusive leptonproduction of vector mesons on transversely polarised protons and deuterons*. Phd thesis, Soltan Institute for Nuclear Studies, March, 2015. https://wwwcompass.cern.ch/compass/publications/theses/2015_phd_sznajder.pdf.
- [100] A. Abragam and M. Goldman, *Nuclear Magnetism: Order and Disorder*. Clarendon Press, Oxford, 1982.
- [101] J. Koivuniemi *et al.*, “Measurement of the charged-pion polarizability,” *J. Phys. Conf.* **150** (2009) 012023.

- [102] C. Bernet *et al.*, “The COMPASS trigger system for muon scattering,” *Nucl. Instrum. Meth.* **A550** (2005) 217–240.
- [103] W. Carena *et al.*, “ALICE DAQ and ECS User’s Guide,”.
- [104] “Coral.” [Http://coral.web.cern.ch/coral](http://coral.web.cern.ch/coral).
- [105] “Phast.” [Http://ges.home.cern.ch/ges/phast/index.html](http://ges.home.cern.ch/ges/phast/index.html).
- [106] K. Gustafsson, “Computation of the Dilution Factor for the Year 2002 COMPASS Data,” 2003. COMPASS note 2003-3.
- [107] A. A. Akhundov, D. Y. Bardin, L. Kalinovskaya, and T. Riemann, “Model independent QED corrections to the process $ep \rightarrow eX$,” *Fortsch.Phys.* **44** (1996) 373–482, [arXiv:hep-ph/9407266](https://arxiv.org/abs/hep-ph/9407266) [[hep-ph](#)].
- [108] **COMPASS Collaboration** Collaboration, P. Abbon *et al.*, “The COMPASS experiment at CERN,” *Nucl.Instrum.Meth.* **A577** (2007) 455–518, [arXiv:hep-ex/0703049](https://arxiv.org/abs/hep-ex/0703049) [[hep-ex](#)].
- [109] R. J. Barlow, *Statistics: A Guide to the Use of Statistical Methods in the Physical Sciences*. Wiley, 1989.
- [110] T. Sjostrand, S. Mrenna, and P. Z. Skands, “PYTHIA 6.4 Physics and Manual,” *JHEP* **0605** (2006) 026, [arXiv:hep-ph/0603175](https://arxiv.org/abs/hep-ph/0603175) [[hep-ph](#)].
- [111] J. Pretz, “Comparison of methods to extract an asymmetry parameter from data,” *Nucl.Instrum.Meth.* **A659** (2011) 456–461, [arXiv:1104.1038](https://arxiv.org/abs/1104.1038) [[physics.data-an](#)].
- [112] J. Pretz and J.-M. Le Goff, “Simultaneous Determination of Signal and Background Asymmetries,” *Nucl.Instrum.Meth.* **A602** (2009) 594–596, [arXiv:0811.1426](https://arxiv.org/abs/0811.1426) [[physics.data-an](#)].
- [113] A. Bravar, K. Kurek, and R. Windmolders, “POLDIS: A Monte Carlo for POLarized (semiinclusive) deep inelastic scattering,” *Comput.Phys.Commun.* **105** (1997) 42–61, [arXiv:hep-ph/9704313](https://arxiv.org/abs/hep-ph/9704313) [[hep-ph](#)].
- [114] “Comgeant.” [Http://valexakh.web.cern.ch/valexakh/wwwcomg/index.html](http://valexakh.web.cern.ch/valexakh/wwwcomg/index.html).
- [115] **New Muon Collaboration** Collaboration, M. Arneodo *et al.*, “Measurement of the proton and deuteron structure functions, $F_2(p)$ and $F_2(d)$, and of the ratio σ_{L} / σ_{T} ,” *Nucl.Phys.* **B483** (1997) 3–43, [arXiv:hep-ph/9610231](https://arxiv.org/abs/hep-ph/9610231) [[hep-ph](#)].
- [116] R. Brun *et al.*, “GEANT Detector description and simulation tool: CERN Program Library Long Wriiteup.,” *Technical Report W5013*, CERN (1994) .
- [117] M. Leshno, V. Y. Lin, A. Pinkus, and S. Schocken *Neural Networks* **6(6)** (1993) 861–867.
- [118] R. Sulej, “Netmaker.” [Http://www.ire.pw.edu.pl/~rsulej/netmaker/](http://www.ire.pw.edu.pl/~rsulej/netmaker/).
- [119] S. Gliske, A. Bacchetta, and M. Radici, “Production of two hadrons in semi-inclusive deep inelastic scattering,” *Phys.Rev.* **D90** no. 11, (2014) 114027, [arXiv:1408.5721](https://arxiv.org/abs/1408.5721) [[hep-ph](#)].
- [120] H. Pereira and J.-M. Le Goff, “COMPASS spectrometer alignment.,” 2004. COMPASS note 2003-4.
- [121] V. Blobel and C. Kleinwort, “A New Method for the High-Precision Alignment of Track Detectors,”. <https://cds.cern.ch/record/576832>.
- [122] R. Brun and F. Rademakers, “ROOT: An object oriented data analysis framework,” *Nucl. Instrum. Meth.* **A389** (1997) 81–86.

Acknowledgements

In the first place I want to thank my Mom who has been the first and voluntary copy-reader of this thesis. I am also grateful to my Dad for the help in the choice of the subject of my PhD studies and many inspiring discussions during my scientific work.

I am sincerely thankful to Konrad Klimaszewski who has been willing to help in the physics and technical problems I encountered and whose programming tools I used during the analysis. A very special thanks to Paweł Sznajder for acquainting me with the technicalities of COMPASS data analysis. I am very grateful to Andrzej Sandacz for his scientific wisdom which he enjoys sharing very much. I thank Luis Silva for doing a fast and trouble-free crosscheck. I am very grateful to the members of the COMPASS collaboration in particular Heiner Wollny and the Transversity group.

Many thanks to Marcin Stolarski whose statistical ideas led to the results I obtained. Finally, I am very grateful to Krzysztof Kurek, my supervisor, who guided me through the beautiful but complicated world of spin physics.